The Effects of Wear on Abradable Honeycomb Labyrinth Seals

Dermot Collins

CRANFIELD UNIVERSITY

SCHOOL OF ENGINEERING

Department of Power, Propulsion & Aerospace Engineering

Degree Sought: EngD - Full Time

CRANFIELD UNIVERSITY

SCHOOL OF ENGINEERING

Department of Power, Propulsion & Aerospace Engineering

Degree Sought: EngD - Full Time

Date of Registration: 7th October 2002 - 6th October 2006

Author: **Dermot Collins**

Title: **The Effects of Wear on Abradable Honeycomb Labyrinth Seals**

Academic Supervisor: Dr. Joao Amaral Teixeira

Industrial Supervisor: Pete Crudgington

Management Supervisor: Dr. Paul Chapman

Date of Presentation: March 2007

Abstract

This thesis reports on work undertaken to understand the effects, due to wear, on the performance of abradable honeycomb labyrinth seals. The phenomena studied are aerodynamic in nature and include compressible flow, turbulent flow, recirculation and separation at a range of pressure ratios from 1.20 up to 3.50. Four primary methods of investigation were used: experimental, numerical using CFD, numerical using theoretical derivations and numerical using established labyrinth seal specific computer codes. Effects of seal clearance, pressure ratio and tooth to groove location have been investigated with overall performance and inter-seal pressure distribution recorded experimentally and numerically for comparison.

Worn experimental results, when compared to their unworn equivalent, recorded large increases in mass flow of up to 50% when the labyrinth teeth are located centrally in the groove. Significant performance enhancements were achieved through offsetting the teeth with respect to the groove, particularly in an upstream sense. There was a marked deterioration with the labyrinth teeth located at the groove exit. Inter-seal pressure distributions showed that the first and final teeth did most of the work achieving significantly larger pressure drops which goes against current seal understanding of increasing pressure drop through the seal.

Numerical work was undertaken to further investigate these effects. However, due to the complex 3-D geometry of an abradable honeycomb labyrinth seal a 2-D simplification technique was developed to speed up the investigative process. Using this technique CFD was found capable of replicating the experimental data regarding overall seal performance and inter-seal pressure distributions. The pressure on the final tooth proved to be the hardest experimental data to recreate using CFD, particularly at high pressure ratios when shocks are likely to form.

Further numerical work was undertaken using computer codes and theoretical derivations. This work proved that the understanding of the seal loss coefficients used by both methods was not adequate for the current study with the experimental data recreated least successfully.

Suggestions are given for enhancement of seal design, including axial location and seal computational routines, which will limit the impact of a 1.5% increase in operational cost that is likely to accrue from seal deterioration.

Acknowledgement

I would like to thank my engineering supervisors, of whom there were two. Professor Paul Ivey helped lay the foundations of the work prior to departing Cranfield University to become the Head of Engineering at the University of Hertfordshire. This increased the already not insignificant involvement of Dr. Joao Teixeira, from an advisory capacity to the role of full engineering supervisor. Without his guidance and insistence for one more pass the work would be of a noticeable lower quality.

Additionally, my management supervisor Dr. Paul Chapman, proved as good a listener as an advisor. I like to think I reminded him of happier times of his previous life as an engineer prior to his current engagement with the black art of demand chain management.

Two other departmental employees and a departmental consultant have speeded the experimental work along in their own unique way: Bernard Charnley, Dick Lutley and Chris Freeman. Bernard provided his knowledge and experience on all things to do with instrumentation and data management. Dick fulfilled all that could be asked of him to ensure the mechanical integrity and sound running of the experiment, albeit with a vastly reduced budget. Chris provided sound advice on all things of a fluid dynamic nature, whilst interspersing these nuggets with enough knowledge to run a farm and write a book on military history.

I would also like to thank all of my family and friends for the support and motivation they have provided. This includes the friends made in my enjoyable (but distracting) year as President of the Cranfield Students Association and the friends that I developed through Bedford Queens Rugby Club where the art of coarse rugby is alive and well.

And last but not least I need to profusely thank my wife, Ann. Without her encouragement, never-ending support and ability to lighten the mood on key occasions this journey would have been a lot more difficult and significantly less enjoyable.

Thank you, all of you,

Dermot

Contents

List of Figures

List of Tables

Nomenclature

Physical Constants

$^\circ$ Angular degree.

$^\circ C$ Degrees Celsius.

ft Foot. British imperial unit. ($=12in$)

g Gramme.

in Inch. British imperial unit. ($=25.4mm$)

K Kelvin. ($=^\circ C+273.1$)

lb Pound. British imperial unit. ($=453.592g$)

m Metre.

nm Nautical mile. ($=1.853184km$)

sec second.

rad Radian.

$Tonne$ Metric tonne. ($= 1000kg$)

Labyrinth Seal Descriptors

Cl Labyrinth seal clearance. (mm)

Gd Groove depth. (mm)

Gw Groove width. (mm)

Hs Honeycomb cell size. (mm)

Ht Labyrinth tooth height. (mm)

L Overall labyrinth seal length. (mm)

n Number of labyrinth teeth.

n_{ID} Ideal number of teeth as used by Egli (1935).

Ph Labyrinth tooth pitch. (mm)

Tp Labyrinth tooth tip thickness. (mm)

Physical Quantities

A Geometrical area. (m^2)

Atm Atmospheric air pressure. $(1\ Atm = 101325Pa)$

b Byte. Unit of meaure of computer storage.

Bar Pressure. $(= 10^5 Pa)$

Bel Logarithmic unit of measure. Non-dimensional.

C_d Discharge coefficient. Non-dimensional. $\left(= \frac{\dot{m}_{ACT}}{\dot{m}_{ID}}\right)$

c_p Coefficient of specific heat at constant pressure. $\left(\frac{m^2}{sec^2 K}\right)$

c_v Coefficient of specific heat at constant volume. $\left(\frac{m^2}{sec^2 K}\right)$

COF Carry over factor. Non-dimensional.

Cm_r Rotor moment coefficient.

D Internal diameter of pipe containing orifice plate. (m)

d Diameter of hole in orifice plate. (m)

e Internal energy. (Joule).

f_x Wall friction.

f_f Fanning friction factor. Non-dimensional. $\left(= \frac{\tau_w}{0.5\rho V^2}\right)$

h_{EFF} Heat transfer coefficient. $\left(\frac{W}{m^2 K}\right)$

k Turbulent kinetic energy. $\left(\frac{m}{sec}\right)^2$

l Turbulent length scale. (m)

L_c Characteristic length. (m)

K_{tc} Thermal conductivity. $\left(\frac{W}{mK}\right)$

$\frac{\dot{m}\sqrt{T_{t(0)}}}{AP_{t(0)}}$ Mass Flow Parameter. $\left(\frac{Ksec}{m}\right)$

Ma Mach number. Non dimensional. $\left(= \frac{V}{\sqrt{\gamma RT_s}}\right)$

M_r Torque acting on a rotating disc. (Nm)

$\dot{m}_{ACT}$ Actual mass flow. $\left(\frac{kg}{sec}\right)$

$\dot{m}_{ID}$ Ideal mass flow. $\left(\frac{kg}{sec}\right)$

N Newton. $\left(\frac{kgm}{s^2}\right)$

Nu Nusselt number. Non dimensional. $\left(= \frac{convective\,heat\,transfer}{conductive\,heat\,transfer} = \frac{h_{eff}L_c}{K_{tc}}\right)$

Pa Pascal. $\left(\frac{N}{m^2}\right)$

Pr Prandtl number. Non dimensional. $\left(= \frac{\mu C_p}{\gamma}\right)$

psi Pound per square inch. $(= 6894.75Pa)$.

$\dot{q}$ Total heat flux due to thermal conductivity. $\left(= -\left(\frac{\partial \dot{q}_x}{\partial x} + \frac{\partial \dot{q}_y}{\partial y} + \frac{\partial \dot{q}_z}{\partial z}\right) dxdydz\right)\left(\frac{Joule}{m^2 s}\right)$

r Radius (m)

r_{ID} Internal radius. (mm)

r_{OD} External radius. (mm)

R Thermocouple Recovery Factor

Re Reynolds number. Non-dimensional. $\left(= \frac{\rho V L_c}{\mu}\right)$

Re_{AX} Axial Reynolds number. $\left(= \frac{\dot{m}}{\mu \pi r}\right)$

Re_D Reynolds number with L_c based on pipe diameter.

Re_{ROT} Rotational Reynolds number. $\left(= \frac{\omega_r r^2}{\nu}\right)$

Re_{T-F} Through-flow Reynolds number. $\left(= \frac{\dot{m}}{r\mu}\right)$

rpm Revolutions per minute.

SFC Specific fuel consumption. $\left(\frac{g}{kWh}\right)$

Ta Taylor number. Non dimensional. $Ta_{CRIT} \approx 1700$ $\left(= \frac{r_{ID}(r_{OD}-r_{ID})^3 {\omega_r}^2}{\nu^2}\right)$

u Velocity component in X direction. $\left(\frac{m}{sec}\right)$

u^* Frictional velocity. $\left(\frac{m}{sec}\right)$

v Velocity component in Y direction. $\left(\frac{m}{sec}\right)$

V Total fluid velocity. $\left(\frac{m}{sec}\right)$

$\mathbf{V}$ Velocity vector field. (ui, vj, wk)

V_t Volt.

w Velocity component in Z direction. $\left(\frac{m}{sec}\right)$

W Watt $(\frac{Nm}{sec})$

y^+ Boundary layer parameter. Non dimensional. $\left(= \frac{y_w u^*}{\nu}\right)$

y_w Distance from the wall. (m)

$\frac{g}{ppkm}$ Grammes per passenger kilometre.

Physical Quantities: Greek Letters

α Under relaxation factor.

β Expansion angle. $(^\circ)$

δ_e Geometric expansion area. (m^2)

ϵ Turbulence dissipation rate. $\left(\frac{k^{\left(\frac{3}{2}\right)}}{L}\right)$

ϵ_x Orifice expansibility factor. Non-Dimensional.

γ Isentropic exponent. $\left(= \frac{c_p}{c_v}\right)$

μ Dynamic viscosity. $\left(\frac{kg}{msec}\right)$

ν Kinematic viscosity. $\left(= \frac{\mu}{\rho}\right)$ $\left(\frac{m^2}{sec}\right)$

ω Turbulence frequency. (Hz)

ω_r Rotational velocity. $\left(\frac{rad}{sec}\right)$

ϕ Variable.

ρ Density. $\left(\frac{kg}{m^3}\right)$

τ_{ij} Shear stress in j direction on a face normal to the i axis. (Pa)

τ_w Wall Shear stress. (Pa)

ξ Average change in cross sectional area of honeycomb labyrinth seal. (Schramm et al. (2002))

Names of Substances

CO Carbon Monoxide.

CO_2 Carbon Dioxide.

He Helium.

H_2O Water.

NO_x Oxides of Nitrogen.

Abbreviations

$Cross$ Cross Manufacturing Ltd.

EU European Union.

GDP Gross Domestic Product.

$IATA$ International Air Transport Association.

IEA International Energy Agency.

$IPCC$ Intergovernmental Panel on Climate Change.

$ISO9000$ Quality Standard: International Standard for Organisation.

$NADCAP$ Quality Standard: National Aerospace and Defence Contractors Accreditation Programme.

$ppkm$ Per Passenger Kilometre.

PUV Perceived use value.

VFM Value for money.

Labels

$A1$ Labyrinth tooth to honeycomb position. Location 1.

$A2$ Labyrinth tooth to honeycomb position. Location 2.

AVG Average.

$G1$ Groove after first stage of wear.

$G2$ Groove after second stage of wear.

H_1 Graphical constant from Abramovich (1963).

H_2 Graphical constant from Abramovich (1963).

$v1$ First set of results.

$v2$ Second set of results

Mathematical Constants

π Mathematical constant. Ratio of a circle's circumference to its diameter.

Mathematical Operators

$\cdot$ Matrix multiplication operator.

Δ Difference.

∇ Vector gradient operator. $\left(i\frac{\partial}{\partial x} + j\frac{\partial}{\partial y} + k\frac{\partial}{\partial z}\right)$

Suffixes

$_c$ Characterstic.

$_{Crit}$ Critical conditions. $(Ma \geq 1)$

$_{eff}$ Effective.

$_{mean}$ Mean.

$_{meas}$ Measured.

$_{MO}$ Momentum mixed out conditions.

$_n$ Condtitions at tooth number n.

$_{nom}$ Nominal.

$_{REF}$ Reference.

$_s$ Static conditions.

$_t$ Total conditions.

Prefixes

G Giga. $(= 10^9)$

M Mega. $(= 10^6)$

k kilo. $(= 10^3)$

d deci. $(= 10^{-1})$

m milli. $(= 10^{-3})$

Chapter 1

Introduction

1.1 Project Overview

In recent years the public have become aware of the environmental impact of their actions. This has led to the development of many environmental and business initiatives including, for example, carbon offsetting and responsible tourism, all of which are aimed at reducing the environmental impact of the public's actions. This, coupled with high fossil fuel prices, have concentrated the minds of businesses into methods of reducing their fossil fuel consumption and hence improving their environmental performance and profitability simultaneously. In this regard the power generation and aviation industries are no different. Aviation is often cited as a large polluter with a rapidly expanding customer base. This, coupled with the uncertain effects of emissions at altitude, may mean aviation is responsible for a disproportionately negative environmental impact. However, with enhanced price competition, both of these industries are keen to operate modern efficient plants using efficient operational techniques. This has enhanced the focus on the design of power plant components, particularly those of a high cost-benefit ratio. Rotating seals, vital components of gas and steam turbines, have consistently been an economic and important area of redevelopment (Stocker (1977), Steinetz and Hendricks (1998)). They operate within part of a vital larger system, the internal air system, which plays a key role in turbine integrity. The internal air system is responsible for vital functions including balancing bearing loads, providing cooling air from relatively cold sections of the gas turbine engine to hot sections, preventing ingress of hot gas into turbine cavities and minimising parasitic leakages throughout the engine. The labyrinth seal is a particular type of rotating seal that was invented over 100 years ago. Since its inception the performance of the labyrinth seal has steadily improved due to enhanced understanding but still today designers have areas of uncertainty regarding performance. This was reported by Zabriske and Sternlicht (1959) who found wide variations of up to 200% in available techniques. Even today

the method of Vermes (1961), which itself is largely based on a previous method of Martin (1908), is still commonly used for preliminary design calculations. Therefore rotating seals, including the labyrinth seal, are still an active and important area of research to the current day.

The labyrinth seal works by throttling flow through small successive openings in series, each one of which converts pressure into velocity which ideally is dissipated in the intervening chambers. However, in an actual seal a portion of the velocity that is created is carried over into the next chamber creating a non-ideal process. The basic design and function of a two tooth labyrinth seal containing a single intervening cavity can be seen in fig. (1.1). Typically a modern labyrinth seal contains 4-5 teeth and with the addition of more teeth the process highlighted in fig. (1.1) is repeated. Rotation of a labyrinth seal is also known to raise the temperature through a windage effect that is primarily dependent upon rotational velocity and surface roughness (e.g. McGreehan and Ko (1989), Millward and Edwards (1996)).

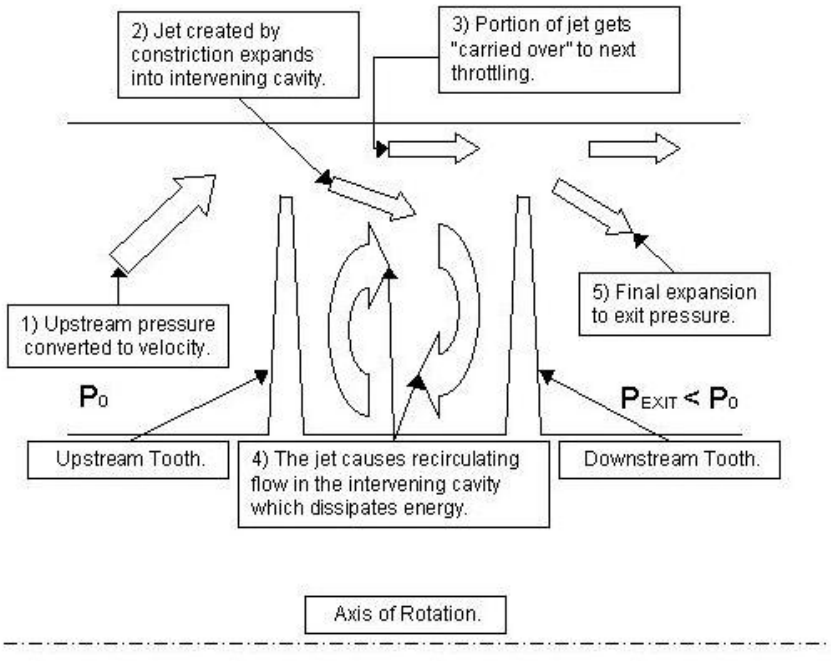

Figure 1.1: Flow Through a Straight Through Labyrinth Seal.

The dominating factor of labyrinth seal performance is the clearance main-

tained between the rotating teeth and the stationary surface. However, to avoid component damage due to relative rotor-stator movements, a minimum clearance needs to be maintained. This has led designers to investigate and use other configurations that reduce the kinetic energy carry over effect, with similar benefits to reducing the clearance. These include the step-up and step-down configurations as shown in fig. (1.2), configurations using inclined teeth, staggered or interlocking configurations (i.e. successive labyrinth teeth project from the rotating and stationary surfaces respectively), and, more recently, using abradable surfaces. The abradable surface, which is attached to the stator facing the labyrinth teeth, is used to reduce the mass flow through the seal by enabling tighter clearances to be maintained. The abradable surface achieves this by absorbing potential wear caused by relative rotor-stator movements. The surface can then be replaced at service intervals and help maintain the design clearance. One surface that is used regularly is the open celled honeycomb, mounted with cell openings facing the labyrinth teeth. This surface has an enhanced frictional effect that reduces the kinetic energy carry over of the seal, is capable of running at high temperatures and has structural properties suitable for the application. However, honeycomb does greatly contribute to windage heating in a labyrinth seal (McGreehan and Ko (1989)) which can be disastrous if unaccounted for in a cooling flow application.

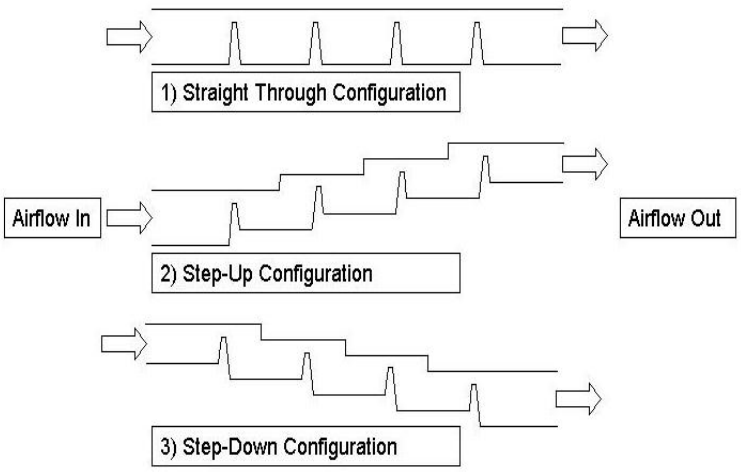

Figure 1.2: Typical Configurations of Labyrinth Seal.

The primary problem in labyrinth seal design is accurately describing the loss coefficients due to the combined effects of flow contraction and flow expansion (which includes the effect of kinetic energy carry over). Historically industry has been re-

liant upon interpolated and sometimes extrapolated experimental data, with much work having been undertaken to extend these experimental datasets. More recently, additional design work has been undertaken using numerical modelling techniques, primarily CFD, that has helped to reduce but not eliminate design uncertainty. These underlying uncertainties, combined with the increasing complexity of the labyrinth seal design (e.g., inclined fins, abradable surfaces), has led to areas in the design process where gaps of knowledge exist. Equally, very little analytical or numerical work has been undertaken that addresses the effects of wear within typical labyrinth seal designs. Therefore the purpose of this research was to investigate and report on the performance of a typical labyrinth seal in conjunction with a smooth metal stator, a honeycomb stator and a worn honeycomb stator.

The project sponsor, Cross Manufacturing Ltd. (*Cross*), have become involved in the project to further their understanding of labyrinth seal flow physics. As will be highlighted, there is a lot of work retro-fitting old gas and steam turbine engines with more efficient components, including rotating seals. *Cross*, like other companies within this sector, have a significant interest in this retro-fitting business, which for a brush seal manufacturer primarily involves replacing labyrinth seals with more efficient brush seals. However, to maintain safe operation this is often achieved through replacing a single tooth of an existing labyrinth, thus achieving a fail safe retro-fitted seal (i.e. the remaining labyrinth teeth from the original design are still present). However, in order to accurately carry out this improvement a full understanding of the labyrinth seal, including seal pressure distribution, is required. Then suitable locations for inclusion of a brush seal can be investigated, with the performance of the new hybrid component predicted and a suitable solution achieved.

1.2 Project Methodology

In order to fully characterise the performance of worn abradable honeycomb labyrinth seals in an engineering conext four primary methods of investigation were used. These were experimental, numerical using CFD, numerical using established computer codes and theoretical derivations that have been presented in the literature. This process is typical of modern industrial design techniques. These investigative methods will be dealt with in turn. In addition, the business benefits and implications to the project sponsor, *Cross*, will be highlighted.

Experimentally a labyrinth seal using a novel configuration was investigated. This involved using a non-rotating 2-D test rig at a range of clearances and pressure ratios with overall flow measurements recorded as well as flow measurements

from within the labyrinth seal. The particular instrumentation configuration chosen enabled the effects of contraction and expansion to be examined robustly and cost-effectively. The experiment involved using a flat honeycomb surface that was progressively worn in two stages using realistic industrial data. The honeycomb section was designed as an insert into the test rig to aid this machining process and to reduce the number of sealing components. Further, the experimental configuration was also capable of changing the tooth to groove location. A baseline test using flat metal was used to account for deviations over time.

Further development work was undertaken using CFD. Firstly, an extensive study was undertaken to verify whether FLUENT was capable of predicting labyrinth seal performance adequately. Then, due to the complexity of the 3-D geometry of an abradable honeycomb labyrinth seal a 2-D simplification technique was developed that greatly reduced the modelling time required. Using this technique, simulations of the experiment were undertaken cost-effectively. Use was made of various CFD modelling techniques with the most appropriate model for the current situation highlighted.

Finally previously developed numerical routines and computer codes used to predict labyrinth seal performance were examined against the experimental and numerical data obtained. With flow measurements taken inside the seal effects due to contraction and expansion can be examined separately against their respective theories. The benefits and drawbacks of the methods examined are analysed and discussed.

1.3 Thesis Description

The aim of this document is to present to the reader a clear reason and background for the research, the research methodologies and techniques used and a comprehensive discussion of their findings both from a technical and business viewpoint. The document will conclude with recommendations for further work. The work breakdown structure of the primary tasks can be viewed in fig. (1.3). As can be seen no one section is designed as a stand-alone section.

The next chapter discusses the relevant literature with respect to labyrinth seal development. Chapter three discusses the details surrounding the experimental design, experimental operation and experimental results. Development work undertaken using CFD is discussed in chapter four, with numerical replication of the experiment detailed in chapter five. Chapter six discusses the business benefits and

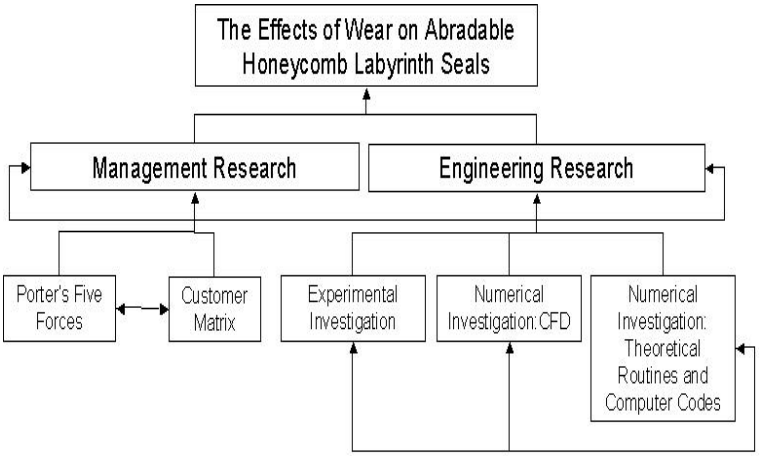

Figure 1.3: Work Breakdown Structure of the Primary Tasks Undertaken.

implications for *Cross* with chapter seven discussing and concluding the findings whilst highlighting areas for future work. Appendix (A) summarises all of the work undertaken. Further information is contained in other appendices and shall be referred to when appropriate.

Chapter 2

Literature Review

2.1 Historical Analysis of the Labyrinth Seal

The labyrinth seal has existed for over 100 years. Early investigations started at the turn of the century with many papers of note including Martin (1908). Martin looked to analyse the labyrinth seal performance by assuming the steam was wire drawn at a great number of points, or in other words that in the expansion process the steam behaved as a perfect gas. In between each expansion all of the kinetic energy was assumed to have been destroyed by friction. The whole process was assumed to be isothermal with small pressure drops across successive teeth. Based on these assumptions Martin derived the first mass flow equation for a seal based upon upstream pressure, pressure ratio and number of sealing points in the seal. Throughout the C_d (as shown in eqn. (2.1)) was assumed to be unity. An iterative correction process to be applied when the last seal becomes choked was also presented. The basic Martin formula can be seen in eqn. (B.1).

$$C_d = \frac{\dot{m}_{ACT}}{\dot{m}_{ID}} \tag{2.1}$$

Stodola (1927) examined the labyrinth packing using the theory of small pressure differences and Bernoulli's equation. This required the assumption of many restrictions so that each one causes a small drop in pressure. In addition, each restriction should be shaped and sized so that the velocity produced is totally destroyed through eddying. Stodola notes that the clearance could be made as small as $0.2032mm$, although often much larger clearances would be used in practice. A leakage equation based upon these assumptions and mass flow continuity was derived. Seals of constant cross-sectional area can only achieve sonic velocity in the final restriction, and a correction for this case is presented. Further corrections for varying geometries are presented. Tests, where the tooth ran inside the groove,

showed that the derivation was reasonably accurate with similar results to Martin (1908).

Egli (1935) examined the labyrinth seal from an adiabatic (zero heat transfer) expansion viewpoint. Initially the labyrinth was treated as a sharp edged orifice enabling use of the Saint-Venant Wantzel equation as shown in eqn. (B.6). A flow coefficient, equivalent to C_d, was introduced to account for the effective area. However, as the last restriction is the first to choke the assumption of small pressure drops as used by Martin (1908) is not accurate and the constancy of C_d was questionable. Below a pressure ratio of 1.25 there was good agreement between theoretical and actual sharp edged orifices. The labyrinth was treated in isolation with the energy either reconverted into pressure, destroyed into heat or carried over to the next throttling. The carry over factor (COF) was defined as the ratio of the actual (n) to the ideal (n_{ID}) number of restrictions. This can be seen graphically in fig. (2.1) where the horizontal-axis ($\frac{\delta}{s}$) and vertical-axis ($\sqrt{\frac{n}{n'}}$) represent ($\frac{Cl}{Ph}$) and ($\sqrt{\frac{n}{n_{ID}}}$) respectively. This figure shows that four actual restrictions at a ratio of ($\frac{Cl}{Ph}$) equal to 0.04 could be replaced by two ideal restrictions (1.4^2). The ideal number of restrictions is then used to graphically determine C_d which is assumed constant. This step was taken for practical reasons as in reality C_d is dependent upon COF and vice versa.

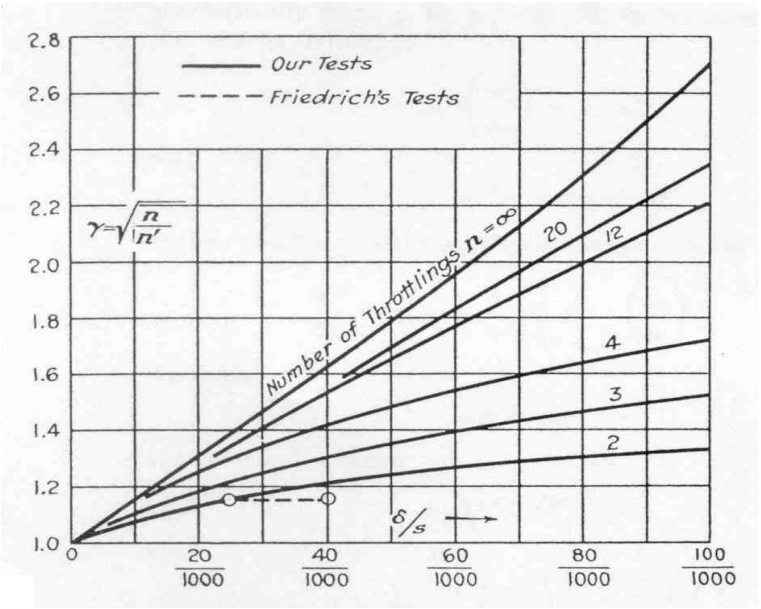

Figure 2.1: Egli (1935). Description of Carry Over Effect.

The Martin (1908) equation was found to be applicable over (n) teeth out of $(n+1)$, assuming (n) is greater than 4. Egli found that stepped seals come much closer to ideal by reducing COF, dependent upon step height. Egli also showed that COF, which can be empirically determined, can be reduced in straight seals by increasing the number of contraction points. Tests were undertaken to find the C_d of sharp edged labyrinths in both straight and stepped seals. The Egli mass flow formula and C_d calculation can be seen in eqns. (B.2) and (B.3) respectively.

Hodkinson (1939) investigated some of the underlying assumptions used so far in labyrinth seal theory. The first assumption that Hodkinson relaxed was that of the perfect gas. Next Hodkinson introduced the idea of a critical pressure ratio using published data. The COF and modelling assumptions were then examined experimentally. The experiment used a stationary 58 tooth labyrinth upon which the C_d was calculated. Initially COF was analysed in a similar manner to Egli (1935). In addition the COF was analysed using an expansion angle viewpoint, where the flow was treated like a jet, a portion of which is carried over. From tests this expansion angle was taken as 1° approximately. However, no vena contracta effects were taken into account. The tests showed that at large clearances full expansion could be achieved. Full eccentricity of the rotor relative to the stator was found to increase mass flow by up to 2.5 times. A new method to calculate the seal leakage was based upon published data, with a C_d assumed to be 0.5 and a COF based on the theory developed by Egli (1935) but using current test data.

Flow through straight labyrinth seals was considered in detail by Jerie (1948). There was a lack of knowledge for flow through labyrinths in between sharp edged and fully rounded nozzles. On one tooth experimental models the C_d was calculated and applied throughout for the whole analysis, even when n exceeded 1. Jerie found that when $\left(\frac{Cl}{Tp} \leq 2\right)$ the C_d was found to increase by up to 26%. The differences from a similar effect seen by Egli (1935) were explained by the tooth sharpness to clearance ratios used. This ratio appeared rather important for small clearances because it could render the flow more similar to that through a well rounded nozzle. In two tooth models the labyrinth function, a function of n, $\left(\frac{Cl}{Ph}\right)$ and $\left(\frac{Cl}{Ht}\right)$, was investigated against pitch. It was found that for ratios of $\left(\frac{Cl}{Ph}\right)$ of approximately 1 - 1.3, the labyrinth function grew independently from number of teeth: i.e. one well designed tooth could be better than two poorly designed ones. Jerie's theoretical analysis was based upon several assumptions including small pressure gradients (density almost constant) and constant clearance, area, diffusion angle and C_d. Low Reynolds number visualisations using water were obtained. The optimum ratio of $\left(\frac{Ht}{Ph}\right)$ was found to be approximately 1.

Kearton and Keh (1952) analysed the flow through staggered labyrinth seals. This is where the running clearance is maintained at the rotor and then the stator on successive knives (i.e. an interlocking seal). Again, several assumptions were used to aid the analysis. These included isentropic airflow, full dissipation of kinetic energy due to the seal design (zero COF) and zero heat transfer. Two distinct labyrinth flow regimes were highlighted: all pressure drops are small or pressure drops are large when the last tooth is choked. Therefore the analysis was broken into two cases corresponding to the two possible flow regimes. For small pressure drops the C_d is assumed constant throughout, whilst for larger pressure drops the C_d is constant until the last tooth. Tests on a single tooth showed weak eccentric effects. Experiments on a staggered labyrinth seal compared well to calculated values. This showed that COF in this type of seal was small, as expected. Kearton (1955) applied the analysis of his earlier paper, Kearton and Keh (1952), to the problem of a radial-flow staggered labyrinth seal. Radially inward or outward flow produced quite different results, primarily due to the decrease or increase in area respectively. The C_d was found to depend upon the ratio of $\left(\frac{Tp}{Cl}\right)$, pressure ratio and tooth width. However, both of these designs exhibit assembly problems. Therefore straight through seals are much more dominant, and carry over factors very relevant.

Zabriske and Sternlicht (1959) found discrepancies in available methods of up to 200%, and therefore devised a new method to calculate labyrinth seal leakage. The general method used was an extension and simplification of previous work based upon frictional techniques and FANNO flow (a solution of the continuity and energy equations for a particular mass flow: e.g. compressible adiabatic flow in a duct with friction. Douglas et al. (1995)). They found that as C_d increased with pressure ratio, choking did not occur at the actual critical pressure ratio because with the increasing pressure ratio the effective area also increased. The C_d values used were taken as an average from Kearton and Keh (1952). This caused two primary errors in their method. Firstly, the average C_d was taken from the average pressure drop whereas the actual pressure drops are assumed to increase in the flow direction. Secondly, the method was based on a single restriction free of up and downstream disturbances. Due to these effects C_d can be assumed accurate to $\pm 10\%$ only. The method derived was within 20% of test data.

Heffner (1960) highlighted that the ideal scenario for accurate labyrinth seal design is to conduct experimental tests. However, testing a complete series of seals is both time consuming and expensive. Therefore a method to correlate test data thus extending its use, particularly for small clearances, was presented. As the knives are geometrically similar the Reynolds number was assumed constant. In reality this can be only be valid if dynamic similarity is achieved. The method developed used a specific leak rate (see eqn. (2.2)) and C_d to correlate across the seal family. Results

were obtained within 3% of test data, significantly better than previous methods. However, discrepancies do arise when too few restrictions or carry over effects are present.

$$Specific\,Leak\,Rate = \frac{V\sqrt{T_{t(0)}}}{P_{t(0)}} \tag{2.2}$$

Vermes (1961) conducted an experimental and quantitative analysis permitting the approach of Martin (1908) to more complicated seal configurations: straight, stepped and combination seals. The main problems Vermes highlighted with the Martin approach are:

- Stationary zone in the cavity cannot develop due to the pitch being too small.
- Complex tooth inflow and outflow.
- Both of the previous conditions prevail.

These effects can easily be related to straight seals, stepped seals and staggered seals respectively. Therefore Martin's approach which primarily considered the thermodynamic effects left some problems of a fluid mechanics nature to be resolved. Vermes derived a more complicated approach relaxing the assumption of an isothermal process. The resulting equation can be seen in eqn. (B.4). This was compared to the approach of Martin. It was found that by changing the constant in the Martin equation agreement within 3% was obtained. For the straight seal it was noted that accurate knowledge of COF, particularly for seals with a small pitch, can significantly aid accuracy. A method to estimate COF was presented that modelled the flow as half a symmetrical jet that originates from a infinitesimally small narrow slot. This was assumed reasonable due to the large diameters and small labyrinth clearances typically encountered. The calculation of COF is based purely on geometry and can be seen in eqn. (B.5). A method to deal with sonic velocities, very similar to the Martin approach, was presented. Good agreement between straight seals and test data was obtained, reasonable agreement for other cases. Tests conducted in off design conditions for the stepped and staggered seals, where the axial location of the teeth changed, proved to be accurate within 10% typically when using the new approach.

Abramovich (1963) studied submerged turbulent jets within a labyrinth seal cavity. As the air moves past the tooth and enters the cavity a jet that has a diverging angle is formed. A constant mass core is separated from this jet, compressed and carried over the next tooth. The remainder travels along the cavity wall to mix anew with the entering jet. In this process two primary losses were highlighted: the

energy difference between the constant mass core at the beginning and end of the labyrinth cavity, and the energy loss upon sudden contraction of the flow. Each of these losses has an upstream and downstream component. The total percentage energy losses for the upstream and downstream regions can be seen in eqns. (2.3) and (2.4) respectively. The downstream loss, which is reliant upon graphical constants H_1 and H_2, does not develop unless the ratio of $\left(\frac{Ph}{\frac{Cl}{2}}\right)$ exceeds 10.5.

$$Upstream\,Loss = 0.032\left(\frac{Ph}{\frac{Cl}{2}}\right) \tag{2.3}$$

$$Downstream\,Loss = 1 - \frac{12H_2}{\sqrt{Ph\left(\frac{Cl}{2}\right)}} + 0.5(1 - 3.16H_1) \tag{2.4}$$

Frederick and Reeves (1970) experimentally analysed the flow through labyrinth seals with very small pressure drops. The pressure ratios studied ranged from 1.001 to 1.01 with both straight and stepped seals tested. Eccentric tests increased were found to increase mass flow by up to 5%. Flow travelling down the step (decreasing radius) had a larger leakage than flow travelling up the step (increasing radius). The Egli (1935) method proved valid for the test conditions. The C_d and COF were not measured directly. Therefore a constant difference between experimental and ideal cases existed. Hence if C_d and COF are known the Egli approach would prove more accurate for small pressure differences.

Koening and Bowley (1972) developed a computer code based upon the method of Egli (1935). The computer code used two variables out of pressure (either one or two pressures), mass flow or pressure ratio across a restriction, iterating to find convergence. Good comparison with limited test data was obtained.

Sneck (1974) conducted a thorough review of the literature available for labyrinth seal flow fields. He noted the skin friction method (e.g. Zabriske and Sternlicht (1959)) was not as widely used as that of Martin (1908) who modelled the flow as that through a series of orifices. Subsequent papers that developed the Martin approach were primarily concerned with relaxing some of the underlying assumptions. Egli (1935), for example, highlighted the importance of kinetic energy carry over to labyrinth seal performance. Vermes (1961) re-derived the Martin equation without assuming an isothermal process.

Sneck summarised the previous literature as having two main problems: lack of knowledge of both C_d and COF. Most techniques used the Martin method by including coefficients to adjust the formula. For ideal seals (seals with zero kinetic energy carry over. e.g staggered or stepped) the Martin approach is adequate. If

there are 4 or fewer restrictions the Saint-Venant Wantzel technique is recommended, otherwise the Martin approach is acceptable assuming sub-critical ($Ma < 1$) flow throughout. When critical or supercritical flow exists the Martin approach using an average C_d is applicable to all but the last restriction were the Saint-Venant Wantzel approach using a different C_d should be used. (Further information on the Saint-Venant Wantzel approach can be found in eqns. (B.6) through (B.9).)

2.2 Modern Analysis of the Labyrinth Seal: Experimental

Meyer and Lowrie (1975) highlighted some of the shortcomings of previous theory. Primarily Meyer and Lowrie were concerned with the variations in C_d which had been shown to be affected by pressure ratio and geometry having no theoretical maximum as assumed by Martin (1908). Even with the addition of a second restriction effects can be felt at the first restriction dependent upon tooth thickness ($\frac{Tp}{Ph}$), pitch and pressure ratio. Therefore it was thought that adding a third restriction would probably affect the first two. Meyer and Lowrie subsequently conducted extensive tests. They found that with a reducing pitch, C_d increased slightly, adding to the expansion angle theory of Hodkinson (1939). Relatively thin seals showed an increasing C_d with pressure ratio which was not seen on relatively thick seals. During two restriction tests a pressure rise was recorded across the second restriction dependent upon seal clearance and pitch. Inclined teeth exhibited a reduction in flow of approximately 10-12%. Ultimately a new method to calculate seal leakage based on the ratio of ideal to critical mass flow and C_d was presented. Whilst the method derived excluded certain assumptions it would require testing for each seal geometry to reveal the accurate C_d.

Stocker (1975) analysed advanced labyrinth seal designs experimentally. The publication highlighted that the internal air system had not kept up with the advances seen in the other major gas turbine components, thus limiting efficiency advancements. For example, a 1% reduction in seal leakage could equate to a 1% increase in thrust and a 0.1% reduction in SFC for a civil aero-engine or a 0.8% increase in thrust and a 0.3% reduction in SFC for a military engine. To address this a three stage study was undertaken using several new seal design configurations, all tested down the step. The test stages involved using a water test at a scale of 10:1, a static air test and a dynamic air test with only suitable configurations progressing. All of the configurations tested showed reductions in mass flow of 10.7% to 25% when compared to the baseline. Rotational effects were found to be negligible ($< 3.5\%$) up to sliding speeds of 240 $\left(\frac{m}{sec}\right)$. Throughout it was found that increased

cavity turbulence increased the overall efficiency by dissipating more energy.

Stocker (1977) experimentally analysed the performance of labyrinth seals with solid, abradable and honeycomb lands. A large number of 2-D tests were used to evaluate which 3-D configurations to test experimentally. Overall Stocker found that honeycomb and abradable lands can have a significant effect on the flow, at times even increasing the mass flow when compared to a smooth land. Honeycomb lands were found to reduce leakage by up to 24% in straight through labyrinth seals. Rotational effects were also found to reduce mass flow unless a honeycomb lining was used when the effect was negligible. Also covered in this publication was a study on the effects of labyrinth seal performance with a porous abradable land containing rub grooves. The rub groove studied was $0.25mm$ deep and $0.60mm$ wide at the surface narrowing to $0.51mm$ wide at the bottom. Tests were conducted with the tooth aligned centrally, upstream and downstream with respect to the groove. The groove in the abradable land actually reduced the leakage flow due to the rub groove actually preventing flow through the porous abradable surface. When using a honeycomb lining a small clearance effect was registered. This is where the flow can bypass the tooth by moving in and out of the honeycomb cell. A peaking of mass flow function was also found near choking conditions. This was thought to be due to increased turbulence. As the cell size reduced this effect was not as noticeable. Finally optimised stepped and straight through seal designs were presented that reduced leakage by 25% and 54% respectively compared to their conventional equivalents. The study proved its economic value by stating that a compressor redesign would cost approximately 4-6 times as much, with a turbine redesign costing approximately 5-20 times as much. Equally, a further 10% increase in cooling airflow would increase SFC by 0.5%. In a further publication, Stocker (1978), the author notes that if 25% leakage reduction was achieved in all locations then an improvement in SFC of 2.7% could be achieved.

Komotori and Miyake (1977) developed a theoretical analysis applicable to the straight through labyrinth seal. Several assumptions were made to aid the analysis:

- At every restriction the area available to the flow contracts. Therefore velocity just upstream of the contraction can be calculated from continuity using this reduced area.
- After the contraction the flow moves into the cavity with a constant diverging angle, taken as 6° from published data.
- In the diverging flow a part of the kinetic energy of the gas changes to static pressure.

- In this process there is a pressure loss, which can be calculated using Borda's formula as shown in eqn. (2.5).

$$P_{t(n+1)} = P_t(n) + \frac{\rho_(n) + \rho_{(n+1)}}{2}\left[\left(V_(n)^2 - {V_{(n+1)}}^2\right) - \left(V_(n) - V_{(n+1)}\right)^2\right] \tag{2.5}$$

This derivation was then compared to the ideal labyrinth (one where all of the kinetic energy is assumed to have dissipated) to reveal the COF as shown in eqn. (2.6).

$$COF = \frac{\dot{m}_{ACT}}{\dot{m}_{ID}} = 1 + \frac{\Delta\dot{m}}{\dot{m}_{ID}} \tag{2.6}$$

The velocity during the expansion was calculated using continuity and the area ratio using the 6° expansion angle. It was found that the COF increased with pressure ratio and $\left(\frac{Cl}{Ph}\right)$ ratio. A range of geometries were subsequently tested using rotational speeds of up to 270 $\left(\frac{m}{sec}\right)$. In previous work it was suggested that a geometrical ratio of $\left(\frac{Ht}{Ph}\right)$ equal to 0.25 minimised the leakage flow in stationary labyrinth seals. Through testing it was found that rotation acted to decrease the leakage, with increasing reductions achieved using smaller clearances and groove depths. Large tooth widths also acted to decrease the leakage with rotation and the importance of $\left(\frac{Ht}{Ph}\right)$ reduced. It was thought that rotation could act to induce helical flows thus adding to friction and increasing the relative pitch, the distance the flow travels between successive teeth, but also decrease the diverging angle. Overall the derivation to estimate the leakage proved acceptably accurate with a 1° variation in expansion angle accounting for approximately 2-3% variation in leakage mass flow.

Benvenuti et al. (1980) examined the labyrinth seal prediction methods that are currently available. Three main approaches were revealed: purely analytical (e.g. Martin (1908), Stodola (1927)), analytical-experimental through the introduction of coefficients (Egli (1935), Jerie (1948), Vermes (1961)) and friction co-efficient methods (Zabriske and Sternlicht (1959)). Of those examined only Jerie, Egli and Vermes included the effects of kinetic energy carry over. Egli returned the widest variations but failed to include the effects of $\left(\frac{Tp}{Cl}\right)$. The other two studies decreased the optimum ratio of $\left(\frac{L}{Ph}\right)$ as $\left(\frac{Tp}{Cl}\right)$ increased. Benvenuti examined the Vermes kinetic energy ratio (eqn. (B.5)) highlighting the drawbacks in the formulation where it could exceed unity for small values of pitch. Therefore the COF was redefined as shown in eqn. (2.7) and assumed zero upstream of the first tooth.

$$COF = \frac{mass\,flow\,with\,kinetic\,energy\,carry\,over}{mass\,flow\,without\,kinetic\,energy\,carry\,over} \tag{2.7}$$

Experiments were undertaken with 12-18 restrictions and compared to predictions. Overall the Vermes technique gave acceptable agreements to the experiment, with the Stodola technique providing the best inter-seal pressure comparison. There was an optimum pitch effect, where the seal length was held constant and the number of restrictions changed. The first 3 teeth showed variations in tooth C_d prior to the variations diminishing, with the first tooth recording larger pressure drops. Further, C_d was found to exceed one dependent upon test conditions and tooth location within the labyrinth seal.

Wittig et al. (1982) and Wittig et al. (1983) investigated the effects of scale on labyrinth seal performance. This was due to the desire for scale models from a testing viewpoint. To enable this comparison the dimensionless parameter C_d was used. Flow regimes analysed covered low Reynolds number (Re) flow and high Mach number (Ma) flow. However, Ma is the true definition of compressibility. (In a jet engine small clearances at high altitude give low Reynolds number conditions). Scale effects were most noticeable at small clearances, with the largest C_d found at the smallest scale. Therefore it was suggested that when analysing low pressure ratios Reynolds number should dominate whilst at high pressure ratios compressibility effects should dominate. FANNO theory was chosen for the subsequent analysis. It was found that unless dynamic similarity is fulfilled errors of 10% can accumulate if using scale models for design calculations. Therefore simultaneous effects of Mach number and Reynolds number need to be considered.

McGreehan et al. (1987) investigated labyrinth seal flow fields using tracer gas injection. This provided a means for testing high temperature and high speed applications where ΔP methods (like an orifice) may lack accuracy due to large thermal gradients placed upon the equipment. It was found, for the cases considered, that up to 30% variability in flow measurements may be recorded. The new method involved injecting tracer gas (e.g. CO_2, He) upstream of the test section and measuring concentrations downstream. The tracer gas mass flow rate was held constant. Even mixing of the gases at inlet proved difficult. However, even with this taken into account 16% accuracy was claimed with 10% aimed for.

Morrison et al. (1988) used laser doppler anemometry to record eccentric labyrinth seal performances. A 7 cavity seal was analysed at a Reynolds number of 28,000 and a Taylor number (Ta) of 7,000. The seal clearance was $1.27mm$,

with a pitch, cavity depth and tooth height of $4.57mm, 3.05mm$ and $1.524mm$ respectively. The radius of the seal was $82.1mm$. The mean velocity distribution and entire Reynolds stress tensor were recorded. It was found that axial and radial velocities and Reynolds stresses became cavity independent by the third cavity. The first cavity had a noticeable vena contracta effect at the region of largest clearance. A three dimensional vortex structure was found that grew in the azimuthal region of increasing clearance and was broken up and swept downstream in the azimuthal region of decreasing clearance. This structure aided the blockage of the seal, with the dissipation process taking longer than that of formation. Another publication, Morrsion et al. (1991) followed which had more details.

Childs et al. (1988) tested for rotordynamic coefficients of straight and staggered labyrinth seals, similar to that studied by Kearton and Keh (1952). At inlet a helical component of velocity was varied positively and negatively with respect to the rotational direction. This helical component of velocity reduced with increasing rotation due to the reducing clearance caused by growth of the rotor under test conditions. However, the rotor growth acted to reduce the clearance and therefore mass flow. Overall the results proved inconclusive, and with no theory to compare the rotordynamics of the staggered labyrinth, only limited conclusions could be drawn. However, staggered labyrinth seals leaked substantially less throughout. In a further publication investigating rotordynamic coefficients, Childs et al. (1989) found that the honeycomb seal offered better leakage when compared to an equivalent labyrinth seal and that the honeycomb seal (an annular honeycomb seal without teeth) acted as a helical velocity brake.

Brownell et al. (1989) used holographic interferometry to conduct a non intrusive investigation into labyrinth seal flow fields using a 2-D test rig. The assumption of ideal seal flow (isentropic, adiabatic, zero COF and the perfect gas law were obeyed) combined with the Saint-Venant Wantzel equation was used for comparison. It was found that C_d advantageously reduces the flow area but that COF has a detrimental effect, particularly on the performance of the first cavity. Honeycomb was found to reduce kinetic energy carry over with each restriction operating closer to the ideal.

Miyake and Duh (1990) tried to clarify the relation between mass flow and rotation experimentally. The experimental equipment was capable of rotating at $2500rpm$ with a maximum peripheral velocity of $260\left(\frac{m}{sec}\right)$. They found that the mass flow decreased in straight through labyrinth seals with increasing peripheral velocity. This decrease was found to be larger when the restriction tip thickness was large and the chamber depth shallow. The effects of rotation were found to be largest for straight as opposed to stepped seals with the step-down seal performing

better than the step-up seal.

Waschka et al. (1990) analysed the effects of rotation on heat transfer coefficients and C_d. Clearance control was used in the experiment with a maximum rotational speed of $3000rpm$. The study was initiated due to contradictory evidence in the literature: the effects of rotation cannot be neglected at small axial Reynolds number and high Taylor number. At low axial Reynolds number (Re_{AX}) the C_d decreased markedly with increasing rotational speed, whilst above an axial Reynolds number of 10,000 the effects due to rotation were marginal at all clearances. With transition from laminar to turbulent flow at an axial Reynolds number of approximately 6,000 this shows that rotation has an effect on laminar flow that is not seen as markedly in turbulent flow. When the ratio of $\left(\frac{Ta}{Re_{AX}}\right)$ exceeds 0.2 the leakage rate is reduced and the heat transfer increased. The largest heat transfer coefficients were seen on labyrinth teeth tips and on the stator wall directly opposite the labyrinth teeth.

Zhu and He (1990) experimentally analysed the leakage characteristics of labyrinth seals. Using a straight through test rig the basic models of Martin (1908) and Vermes (1961) were analysed. The losses depended upon the geometry, viscosity, pressure and compressibility. Bernoulli's equation was applied to the cavity entrance and exit and was also experimentally measured. A loss coefficient was presented, with the numerical-experimental agreement within 5%. An advanced model using the technique of Komotori and Miyake (1977) was developed.

Ha and Childs (1992) measured the Fanning friction factor (f_f) of smooth and honeycomb surfaces in a 2-D experiment with the smooth surface used as a verification test. The honeycombs analysed varied in size from $0.40mm$ to $1.60mm$, with the cell depths varying from $2.30mm$ to $3.80mm$. The Reynolds number was varied from $5,000$ to $130,000$. The location of the honeycomb on the top plate with respect to the honeycomb on the bottom plate was not recorded. The differences between labyrinth seal flow (narrow channel flow) and pipe flow exist because the pipe is axisymmetric. Therefore boundary layers in a pipe are farther apart and the pipe surface roughness is much smaller than pipe diameter. The Reynolds number was defined using the hydraulic diameter as the characteristic length, similar to duct flow. For non-critical flow ($Ma < 1$) it was found that the friction factor was almost uniform. A phenomenon labelled friction factor jump was recorded at high Reynolds number and explained in Ha et al. (1992) as acoustic excitation due to placement of instrumentation. Generally a cell depth of $3.05mm$ showed the largest friction factors. The small clearance effect seen by Stocker (1977) was recorded. Increasing clearance generally increased the friction factor recorded.

Prasad et al. (1997) examined straight through labyrinth seals experimentally and numerically. In the paper a table highlights geometric variations studied by previous authors. To reduce leakage flow the authors note previous work concluding that reducing clearance, adding restrictions, using sharp corners, having a low $\left(\frac{Tp}{Cl}\right)$ and using rough abradable stator surfaces all act to reduce C_d. Increasing seal height or pitch will also increase the pressure loss. The numerical cases repeated the experimental cases within 8.6% using FLUENT. The numerical work proved that the assumption of the ideal labyrinth (zero COF) is not valid for the straight through case. It was shown that the turbulent kinetic energy increases through the seal which contributes to the pressure drop.

Allcock (1999) undertook a comprehensive study of abradable honeycomb labyrinth seal flow fields. Three sizes of honeycomb ($0.80mm$, $1.60mm$ and $3.20mm$) had their Fanning friction factor determined experimentally which was then used to calculate an effective roughness for use in a numerical study. Smaller cell sizes acted more like a flat plate. Clearance effects similar to duct flow, where a reduction in clearance causes an increase in relative roughness, were found. At small clearances the flow is more jet-like and much more pressure driven. Until the flow was fully developed a marked dependence on Reynolds number was found. The numerical study used FLUENT and idealised seal geometries (sharp corners). The effective roughness measured experimentally was applied to the stator wall using extrapolation to account for stator-tooth and stator-cavity regimes. This work was reported on in two later papers, Allcock et al. (2002a) and Allcock et al. (2002b).

He et al. (2001) conducted an experimental investigation of the sealing performance of an annular honeycomb seal (without labyrinth teeth) through comparing results with a typical labyrinth seal. Three honeycomb cell sizes, $0.80mm, 1.60mm$ and $3.20mm$, were studied all with a depth of $3.00mm$. Rotational effects that reduced the mass flow by up to 4.8% at the highest rotational speed were found. At the smallest clearance ($0.06mm$) the labyrinth seal recorded the smallest mass flow. This conclusion contradicted Childs et al. (1989) who found that the honeycomb seal always performed better than the labyrinth seal. However, their study was at larger clearances of $0.41mm$, not $0.12mm$. Therefore at small clearances honeycomb seal leakage reduction is questionable but rotor stability can be enhanced.

Willenborg et al. (2001) studied the effects of Reynolds number and pressure ratio on leakage loss and heat transfer in a 2-D, stationary, stepped, labyrinth seal. The Reynolds number study (based on hydraulic diameter) covered extremes of jet engine operation: high Reynolds number (low altitude, high mass flow) and low Reynolds number (high altitude, low mass flow). Two scales of labyrinth seal were tested, 1:1 and 4:1, with the 1:1 scale having rounded teeth tips. It was found that

the C_d of the 1:1 model increased with Reynolds number, whilst at 4:1 the Reynolds number was higher with C_d linked to pressure ratio. Above a Reynolds number of $30,000 - 40,000$ C_d depended purely upon pressure ratio. At high Reynolds number the effective flow area is independent of Reynolds number, causing a constant C_d. Below this as the effective area increases, the Reynolds number decreases. Therefore the pressure ratio effects on Nusselt number (Nu) have a limited effect with the primary driver being Reynolds number.

Schramm et al. (2002) looked at the effects of using an abradable honeycomb lining on the flow through a stepped labyrinth seal. A non-rotating 2-D experiment compared smooth and honeycomb seals. TASCFLOW was used to compute numerical CFD simulations with a grid interface used to join honeycomb cells to the labyrinth cavity. In the paper an analysis of effective gap based on labyrinth and honeycomb geometry is presented. As the ratio of $\left(\frac{Cl}{Hs}\right)$ increased the change in effective area was found to approach one, with a maximum predicted increase of 66%. The C_d was also found to decrease with increases in gap width. It was found that the flow pattern in stepped seals causes less abradable area to be in contact with the main flow path. Denecke et al. (2003) added to this paper by noting that the non-rotating model was adequate as long as the axial velocity exceeds the helical velocity. From experimental visualisations small clearances were seen to increase the cavity flow recirculation.

Willenborg et al. (2002) analysed heat transfer effects due to honeycomb in stepped labyrinth seals. Overall no heat transfer effects on the stator due to clearance were found. Honeycomb was actually found to reduce heat transfer on the stator by up to 5 times which was thought to be due to fluid trapped in the honeycomb cells. On the rotor much smaller differences were seen between the smooth and honeycomb condition.

Rhode (2002) measured flow oscillations and instabilities in labyrinth seal cavities. It was found that downstream impingement can cause increased vorticity upstream. Therefore the possibility of flow disturbances feeding back upstream can be enhanced, particularly if constant density can be assumed. (The author assumed that for $Ma < 0.4$ constant density was a reasonable assumption).

Michaud et al. (2003) experimentally studied labyrinth seal flow using a 2-D stationary, stepped, large scale labyrinth seal flow rig. Pressure measurements, flow visualisations and particle image velocimetry were all used to analyse performance. All measurements were taken at a scale of 5:1 using a clearance of $5.6mm$, except flow visualisations where a 10:1 scale was used. Michaud et al. highlighted that using the 25% measured mass flow reduction of Stocker (1977), 16 million barrels

of jet fuel could be saved in the US alone, based upon 1998 figures. In the experiment various formations including inclined teeth and steps along the stator were compared against a baseline. Loss mechanisms seen through visualisations are viscous dissipation within the turbulent jet at each restriction, viscous losses because chamber vortices are driven by shear flows, losses at stagnation areas due to non-reversible processes and losses due to sudden, sharp, changes in flow direction. It was generally found that an increase in tooth inclination angle, or larger flow deflection steps, reduced flow coefficients. This was due to a relative sharpening of the teeth (decreasing flow area) and increased turbulence respectively. The best case analysed achieved a 17% reduction in mass flow.

Vakili et al. (2005) used an experimental and numerical approach to study a straight through labyrinth seal. Various configurations were tested with the best performing configuration reported with respect to the baseline case. Experimentally six restrictions with two rectangular steps along the stator were tested, with twelve restrictions tested numerically. The rectangular steps helped to form a staggered seal geometry. The CFD work undertaken used the $k - \epsilon$ turbulence model and standard wall functions available in FLUENT. First order discretisation was used for the turbulence quantities with second order used for other quantities. Total pressure variations along a streamline through the seal began to collapse onto each other above a pressure ratio of 4, once the seal was choked. The remaining variations seen above this pressure ratio are because of the differences in the effective area caused by the pressure ratio. The best configuration used inclined teeth and with rectangular steps located on the stator. Increased levels of stagnation, flow bending and turbulent throttling were recorded thus maximising energy losses through the seal. A 3-D study was planned to look for the effects of eccentricity.

Paolillo et al. (2006) and Kool et al. (2006) discussed the development and commissioning of an advanced seal test rig along with comparing initial experimental results with CFD. Paolillo et al. highlighted a 25-50% reduction in parasitic leakage was sought to meet next generation performance goals. Their CFD model used FLUENT with the standard $k - \epsilon$ turbulence model and enhanced wall functions. Other turbulence models showed the same trends so were discontinued. It was found that the tooth edge radius affected the separation region over the tooth and therefore a radius had to be included to successfully repeat experimental cases. At low rotational speeds the CFD failed to accurately predict the experimental honeycomb seal data. Significant improvements were made at high rotational speeds. It was suggested that further 3-D CFD models including honeycomb would be required to determine the influence of inlet helical velocity components on the air flow within the experimental rig. Kool et al. primarily discussed development of the advanced seal test rig which used active clearance control. The test rig specification is as

follows:

- Upstream Temperature: $20 - 815°C$
- Upstream Pressure: 12.0 - 24.0 Bar
- Pressure Difference: 1.0 - 7.0 Bar
- Sliding Speed: 0 - 365 $\left(\frac{m}{sec}\right)$
- Seal Clearance: 0.1 - 0.4mm
- Mass Flow: 0.04 - 0.8 $\left(\frac{kg}{sec}\right)$

It was found that the actual windage heating experienced by the labyrinth seal was significantly higher than that which was predicted. Development tests using a known test article proved successful. It has taken longer than initially planned to operate at full design conditions.

Vakili et al. (2006) continued to develop the approach of Vakili et al. (2005) for steam turbines. The goal was to find an advanced seal design that would prove compliant in the rub condition. This involved using C shape labyrinth teeth and rectangular steps located along the stator wall. The C shape was chosen as this would deflect under contact conditions and offered potential benefits as found with inclined teeth (e.g. Meyer and Lowrie (1975)). The best improvement over the baseline was 42%. It was highlighted that the new design would only prove better if the teeth integrity and flexibility was maintained over a period of time. However, as the rotor moves towards the stator the pressure will increase behind the tooth causing further movements of the tooth towards the rotor potentially adding to wear. How this condition was to be avoided was not discussed.

2.3 Modern Analysis of the Labyrinth Seal: Numerical

Stoff (1980) analysed labyrinth seal flow fields numerically using incompressible flow. Numerical predictions of turbulent kinetic energy (k) and turbulent dissipation rate (ϵ) were compared to experimental laser measurements. Using the $k - \epsilon$ turbulence model it was found that ϵ was re-created least successfully. However, it was also subject to the most modelling assumptions.

Rhode and Sobolik (1986) used a computer code to calculate the pressure drop across a seal because this approach would not require the estimation of COF. Single cavities were studied using QUICK discretisation and a 33x33 grid in the cavity. Numerical solutions were obtained for several velocities with the calculated pressure ratio inserted into a further computer code using a 2^{nd} order polynomial representation of $\left(\frac{\log\left(P_{t(n)}-P_{t(n+1)}\right)}{\frac{1}{2}\rho_{(n)}V_{(n)}^2}\right)$ versus $\left(Ma_{(n)}\right)$. This code was designed for upstream inputs of mass flow, pressure and temperature, with $P_{t(n)}$ calculated above each tooth in a marching fashion. The static pressure was calculated from mass flow and total pressure at inlet to the seal cavity and based upon a polynomial. Outlet density was calculated using the ideal gas law while outlet velocity and Mach number were calculated from conservation equations using an assumed constant C_d. Then the process repeats for the next tooth. A variation to account for choked flow was based on FANNO flow with a Bernoulli approximation.

Wittig et al. (1987) numerically predicted measurements of C_d and compared these to experiments on a 2-D test rig with a high aspect ratio ($\frac{duct\,width}{clearance} > 100$). Up to six $2.50mm$ thick fins were modelled with clearances varying from $0.50mm$ to $2.50mm$, with a tooth height and pitch of $10.50mm$ and $12.00mm$ respectively. The agreement between numerical and experimental results was good when a high number of teeth were used. The dependence on seal clearance reduced with the number of teeth, with stepped seals showing less gap width dependence and a lower C_d.

Chan et al. (1987) highlighted the requirements for improved sealing technology due to current engine development trends which are characterised by increases in pressure ratio, turbine entry temperature and rotational velocity. In order to reduce SFC by 2% reduction in leakages of 4% are required which were considered achievable. The empirical relations currently used are somewhat outdated with Navier Stokes solutions offering practical alternatives. Seal clearance had a significant effect on the overall damping characteristics of the seal. Transient solutions for an eccentric rotor condition were obtained through a basic computer code.

Zimmermann and Wolff (1987) compared existing empirical and numerical labyrinth correlations. When designing an internal air system it is desirable to only use simple empirical models to avoid the necessity of many calculations throughout the operating envelope. However, existing numerical and visualisation test results had shown that flows can change from tooth to tooth. Therefore an improved method that used different values of COF and C_d for the first tooth was developed. This was because it was found that the first tooth did more work than the rest, typically achieving a lower value of C_d. For the second tooth onwards the derivation

of Martin (1908) was utilised. Overall the new method predicted data within 5% as opposed to approximately 30% when using the traditional approaches of Martin, Stodola (1927) or Egli (1935). Worn seals were highlighted as an area with little information and much more work to be carried out.

El-Gamal et al. (1987a) and El-Gamal et al. (1987b) created a mathematical model for labyrinth seals to study geometric effects. The flow was modelled as 1-D, steady, laminar, incompressible and assumed stationary upstream of the seal. Three formations were analysed: straight seal with teeth on stator, straight seal with teeth on rotor and a stepped seal. For both the teeth on stator and teeth on rotor two counter-rotating vortices were found that travelled radially outward and inward at half pitch respectively. The stepped seals analysed only exhibited one vortex. Overall the tooth on rotor and stepped formation proved better than the tooth on stator formation.

Sturgess (1988) looked at the benefits offered by CFD to gas turbine engine secondary flow systems, particularly as it was anticipated that the gas turbine engine rate of improvement should double. It was thought that half of these improvements could come from advanced materials with half from improved component efficiencies. The CFD code used was verified as applicable to labyrinth seal situations by replicating flow through orifice plates and some of the tests of Stocker (1978) with reasonable accuracy. Ultimately careful modelling of the labyrinth restrictions did give accurate solutions. With improvements in the code the use could be more widespread.

Rhode and Hibbs (1989) comparatively investigated labyrinth seals with annular seals (seals without labyrinth teeth) of an equivalent clearance. The model was a development of an earlier model of Demko et al. (1990). Stocker (1977) was used as a test case with good agreement of 8% found with the numerical and experimental results. Overall it was found that labyrinths were 20% better than their equivalent annular seals as a result of the recirculation zones and more intense turbulent shear stresses. The importance of these stresses reduced with clearance. The labyrinth with tooth on rotor formation was found to increase helical velocity leading to an increased potential of self excited rotordynamics. It was found that the 3^{rd} tooth of 3 had the largest pressure drop, 30% and 20% higher than the 2^{nd} tooth at clearances of $0.51mm$ and $0.13mm$ respectively. The annular seal recorded a higher components of helical velocity at exit. Radial velocity profiles showed the importance of the restrictions and free shear layer along the stator wall in the labyrinth seal because the highest values of velocity were found here.

Zimmermann (1990) studied secondary air systems suggesting areas where a

lack of knowledge remained. Often in the secondary air system only basic aerodynamics are known, with a lack of experimental-numerical agreement. However, CFD could be used to extend the knowledge of component performance and with numerical replication of experimental data confidence in numerical results would be gained. Zimmermann also noted that with stationary 2-D tests rotational effects are not registered. This misses certain situations like high altitude conditions, where low Reynolds numbers prevail. With particular reference to labyrinth seal modelling Zimmermann noted that it is a cost and time intensive process. Therefore it is suggested that correlations should be sought that covered effects of geometry, form (e.g. straight or stepped), entry conditions, rotation, Reynolds number, pressure ratio, eccentricities and distorted geometries like start up and worn conditions.

Demko et al. (1990) analysed the effect of shaft rotation on incompressible flow in a labyrinth seal. The tooth thickness and clearance was $6.35mm$, with the pitch and tooth height of $16.35mm$ and $19.05mm$ respectively. It was found that at high rotational speeds a secondary recirculation zone was found that propagated from the bottom downstream corner into the cavity. As the rotation was increased the secondary zone could take up to 50% of the cavity. However, the effect was only seen at prohibitively high rotational speeds. For the situation analysed this meant rotational speeds in excess of $100,000rpm$. Experimental work was undertaken that compared the mean axial velocity, helical velocity and turbulent kinetic energy. The helical velocity agreement was best with other agreements deteriorating with rotation.

Rhode and Nail (1992) studied cavity by cavity flow development in labyrinth seals using a CFD code. The study was undertaken to investigate deviations away from ideal conditions. The false diffusion due to recirculation was reduced using QUICK discretisation. Teeth on rotor and teeth on stator labyrinth seals were analysed with the teeth on rotor formation in comparatively reducing mass flow by 10%. The teeth on rotor formation also exhibited a greater development of helical velocity, attributed to the larger rotating surface area. Due to lack of experimental data the results could not be verified.

Rhode and Hibbs (1992) used a computer code to investigate tooth thickness effects. A comparison to Stocker (1978) achieved accuracy to within 7.5% prior to changing tooth thickness. Straight seals exhibited leakage behaviour that was independent of tooth thickness with the last cavity showing a definite increase in turbulent energy and length scale over the first. This contradicts what would normally be expected. Pressure drops were found to increase through the seal, as did Mach number and frictional effects.

Rhode and Guidry (1993a) highlighted the importance of increasing labyrinth throughflow deflection, thus enabling larger clearances, without increasing leakage. This was achieved by using stepped seals and measuring the effect that inlet skewness had on C_d. Inlet skew was found to reduce C_d although there was a decreasing rate of return at high values of inlet skew. In a further paper, Rhode and Guidry (1993b) utilised a finite difference code to enable better understanding of labyrinth seal performance. The study was conducted for a specific application, the space shuttle high-pressure oxidiser turbopump, that used hydrogen in a stepped labyrinth seal design with a pressure drop of $33.1MPa$. Small radii, $0.076mm$, were applied to key corners in the seal using a stair-step approach. It was found that using perfectly sharp corners reduced mass flow by up to 30%. Use of a stator through flow deflection groove was found to reduce leakage by a further 20% by providing an increased expansion area.

Rhode et al. (1994a) used a Navier Stokes code to find previously unknown effects like that of step height. Due to computational demands only one cavity was modelled at a time. With regard to step height an optimum value was found below which radial velocity components were reduced and above which leakage passed through unaffected. Ultimately when designing a step the designer should aim to achieve the maximum generation of turbulence which in turn causes the maximum viscous dissipation of turbulent energy into heat and therefore causes the maximum pressure drop. The study produced an optimised seal design using 9 cavities that was tested against a baseline 3 cavity seal with a 60% reduction in mass flow.

Rhode et al. (1994b) conducted an experimental and numerical investigation of an advanced labyrinth seal. The stepped seal used a groove located near the tooth in a similar method to that used by Rhode and Guidry (1993b). It was found to reduce leakage by up to 20% whilst introducing negligible shaft speed effects.

Athavale and Hendricks (1996) attempted to use 3-D CFD simulations to try and replicate the experiment of Ha and Childs (1992). Only 6 honeycomb cells could be modelled in the flow direction at a reasonable cost, using $90,000$ computational cells. Only the $0.80mm$ honeycomb cell at a clearance of $0.38mm$ was modelled at two cell depths, $3.05mm$ and $3.80mm$. From Ha and Childs previous work this represented conditions that recorded the friction factor jump and normal flow respectively. It was found that the calculated friction factor of 0.043 remained constant for all cases analysed. This was quite different from the experimental work where friction factors of $0.027-0.038$ and $0.06-0.149$ were measured for cell depths of $3.05mm$ and $3.80mm$ respectively. Therefore the results proved inconclusive with a general lack of experimental replication.

El-Gamal et al. (1996) used numerical methods to study the effects of rotation on several labyrinth seal types: straight through with labyrinth teeth on rotor, straight through with labyrinth teeth on stator, step-up and step-down seals. Small tooth height to seal radius ratios were examined throughout. Rotation was found to have little effect on straight seals (both variants), a positive effect on step-up seals and a negative effect on step down seals. Whilst stationary stepped seals showed two vortices in each seal cavity. With rotation only one vortex was found in the same seals, the same as found in straight seals. Increasing the ratio of $\left(\frac{Ht}{Tp}\right)$ improved performance of stationary seals. Stepped seals showed improvements when the ratio was above 2.

Zimmermann and Wolff (1998) examined labyrinth seal correlations. The purpose of the work was to gain a new method to correlate labyrinth seal data to get away from general unrelated design principles towards a design useful guide. Heat transfer effects were excluded with the authors' judgement used throughout. The correlations were based upon ideal seal flow (the equation of Martin (1908) (eqn. (B.1)was assumed ideal), COF and C_d with the latter covering many simplifications. Correlations for COF were presented. The C_d (and therefore mass flow) was found to increase if a groove was present. A honeycomb correction factor, derived from Stocker (1978), agreed well with company data: small clearances used an effective gap method whilst large clearances used a friction approach. Effects of rounded tooth corners were accounted for using rounded orifice data. This had less effect on straight through seals than stepped seals. An optimum chamber depth was realised at a ratio of $\left(\frac{Ht}{Ph}\right)$ equal to $\left(\frac{1}{4}\right)$. However, to realise these dimensions in designs could lead to thermal stability problems with shorter teeth in the rub case. Windage effects were included using the approach of Millward and Edwards (1996). It was found that Reynolds number effects are only significant whilst the flow is laminar. The authors note that all correlations could, and perhaps in time should, be improved upon, particularly with regard to stepped seals.

Rhode and Adams (2001a) conducted a numerical analysis of rub groove size on stepped labyrinth seal performance. Grid independent solutions, based on differences of C_d, were obtained. Only square grooves were analysed which was previously found acceptable by Rhode and Allen (1998). Groove widths of $0.762mm$ and $1.524mm$ were analysed at depths and clearances of $0.102mm$ and $0.203mm$. The cases analysed showed little Reynolds number dependence but a substantial step height dependence. It was found that the rub groove limited the separative nature of the stepped labyrinth seal, particularly when the running clearance was small.

Li and Merkle (2001) utilised CFD to enable predictions of leakage characteristics for steam turbines. Stepped seals were analysed with straight seal cases used

as validation. The meshes used were unstructured containing up to 16,000 cells and the steam was modelled as air using the perfect gas setting. Sonic flow was observed upstream of the exit plane above the final tooth. As exit pressure reduced further the fraction of supersonic flow over the last tooth increased until choking conditions were reached.

Chocua et al. (2001) developed a low Reynolds number computational approach to compare to the experimental data of Ha and Childs (1992). Steady state solutions showed that as Reynolds number increased the primary vortex penetrated deeper towards the bottom of the honeycomb cell. Friction factors were found to increase with Reynolds number with the friction factor jump recorded experimentally not seen computationally.

Moore (2001) used CFD to compute rotor-dynamic coefficients. Traditionally designers use bulk flow models which have tremendous efficiency but lack accuracy due to underlying assumptions. The accuracy of the bulk flow model was particularly poor when small clearances, high running speeds or high pressure conditions prevail. When using CFD good agreement was found but with limits on computer power it is unlikely that CFD will become the primary design tool.

Hirano et al. (2003) used CFD to aid understanding of rotor-dynamic forces. Using TASCFLOW the results were compared to an existing bulk flow model, DYNLAB. The bulk flow model under-predicted the forces involved but was significantly faster at 0.1 seconds compared to 4-19 hours for CFD answers.

Dereli and Eser (2003) numerically studied teeth on rotor and teeth on stator labyrinth seals where the chamber depth was equal to half the pitch. The seal analysed had 15 teeth, with a pitch, tooth height and tooth width of $6.35mm, 3.175mm$ and $0.2mm$ respectively. The seal had a clearance of $0.127mm$ and a radius of $76.2mm$. The authors describe a method to calculate both COF and C_d from the geometry and operating conditions in a similar manner to Vermes (1961). The helical velocity was calculated throughout using a balance of momentum and shear forces. Their results lacked independent comparison.

Dong-Chung and Rhode (2003) developed a simplified 2-D approach for computing 3-D honeycomb labyrinth seals. Experimental work was used as a comparison. The running clearance varied from $0.25 - 0.38mm$. In 3-D convergence proved impossible if honeycomb cells with wall thickness were used. Therefore 2-D CFD was used which modelled the honeycomb as baffles of zero thickness. The technique developed proved capable when compared to limited experimental results.

Rhode and Adams (2004a) numerically studied the effect of tooth location on the performance of straight through labyrinth seals with a worn stator. Two-dimensional CFD using the $k - \epsilon$ turbulence model and wall functions were used throughout. All of the grooves studied were rectangular, with their sizes based on the previous work of Zimmermann et al. (1994) and Stocker (1977). The groove depths of $0.102mm$ and $0.305mm$ were analysed at groove widths of $0.762mm$ and $1.524mm$, all at a clearance of $0.203mm$. The tooth location was varied up and downstream of the groove centreline. The most sensitive groove to tooth axial location was the deep-wide groove with the shallow-narrow groove least sensitive. The centred tooth to groove performance was least efficient for the deep-wide groove and most efficient for the deep-narrow groove.

Rhode and Adams (2004b) numerically studied straight through labyrinth seals to see the effects of rub groove width and depth. The model used the same technique as Rhode and Adams (2004a) with validation against Stocker (1977). A four tooth labyrinth seal was studied with all grooves being rectangular. The best results were obtained for the no rub situation. Using a narrow groove gave the best worn stator results due to the effective area dominating. The effect of groove depth reduced as the groove width narrowed or clearance reduced.

Dereli and Eser (2004b) used two control volumes to calculate the performance of the labyrinth seal. One volume represented the seal clearance of the seal whilst the second volume represented the seal cavity. This created a shear stress interface between the two volumes, in addition to that found on the rotor and stator surfaces. The shear stress was calculated using the friction models of Moody and Blasius (e.g. Douglas et al. (1995)) with the overall results compared. The Blasius model generally predicted larger drops in circumferential velocity throughout the seal. A follow up paper, Dereli and Eser (2004a), reporting on the Moody model, compared the results to existing experimental work with reasonable agreement found.

Jinming et al. (2004) used the same numerical technique as Rhode and Adams (2004a) to study the effects of groove shape on the performance of stepped labyrinth seals with an abradable land. The angle of the groove downstream face was varied from $0^\circ - 78^\circ$ as measured towards the flow direction with the upstream face kept constant. One groove geometry was studied at clearances of $0.381mm$ and $\pm 0.127mm$. The groove downstream face angle affected the flow angle entering the seal cavity, quite dramatically above 60°. Whilst this dimension proved important it was not the deciding factor in overall performance. Increasing the angle of the groove downstream face or axially locating the tooth downstream of the groove centreline also reduced the change in the flow direction due to the step by re-aligning the flow towards the axial direction. Further, it acted to reduce the mass flow until

the tooth was located at the groove exit when the mass flow increased.

Wang et al. (2004) studied stepped labyrinth seals in the presence of axial disengagement. This is when the step to tooth position of the labyrinth seal changes enabling, in the worst case, a clear line of sight through the seal. FLUENT using the $k-\epsilon$ RNG turbulence model proved to be the most accurate when compared to Wittig et al. (1987). Non-equilibrium and standard wall functions were used with no significant gains in accuracy recorded by using the more computationally demanding approach. Five teeth were modelled at an external rotor diameter of $310mm$. Each tooth height was $9mm$, with a tooth thickness, clearance, pitch and step height of $2.5mm$, $1mm$, $28mm$ and $3.8mm$ respectively. Overall the performance was dictated by the tooth tip to step distance. Small changes due to axial movements were recorded until the tooth tip disengaged with the step when large changes were recorded. When the seal was engaged two rotating vortices were seen within the labyrinth cavity, broken by the step. When axially disengaged only one vortex was recorded. Radial disengagement, due to different thermal growths for example, was not covered.

Denecke et al. (2005b) used a vast amount of numerical simulations (1152) to highlight the effects of scaling between lab and engine conditions. It was known that the C_d of two seals will be identical if the seals have similar geometry and matching pressure ratio, axial Reynolds number, and turbulence level. The authors were looking for similar reasonings to apply to the development of helical velocity and windage heating in rotating seals. This was particularly useful because many of the seal tests conducted are large scale which allow the use of smaller pressures and temperatures than in engine conditions and reduce the effect of manufacturing uncertainties. Using the Buckingham-π dimensional analysis theory (e.g. Douglas et al. (1995)) suitable candidate variables were highlighted prior to the numerical programme beginning and a scaling factor was also developed. The scaling factor enabled the C_d to remain constant between lab and engine conditions for different boundary conditions of total temperature upstream $\left(T_{t(0)}\right)$ and static pressure downstream $\left(P_{s(n)}\right)$. To enable such a large amount of numerical cases the process from the grid generation through to the convergence checking and grid-adaption procedures was automated. The standard $k-\epsilon$ turbulence model was used throughout with first order discretisation. The numerical study involved geometrically similar seals using a constant helical Mach number being analysed at the same radius, identical seal geometries being analysed at two radii, with the effects of rotation incorporated last. Geometrically similar seals at different radii displayed C_d within calculated uncertainties. Constant seal geometries at different radii exhibited $< 5\%$ deviation in windage heating and helical velocity results. The helical Reynolds number and turbulence intensity were found to have weak effects and therefore ignored.

The windage heating was found to depend upon $\left(\frac{rotor\,surface\,speed}{axial\,fluid\,velocity}\right)$ for geometrically similar seals. The windage heating was also found to decrease with increasing helical velocity at inlet. The inlet helical velocity only had a small impact on mass flow and axial velocity. The helical velocity at outlet approached an asymptote even if the inlet helical velocity was higher. This suggests that with enough teeth the helical velocity imparted by the rotor will be the driving factor in the exit helical velocity achieved. In conclusion C_d, windage heating and helical velocity exiting from a rotating seal were found to be dependent upon pressure ratio, axial Reynolds number, helical Mach number, inlet helical velocity, seal geometry and isentropic exponent. The Prandtl (Pr) number is also required for 3-D effects. When studying air this can be assumed constant.

Collins et al. (2006) developed a 2-D simplification technique that was used to predict the behaviour of 3-D abradable honeycomb labyrinth seals. Due to computational costs only 5 cells were modelled circumferentially with a one tooth labyrinth seal. The simplification technique involved replicating a slice of the 3-D domain and was applied to two cell sizes ($1.60mm$ and $3.20mm$) successfully. Comparisons of inter-seal cavity pressure profiles showed average errors of 5% approximately. In 3-D effects due to the honeycomb surface that propagated into the cell cavity were found. Comparisons between the C_d proved accurate.

2.4 Modern Analysis of the Labyrinth Seal: Windage

McGreehan and Ko (1989) studied power dissipation in smooth and honeycomb labyrinth seals. This was because one of the basic assumptions used thus far, that rotation has no effect, was not totally valid. Rotation had shown no strong effect with regards to leakage. However, when the flow concerned is high-speed and high-pressure, flowing through a small clearance, the power dissipation can increase the temperature of the gas and reduce leakage through a Rayleigh line effect (a solution of the continuity and momentum equations for a particular mass flow: e.g. frictionless flow with heat transfer Douglas et al. (1995)). Therefore labyrinth seals were investigated with 5 main goals in mind:

- Determine seal leakage characteristics.
- Evaluate seal heat generation.
- Identify configurations for reduced leakage and heat generation.
- Develop better flow measurement systems.

- Understand the basic mechanisms in the flow process.

The windage model developed, similar to Daily and Nece (1960), was based on the power absorbed into the fluid through rotor and stator moments with skin friction coefficients. The effects of heat transfer were ignored. An experimental study was undertaken using a $15,000rpm$ rig and worn stators with grooves typically $0.51mm$ deep and $1.52mm$ wide with the teeth aligned centrally to the groove. It was found that most of the windage heating occurred in the first pocket or first half of the seal. With an inlet helical velocity component this effect can be significantly reduced. The surface friction of the rotor is more important as this is the driving force of the system. Smooth stators potentially equate to lower power generation. Once the core velocity is reached the only heat generated is due to transfer of momentum from the rotor to the air to the stator. At lower speeds or larger seal clearances the temperature rise is lower, due to the change in dwell time at lower pressures. As the ratio of helical velocity to rotor speed increases the temperature rise decreases sharply. It was found that heat transfer effects are important to seal temperature rise and therefore rotational effects on labyrinth seal performance are not always negligible.

Wittig et al. (1988) experimentally analysed the effects of heat transfer in labyrinth seals using scaled up models. It was found that heat transfer coefficients increased with pressure ratio with the maximum heat transfer on the stator seen opposite the labyrinth teeth tips and on the rotor at the top of the labyrinth teeth. It was noted however that due to re-circulation more thermocouples would be required in the step area for experimental confirmation. A further numerical study over-predicted the heat transfer effect. In particular the numerical results for the stator gave better agreement with the errors put down to the high level of turbulence seen numerically. It was thought that the grid was too coarse to enable accurate measurement of heat transfer.

Wittig (1992) studied heat transfer effects in rotating gas turbine components. Four techniques to determine heat transfer effects dominate. These are:

- Heat-mass transfer analogy.
- Transient techniques.
- Temperature gradient in flow field component.
- Constant wall heat flux method.

Rotational effects on heat transfer are generally ignored. This cannot be a reasonable assumption at conditions of low Reynolds number and high Taylor number.

At low rotational speeds helical momentum dominates with heat transfer effects increasing with rotation.

Bayley and Childs (1994) examined air temperature rises in compressor and turbine stator wells. The shearing forces on the fluid caused by the boundaries in these cavities are balanced by an enthalpy rise causing windage heating. It was found that decreasing clearance, increasing chamber depth and raising the rate of radial flow increases this effect. With regard to labyrinth seals it was found that increasing the mass flow through the labyrinth by increasing circulation through the system reduces the temperature rise seen towards an asymptotic value. As expected the temperature increased with rotation.

Millward and Edwards (1996) examined windage heating of air passing through labyrinth seals. Whilst it is known that the viscous drag on rotating components equals the windage effect, a lack of detailed knowledge existed. Therefore an experimental and numerical programme examining the performance of 4 different types of seal was undertaken: straight through seal with radial teeth, straight through seal with inclined teeth, stepped seal with radial teeth and a two-stage brush seal. Previous tests gave confidence to rotor-growth models and all instruments were triplicated. The simplicity of the test, only making static measurements before and after the seal, adds to the paper's value. Of the variants tested the brush seal proved best from a leakage viewpoint recording the lowest mass flow. It was found that a relationship between windage heating and mass flow existed that was largely independent of clearance. All of the other produced similar effects, with honeycomb linings adding 15% to the windage heating effect measured. Feltmetal exhibited even stronger windage effects than honeycomb linings. The windage heating in the brush seal was very low. A comparison to the method of McGreehan and Ko (1989) found agreement within 25%. The model developed offered significant benefits over CFD simulations.

Hannis and Corry (1996) developed a disc cooling approach that could be applied to the $4.9MW$ EGT Typhoon industrial turbine. The approach involved using a 1-D gas turbine specific air flow network analysis tool and CFD analysis, with validation tests on an actual engine. The design and analysis of modern gas turbine air systems has had to become more complex due to the thermal loads that are experienced. These thermal loads, according to the authors, primarily come from:

- Increased thermal loads from gas path components to disc rims.
- Higher rim speeds and pressures, both of which act to increase windage.

- Higher mainstream temperatures increasing the seriousness of hot gas ingestion into the disc wheel spaces.
- Increased cooling air supply temperatures from higher pressure ratio compressors.
- Interaction between blade and disc cooling systems.
- The increasing need to minimise cooling air usage and leakage in order to optimise life cycle efficiency and pre-mixed low emissions combustion system performance.

The model developed was used to control hot gas ingestion and compared to tests with reasonable accuracy. The CFD results correlated with the model. Only when the hot gas ingestion was modelled were realistic effects on blade life seen.

Lewis (2002) studied temperature rises in axial compressor stator cavities. Full size development tests were undertaken with measurements of temperature change due to stator well and connecting labyrinth seal presented. All of the tests followed a square cycle approach: stabilisation at idle, throttle slam to max power followed by a stabilisation period with the same in reverse. The analytical method was based on that of Bayley and Childs (1994). Generally the method over-predicted windage and it was suggested that a further factor be added to aid accuracy. Approximately 0.3% of the annulus flow flowed back through the compressor from the downstream high-pressure state to the upstream low-pressure state. Regarding the labyrinth seal it was found that seal windage reduced with an increasing inlet helical velocity fraction. A well designed stator well should have stator well heating of $10 - 20K$ with the labyrinth seal contributing up to $15K$.

Denecke et al. (2005a) studied rotating labyrinth seals for windage heating and helical velocity effects. The labyrinth seal performance, in terms of mass flow, is generally well known. However, predictions of labyrinth seal temperature rise and helical velocity development can carry large errors. Step-up and step-down seals were tested experimentally at various rotational speeds, pressure ratios and fractions of inlet helical velocity components. Further, both smooth and honeycomb stators were studied. The results were compared to the existing models of McGreehan and Ko (1989), Millward and Edwards (1996) and numerical results. The numerical results used the $k - \epsilon$ realisable model and used wall functions for the near wall region. The non-dimensional numbers from Denecke et al. (2005b) were used throughout. Overall it was found that the Millward and Edwards model under predicted windage heating. This model was based upon experiments where inlet helical velocity was not accounted for. As the mass flow increased the temperature rise

seen reduced with heat transfer effects becoming less important. Step-up seals were found to reduce mass flow, typically by up to 30%. The honeycomb surface acted to reduce helical velocity by up to 25%. Laser doppler velocimeter measurements, similar to that conducted by Stoff (1980), were compared to CFD which predicted axial and helical velocities well with the largest deviations seen in step up seals due to the backward facing steps. It was suggested that detached eddy simulations could improve accuracy for these cases.

2.5 Modern Analysis of the Labyrinth Seal: Worn Conditions

Zimmermann et al. (1994) were amongst the first authors to look in detail at worn labyrinth seals using experimental and numerical techniques. Due to fin coatings and relative movements of rotor and stator there may be large surface imperfections like rounded teeth tips and grooved lands. The vast majority of the previous literature was concerned with ideal conditions. For this paper the two primary loss coefficients, C_d and COF, were considered as one variable. When using rounded corners the effects on orifice flow is much more marked than that of a labyrinth seal, with the straight through seal least sensitive to corner rounding. It was found that under laminar conditions the flow contractions above the teeth were not as marked as for turbulent conditions due to the stator wall boundary layer development. Grooves, $0.20mm$ deep and $0.75mm$ wide, representative of typical engine conditions, were analysed experimentally at clearances of $0.20mm$ and $0.40mm$. The results showed an effect due to tooth location which was not expanded upon. Seal performance deteriorated substantially with the rub grooves present, particularly noticeable for the stepped seal analysed. It was noted that aircraft, particularly fighter aircraft experience extremes in terms of Reynolds number: high altitude and low speed cause low Reynolds number, low altitude and high speed cause high Reynolds number.

Rhode and Allen (1998) studied worn labyrinth seals experimentally using water in a large scale, 2-D test rig. Visualisation techniques were used to gain insights into flow field behaviour. Several groove sizes and shapes where analysed. Rounded groove corners only showed small differences from rectangular shaped grooves so they were discontinued. Rounded teeth tips were not included as hardened teeth tips and very soft lands was the primary focus. At small clearances the medium groove size (twice the tooth width) gave the worst results with throughflow jet angles of 50°. Displacing the groove with respect to the teeth improved the leakage resistance, as did reducing the groove width.

Chappel et al. (2001a) studied the temperature rise of blades during low speed rub events on abradable lands. The maximum sliding and incursions speeds analysed were 60 $\left(\frac{m}{sec}\right)$ and 25.4 $\left(\frac{mm}{sec}\right)$ respectively. Against a honeycomb lining it was found that the blade temperature oscillated. This was due to the temperature increasing due to the rub event followed by the honeycomb wall weakening and clearance increasing. Of all the surfaces tested at low speed fibremetal and nickel-graphite proved to have the lowest temperature rises. Honeycomb was only marginally suited to this application because it caused damage on the blade. Additionally, when using a honeycomb stator, higher temperatures were recorded in the rub situation.

Chappel et al. (2001b) examined various abradable materials at utility gas and steam turbine operating conditions. The study was carried out to extend knowledge already available to the aerospace market to the utility and industrial sectors. The typical differences between the aero and utility operating conditions are shown in table (2.1).

	Aero Sector	Utility Sector
Max Tip Speed $(\frac{m}{sec})$	425	365
Max Temp. $(°C)$	700	650
Incursion Rate $(\frac{mm}{sec})$	0.25	0.0025
Incursion Depth (mm)	0.50	1.00+
Tooth Material	TiNi	Steel
Tooth Thickness (mm)	0.50	7.60

Table 2.1: Primary Differences between Aero and Utility Gas Turbine Operating Conditions.

Fibremetal, honeycomb, nickel-graphite surfaces along with a sprayed coating (CoNiCrAIY/hBN/PE) were tested using both high speed, low speed and erosion tests. In the high speed test the fibremetal caused the least wear to the blade with the sprayed coating and nickel-graphite surfaces causing the most. At low speed almost all of the wear from the test was found on the abradable surface. The surface temperatures from the low speed test showed fibremetal had the largest surface temperature rise. This was thought to be due to the proportion of air acting as an insulator for the fibremetal. However, no instrumentation took readings from the blade, or from the honeycomb or nickel-graphite surfaces for comparison. However, in these cases a noticeable temperature rise to the touch was recorded. It was also seen that as the fibremetal ultimate tensile strength increased so did the temperature rise. Honeycomb was the least affected surface by particle size in the erosion test with the feltmetal surface most affected. Overall thermal sprays proved the worst match, with wear on the blade approximating wear on the abradable surface.

Rhode and Allen (2001), in a similar study to Rhode and Allen (1998), analysed the effects that rounded teeth tips and rub grooves had stepped labyrinth seal performance. Both rounded teeth and rub grooves were found to degrade performance with more effect caused by rub grooves than rounded teeth tips.

Denekce et al. (2002) used large scale (4:1) tests using air and water to analyse the influence of rub grooves on straight through, step-up and step-down labyrinth seal leakages. Rectangular grooves were studied at various clearances including a negative clearance (tooth tip located inside the groove). The method of effective area from Schramm et al. (2002) was utilised to calculate C_d thus accounting for zero and negative areas. At positive clearances the dominating factor was found to be COF. A minimum C_d was found for all configurations between a $\left(\frac{Cl}{Cl+Gd}\right)$ of $0.3 - 0.7$. At smaller clearance to groove depth ratios it was found that the seal type was negligible with the geometry of both the rub groove and seal dominating. For straight through labyrinth seals at larger clearances COF effects dominate and effectively increase C_d. For step down seals COF is reduced due to the step thus reducing the C_d. Step up seals with rub grooves showed an increase in leakage.

Chougule et al. (2006) developed a 3-D technique to model the performance of worn abrabdable honeycomb lands using CFX. The groove profiles were taken from in service measurements on a real engine. One complete honeycomb cell was modelled in the circumferential direction. Repetition of some of the data of Stocker (1977) was used to gain confidence in the approach with reasonable agreement obtained. Comparing against in house test data proved less successful. The worn seal leaked more at all pressure ratios and clearances.

2.6 Modern Analysis of the Labyrinth Seal: Computer Codes

McGreehan and Ko (1988) made the first attempt to write a stand alone computer code, *Labflo*, that could predict labyrinth seal performance. Geometric, fluid and operating information were required in the programme that used the approach of Vermes (1961) as a first approximation. Using the calculated Vermes flow rate a pressure drop through the seal is calculated, with a final check on exit pressure to check for convergence and choking conditions. Windage heating was included through a model that assumed the fluid rotated at some fraction of the rotational speed. The static pressure downstream of a restriction was calculated using isentropic relations. The total pressure downstream was then calculated from the static pressure downstream and COF using approach of Vermes (see eqn. B.4). This can

be seen in eqn. (2.8).

$$P_{t(n+1)} = P_{s(n+1)} + COF(P_{t(n)} - P_{s(n+1)}) \tag{2.8}$$

An effective C_d was used to account for tooth corner radii, tip width, tooth angle, surface roughness and Reynolds number.

Williams and Flack (1993) developed *Laby 3*, a computer code that would enable calculation of rotor dynamic coefficients in addition to labyrinth performance models. Several assumptions simplified the analysis:

1. Circumferential velocity and pressure within a labyrinth chamber are constant in the axial direction and functions of angular position in the perturbed case only.
2. Temperature rise within each cavity assumed constant.
3. Fluid considered to behave as an ideal gas.
4. Inter-cavity pressure variations are small in comparison to those across a tooth.
5. Rotor eccentricity is small compared to running clearance.
6. The frequency of acoustic resonance in the cavity is much higher than that of the rotor.
7. When determining circumferential shear stress axial velocity is neglected.
8. Contribution of shear stress to stiffness and damping coefficients is neglected.

Based on these assumptions and the principles of conservation of mass and circumferential momentum, the flow within a labyrinth seal can be described. To calculate the mass flow a routine similar to that of *Labflo* starting with the modified model of Vermes (1961) was applied. Pressure drops across each restriction are calculated using the approach of Benvenuti et al. (1980), with the mass flow adjusted until the exit pressures are within a reasonable tolerance.

Shapiro and Chupp (2004) provided the most complete of the available solutions, *Knife to Knife* (KTK). Each contraction was split into three parts: contraction upstream of tooth, venturi and friction effects over the tooth and expansion (partial or full) after the tooth with each accounting for a pressure loss. The overall performance of the seal came from the Saint-Venant Wantzel equation (eqn. (B.6))

and isentropic relations. In order to determine the loss coefficients the effects of contraction, friction and expansion needed to be separated. Therefore data pertaining to one tooth experiments (complete expansion) was examined. It was assumed that the radius of the tooth leading edge upstream would only affect the contraction and that tooth tip thickness only affected the frictional effects. Experimental data was then analysed with correlations found. With the addition of multiple teeth COF and its influence on single tooth parameters needed to be included. To do this the COF was treated as an expansion angle problem, with the actual expansion angle calculated as shown in eqn. (2.9). Typically 6° was found acceptable.

$$\beta = 3.79\sqrt{\frac{Ph - Tp}{Ht}} \tag{2.9}$$

By using single tooth data, adjusted to account for area contraction or expansion ratios, COF could be included in both the contraction and friction coefficients of each tooth. The calculated coefficients were checked against an experimental database. The effects of wall roughness, including the potential associated increase in area, were included in the friction loss term. The area over which the friction acted varied dependent upon tooth position in the seal. For stepped seals COF was assumed negligible. However, the flow into a tooth might have an angle that could affect the contraction and friction effects of that tooth. Therefore an area multiplier was used to account for flow distortion, distance to contact and any COF that may be present. Friction was accounted for in the same manner as straight through seals except the tooth tip thickness was taken as the characteristic length.

2.7 Modern Analysis of Gas Turbine Sealing

Smith (1978) highlighted issues involved with seal operation and maintenance. Normal engine deterioration can account for 4% in loss of performance, which is generally not recoverable after retrofit activity. This can amount to a fuel bill of approximately $1.2 million based on a 12 plane fleet using high bypass engines. Through differing levels of wear in different parts of the engine speed mismatch can occur, causing potential engine stalls with expensive operating and overhaul costs (up to $6 million per year for a US operator). Problems with seals that have led to engine overhauls were presented over a seven year period as a percentage of total engine overhauls. For early turbofans ($\approx$ 1959), medium bypass engines ($\approx$ 1965) and high bypass engines ($\approx$ 1970) this equated to 32%, 50% and 32% respectively. The costs associated with seals were given as 1.5% of total engine material cost for parts ($750k) and 5% of total engine labour cost ($700k). However, when access costs are included a further $6 million is spent annually just to reach the seals inside an engine. Due to these costs and operational limitations it was suggested that 8,000 - 10,000 hours of

operation within an acceptable deterioration and failure rate should be targeted.

Ferguson (1988) was the first author to write about the benefits of the brush seal, which at the time was a relatively modern development. Throughout the years many authors have written about labyrinth seal flow, and still today its performance is largely clearance dependent. Therefore reducing the clearance has been a priority for seal designers. By using a brush seal instead of an optimised labyrinth seal at a clearance of $0.70mm$ the mass flow can be reduced by 10%. Further, difficult sealing conditions in gas turbines need new technology to help overcome them: $300\left(\frac{m}{sec}\right)$, $650°C$ and $1400kPa$. Brush seals are able to accommodate transient movements without hugely affecting leakage, they are easy to repair and can maintain a high pressure differential. However, as they generally contact the rotor there is an obvious drag factor. They cannot be expected to cope with excessive distortion, eccentricities or rotor orbiting. Additionally less is heat generated in a brush seal than windage in a labyrinth seal.

Munson and Steinetz (1994) used a comparative study based upon two engines to highlight the benefits of advanced seal technology. The two engines concerned were a small turboshaft engine for a helicopter and a regional aircraft turbofan which produce 2000+ horsepower and $20,000 - 24,000$ lbs thrust in advanced form respectively. A hypothetical mission was used to enable clear analysis, with only unplanned leakages treated as losses. For the regional jet it was found that 5 locations alone accounted for 75% of the total leakage, for the helicopter engine 4 locations accounted for 50%. The best benefits were thought to come from seals with active clearance controls and film riding seals in key locations where brush seals are unsuitable. By covering the most important seals (compressor tip seals, rim seals) an improvement of 2.6% and 5.2% in SFC can be achieved for the regional turbofan and turboshaft engine respectively without employing active clearance controls. It is clear that advances made in engine design should not be eroded through poor sealing technology.

Mahler and Boyes (1995) examined how to include brush seals into an actual engine as opposed to just providing test results. These seals operated on diameters of up to $620mm$, with sliding speeds of $350\left(\frac{m}{sec}\right)$ and maximum pressure drops of $12.5Bar$. Sub-scale test rigs typically operated at $175 - 205mm$ diameter. Mahler and Boyes used sub scale rig tests that examined wear properties, performance and endurance prior to inclusion into an engine design. Over one overhaul cycle, typically $3,000$ cycles, brush seals had a small drop in performance with an estimated 0.4% improvement in fuel consumption when compared to an equivalent labyrinth. Engine and in-flight tests confirmed the results.

Fellenstien et al. (1996) examined brush seal wear characteristics using a tuft (small section of brush) testing technique. State of the art brush seals were operating at $700°C$, $305\left(\frac{m}{sec}\right)$ sliding speeds and pressure drops per brush stage of $550-690kPa$. In the future brush seals are expected to operate at $815°C$, $500\left(\frac{m}{sec}\right)$ sliding speeds and $960kPa$ pressure drop per brush. Five types of bristle were tested against a smooth and a chrome carbide surface using 920 bristles of $0.071mm$ diameter. Fifty hours of testing at up to $17,000rpm$ and $700°C$ were conducted with only two types passing this test. Other materials were worn away in under 5 hours, or suffered flaring and buckling failures. Overall the technique proved a cost effective examination of wear properties of the brush seal.

Wolfe et al. (1997) reported upon the benefits of the brush seal to the industrial gas turbine. As a baseload industrial machine could have $8,000$ hours of operation in one year the potential for fuel savings are significant. However, the differences between aero and industrial gas turbines make this a complex problem. These differences include larger diameters, longer running times and therefore increased robustness requirements, fewer transient excursions, split casings with accompanying ellipticity, and larger tolerances. The benefits of advanced sealing solutions are the same though, particularly at the compressor discharge ((H)igh (P)ressure (P)acking) and turbine interstage seals. (Packing is another label that can be applied to rotating seals.) Brush seals had been developed specifically for the HPP and middle bearing location on the General Electric E-Class of gas turbine. These seals augment the existing labyrinth seals by replacing a labyrinth tooth in the original design, thus making implementation fail safe. Three factors beyond material properties affect brush seal wear: interference, pressure drop and surface speeds. Tests and field measurements expect performance to be maintained to the service intervals of $48,000$ hours. The maximum brush seal benefit was recorded as 1.9% improvement in power output and 0.7% in heat rate, with 1.3% and 0.7% guaranteed.

Steinetz and Hendricks (1998) highlighted the role that sealing technology has in achieving next-generation turbine engine goals. As studies had shown that increased pressure and temperature are desired to improve performance there is also a desire to reduce weight. Sealing technology therefore has a crucial role to play in maintaining SFC, thrust to weight ratios, durability and operating costs. NASA developed goals to aid turbine engine manufacturers whilst improving vehicle performance and reducing direct operating costs. These are:

- Reduce commercial aircraft operating costs by 3% for large engines, 5% for regional engines.
- Reduce engine fuel burn by up to 10%.

- Reduce NO_x by more than 50%.
- Reduce airport noise by $7dB$ or achieve a $\left(\frac{3}{4}\right)$ reduction in acoustic energy.

With the airline industry becoming more cost conscious NASA planned to focus on technologies with a high performance to cost ratio. This is because ownership, maintenance and fuel are over 70% of the operating costs for a small 100 seat passenger plane. Seals, which can be improved at 20% to 25% of the cost of other parts of the engine, are having to operate at higher pressure, temperature and surface speeds. As rotor excursions cause a loss in design clearances, and therefore more unplanned leakage, more throttle is required to maintain performance. However, exceeding exhaust gas temperatures also requires more overhaul. A study on a typical regional jet showed that a 2% reduction in leakage from HP turbine seals could enable either more power for the same conditions (turbine entry temperature and fuel flow), 2.5% higher engine thrust to weight ratio or 0.24% lower take off weight. By just concentrating on 3 seal locations a reduction of 0.89% in direct operating costs could be realised.

Dinc et al. (1998) looked at the application of the brush seal to the interstage section of industrial turbine engines. The previous work of Wolfe et al. (1997) highlighted the benefits of using a brush seal at the HPP location: 0.7% increase and 0.2% decrease in power output and heat rate respectively. The new design utilised two pressure balance systems from Cross Manufacturing Ltd., passive and active. In both systems the brush seal had a downstream cavity to reduce the large axial loads experienced. In the active seal this flow was metered through an orifice whilst in the passive seal it was not metered accurately. The velocity experienced in the bristles caused a pressure closure effect, where the helical velocity acts to change the lay angle of the bristles moving them towards the rotor. The helical velocity also adds to hang up problems, which have been reduced by both the passive and active designs. This effect increases with velocity and therefore pressure drop. Under test conditions the brush seal recorded $25 - 40\%$ reduced mass flow when running hot, and 30% when rotating due to the increased number of bristles the flow passes. The seal designs have enabled a further 0.7% increase and a 0.2% decrease in power output and heat rate over the service intervals of 48,000, hours beyond that reported by Wolfe et al. respectively.

Menedez and Xia (2000) examined brush seal design processes for large industrial gas turbines. This was undertaken due to the underlying conditions changing due to seal location from relatively benign conditions to high temperature, high sliding speeds and high pressure drops. The current approach of wearing in brush seals by applying a cold build clearance during start-up is only successful for the

more benign locations with low speeds, small interferences and low contact pressures. Under this design process the interference aids performance until a fully worn condition is reached. This deterioration is predictable between service intervals. However, as brush seal locations move away from the centreline of the engine thermal distortions and sliding speeds increase. This increases bristle pressure and heat generation (possibly up to 9 times) potentially leading to excess wear and therefore a deterioration of performance beyond design conditions. The new design approach involves using the pressure closure effect of the brush seal to reduce clearance in the steady state. This acts to extend component lives, enables minimal interferences, and reduces contact loads. Several case studies highlighted the potential benefits in applications.

Pastrama et al. (2001) highlighted benefits of using brush seals in steam turbines. Steam turbines present sealing problems that include very high pressure, steam chemistry and rotordynamic forces. Losses in a typical steam turbine are highlighted, with tip leakage and shaft packings highlighted as primary areas of sealing benefit. These account for 22% and 7% of total leakage flows respectively. In an industrial turbine approximately 1% leakage reduction can be achieved in interstage packings and turbine tip seals. Pressure drops of up to $2.75Bar$ can be achieved by a single stage, $4.2Bar$ in combination. Rotor stiffness, brush seal location and bristle stiffness all need to be fully understood to avoid self excitation problems.

Chupp et al. (2001) studied the potential of advanced seals for industrial turbine applications. They noted that generally brush seals have reduced labyrinth leakages in the same locations with a $0.2-0.6\%$ reduction in heat rate and a $0.3-1.0\%$ increase in power output. The cost-benefit approach can highlight the best areas for retro-fitting. Several seals are analysed using a six-sigma approach, including cloth seals. However, it is noted that whilst abradables have been used in aviation since the 1960s their transition to industrial turbines has not progressed rapidly due to the longer service periods required.

Munson et al. (2001) looked at the development of foil face seal development. In gas turbines the requirement for temperature and surface velocity capabilities in excess of other applications have limited the use of foil face seals. However, these seals have been accepted in other areas, notably the pipeline and process industry, and with the connection between better seals and better performance future possibilities cannot be ruled out.

Chupp et al. (2002a) studied dynamic seal development for industrial turbine applications. Brush seals developed for the GE90 engine have been transferred

across to industrial turbines giving improvements in power output of $0.3 - 1.0\%$ per location. At time of publication 205 brush seals had been fitted to industrial turbines with one seal seeing $40,000$ hours service. The brush seal dimensions have been chosen to avoid the contact situation with the pressure controlled by bristle diameter, bristle density and number of brush seals in series. It could also be possible to apply brush seals to steam turbines. Abradable seals are generally classified by temperature and offer the simplest way to reduce running clearances. Abradables need to consider relative motions (blade tip speed, incursion rate, depth of cut), temperature, contaniments, geometry and material properties. Therefore, despite off the shelf materials, often each seal needs to be modified or redesigned to suit particular requirements.

Chupp et al. (2002b) looked at applying abradable seals to industrial gas turbines. For tip clearance seals up to 0.6% improvement can be achieved by using honeycomb linings. For abradable seals the temperature regime needs to be defined as either low temperature ($< 400°C$, LP compressor), mid range ($< 760°C$, LP and HP compressor) or high temperature ($< 1150°C$). Additionally at low incursion speeds honeycomb cell walls partly deform and wear away. Therefore as the speed or temperature increases deformation becomes more dominant. At high surface speeds ($> 100\left(\frac{m}{sec}\right)$) wear mechanisms become difficult to study by normal tribology which is predominantly a low speed science. At these speeds the seal is also susceptible to gas and solid particle erosion.

Stephen and Hogg (2003) reported on work undertaken to extend the brush seal to steam turbine applications. Most of the retrofit activity currently undertaken involves gas path components like blades. However, the brush seal offered an attractive alternative to existing sealing solutions. Aerodynamic stiffening of brush seal acts to increase the mechanical stiffness of the packing, which results in much higher torque requirements and associated wear issues. Brush seals in series, or as part of a labyrinth can also acts to cause rotor excitations. This occurs when the rotor is out of centre causing circumferential pressure variations that acts as cross coupled forces. The steam turbine seal model developed required less accuracy than their gas turbine equivalents due to the cooling requirements in gas turbines. The brush seals were not a cheap sealing option costing $\$10,000$ per stage, significantly more than an equivalent labyrinth. However, for typical blade tip seals, a leakage increase due to deterioration of 0.5% is common. Therefore, on a $15MW$ stage, the resulting cost of $\$150/kW$ can easily be calculated.

Ghasripoor et al. (2004) analysed wearing of another labyrinth seal competitor, the strip seal. The strip seal consists of sheet metal that protrudes into the flow like the labyrinth teeth with the base secured by retaining wire. This design offers

benefits as it is easily replaceable, cheap and can also be used against an abradable land. However, at high speeds ($> 50\left(\frac{m}{sec}\right)$) the seal has a tendency to melt and snap off instead of wear. At these high speeds the wear of the seal is primarily dependent upon conductance of the material and not the seal strength.

Proctor and Delgado (2004) investigated the leakage and power loss of competing designs of a labyrinth seal, a brush seal and a finger seal at typical engine conditions. The finger seal is a variant of the brush seal primarily offering cost savings in the assembly process. The test was capable of a pressure drop of $517kPa$, temperatures up to $922K$ and surface speeds of up to $366\left(\frac{m}{sec}\right)$. The labyrinth seal investigated had four teeth, a tooth height and pitch equal to $2.286mm$ and $3.175mm$ respectively and a cold build clearance of $0.229mm$. Although the labyrinth seal was not investigated dynamically it was anticipated that to avoid contact under rotating conditions at $922K$ the cold build clearance should increase to $0.305mm$, giving clearances of $0.254mm$ and $0.394mm$ at temperatures of $700K$ and $922K$ respectively. The brush seal analysed used bristles of $0.102mm$ diameter packed at $675\left(\frac{bristles}{cm}\right)$ with an initial radial interference of $0.0965mm$. The finger seal used a sheet cobalt-base alloy with a radial interference of $0.165mm$. The static tests showed the brush seal leaked 24% less than the labyrinth seal and used 38% of the axial space. The static test at $700K$ and $922K$ showed the finger seal passed $60 - 75\%$ and 14% of the brush seal mass flow respectively. Under a four hour endurance test the finger seal fared better than the brush seal, with the brush seal showing a marked deterioration after 2 hours. It was thought that this was due to the effects of temperature on the test components. When considering the power loss results the finger seal was marginally better than the brush seal, with the difference more apparent when allowances are made for test set-up. The finger seal caused approximately 24 times more wear than the brush seal to the rotor but did start with twice the radial interference.

Franceshini et al. (2006) presented details of a low speed brush seal characterisation rig. This was to be used to help the authors understand the problems of pressure stiffening, when the compliance of the seal is reduced due to the pressure within the bristle pack, and bristle hang-up, when the bristles remain eccentrically located after a rotor excursion. Eccentric effects could also be measured with the torque, stiffness and mass flow measurements recorded throughout. Overall the rig would aid understanding of future designs.

Matthias et al. (2006) studied the longevity of brush seals with respect to steam turbines, highlighting some situations where up to seven years of service had been attained. It was found that the wear on the seal was primarily located within the initial start up period. Bristle wear, due to frictional rubbing of the bristles, was

also found. However, as wear reduces the bristle length the bristle stiffness increases thus reducing the pressure stiffening effect. This reduces the contact force and wear experienced but increases the mass flow.

Childs et al. (2006) reported on the work undertaken as part of the ICAS-GT2 research programme. This concerned the design and operation of high pressure, high speed rigs that could nearly represent in-engine conditions. In a modern turbofan the effect of cooling flow may cost up to 6% in SFC. A 1% saving in SFC could equate to a 0.5% reduction in direct operating costs and a saving of 560 tonnes of fuel per annum. Regarding the test rigs that were designed and developed one of the main difficulties involved obtaining accurate measurements of heat transfer.

2.8 Discussion

Over the past 100 years the labyrinth seal has been an active area of research. In this time the labyrinth seal whilst refined since those early beginnings is still very much in a similar form to that studied 100 years ago. However, modern gas and steam turbines require sealing technology that has to withstand increased pressures, temperatures and sliding speeds all whilst operating reliably. However, end users of turbine engines do not make purchase decisions based upon the sealing solutions applied within the turbine. These users are focussed on power output, efficiency, fuel economy and cost as this is what dictates their eventual profitability. Regarding aircraft operations Steinetz and Hendricks (1998) highlighted that for a regional jet aircraft (an aircraft with approximately 100 seats) maintenance and fuel account for 70% of the ownership cost. However, since 1998 the proportion of cost attributed to fuel can reasonably be assumed to have increased due to the rising cost of fossil fuel. Therefore turbine manufacturers have had an increased focus on improving their market position by investing in areas with a high cost-benefit ratio. Seals, which can be developed at a fraction of the cost of other areas of the engine, notably 5% of turbine redevelopment cost (Stocker (1978)), offer the potential to improve performance and therefore market attractiveness cost effectively. Several authors have highlighted this link between efficient sealing solutions and reductions in fuel use. Therefore efficient seals lead to lower operational costs and an increased market attractiveness. For a civil aircraft engine Stocker (1975) highlighted that if a leakage reduction of 1% was achieved a saving of 0.1% SFC would be achieved. Further, Stocker (1977) showed that if cooling air flow increased 10% SFC could increase by 0.5%. Further, Stocker (1978) highlighted that if a 25% leakage reduction was achieved in the internal air system then a 2.7% improvement in SFC could be made. From an aircraft operations viewpoint Smith (1978) found that deterioration of seals

in service could equate to a performance loss of 4%. Further, due to seal maintenance and deterioration, typical material and labour costs incurred were 1.5% and 5% of total engine cost respectively. Therefore it was suggested that in aviation seals should aim for 8,000-10,000 hours of service. Chan et al. (1987) found that a 4% reduction in leakage could achieve a 2% SFC saving. Sturgess (1988) highlighted that the rate of gas turbine development should double, half of which should come from advanced materials and half from improved component efficiencies. Munson and Steinetz (1994) showed that 5 seal locations accounted for 75% of the the total leakage within a regional jet engine. For a helicopter engine 4 locations were found to account for 50%. Further, by concentrating work on the most important seals in these engines SFC savings of 2.6% and 5.2% respectively were found. Steinetz and Hendricks (1998) reported that a 2% reduction in HP turbine leakage could lead to 2.5% higher thrust to weight ratio or 0.24% lower take off weight. Further, NASA aircraft engine development goals focussed on improving vehicle performance and reducing direct operational costs. Of these goals efficient seals can contribute to two:

- Reduce commercial aircraft operating costs by 3% for large engines, 5% for regional engines.
- Reduce engine fuel burn by up to 10%.

Michaud et al. (2003) applied the 25% leakage reduction highlighted by Stocker (1978) to show that, based on recent figures, 16 million barrels of jet oil could be saved in the US alone. Childs et al. (2006) showed that up to 6% of SFC can be used in cooling applications and that if a 1% SFC saving could be made operating costs and fuel use could reduce by 0.5% and 560 tonnes annually.

Therefore whilst the basic design of the labyrinth seal could be thought of as simple it has proved an economic and beneficial area of research for many years. Recently, however, the labyrinth seal has faced increased competition from other types of seal, notably the brush seal since the 1970s (Ferguson (1988)) and in recent years the finger seal (Proctor and Delgado (2004)). Ferguson (1988) found up to 10% reductions in mass flow when using a brush seal as compared to an equivalent labyrinth seal. Additionally, the brush seals were found easy to repair and could withstand high pressure differentials. However, as the brush seal is a contact seal there was an associated drag factor. Mahler and Boyes (1995) reported that whilst brush seals do wear, over one maintenance cycle savings of 0.4% fuel consumption compared to a labyrinth were found. When retrofitting existing gas turbines with brush seals Wolfe et al. (1997) guaranteed performance improvements of 1.3%. Further, brush seals were found to have performed adequately for up to 48,000 hours. Menedez and Xia (2000) found that as brush seals moved to larger radii thermal

distortions and sliding speeds were found to increase. This led to increased bristle pressure and heat generation causing excess wear and performance deterioration. Stephen and Hogg (2003) found that the increased expense of brush seals was justified with a typical 0.5% improvement of a $15MW$ stage equating to $\$150/kW$. The same brush seals did have higher torque requirements and wear due to the effect of pressure stiffening. Whilst the brush seal does offer benefits the labyrinth seal still offers many advantages that are yet to be fully realised by other techniques:

- Friction free running with no lubrication required.
- A high temperature capability.
- Large sliding speed capability.
- Mechanical Integrity.

Considering the long history of the labyrinth seal it may be thought surprising that even today the first analytical approach of Martin (1908), often with the further refinements of Vermes (1961), is still used by many designers as a baseline calculation. The Martin approach does not include COF and assumes small pressure drops across each tooth with the seal treated isothermally. Vermes relaxed the isothermal assumption and developed a technique to calculate COF based upon seal geometry. Egli (1935) applied the Saint-Venant Wantzel technique whilst introducing a flow coefficient equivalent to C_d. Egli found that Martin's approach was applicable to all but the last tooth assuming there are four or more teeth. Later, Sneck (1974) highlighted the drawbacks of using the standard Vermes approach for 4 teeth or less suggesting the Saint-Venant Wantzel technique should be used for these circumstances. The importance of COF, which can be reduced by using a stepped configuration or more teeth, was highlighted. These findings were later confirmed by Kearton (1955) who, when studying a staggered labyrinth seal with inherently low kinetic energy carry over, successfully used a constant C_d on all but the last tooth. Jerie (1948) found from experiments that one well designed tooth could perform better than two poorly designed ones thus highlighting the importance of understanding the interaction of C_d and kinetic energy carry over. Benvenuti et al. (1980) found that the first 3 teeth of 14 showed variations in C_d with a larger pressure drop recorded over the first tooth. This led to calculated values of C_d exceeding one dependant upon tooth location. This variation in first tooth pressure drop was seen again by Zimmermann and Wolff (1987) who applied a different C_d and COF for the first tooth. Different tooth effects were reported by Rhode and Hibbs (1992) who found an increasing Mach number and pressure drop through the labyrinth seal. Rhode and Sobolik (1986) used numerical techniques

to predict performance in order to negate the need to estimate the kinetic energy carry over. To reduce the COF and improve seal performance Rhode and Guidry (1993a) and Vakili et al. (2005) used blocks on the stator wall. Numerically Rhode and Guidry (1993a) and Paolillo et al. (2006) have reported significantly enhanced performance due to perfectly sharp labyrinth teeth corners causing an enhanced, but artificial, tooth separation effect. Whilst labyrinth tooth rounding can have an effect Zimmermann et al. (1994) reported that straight seals were least sensitive. Further, Rhode and Allen (2001) found that worn stators have a larger effect on labyrinth performance than rounded teeth tips. Therefore the basic problems that have led to ongoing research are understanding the combined effects of C_d and COF and how they interact.

Several authors have used the expansion angle theory to analyse the performance of labyrinth seals. Hodkinson (1939) was the first author to analyse COF as a jet with an expansion angle, taken to be 1°. Vermes (1961) used an expansion angle approach to calculate the carry over factor for straight through seals by modelling the flow as half of a symmetrical jet. This approach can be seen in eqn. (B.5). Meyer and Lowrie (1975) found pitch effects that backed up the expansion angle theory of Hodkinson, with an increasing pitch reducing leakage. Komotori and Miyake (1977) further developed the expansion angle theory of Hodkinson using a constant angle of 6°. It was calculated that a variation of 1° in expansion angle could equate to 2-3% variation in mass flow. Therefore variations of 10-15% would be expected between the techniques of Hodkinson and Komotori and Miyake. The expansion angle was further utilised by Shapiro and Chupp (2004) in the development of their computer code, *Knife to Knife*. The expansion angle calculated was based purely upon geometry as shown in eqn. (2.9). Typically 6° was found acceptable. The basic problems with the expansion angle theory are that the angle will vary with pressure ratio, tooth location location within the seal and tooth geometry. None of these methods account for these variations.

Reynolds number effects have been reported by several authors including Zimmermann et al. (1994), Zimmermann and Wolff (1998), Rhode and Adams (2001a) and Waschka et al. (1990). Zimmermann and Wolff and Waschka et al. only found effects under laminar conditions that were not as significant when the flow was turbulent. However, when studying worn labyrinth seals Zimmermann et al. found enhanced flow contraction over the teeth with turbulent flow that was explained by the development of the stator wall turbulent boundary layer. Rhode and Adams found no dependence upon Re.

Stocker (1975), (1977) and (1978) experimentally tested honeycomb linings finding reduced leakages and a small clearance effect dependent upon cell size. Childs

et al. (1989) found that a honeycomb seal offered leakage reduction whilst improving rotor stability over a typical labyrinth seal and also acted as a brake to components of helical velocity. This finding was contradicted by He et al. (2001) who found that at small clearances ($0.12mm$ as opposed to $0.41mm$ used by Childs et al.) the honeycomb seal performed better. Brownell et al. (1989) found that honeycomb acted to reduce the carry over effect with each restriction operating closer to ideal. Ha and Childs (1992) measured honeycomb friction factors finding that they increased with clearance. The Stocker small clearance effect was also recorded. Using a similar test Allcock (1999) found that small cell sizes act more like a flat plate and a reducing clearance added to the relative roughness. Schramm et al. (2002) highlighted the differences in area available to the flow when using honeycomb, which is the foundation of the small clearance effect. The abradable area in contact with the flow was also found to reduce in a stepped configuration. Willenborg et al. (2002) found heat transfer effects reduced whilst using honeycomb which was thought to be because of trapped fluid in the honeycomb cell acting as an insulator. Effects due to variations in clearance were not recorded.

The first authors to model honeycomb numerically were Athavale and Hendricks (1996) who tried to replicate the study of Childs et al. (1989) with limited success. Chocua et al. (2001) replicated the same study showing penetration into the honeycomb cell at higher Reynolds numbers. The friction factor jump seen experimentally was not replicated. Dong-Chung and Rhode (2003) tried to create 3-D numerical solutions of honeycomb labyrinth seals. However, in 3-D convergence proved impossible but reasonably accurate 2-D solutions with the honeycomb walls modelled as baffles were obtained. Recently CFD models of honeycomb labyrinth seals have been developed by Chougule et al. (2006) and Collins et al. (2006). These have proved successful at replicating in engine wear conditions and creating a 2-D simplification technique respectively. Paolillo et al. (2006) are planning to model abradable honeycomb labyrinth seals in 3-D to aid verification of experimental results. Overall honeycomb has proved to be beneficial when used in conjunction with a labyrinth seal. In addition to the reduced leakage, honeycomb can enhance rotor stability, reduce components of helical velocity and have beneficial heat transfer effects for the stator. However, there is a lack of work that analyses worn honeycomb surfaces and the effect of tooth location on the overall performance.

Several authors have studied rotational effects experimentally: Stocker (1975), (1977) and (1978), Komotori and Miyake (1977), McGreehan and Ko (1989), Miyake and Duh (1990) and Waschka et al. (1990) amongst others. All reported similar findings with rotation acting to decrease leakage, particularly when using small clearances and tooth heights. Waschka et al. found benefits due to rotational effects under laminar conditions that reduced under turbulent conditions. Two authors,

Stocker and Miyake and Duh, found that when using honeycomb linings rotational effects were negligible. This finding was somewhat confirmed by Childs et al. (1989) who found that in an annular honeycomb seal helical velocity was significantly reduced. Komotori and Miyake concluded that under rotating conditions the effects on their approach of using an expansion angle are not negligible, particularly when using small clearances or groove depths. McGreehan and Ko found that whilst rotation had no strong effect on leakage it could have a strong effect on windage heating, particularly during the first half of the seal. Millward and Edwards (1996) found that honeycomb surfaces could create up to 15% more windage. El-Gamal et al. (1996) in a numerical study concluded that rotational effects on leakage are negligible for straight through labyrinth seals. As can be seen, understanding the combined effects of rotation and honeycomb surfaces needs further work, particularly regarding windage and heat transfer effects. However, whilst rotation has been found to reduce leakage this is most likely due to the helical velocity generated which effectively increases the relative pitch. However, as honeycomb acts to reduce helical velocity rotational effects due to abradable honeycomb labyrinth seals have been found to be negligible. Therefore the overall effect of rotation on leakage of abradable honeycomb labyrinth seals can be assumed small, particularly as any effects diminish with turbulence.

Regarding temperature rises in the labyrinth seal Millward and Edwards (1996) found that honeycomb linings could increase windage by up to 15%. Willenborg et al. (2002) reported that honeycomb reduced heat transfer to the stator, most likely through an insulation process. Lewis (2002) recorded temperature rises in stator cavities noting that a well designed cavity should have heating effects of $10 - 20K$ with the labyrinth seal contributing up to $15K$. Denecke et al. (2005a) experimentally found that the model of Millward and Edwards under-predicted windage heating by not accounting for an inlet helical velocity component. Therefore regarding the abradable honeycomb labyrinth seal where the helical velocity component is reduced the model of Millward and Edwards should suffice. Childs et al. (2006) highlighted that a major difficulty for current experimental investigations is accurately measuring heat transfer.

Zimmermann and Wolff (1987) highlighted that worn seals did not have much available information. Rhode and Allen (1998) studied worn labyrinth seals using water in a large scale rig finding no marked difference between rectangular or realistic rub groove profiles but interesting tooth to groove location effects were reported. Denekce et al. (2002) analysed labyrinth seals with rub grooves finding that at positive clearances carry over effects dominated. Two numerical papers, Rhode and Adams (2004a) and Rhode and Adams (2004b), studied tooth to groove axial location and rub groove shape and size respectively using the findings of Rhode and

Allen (all rub grooves analysed were rectangular). The least sensitive groove to axial location was found to be the shallow-narrow groove with the narrow groove performing best showing that the effective area dominates. Jinming et al. (2004) found performance benefits when the tooth and rub groove are out of alignment until the labyrinth tooth was located at the groove exit when a performance deterioration was recorded. Chougule et al. (2006) wrote the first numerical paper regarding worn abradable honeycomb labyrinth seals. Test data was replicated with reasonable success. Wear profiles have been found to significantly affect performance with the effects due to carry over and expansion angles changing. However, the overall study of wear on abradable honeycomb labyrinth seals has yet to be fully understood.

Throughout the years seal designers have been trying to find better ways of modelling the two primary loss coefficients, C_d and COF, whilst trying to find ways of understanding their interaction. Historically this was undertaken using correlations based on available data sets with much work undertaken to develop suitable data sets. Recently, with the development of computers, there is much more design work undertaken numerically with experimental testing reserved for validation purposes. This saves cost and time for equipment manufacturers. There are also more generic labyrinth flow solver codes, of which the most complete publicly available code is arguably the *Knife to Knife* code of Shapiro and Chupp (2004). This code breaks each restriction into three sections: contraction, friction and expansion, each of which has an associated loss coefficient. However, the fundamental reason why the labyrinth seal is still an active area of research and why the models of Martin (1908) and Vermes (1961) are still used is that the physics of the seal have yet to be fully captured with a simple model. Often the simplifications used whilst aiding analysis do not fully capture the physics, thus leaving areas were there is a lack of knowledge. This is particularly true as labyrinth seals have become more complex either through geometrical configuration, the inclusion of abradable linings or other seal design concepts and operating requirements. Whilst the complexities of labyrinth seal performance are not yet fully understood the internal air system is an area were redevelopment is economic. It is for these reasons that there is a revived interest in labyrinth seal performance and why Kool et al. (2006) have developed a seal test rig that is capable of in-engine or near in-engine conditions thus avoiding the scaling problems highlighted by Wittig et al. (1983). It is also why *Cross* have become involved with this project, to aid their understanding of the labyrinth seal.

Chapter 3

Experimental Programme

3.1 Introduction

The current practice of seal design in industry is to design the seal assuming no wear and allow a degradation factor to be applied. However, wear is inherent in a labyrinth seal with the actual wear profiles being specific to a particular set of conditions. It was not the aim of this test to study variations in, and causes of, wear profiles but rather look for overall effects on performance due to worn abradable honeycomb lands. Therefore wear data received from industry, based upon a civilian aerospace gas turbine, was used to ensure that the test was representative of actual worn abradable honeycomb labyrinth seal conditions. To cover a range of realistic engine conditions the experimental set-up used had to be capable of simulating axial and radial movements whilst passing a range of mass flows. It is for this reason that a generic labyrinth seal geometry, applicable to that seen both in the literature and application, was chosen for the study.

3.2 Experimental Design

The purpose of this experiment is to look for the effects of wear on the performance of a worn abradable honeycomb labyrinth seal. In order to study the effects of wear upon labyrinth seal performance adequately it was important to use labyrinth teeth in the test section and obtain experimental results at different clearances, pressures and different relative tooth-to-groove positions. For simplicity the test section used was effectively two-dimensional. Rotational effects are small provided the axial Reynolds number is greater than $5,000 - 10,000$ (Reynolds number dependent upon clearance) with the limiting Reynolds number increasing with increasing clearance (Waschka et al. (1990)). Further, by maintaining the aspect ratio ($\frac{duct\,width}{Cl}$) of the

test section above seven at all positions the flow along the centreline of the duct can be considered two dimensional (Dean (1974)). The duct width for the experimental programme, $108.00mm$, was chosen to match that used by Allcock (1999).

As very little work has been undertaken on worn labyrinth seals it was also decided to place instrumentation inside the seal. These measurements would help to characterise the performance of the seal with a worn honeycomb land. How the dimensions of the labyrinth seal and groove were chosen will be discussed in section (3.2.1).

3.2.1 Labyrinth Seal Wear

The wear of (and due to) the labyrinth seal is caused by the relative movements between the rotor and the stator. There are two main movements between the rotor and stator: radial and axial. These movements are primarily caused by centrifugal loads, pressure loads, thermal loads and transient loading sequences. Additionally, the magnitude of movement at any location within the turbine engine depends on the bearing arrangement and the point of operation within the cycle. Other causes of relative motion are precessional moments of the rotor inside the nacelle and turbulent flights. All of these movements effectively act to change the running clearance and axial position of the seal dynamically, potentially causing wear. Published work has found some interesting effects related to labyrinth seal wear. Zimmermann et al. (1994) found a large performance deterioration, especially with stepped seals. Rhode and Allen (1998) found important effects related to the tooth to groove location and that using rectangular rub grooves, as opposed to in-engine wear profiles, made no difference to their results. Chappel et al. (2001a) found interesting labyrinth teeth temperature effects during rub events, particularly when abradable honeycomb is used. Rhode and Allen (2001) found stronger performance effects relating to rub grooves than that of rounded teeth tips. Jinming et al. (2004) found performance improvements with the tooth running out of line with the groove prior to performance deterioration with the tooth located at the groove exit. As can be seen previous work is generally in agreement. However, there is yet to be a complete methodical study undertaken.

3.2.2 Geometry of Labyrinth Seal

Many different sizes and types (step-up, step-down, straight-through and inclined) of labyrinth seal have been tested in the literature. Additionally, for each seal type many different geometries have also been studied, often as large scale models: Wittig

et al. (1988), Rhode et al. (1993) for example. Wittig et al. (1983) found that scale models used for design calculations could have errors of up to 10% unless dynamic similarity is fulfilled. Therefore it was decided that for this test of a straight through labyrinth seal a generic size of approximately full scale would be used. Four teeth were chosen for the current experiment, which is reasonable when compared to other tests and engine designs. It was important for application and comparability that the seal sizes chosen for the current study fell within geometrical ratios that related to common seal sizes.

Currently, labyrinth seal teeth heights vary with the majority in the $3-12mm$ range. For most straight through labyrinth seals it is common for the aspect ratio of the cavity (tooth height to pitch ratio) to be approximately 1. As these dimensions reduce, the effects of machining limits increase, for example on tooth corner radii (Wittig et al. (1983)). Also, at smaller tooth heights smaller variations in clearance are required to keep within geometrical ratios of interest: pitch to clearance ratio for example. For these reasons a $10mm$ tooth height, and therefore pitch, was chosen for the current study.

The pitch to clearance ratio has a large range of common sizes, although the range from $5-20$ appears frequently: Stocker (1977), Wittig et al. (1987), Zimmermann et al. (1994), amongst others. Therefore with a pitch of $10mm$ the clearances of interest where $0.50mm$, $1.00mm$ and $2.00mm$. Additionally, tests using the honeycomb surface were taken at zero nominal clearance to look for effects of the groove, small clearance effects and the effect of honeycomb placement.

Other key geometric sizes could not be decided until the rub data provided was analysed.

3.2.3 Groove Shape and Size

Typical groove profiles created by labyrinth teeth in an actual engine were provided by private communication. The size and shape of these grooves were non-dimensionalised and applied to the labyrinth geometry. The groove data received was v-shaped about the groove centreline. However, it is accepted that all wear profiles could be different in shape, size, and form, and that this data relates to one seal position in one engine.

As has already been seen there are two main components of wear, axial and radial, which are very difficult to recreate dynamically in a labyrinth seal test. However, for the test to try and replicate engine conditions the geometry of the labyrinth

seal needed to be related to that of the groove. It is common knowledge that the running clearance has a dominating factor on labyrinth seal performance. For this reason the depth of the groove was related to the clearance of the seal. From the rub data provided this gave $\left(\frac{Cl}{Gd}\right)$ of 0.87 to be applied to the test. This meant that nominal groove depths for the test were $0.57mm$, $1.15mm$ and $2.30mm$ at the clearances of $0.50mm$, $1.00mm$ and $2.00mm$ respectively.

The width of the groove was related to the tooth pitch and the tooth tip dimension seen by the stationary land. From the data received $\left(\frac{Gw}{Ph}\right)$ was 0.5 with a $\left(\frac{Gw}{Tp}\right)$ of 11.70. Applying this to the current test gave a groove width of $5.00mm$ and a tooth width of $0.43mm$. However, to enable placement of instrumentation on the teeth tips and confident machining for the instrumentation the tooth width was increased to $0.50mm$. Therefore the groove width chosen was $5.85mm$.

In order to characterise the effects of the groove, readings were taken using a flat honeycomb surface. This surface was then machined in two stages, providing a partially and fully worn condition. The planned sizes for the test are given in table (3.1). The actual sizes achieved were checked with a clock gauge and are shown in brackets.

	Groove Width(mm)	Groove Depth(mm)
Test 1 (Flat HC)	-	-
Test 2 (G1)	3.00 (3.40)	0.60 (0.55 - 0.60)
Test 3 (G2)	6.00 (6.00)	1.20 (1.15 - 1.20)

Table 3.1: Planned (and Actual) Groove Sizes for Test

As the stator wall contained the abradable honeycomb land, and therefore whatever rub grooves were tested, inter-seal pressure measurements were not able to be taken using the stator wall. In order to further characterise the performance of worn abradable honeycomb labyrinth seals, effects caused by tooth to groove axial location were also measured. This was achieved by keeping the honeycomb section stationary whilst moving the labyrinth teeth. In order to fully understand the potential of these effects the performance was measured with the tooth located in an upstream and downstream position relative to the mid position. Considering the groove widths studied, the teeth were offset by $\pm 1.50mm$ and $\pm 3.00mm$. Whilst studying the $3.00mm$ groove, the tooth was located at the start and end of the groove and also fully upstream and downstream of the groove. Whilst studying the $6.00mm$ groove, the tooth was located at the start and end of the groove and at two positions located within the groove but offset from the groove centreline. This

can be seen diagrammatically in fig. (3.1) which shows the groove sizes and the respective upstream and downstream tooth locations. Further, fig. (3.1) shows the honeycomb alignment with respect to the instrumentation plane.

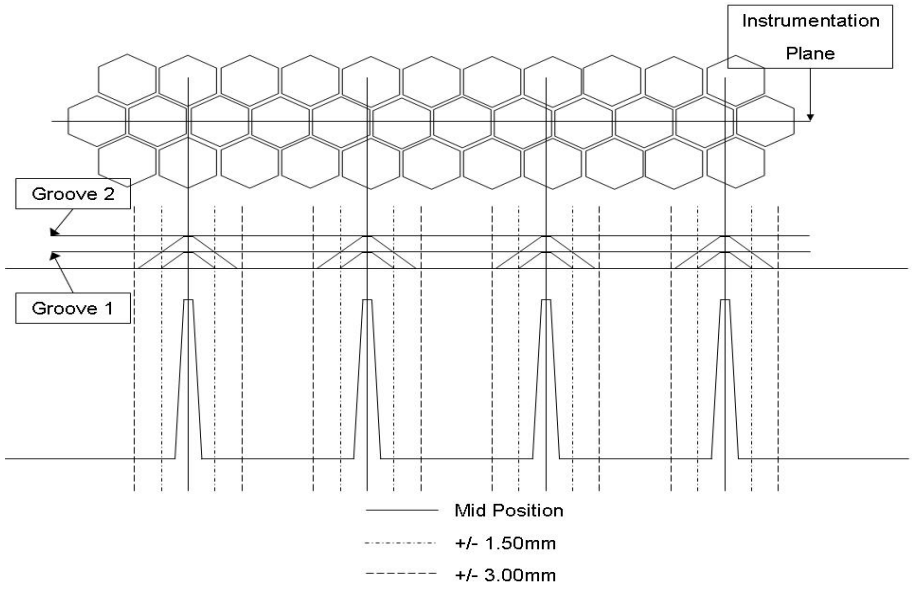

Figure 3.1: Geometrical Effect of Tooth Axial Movement in Relation to both the Groove and Honeycomb Land. Flow from left to right.

3.2.4 Honeycomb Cell Size

In engine applications three sizes of honeycomb are most common: $0.80mm$, $1.60mm$ and $3.20mm$, all given as a distance across the flats of one cell. Generally test results have shown that:

- As cell size increases the friction factor increases.
- As cell size decreases the honeycomb acts more like a flat plate.
- As cell size decreases there is less chance of registering a small clearance effect.

For this test it was decided to use the $3.20mm$ cell size. This was primarily because the rig, which is trying to replicate actual engine conditions, is a large version of common labyrinth seal sizes. Additionally, for the numerical analysis, it was viewed helpful to have used one of the previous sizes studied at Cranfield

University (Allcock (1999)) which has a wealth of friction factor data. This size also enabled the possibility of measuring a small clearance effect where flow can bypass the tooth by moving into and out of the honeycomb cells. However, the importance of correctly choosing the appropriate honeycomb cell size to match the application is noted by Stocker (1977).

3.3 Experimental Measurements

In order to characterise the performance of a labyrinth seal certain key measurements are required. Primarily these are the mass flow, from which the C_d can be calculated (Eqn. 3.1), and the pressure loss through the seal, from which COF can be calculated. The COF is a measure of pocket efficiency and can be seen as defined by Allcock (1999) in eqn. (3.2).

$$C_d = \frac{\dot{m}_{ACT}}{\dot{m}_{ID}} \tag{3.1}$$

$$COF = \frac{dynamic\,head\,at\,pocket\,exit}{dynamic\,head\,at\,pocket\,entry} \tag{3.2}$$

In order to compute these variables readings of total pressure, static pressure and total temperature are required. The mass flow measuring device, the orifice plate, relies upon measuring the ΔP_s that is created by the reduction in area. The pressure ratio across the seal, total pressure upstream of the test section to atmospheric pressure, had to be recorded in order to calculate the ideal mass flow. Pressure measurements were taken inside the seal at the teeth tips and intervening cavities thus enabling the possibility of calculating the COF directly, which, to the author's knowledge, has never been undertaken before.

3.3.1 Measurements: Pressure

In the experiment it was required to measure the static pressure at 12 locations: the orifice plate (2), labyrinth teeth tips (4), intervening cavities (3), half a pitch upstream and downstream of the first and final teeth respectively and a reference atmospheric pressure which was used to account for gauge pressure effects. The location of the 9 inter-seal static tappings can be seen in fig. (3.2). All of the inter-seal static pressure measurements were located along the centreline of the experimental test section. The total pressure was measured at one location upstream of the test section, in the delivery pipe, to verify the pressure ratio across the seal. In this

study the pressure ratio across the seal is defined as the ratio of the upstream total pressure to the atmospheric pressure.

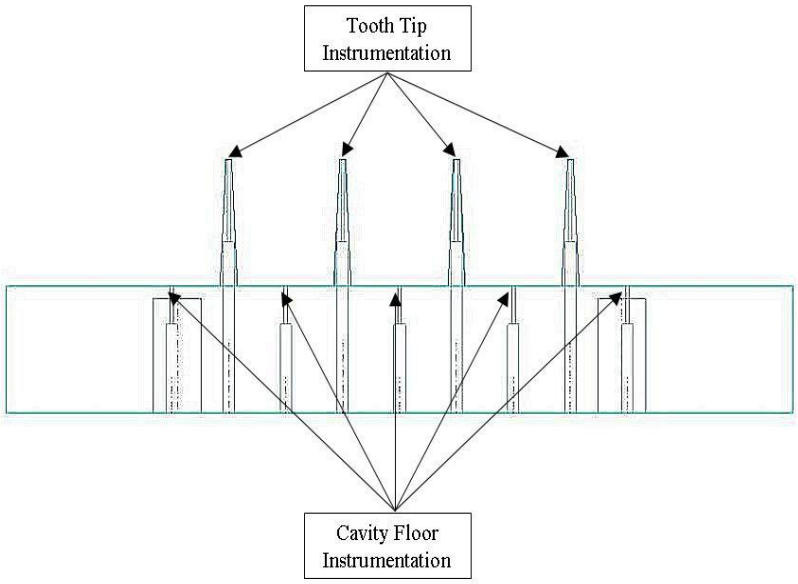

Figure 3.2: Location of the 9 Inter-Seal Static Pressure Tappings: 4 located on the teeth tips and 5 located on the cavity floor.

There are several methods that can be used to take pressure measurements, with some of the more relevant methods shown below.

- Pressure Sensitive Paint.
- Laser Beam Interferometry.
- Bragg Gratings.
- Static Tappings.

Pressure sensitive paint has not been used for internal flow situations before, having its main uses on external surfaces in wind tunnel tests for example. Laser

beam interferometry, which works on the principle that the refractive index of air changes with pressure, requires the test sections to be transparent. Bragg gratings placed inside a fibre optic cable essentially cause a polarisation effect when a shear stress (from the flow) is applied. These cables would need to be fixed to a surface prior to testing, causing potential blockages and surface imperfections. These two systems are expensive to set up and operate. Static tappings are a well known method of pressure measurement and are used with traditional metering techniques like flow through orifice plates. The static tapping, which consists of a small hole, is typically placed at right angles to the surface of measurement with the pressure reading displaced to a remote pressure measurement system by interconnecting small-bore tubes. Due to the relative simplicity of static tappings this was chosen throughout for all static pressure measurements. An equally robust solution, a pitot tube, was used upstream of the test section to measure the pressure drop across the section. However, the author notes that inside a labyrinth the flow will be much more complex than what static tappings are typically used for. This is because inside a labyrinth seal the flow will separate and recirculate, particularly over the labyrinth teeth tips. As highlighted by Arts et al. (1994) the best results when using wall static pressure measurements are obtained with small, sharp edged holes, perpendicular to a wall, that is parallel to a laminar flow. As seen in later chapters, CFD was used to compare with these measurements.

A Scanivalve capable of scanning 48 pressure channels sequentially was used to link the pressure instrumentation to the pressure transducer thus enabling a single *Druck-DPI-145* pressure indicator to be used. The setting used had capabilities of up to $20Bar$ with a reading precision of $\pm 0.025\%$. To enable accurate use of the Scanivalve one channel was connected to atmosphere and read at the start and end of each scan. The deviation from atmospheric conditions was calculated and used to adjust measurements throughout.

3.3.2 Measurements: Temperature

Temperature measurements were made using three type-k thermocouples at three locations: downstream of the orifice plate, upstream of the test section and a reference temperature in an ice cell. Thermocouples make use of the Seebeck effect where a conducting wire that spans a thermal gradient will see a voltage across its ends: ESDU (82035). In reality two different materials are used with one junction measuring the fluid temperature and the other held constant. This process of *cold junction compensation* enables the voltage across the ends of the thermocouple to be converted to a temperature accurately. Type-k thermocouples use Chromel/Alumel with nominal voltages of $4.5mV_t/^{\circ}C$.

It is impossible to measure the static temperature of a moving fluid accurately with a stationary thermocouple because in a moving fluid a temperature ratio must be present (see Eqn. 3.3). Equally Benedict (1959) found that the true total temperature cannot be measured due to impact, viscous shearing and heat conduction effects within the gas and heat transfer effects within the thermocouple. The actual temperature measured therefore is neither the true total or the true static temperature.

$$\frac{T_t}{T_s} = 1 + \left(\frac{\gamma - 1}{2}\right) Ma^2 \tag{3.3}$$

Therefore thermocouples have a recovery factor so that the actual total temperature can be deduced from the thermocouple measurements (see Eqn. 3.4): Doebelin (2004). For fully shielded probes this is often taken as 0.80 and for half shielded probes as 0.97. For this test half shielded probes were used at the orifice plate and upstream of the test section while a fully shielded probe was used in the ice cell.

$$RecoveryFactor(R) = \frac{T_{t(meas)} - T_s}{T_t - T_s} \tag{3.4}$$

As can be seen from eqn. (3.4) if $T_{t(meas)} = T_t$ then $R = 1$. Equally if $T_{t(meas)} = T_s$ then $R = 0$. By combining eqn. (3.3) and eqn. (3.4) into eqn. (3.5) it can be seen that at low Mach numbers the importance of R reduces due to the ratio of $(\frac{T_t}{T_s})$ approaching 1.

$$T_s = \frac{T_{t(meas)}}{1 + R\left(\frac{\gamma-1}{2}\right) Ma^2} \tag{3.5}$$

For the temperature measurements taken the impact of the recovery factor has been neglected. This is because in the ice cell the physics are different, whilst in the moving fluid the Mach number does not exceed 0.10 at the points of measurement. With the Mach number in the denominator of eqn. (3.5) and high recovery factors the effects on the actual static temperature can be satisfactorily neglected.

3.3.3 Measurements: Data Acquisition System

All of the data was collected using a *National Instruments* module, the *NI-SCXI-1100*, a 32-Channel analog input module. This module was controlled using a specially designed Visual Basic 5.0 programme from a computer using a Pentium Pro $200MHz$ processor with $64Mb\ RAM$. The experimental set-up can be seen in fig. (3.3).

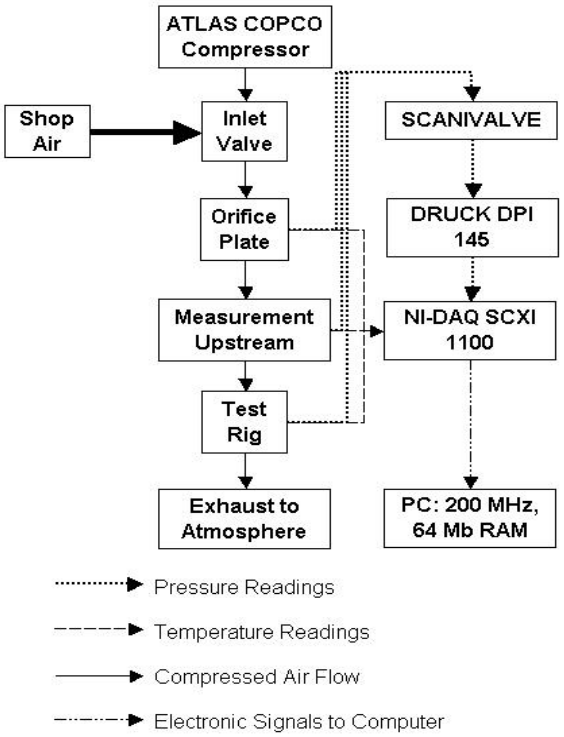

Figure 3.3: Diagrammatic Representation of Experimental Set-Up.

Pressure calibration happened on every day of testing. This was carried out using a *Druck* constant pressure source connected to the data acquisition system via the Scanivalve. Daily readings of the atmospheric pressure were entered into the data acquisition programme at the start of each day of testing. Additionally, variations in atmospheric pressure were recorded during each test. These readings ensured that gauge pressure effects were taken into account. The pressure transducer was accurate to $\pm 0.025\%$ reading. Overall the pressure reading system was calibrated to within $\pm 0.50\,\%$ across the full scale of the *Druck* constant pressure source with lower pressures having the largest absolute errors. The static pressure

tappings placed on the teeth tips will have a larger error than those placed on the cavity floor. This is because these pressure tappings are $0.30mm$ diameter on a tooth tip of $0.50mm$. Therefore the actual pressure read on each tooth was an average tooth pressure. Static pressure tappings are also usually placed at right angles to the flow but on the teeth tips a more complex flow domain will be seen.

All of the thermocouples used were calibrated at $0.00°C$ and $100°C$ using an ice bath and boiling water respectively, on a day when the atmospheric pressure was recorded. During the experiment an ice cell provided a $0°C$ reference reading with a variation of $\pm 0.50°C$. The *NI-SCXI-1100* has a built in cold junction compensation facility which was used for the thermocouple measurements. Through this calibration routine confidence can be taken that the thermocouples measured temperatures to an accuracy of $\pm 0.50°C$.

3.3.4 Measurements: Mass Flow

The mass flow was measured using an orifice plate utilising two static pressure tappings at (D) and $\left(\frac{D}{2}\right)$ positions and one temperature measurement downstream (for further information on orifice plates see Appendix (D)). For the diameter ratios used, 0.20, 0.24 and 0.30, the lowest error in mass flow that could be achieved is 1.50% (Baker (1988)). However, for the range of pressures tested the error in mass flow measurement has been calculated throughout using maximum and minimum values. From the errors in pressure and temperature above and the known error in the C_d eqn. (D.2), the errors ranged from $2 - 6\%$, with the largest errors corresponding to the lowest pressure ratios. This is because of the dependence of the mass flow on the orifice ΔP_s, which did not change as rapidly as the actual pressure readings. When discussing mass flow the actual error is based on this reasoning.

3.4 Experimental Assembly

Using an epoxy resin the honeycomb was glued into the recessed honeycomb holder prior to being screwed into the recessed section in the top plate. (See fig. (3.4)). This enabled easy machining of the honeycomb holder (including honeycomb) as a discrete component with the grooves created in the honeycomb holder wall filled in to maintain sealing effectiveness. This design also enabled the possibility of switching to other types of surface. The only other surface tested was a flat metal surface and this served as a baseline reference test.

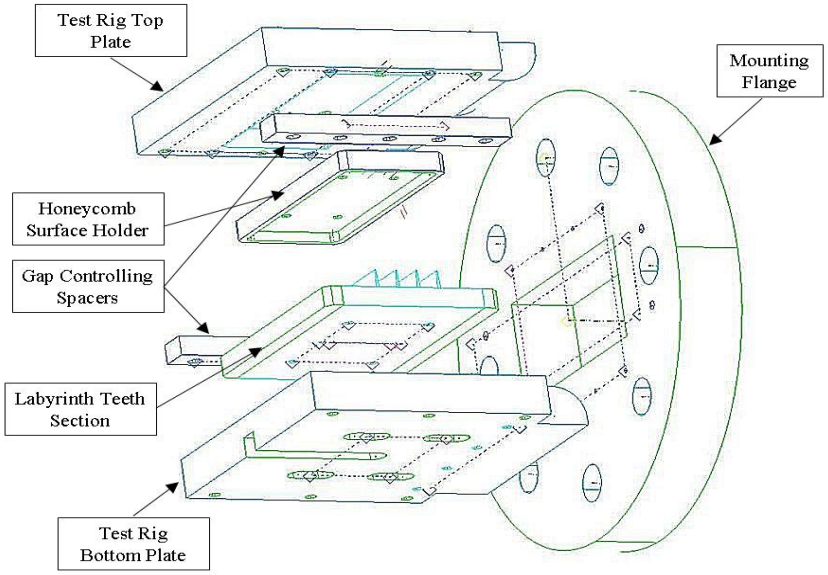

Figure 3.4: Test Section Components and Assembly.

The teeth section, with inserts that controlled tooth to groove location, were placed into a recessed section in the bottom plate as shown in fig. (3.5). Both of these recessed sections in the top and bottom plates did not extend to the full width of their respective plate thus reducing the number of components with a sealing requirement.

The top and bottom plates of the test section were aligned with dowel pins prior to final assembly. Seal clearances were maintained by specially manufactured spacers which acted to keep the top and bottom plates separated by a fixed distance. The tooth location relative to the honeycomb surface was controlled using inserts to the fore and aft of the teeth section. Sealing at the sides of the labyrinth teeth was maintained by compressing the spacers against the sides of the labyrinth teeth with a g-clamp prior to securing the top and bottom plate together using 6 cap head screws. Once assembled the test section was attached to a specially designed flange using 4 bracket sections. The top and bottom test plates protruded beyond the upstream face of the flange by $5.00mm$ to ensure no flow disturbances were introduced. The flange was then attached to the end of the $203.20mm$ diameter delivery pipe with 6 bolts. The final assembly can be seen in fig. (3.6).

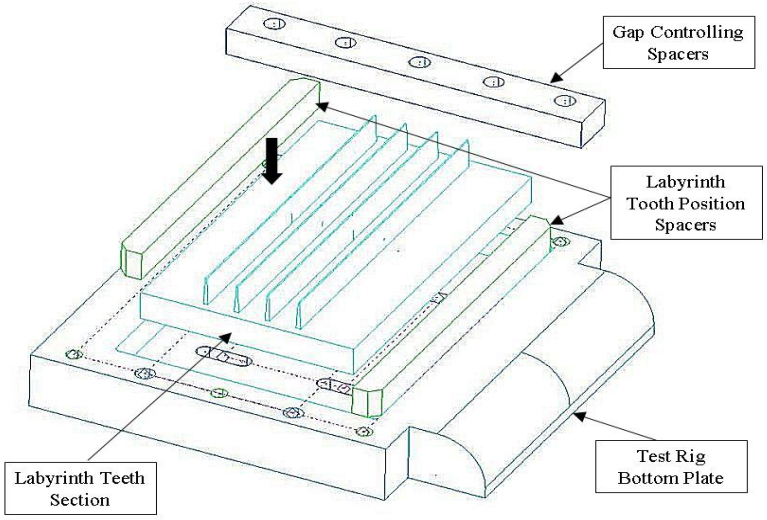

Figure 3.5: Test Section Tooth Assembly.

3.4.1 Experimental Rig: Sealing

It was important that the test facility sealed adequately in order to have confidence that the measured mass flow passed through the test section without unplanned leakage. This was particularly important due to the calculation of the C_d, where an abnormally high mass flow reading (due to leakage) would artificially increase the results. In order to reduce the chances of leakages occurring, recessed sections, both for the honeycomb and for the teeth section (see figs. (3.4) and (3.5)), were used. This meant that the sealing requirement was left to fewer components, namely the entrance flange, entrance brackets, and the spacers in conjunction with the top and bottom plates. All of the key surfaces were ground to ensure good sealing between components. During the experiment leaks were checked for by hand and by using an oil film.

3.4.2 Flow Entry into Section

To guarantee fully developed turbulent flow in a pipe a length of 60 diameters of pipe is required: Douglas et al. (1995). Due to cost and space requirements this was unfeasible. Therefore, to have confidence in the uniformity and development of the flow into the test section a CFD analysis of the entrance and test section was carried out. The models used were 2-D and assumed an unworn flat wall boundary con-

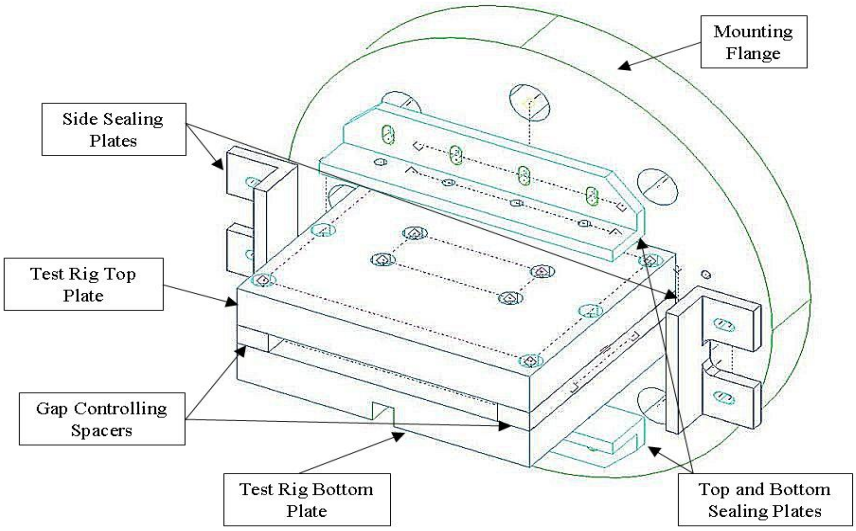

Figure 3.6: Test Section Final Assembly.

dition instead of modelling the honeycomb surface. Cases at $0.50mm$ and $2.00mm$ clearance, the maximum and minimum clearances for the test, were computed with pressure ratios ranging from 1.20 to 3.00. A traverse of flow angle relative to the top and bottom plate is presented in figs. (C.1) and (C.2). These flow angles are taken along a line $37.50mm$ upstream from the first tooth which represents the start of the 2-D test section. These graphs show that the flow can be taken to be uniform at the entrance to the test section with the small flow angles seen ($< \pm 0.5\,^{\circ}$) being unable to be measured with any reliability. The highest x-velocity seen in the entrance is almost $25\left(\frac{m}{sec}\right)$, arising at a pressure ratio of 3.00 with $2.00mm$ nominal clearance. This gives y-velocities for the same case and position as $0.05\left(\frac{m}{sec}\right)$ approximately. Therefore no account of inlet flow skewness needed to be applied.

3.5 Experimental Facility

The experimental facility used for this study is very similar to that used by Allcock (1999). The compressed air was delivered from the Atlas Copco compressor into the test section via an orifice plate. The Atlas Copco compressor used was capable of delivering $1.40\left(\frac{kg}{sec}\right)$ at $3.00Bar$ gauge pressure. The orifice plate is located in a pipe of $80.85mm$ internal diameter. Three diameter ratios of orifice plate were used in the study: 0.20, 0.24 and 0.30. The orifice plates were used and operated

within the guidelines stated in BS (1042.1) where possible. However, for some of the tests with a small mass flow the limit on Reynolds number could not be maintained above the minimum required by BS (1042.1) so these results have been excluded. (Further information on orifice plates can be found in Appendix (D)). Final delivery into the test section was via a pipe of $203.20mm$ internal diameter where a bolted flange connected the test section securely to the end of this pipe. The test section exhausted to atmosphere. A flow diagram of the experimental set-up can be seen in fig. (3.3).

A total pressure probe placed upstream of the test section recorded the pressure drop across the section. Once the appropriate pressure ratio was reached the data acquisition routine began. All channels were read eight times per scan and averaged. To change the geometrical form of the test the process described in section (3.4) was followed. A summarised form of the experimental runs undertaken can be seen in chronological order in table (A.1).

3.6 Experimental Results

3.6.1 Experimental Repeatability

To be sure of repeatable tests over the time of the experimental programme a baseline test was conceived. This involved placing a flat metal insert into the recessed section of the top plate. At the start of the experimental programme baseline results were taken at all clearances. Immediately prior to the three stages of honeycomb testing the baseline test was repeated to check repeatability. The overall mass flow parameter $\left(\frac{\dot{m}\sqrt{T_{t(0)}}}{P_{t(0)}}\right)$ for the $0.50mm$ clearance can be seen in fig. (3.7). Figures for $1.00mm$ and $2.00mm$ clearance can be seen in figs. (C.3) and (C.4) respectively.

Each figure shows results taken prior to the three stages of honeycomb testing: Flat HC, G1 and G2, as described in table (3.1). For the Flat HC condition at least two sets of data were taken and averaged (AVG) with this data plotted on the graphs. Included in these figures are the errors based maximum and minimum results (see section (3.3.3) for further details). As can be seen the tests record the same trends. Further, results (including error bands) from one test, lie within the limits of uncertainty of the other tests and therefore confidence can be taken that the test is repeatable. The errors do increase at lower pressure ratios due to the ΔP_s effect discussed in section (3.3.3). This effect is most apparent in fig. (C.3) because the orifice plates used were of two different diameter ratios: 0.20 for both the Flat HC and the G1 condition and 0.30 for the G2 condition. Using the larger size greatly reduced the pressure drop and therefore disproportionately increased

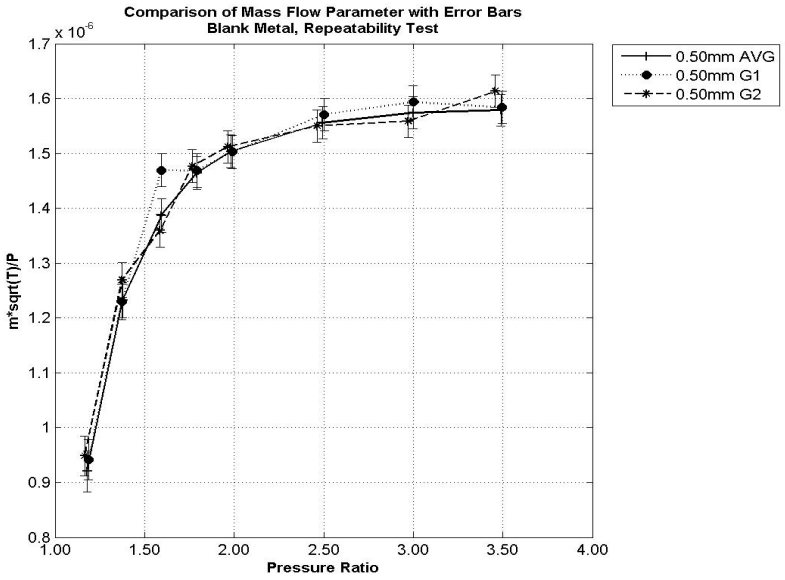

Figure 3.7: $\left(\frac{\dot{m}\sqrt{T_{t(0)}}}{P_{t(0)}}\right)$ for Repeatable Tests at Gap = $0.50mm$

the size of the error band due to the ΔP_s effect. However, even taking this into account it is pleasing to note the similarity with the other tests. Graphs showing the comparison across the gaps are presented in fig. (C.5). Again it is pleasing to note the similarity of form across the tests and the approximate doubling of mass flow as the gap doubles.

The static pressure variations recorded through the seal can be seen in fig. (3.8) for the $0.50mm$, $1.00mm$ and $2.00mm$ clearances respectively. As can be seen for all cases the static pressure losses are disproportionately loaded towards the first and final teeth with the intervening teeth displaying clearance dependent effects. At $0.50mm$ clearance marginal pressure drops are recorded over these intervening teeth. At $1.00mm$ clearance almost no pressure drops are recorded over these teeth. For the $2.00mm$ clearance a pressure rise was recorded over the second tooth across the range of pressure ratios investigated. This effect due to clearance was unexpected and requires further investigation.

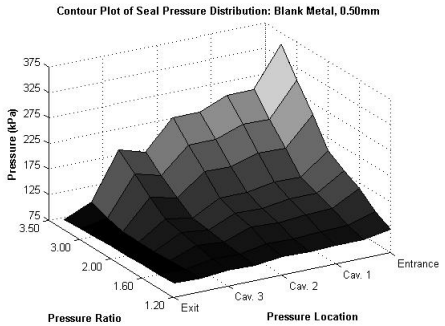

(a) 0.50mm Running Clearance

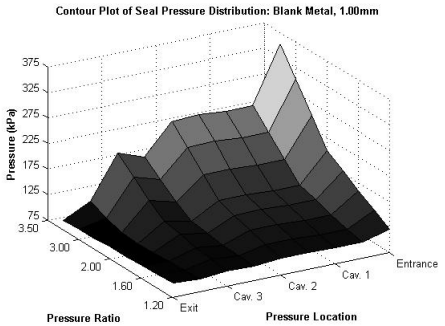

(b) 1.00mm Running Clearance

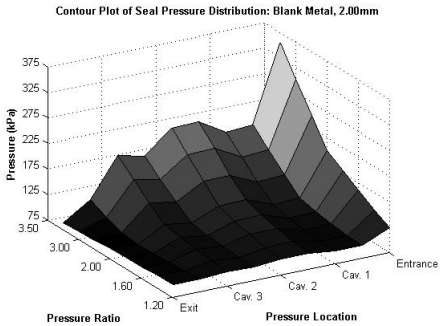

(c) 2.00mm Running Clearance

Figure 3.8: Seal Static Pressure Distribution: Blank Metal, All Gaps.
X-Axis: Pressure Location. Y-Axis: Pressure Z-Axis: Pressure Ratio.

3.6.2 Experimental Results: Flat Honeycomb

To verify the effect of honeycomb placement on the instrumentation several results were taken moving the teeth relative to the honeycomb surface ($1.50mm$ upstream, approximately $\left(\frac{1}{2}\right)$ a honeycomb cell) prior to any wear profiles being created. No overall effect on $\left(\frac{\dot{m}\sqrt{T_{t(0)}}}{P_{t(0)}}\right)$ was recorded for three different clearances. This is to be expected because all teeth move by approximately half a cell size and therefore any overall effect would be averaged out. No results for the $0.00mm$ clearance at the lowest pressure ratio of 1.20 were recorded. This is due to the orifice plate operating outside of the limits stated in BS (1042.1) due to a low mass flow and an example of the filtering process described in section (3.5). The results comparing the inter-seal pressure measurements for the $0.00mm$, $0.50mm$ and $1.00mm$ clearances can be viewed in fig. (3.9). The figure highlights two positions for the three clearances: the central-position and a relative position compared to the central-position of the test.

As can be seen at clearances of $0.50mm$ and $1.00mm$ there is very little variation between the two geometrical situations. Only at $0.00mm$ clearance has a variation between the two cases been recorded, most noticeably for measurements taken on the teeth tips. At $0.00mm$ it can be seen that running in an upstream position recorded tooth pressure measurements that are lower. Further, from fig. (3.1) it can be seen that in the central position the labyrinth teeth are aligned close to honeycomb cell walls at the plane of measurement. Therefore by moving the labyrinth teeth $1.50mm$ upstream the labyrinth teeth align with honeycomb cell pockets. In this position flow can bypass the teeth through the small clearance effect. The dynamic head maintained during this bypass process explains these reduced measurements of static pressure. However, with a labyrinth tooth aligning to a honeycomb cell wall, the flow will experience complex changes in dynamic head. These complex changes come from a large localised acceleration upstream due to the mass flow passing through a small clearance and a further reduced effective area. However, the exact locations of these accelerating and decelerating fluid domains are unknown. Therefore whilst there is no overall effect, there is a localised effect related to instrumentation and honeycomb location which is small and only appears at very small clearances. Essentially, whilst the flow over the honeycomb surface is uneven, this unevenness is not strong enough to get projected through the jet and tooth boundary layer created by the flow, to the instrumentation locations unless the size of the jet is very small.

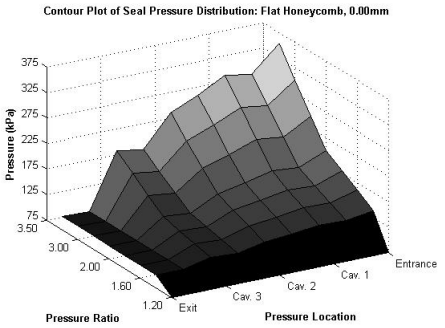

(a) 0.00mm: Cental Position

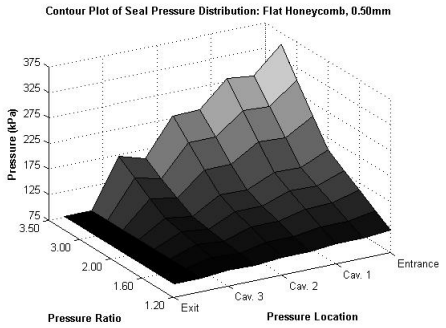

(b) 0.50mm: Central Position

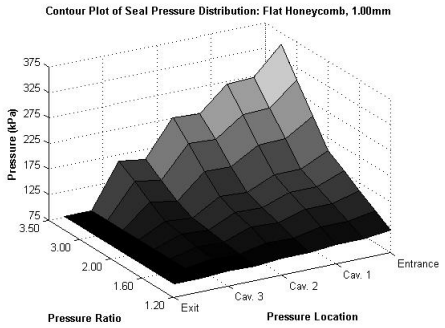

(c) 1.00mm: Central Position

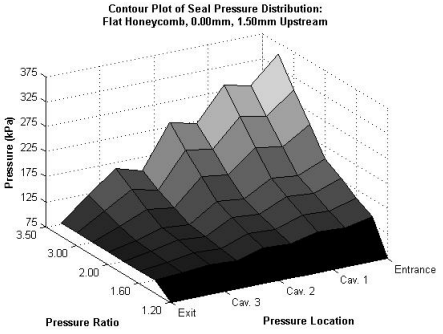

(d) 0.00mm: 1.50mm Upstream

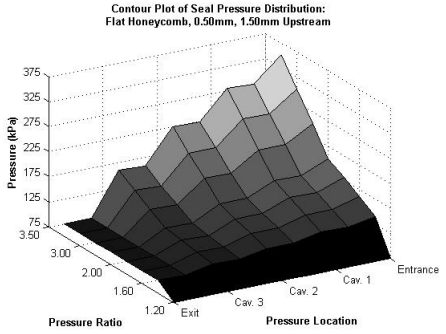

(e) 0.50mm: 1.50mm Upstream

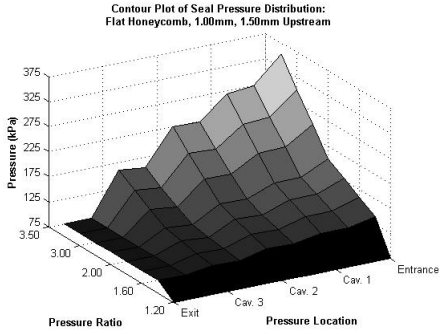

(f) 1.00mm: 1.50mm Upstream

Figure 3.9: Static Pressure Variations for Flat Honeycomb between Central Position and 1.50mm Upstream Position X-Axis: Pressure Location. Y-Axis: Pressure Z-Axis: Pressure Ratio.

The overall results of $\left(\frac{\dot{m}\sqrt{T_{t(0)}}}{P_{t(0)}}\right)$ were also recorded and can be seen in fig. (3.11). These results show a similar form to that of the blank metal tests (fig. (C.5)). Generally when using honeycomb choking is seen to occur at higher pressure ratios. Also there is a more gradual increase of $\left(\frac{\dot{m}\sqrt{T_{t(0)}}}{P_{t(0)}}\right)$ at lower pressure ratios. Further, at $0.50mm$, when using a honeycomb stator there is an increase in $\left(\frac{\dot{m}\sqrt{T_{t(0)}}}{P_{t(0)}}\right)$ when compared to the blank metal test. This effect is reversed at clearances of $1.00mm$ and $2.00mm$ when the effect due to the honeycomb surface reduces $\left(\frac{\dot{m}\sqrt{T_{t(0)}}}{P_{t(0)}}\right)$ relative to the flat metal test. This is the basis of the small clearance effect when flow can bypass the labyrinth tooth by passing into and out of the honeycomb cells. The small clearance effect registered at $0.50mm$ clearance accounts for increases in $\left(\frac{\dot{m}\sqrt{T_{t(0)}}}{P_{t(0)}}\right)$ of up to 10% dependent upon pressure ratio. To further investigate the small clearance effect measurements were taken whilst using the flat HC stator at $0.00mm$ clearance. These measurements of $\left(\frac{\dot{m}\sqrt{T_{t(0)}}}{P_{t(0)}}\right)$ were approximately 60% of those values calculated at $0.50mm$ clearance. This shows that the small clearance effect is significant. As already highlighted with the increased gap size the deviation between the flat metal and honeycomb stator also increases. This implies that at larger gaps there is more space for the turbulence developed by the honeycomb surface to affect the flow thereby reducing any small clearance effects.

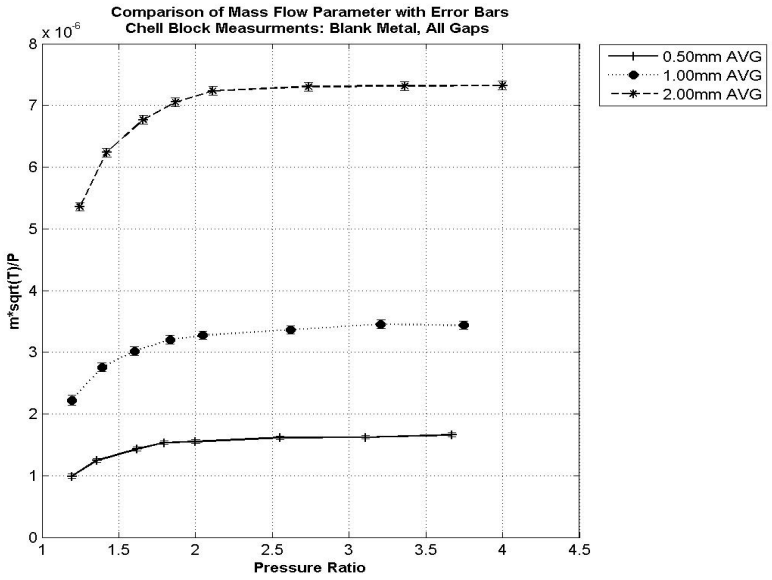

Figure 3.10: $\left(\frac{\dot{m}\sqrt{T_{t(0)}}}{P_{t(0)}}\right)$ When Using Chell Blocks: All Gaps

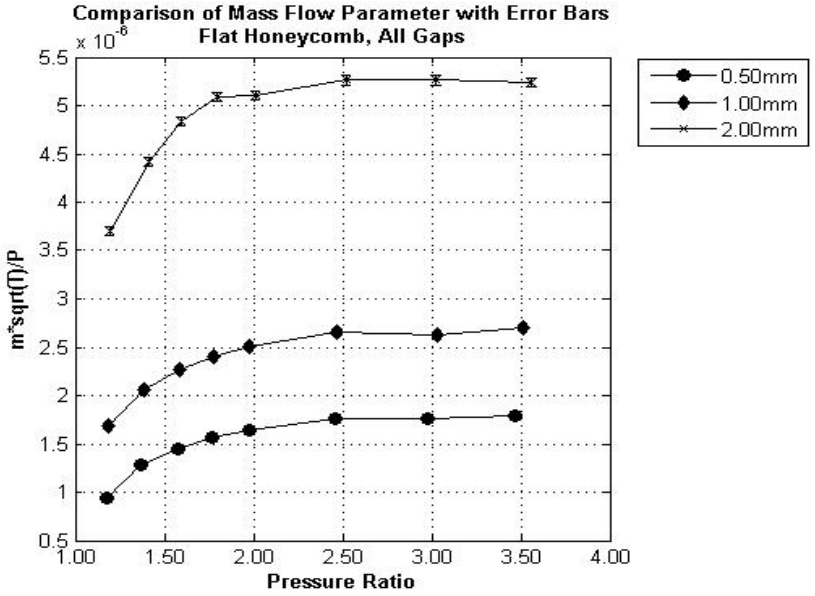

Figure 3.11: $\left(\frac{\dot{m}\sqrt{T_{t(0)}}}{P_{t(0)}}\right)$ for Flat Honeycomb. All Gaps

Further insight into the unworn honeycomb surface will be provided whilst analysing the worn honeycomb conditions.

3.6.3 Experimental Results: Worn Conditions

The results recorded after the first and second stage of groove creation (G1 and G2) can be viewed in fig. (3.12) and (3.13) for the $0.50mm$ clearance. Further worn honeycomb results for different clearances are available in figs. (C.6) through (C.11). These figures show $\left(\frac{\dot{m}\sqrt{T_{t(0)}}}{P_{t(0)}}\right)$ for each gap size and tooth position. The original flat honeycomb results have been included throughout to aid understanding.

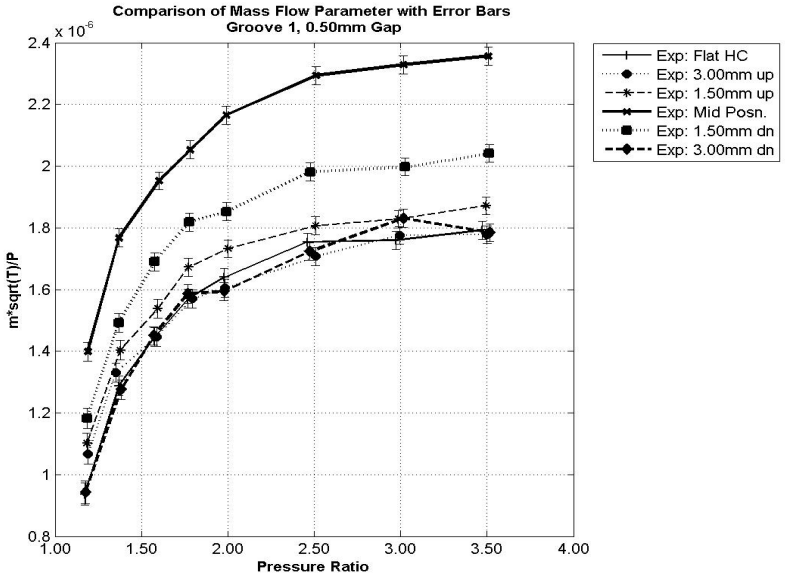

Figure 3.12: $\left(\frac{\dot{m}\sqrt{T_{t(0)}}}{P_{t(0)}}\right)$ with Groove 1: Gap = $0.50mm$

It is clear from this collection of figures that the seal configuration with the highest mass flow is when the tooth is centrally located in the groove. In the same figures the seal with the lowest mass flow is often the flat honeycomb test, or when the tooth runs outside of the groove as one would expect. At $0.00mm$ running gap (figs. (C.6) and (C.9) for G1 and G2 respectively) the variations between the flat honeycomb and locating the tooth upstream or downstream can easily be identified. For the G1 condition (fig. (C.6)) all of the teeth offset positions are effectively out of line with the groove and achieve similar results. For the G2 condition (fig. (C.9))

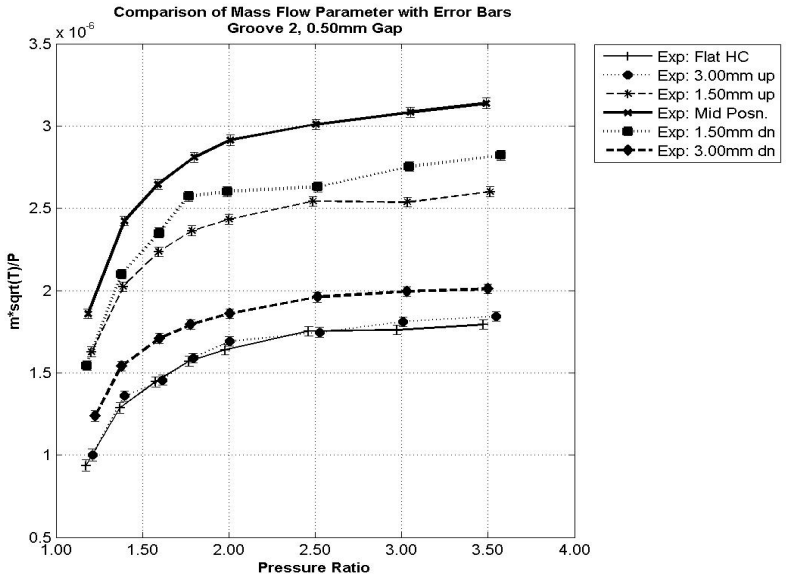

Figure 3.13: $\left(\frac{\dot{m}\sqrt{T_{t(0)}}}{P_{t(0)}}\right)$ with Groove 2: Gap = $0.50mm$

this is only achieved for the $\pm 3.00mm$ positions which is the equivalent out of line condition. Effectively these out of line experiments are registering a small clearance effect, the impact of which has diminished when the tooth is located centrally in the groove due to the effective area available for the flow. At a running clearance of $0.50mm$, fig. (3.12) and (3.13) for the G1 and G2 conditions respectively, the centrally aligned case again passes the highest mass flow with the $1.50mm$ downstream position recording the next highest mass flow. All other positions after the first stage of groove creation perform similarly to the flat honeycomb condition. After the second stage of groove creation only the $3.00mm$ upstream case performs similarly to the flat honeycomb condition, with an advantage of running in an upstream position becoming clear. At $1.00mm$ (figs. (C.7) and (C.10)) and $2.00mm$ (figs. (C.8) and (C.11)) this general trend of better performance whilst running in an upstream position continues with fewer positions that are able to match the performance of the flat honeycomb test. However, some of these results also show uncertainties arising from the experimental programme. This is particularly noticeable in fig. (C.8) where $\left(\frac{\dot{m}\sqrt{T_{t(0)}}}{P_{t(0)}}\right)$ is seen to follow an unexpected form. (This effect can also be seen at $0.00mm$ in fig. (C.6). However, at $0.00mm$ effects dependent upon geometry (i.e. instrumentation to honeycomb location) could be recorded as highlighted in section (3.6.2).) Normally $\left(\frac{\dot{m}\sqrt{T_{t(0)}}}{P_{t(0)}}\right)$ would be expected to rise with pressure ratio until

choking occurs and then return a constant value irrespective of further increases in pressure ratio (e.g. see fig. (3.11)). Therefore further experimental investigations were undertaken to aid understanding.

3.6.4 Experimental Results: Chell Blocks

It was found during the data processing phase that the original experimental set-up provided results that at times were unexpected. It was deemed that the period of time that the scanivalve took for a full scan could allow for the possibility of pressure fluctuations within the measurement section to be recorded. This was because a butterfly valve upstream of the test section was used to control the pressure drop. Initially the balancing pressure on the butterfly valve was provided by a reciprocating air compressor that operated at a nominal pressure of $5.1Bar$. However, this pressure varied between limits and therefore the system pressurised and depressurised dependent upon these limits in a manner that was uncontrolled with regard to experimental data acquisition routines. Therefore to check for the possibility of pressure fluctuations during the data acquisition routines a different pressure measurement set-up was used for verification. The shop air supply was changed from the reciprocating compressor to an axial compressor that was capable of achieving a constant pressure output. The pressure measurement system was changed from the Scanivalve to Chell blocks (the original experimental flow diagram can be seen in fig. (3.3)). The Chell blocks used were capable of measuring 16 pressures simultaneously, as opposed to the Scanivalve routine that took time for each channel to be read. Therefore the scan routine changed from a time averaged scan to an instantaneous scan. While using the Chell blocks 8 scans were still taken and averaged to provide the pressure readings. As the groove creation process was a lost material process it was impossible to re-test the flat honeycomb and intermediate groove (G1) results. However, results were taken against the baseline and fully worn (G2) test cases. Initially the Chell Blocks were used to test the flat metal stator and provide comparisons to the original experimental set-up. The results of this process can be seen in figs. (3.14) for the $0.50mm$ clearance and (C.12) and (C.13) for the $1.00mm$ and $2.00mm$ clearance respectively. Each set of results was taken twice ($v1$ and $v2$) and compared to the average result of the original experimental set-up. Both sets of Chell block data were found to lie within each others uncertainty limits. Additionally, good agreement with the previous test set-up was found. Generally the new test set-up predicted higher levels of mass flow particularly at higher pressure ratios.

Performance for various running clearances can be seen in fig. (3.10) which again shows the approximate doubling of the mass flow as the gap doubles. Further, very similar forms and magnitudes between the current and previous experimen-

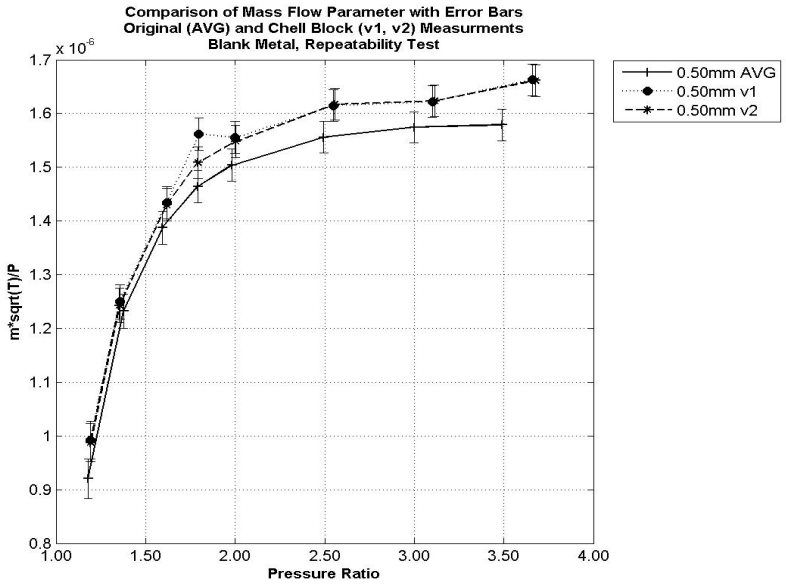

Figure 3.14: $\left(\frac{\dot{m}\sqrt{T_{t(0)}}}{P_{t(0)}}\right)$ for Repeatable Tests When Using Chell Blocks (v1, v2) Compared Against Original (AVG): Gap = $0.50mm$

tal set-up are found (compare fig. (3.10) with (C.5)). The worn test results for the $0.50mm$ clearance can be viewed in fig. (3.15) with results for clearances of $0.00mm$, $1.00mm$ and $2.00mm$ available in figs. (C.14) through (C.16).

Throughout, as done previously, the baseline flat honeycomb has been shown for comparison. However, the flat honeycomb data was taken using the original test set-up as there was no opportunity for re-testing. Comparing the current results to the initial results reveals that trends characterised by the rising and falling of $\left(\frac{\dot{m}\sqrt{T_{t(0)}}}{P_{t(0)}}\right)$, as experienced previously, were not repeated. At higher pressures the more typical choking condition of constant $\left(\frac{\dot{m}\sqrt{T_{t(0)}}}{P_{t(0)}}\right)$ has been achieved. Further, whilst the magnitude of some of the results has changed the general form of the results for both experimental set-ups have been repeated. This adds confidence to the work undertaken. Further comparisons of the worn honeycomb inter-seal static pressure measurements can be found in figs. (3.16) and (3.17) for the $0.50mm$ clearance and figs. (C.17) through (C.22) for other clearances. The tooth to groove and tooth to honeycomb location in the offset positions can be found by referring to fig. (3.1). At the smallest clearance (figs. (C.17) and (C.18)) the position of the tooth with respect to the honeycomb groove appears to have an effect on inter-seal pres-

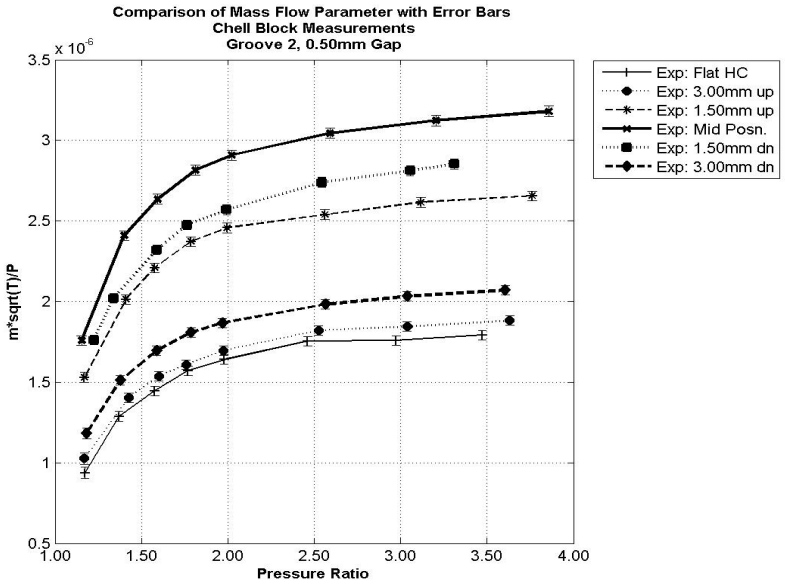

Figure 3.15: $\left(\frac{\dot{m}\sqrt{T_{t(0)}}}{P_{t(0)}}\right)$ with Groove 2 Using Chell Blocks: Gap = $0.50mm$

sure measurements. Whilst running in a downstream position, the largest pressure losses appear towards the exit of the seal. When running in an upstream position the pressure losses through the seal are more evenly distributed. This effect was less marked at $0.50mm$ (figs. (3.16) and (3.17)). At the larger $1.00mm$ and $2.00mm$ clearance (figs. (C.19) through (C.22)) this effect had virtually disappeared with respective upstream and downstream tooth positions recording very similar pressure distributions.

3.7 Conclusions

It is clear from the experimental work undertaken that the results are repeatable. This has been proven over time by using the baseline test and by using two data acquisition routines. Comparisons of the flat honeycomb test with the flat metal baseline test revealed a small clearance effect. At $0.50mm$ measurements of $\left(\frac{\dot{m}\sqrt{T_{t(0)}}}{P_{t(0)}}\right)$ are 2-10% higher than equivalent flat metal measurements. Further, measurements recorded using flat honeycomb at $0.00mm$ record values of $\left(\frac{\dot{m}\sqrt{T_{t(0)}}}{P_{t(0)}}\right)$ that are $\approx 60\%$ of that recorded at $0.50mm$. At the larger clearances the turbulence generated by the honeycomb surface acted to reduce the seal mass flow compared to

the flat metal performance. This was also found by Zimmermann et al. (1994) who recorded an effect, similar to a reduction in effective area, under turbulent conditions.

The effect of tooth location to honeycomb surface was investigated prior to wear profiles being created in the honeycomb. No overall effect on seal performance was found. However, at small clearances localised pressure distribution effects on the labyrinth teeth tips were found. This was explained by highlighting the position of the honeycomb cell walls relative to the labyrinth teeth tips and by highlighting the recorded cavity floor measurements which were similar. Essentially whilst the pressure varied locally these variations were not strong enough to be projected through the jet created by the labyrinth to the tooth tip pressure measurement locations unless the running clearance, and therefore jet, is very small.

When testing worn honeycomb surfaces, performance benefits were found when running out of line with the groove and when running in an upstream position with respect to the groove. Benefits when running with the teeth out of line with the groove have been recorded previously by Rhode and Allen (1998) and by Jinming et al. (2004), who recorded benefits until the tooth is located at the groove exit. Further, Rhode and Allen (1998) and Rhode and Adams (2004a) both found beneficial effects by reducing the groove width, as was recorded experimentally. The detrimental performance when the labyrinth tooth is located in a downstream position can be explained through the geometry created by the groove analysed which is v-shaped. In a downstream position this therefore creates a funneling effect for the flow, changing the fundamental labyrinth flow regime from that akin to an orifice plate to that akin to a venturi meter. Therefore, if knowledge of the groove shape is easy to obtain this opens the possibility of active or passive control of labyrinth seal teeth location. Obviously a cost benefit approach would highlight seal locations where this level of control may prove beneficial. The presence of groove profiles was only found to affect pressure distribution at $0.00mm$ clearance. This highlighted that when running out of line with the groove sharper changes in pressure distribution were recorded. This change in pressure distribution is what would be expected due to the increasing and decreasing area available for the flow, with a smaller area corresponding to a larger pressure loss and therefore the performance benefits found. However, the benefit of running in an upstream position requires further investigation. This is especially true because whilst the flow conditions for each tooth varied, as recorded by Zimmermann and Wolff (1987), Mach number and pressure drop were not found to increase through the seal, thus contradicting Rhode and Hibbs (1992). Further, as upstream and downstream positions are equal and opposite the position of the tooth to honeycomb surface will vary. However, these variations will, on average, be small due to the annular nature of the seal. Therefore the benefit of locating the tooth upstream relative to the groove is due to the flow physics created

by the groove. This effect requires further investigation.

To undertake further analysis at this point requires the use of other engineering tools. Therefore these conclusions shall be developed and expanded upon in later chapters.

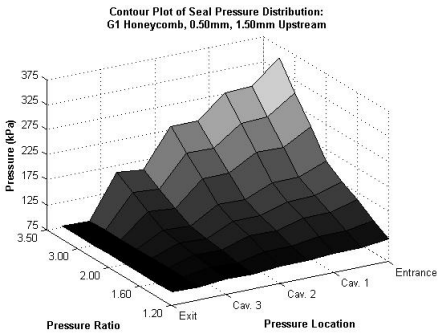

(a) 1.50mm Upstream

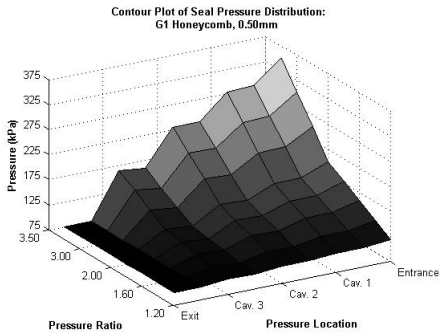

(b) Cental Position

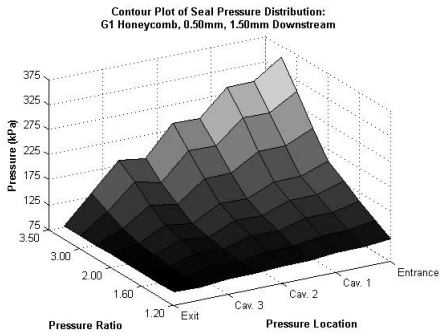

(c) 1.50mm Downstream

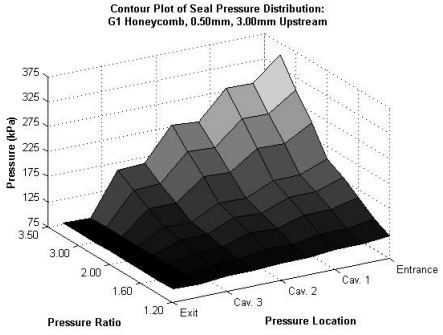

(d) 3.00mm Upstream

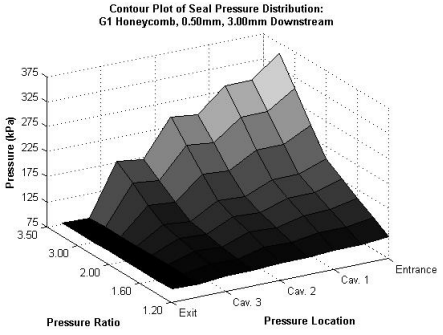

(e) 3.00mm Downstream

Figure 3.16: Static Pressure Variations for G1 Honeycomb: 0.50mm Gap, All Positions
X-Axis: Pressure Location. Y-Axis: Pressure Z-Axis: Pressure Ratio.

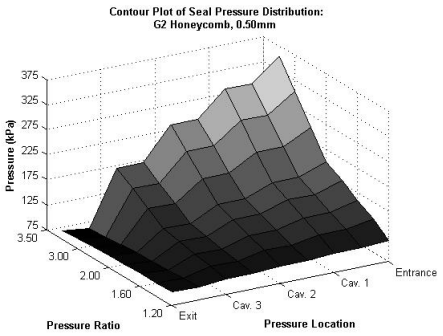

(a) Cental Position

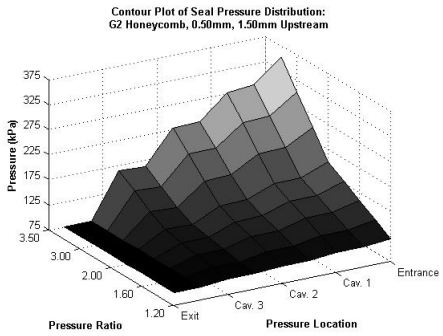

(b) 1.50mm Upstream

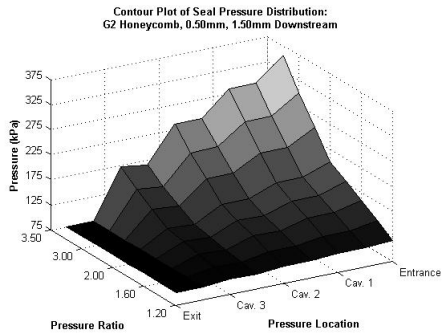

(c) 1.50mm Downstream

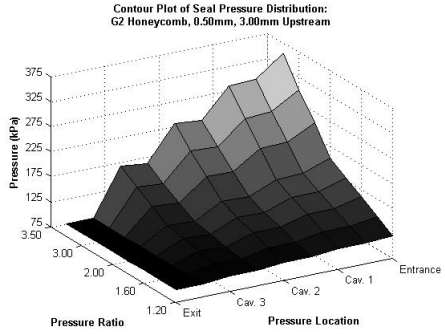

(d) 3.00mm Upstream

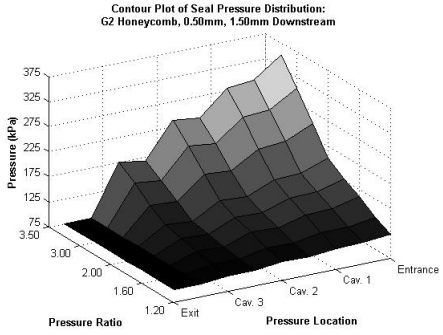

(e) 3.00mm Downstream

Figure 3.17: Static Pressure Variations for G2 Honeycomb: 0.50mm Gap, All Positions
X-Axis: Pressure Location. Y-Axis: Pressure Z-Axis: Pressure Ratio.

Chapter 4

Numerical Theory and Development

4.1 Introduction

Computational fluid dynamics, or CFD, is a numerical technique that solves the governing fluid flow equations of continuity, momentum (the *Navier Stokes* equations) and energy using a computer. This complete set of equations is often referred to as the complete *Navier Stokes* equations. CFD offers the ability to gain an insight into flow field characteristics without the need for laboratory tests. Numerical solutions like these are thought to cost approximately 10% of the cost of laboratory tests and therefore in engineering much development is undertaken using CFD. This project used CFD in this manner thus limiting the volume (and therefore cost) of the experimental work. The numerical theory of CFD, verification of FLUENT (commercially available CFD software) as a suitable investigative tool and development of a simplification technique used to model abradable honeycomb labyrinth seals are discussed in this chapter. The simplification technique developed used a constant seal geometry throughout that included a tooth width of $1.00mm$. The dimensions for the simplification study were chosen prior to finalising the experimental design. FLUENT, the CFD package used throughout, is a generic code capable of solving a wide range of flows. However, it is noted by Herring (2006) that in recent years the progress of numerical investigation has far exceeded that of experimental investigation. Therefore experimental investigation has primarily become a method used to verify numerical approaches.

FLUENT, a finite volume conservative code, and GAMBIT, the associated grid generation package, have been used throughout. This software has been used by several authors to predict labyrinth seal flow fields: Prasad et al. (1997), Allcock (1999), Wang et al. (2004), Vakili et al. (2005) and Paolillo et al. (2006). Generally

it has proved capable of predicting the complex flow within a labyrinth seal. The complete set of the governing equations relating to the integral and conservative form used by FLUENT can be seen in equations (4.1) through (4.3). FLUENT only solves the energy equation (4.3) when effects due to compressibility or heat transfer are being modelled.

4.2 CFD: Numerical Theory

As already mentioned CFD solves the governing fluid flow equations of continuity, momentum and energy using a computer. At their most general these equations can be expressed in either an integral or differential form, dependent upon how the model is defined. Two primary methods to compute the flow field exist: finite volume and infinitesimal fluid element which lead to the integral or differential forms of the governing equations respectively. Of these two forms the integral form of the governing equations is considered more fundamental. This is because the integral form allows the formation of discontinuities in the flow, such as shocks. Further, both of these methods can be defined by constant volumes that are fixed in space or as volumes of fixed mass that move with the flow, leading to the conservative or non-conservative forms of the governing equations respectively. All of these 4 forms (which can be related to each other: Anderson (1995)) reveal a highly coupled set of 5 non-linear partial differential equations that currently do not have a closed form. These 5 governing equations also contain 7 unknowns: density (ρ), pressure (P_s), 3 velocity components (u, v, w), temperature (T) and internal energy (e). However, the equations can be closed if certain assumptions or simplifications are made. In many circumstances a 2-D model will adequately represent the 3-D flow situation. Equally, in many situations modelling the gas as a perfect gas is a reasonable assumption enabling the ideal gas equation to be used in addition to those above. FLUENT uses the finite volume approach and conservative form of the governing equations. These governing equations are continuous throughout the flow field domain and can be seen in their differential form in eqns. (4.1) through (4.3), representing the equations of conservation of mass (continuity), conservation of momentum and conservation of energy respectively.

Continuity

$$\frac{\partial \rho}{\partial t} + \nabla \cdot (\rho \mathbf{V}) = 0 \tag{4.1}$$

Momentum

X-Component

$$\frac{\partial(\rho u)}{\partial t} + \nabla \cdot (\rho u \mathbf{V}) = -\frac{\partial P_s}{\partial x} + \frac{\partial \tau_{xx}}{\partial x} + \frac{\partial \tau_{yx}}{\partial y} + \frac{\partial \tau_{zx}}{\partial z} + \rho f_x$$

Y-Component

$$\frac{\partial(\rho v)}{\partial t} + \nabla \cdot (\rho v \mathbf{V}) = -\frac{\partial P_s}{\partial y} + \frac{\partial \tau_{xy}}{\partial x} + \frac{\partial \tau_{yy}}{\partial y} + \frac{\partial \tau_{zy}}{\partial z} + \rho f_y$$

Z-Component

$$\frac{\partial(\rho w)}{\partial t} + \nabla \cdot (\rho w \mathbf{V}) = -\frac{\partial P_s}{\partial z} + \frac{\partial \tau_{xz}}{\partial x} + \frac{\partial \tau_{yz}}{\partial y} + \frac{\partial \tau_{zz}}{\partial z} + \rho f_z \tag{4.2}$$

Energy

$$\begin{aligned}
&\frac{\partial}{\partial t}\left[\rho\left(e + \frac{V^2}{2}\right)\right] + \nabla\left[\rho\left(e + \frac{V^2}{2}\right)\mathbf{V}\right] = \rho\dot{q} \\
&+\frac{\partial}{\partial x}\left(K\frac{\partial T_s}{\partial x}\right) + \frac{\partial}{\partial y}\left(K\frac{\partial T_s}{\partial y}\right) + \frac{\partial}{\partial z}\left(K\frac{\partial T_s}{\partial z}\right) - \frac{\partial(uP_s)}{\partial x} + \frac{\partial(vP_s)}{\partial y} + \frac{\partial(wP_s)}{\partial z} \\
&+\frac{\partial(u\tau_{xx})}{\partial x} + \frac{\partial(u\tau_{yx})}{\partial y} + \frac{\partial(u\tau_{zx})}{\partial z} + \frac{\partial(v\tau_{xy})}{\partial x} + \frac{\partial(v\tau_{yy})}{\partial y} + \frac{\partial(v\tau_{zy})}{\partial z} \\
&+\frac{\partial(w\tau_{xz})}{\partial x} + \frac{\partial(w\tau_{yz})}{\partial y} + \frac{\partial(w\tau_{zz})}{\partial z} + \rho \mathrm{f}\mathbf{V}
\end{aligned} \tag{4.3}$$

Definitions for $\mathbf{V}$ and ∇ are shown in eqns. (4.4) and (4.5) respectively.

$$\mathbf{V} = (ui, vj, wk) \tag{4.4}$$

$$\nabla = i\frac{\partial}{\partial x} + j\frac{\partial}{\partial y} + k\frac{\partial}{\partial z} \tag{4.5}$$

The dot product of eqns. (4.4) and (4.5), $(\mathbf{V} \cdot \nabla)$, represents the convective derivative. Physically the convective derivative represents the changes due to transport of the fluid element from one point to another. Derivatives with respect to time represent the local derivatives. Physically the local derivative allows the fluid properties to vary with time. Several modelling assumptions are used to aid the calculation procedure. For example, if the flow is steady (or assumed steady) local derivatives are zero. If the flow is incompressible ($Ma \leq 0.3$) then derivatives of density can be assumed zero. When studying a frictionless flow, shear stress components (τ_{ij}) are set to zero. For Newtonian fluids, where the viscous stresses are

proportional to the elemental strain rates and viscosity coefficient, terms that involve viscosity and velocity gradients can be substituted for (τ_{ij}). Temperature has a strong effect on viscosity with increasing temperature causing an increase in the viscosity of a gas and decreasing the viscosity of a fluid. There is only a small effect on viscosity due to pressure. (Increasing air pressure from 1 Atm to 50 Atm only causes a 10% increase in viscosity: White (2003)).

Equation (4.1) can be applied to compressible and incompressible flows, steady and unsteady flows and, in addition, viscous and frictionless flows. However, in the differential form shown, it does not allow for sink or source terms within the finite volumes (White (2003)). Due to the complexity of the energy equation it is practicably too difficult to analyse except on a digital computer (White (2003)).

The equations shown, whilst complicated, can be expressed by one equation of column vectors which is particularly well suited to computational solutions: Anderson (1995). This system of equations is well posed and can be solved analytically for a limited number of simplified cases, subject to adequate boundary conditions and suitable initial values, or numerically for he vast majority of problems. The system is suitable for unsteady flow analysis being time dependent, but can also be used to approach a steady state solution by using large time steps.

FLUENT offers the capability to solve these governing equations sequentially (segregated) or in a coupled fashion, with the segregated solver being less computationally demanding. The governing equations are then linearised implicitly or explicitly for the dependent variable in every computational cell. With implicit linearisation the unknown is computed from a mixture of known and unknown surrounding data whereas for explicit linearisation only known data is used to compute the unknown variable. Using the segregated solver only explicit linearisation is available whereas using the coupled solver both linearisation techniques are available. FLUENT then discretises the governing equations using the finite volume method. (The finite volume method is well suited to complex geometries as it can accommodate structured and unstructured grids.) This means that the solution domain is subdivided into finite volumes, each with a cell centred computational node that contains all of the variables to be calculated (Ferziger and Peric (2002)). The result is an algebraic equation for each finite volume that contains a number of neighbouring nodal values. These equations are then discretised about their finite volumes thus yielding discrete equations that conserve each quantity on a control volume basis (Fluent Manual, v6.2). Several discretisation schemes are available in FLUENT. These are:

- First Order Upwind

- Power law scheme
- Second Order Upwind
- QUICK scheme
- Central difference scheme

These schemes exist because FLUENT stores variables as cell centre values. However, face values are required for the convection terms in the governing equations and these must be interpolated from cell centre values. Upwinding schemes mean that the interpolated value is derived from values in the cell upstream with respect to the normal velocity at that face. For first order accuracy the cell centre values are assumed to be constant throughout the cell, even at the faces. In the Power law scheme a 1-D convection diffusion equation can adjust the upwind value to account for heavily convective or diffusive flows. Second order schemes adjust for the gradient in the upstream cell, for which FLUENT uses a Taylor series expansion. The QUICK scheme, which can only be applied on structured grids or structured sections of grids, is a weighted average of second order upwind and central interpolations applied over one more node in each direction (Ferziger and Peric (2002)). The central differencing scheme is only available with the LES (large eddy simulation) turbulence model.

Due to the non-linear form of the equations that FLUENT solves the change in the computed variable needs to be controlled, particularly early in the calculation phase. Under-relaxation factors are used for this purpose, as shown in eqn. (4.6).

$$\phi = \phi_{old} + \alpha \left(\Delta\phi\right) \tag{4.6}$$

As the solution iterates the variable (ϕ) is dependent upon the variable at the previous iteration (ϕ_{old}) plus a portion (dependent upon the under-relaxation factor, α) times the calculated change in the variable ($\Delta\phi$).

4.3 Turbulence

Turbulent fluid flow could be described as a disorderly, chaotic behaviour of the fluid. It is characterised by strong, high frequency and random motions of the fluid particles that vary constantly with time and space, although the overall variations in the time mean may be small (White (2003)). The transition from an orderly laminar flow to a disorderly turbulent flow is not well defined and affected by many

factors like wall roughness and inlet fluctuations. The primary parameter in defining turbulence is the Reynolds number as shown in eqn. (4.7).

$$Re = \frac{\rho V L_c}{\mu} \tag{4.7}$$

No exact point of transition has been defined with the Reynolds number acting as a guide to the flow condition. High Reynolds number ($> 10^5$ typically) corresponds to turbulent flows, low values ($< 10^3$ typically) correspond to laminar flows with the region in between defined as transitionary. Turbulence acts to dissipate energy within the flow. This energy dissipation occurs because turbulent flows brings together regions with different momentum (e.g. free stream flow and boundary layer flow), and therefore kinetic energy, together. This process is imperfect thus energy is irreversibly lost into the internal energy of the fluid (Ferziger and Peric (2002)).

Due to mathematical demands of solving for these fluctuations and the fact that for many practical engineering simulations only mean values of the flow are of interest, three techniques have been developed that enable the governing equations to be solved. The first and more dominant technique, Reynolds averaging Navier Stokes (RANS) equations, involves replacing each property in the governing equation with a mean (either time or ensemble averaged) and a fluctuating component (White (2003)). This assumes that over time the fluctuations reduce to an average of zero, with their RMS value representing the turbulence intensity of the flow. To complete closure of the governing equations however, turbulence models are required (Ferziger and Peric (2002)). (More information on turbulence models can be found in section 4.3.1). The second technique, which is only discussed briefly here, involves filtering the small scale fluctuations thus modelling less turbulence and resolving more. The size of the filter is usually taken as the mesh size (Fluent Manual, v6.2). This technique is more computationally demanding and has not been used in this study. A third technique, direct numerical simulation (DNS), does not model the turbulence but solves the governing equations without averaging or approximations. However, whilst this solution is more accurate having only discretisation errors, the grid needs to have many points in order to solve for all scales of turbulence. This makes a DNS solution impracticable to most users due to the computational costs.

4.3.1 Turbulence Models

In order to close the governing equations using RANS approximation a turbulence model must be introduced. The goal of the turbulence model is to model the Reynolds stress terms in the governing equations. The simplest description of tur-

bulence involves two parameters: the turbulent kinetic energy, k, and a length scale, l, forming mixing length models (Ferziger and Peric (2002)). For a simplistic turbulence model k can be determined from the velocity field with l determined from the grid spacing. However, determining l from the grid spacing can lead to inaccuracies and with an accurate prescription of l being very difficult, particularly for flows that have separated or have strong 3-D components, other techniques that describe turbulence have been developed. Another technique, the Boussinesq hypothesis, relates the Reynolds stresses to the mean velocity gradient and is used for one and two equation turbulence models in FLUENT. Several turbulence models are available to the user in FLUENT with a short description of each below.

The Spalart Allmaras Turbulence Model

The Spalart Allmaras model solves one extra equation to model the turbluent viscosity and is the simplest turbulence model available to the user in FLUENT.

The $k-\epsilon$ Turbulence Model

The most popular turbulence model, the two equation $k-\epsilon$ model, includes the turbulent kinetic energy, k, and a turbulence dissipation rate, ϵ. The model solves two additional equations, allowing the turbulent velocity and length scales to be independently determined. Essentially energy is cascaded from largest to the smallest scales where it is dissipated (Ferziger and Peric (2002)). As strengths and weaknesses of the standard $k-\epsilon$ model have been highlighted over the years several other versions have been developed. The $k-\epsilon$ RNG (renormalisation group theory) model should enhance the accuracy of strained flows, swirling flows and flows with low Reynolds numbers. The $k-\epsilon$ realisable model meets certain mathematical constraints applicable to turbulent flows (Fluent Manual, v6.2). This model should enhance solutions of round or planar jets, rotational fields, recirculation and separation.

The $k-\omega$ Turbulence Model

Another two equation model, the standard $k-\omega$ model, solves for the turbulent kinetic energy, k, and the turbulence frequency, ω. This model incorporates low Reynolds number modifications, shear flow spreading and compressibility effects (Fluent Manual, v6.2). A variation of the standard $k-\omega$ model, the $k-\omega$ SST (shear stress transport model), combines the robust near wall formulation of the $k-\omega$ model with the free stream independence of the $k-\epsilon$ model in the far field by

using a blending function. This makes the $k-\omega$ SST model applicable to a wider range of flows.

The Reynolds Stress Turbulence Model

A further turbulence model that does not use the Boussinesq hypothesis, the Reynolds stress model (RSM), is available to the user in FLUENT. This model solves transport equations for the Reynolds stresses directly with an equation describing their dissipation rate. This produces an extra 4 equations in 2-D and 7 in 3-D.

Computationally the Spalart Allmaras model is the least demanding followed by the basic two equation $k-\epsilon$ and $k-\omega$ models. The $k-\epsilon$ realisable model has similar computational demands to the standard model, with the $k-\epsilon$ RNG model taking on average 15% more CPU time. The most elaborate model, the RSM, requires 50-60% more CPU time per iteration than the basic two equation models with an additional 15-20% more memory.

4.4 Wall Treatments

Velocity boundary layers (i.e. viscosity dominated regions) and thermal boundary layers (i.e. conductivity dominated regions) in high Reynolds number flows are very thin and require many calculation points in order to accurately replicate the physics of the flow in this region. For most engineering simulations (typified by high Reynolds number flows) this is not practical so this near wall region is modelled. This is undertaken knowing that the near wall viscosity dominated region and the outer turbulent shear dominated region have a logarithmic overlap layer (White (2003)). Therefore by simulating the logarithmic overlap layer wall functions can be applied across the viscous region. To solve wall bounded flows FLUENT offers the user several options. These are:

- Standard wall functions.
- Non-equilibrium wall functions.
- Enhanced Wall Treatment.

Using standard wall functions the viscous sub-layer ($Y+ \leq 30$) is modelled by relying on the logarithmic region in the velocity profile outside of the viscosity dominated region ($30 \leq Y+ \leq 100$). The non-equilibrium model is a two-layer model, adjusting the standard wall functions at the wall to account for turbulent kinetic

energy. This approach offers benefits over the standard wall function approach as it is partly able to account for pressure gradients and departures from equilibrium. Enhanced wall treatments adjust the turbulence models to enable the viscosity-affected region to be resolved with a mesh all the way to the wall, including the viscous sub-layer ($Y+ \approx 1$) (Fluent Manual, v6.2). However, resolving the viscous sub-layer in this manner places a substantially increased pressure on computational resources. Often for practical engineering purposes (high Reynolds number flows) the wall function approach is used for robustness and speed.

4.5 Verification of FLUENT as an Investigative Technique

To verify whether FLUENT is capable of solving labyrinth seal flow fields several test cases were examined. These test cases included two rotor-stator cavity papers from the literature, Daily and Nece (1960) and Zimmermann et al. (1986), and the examination of flow through orifice plates. Details of these studies can be found in sections (4.5.1) and (4.5.2) respectively. Throughout this section reference will be made to equations (4.8) through (4.10) representing rotational Reynolds number (Re_{ROT}), torque acting on a rotating disc (M_r) and rotor moment coefficient (C_{mr}).

$$Re_{ROT} = \frac{\omega_r r^2}{\nu} \tag{4.8}$$

$$M_r = 2\pi \int_0^r r^2 \mu \frac{du}{dx} dr \tag{4.9}$$

$$C_{mr} = \frac{2M_r}{\rho \omega_r^2 r^5} \tag{4.10}$$

Where u represents tangential velocity component and x represents the distance normal to the rotor.

4.5.1 Rotor-Stator Cavities

Two papers from the literature, Daily and Nece (1960) and Zimmermann et al. (1986), have been replicated numerically using 2-D CFD. Daily and Nece examined rotor stator cavities containing water with no through-flow. The ratio of disc radius to axial clearance was varied in finite steps from 0.0127 to 0.217. Measurements of torque data were taken across a range of rotational Reynolds number

$(10^3 \leq Re_{ROT} \leq 10^7)$ with velocity traverses through the cavity recorded at specific ratios of disc radii to cavity width for certain laminar and turbulent conditions. Their experimental set-up can be seen in fig. (4.1).

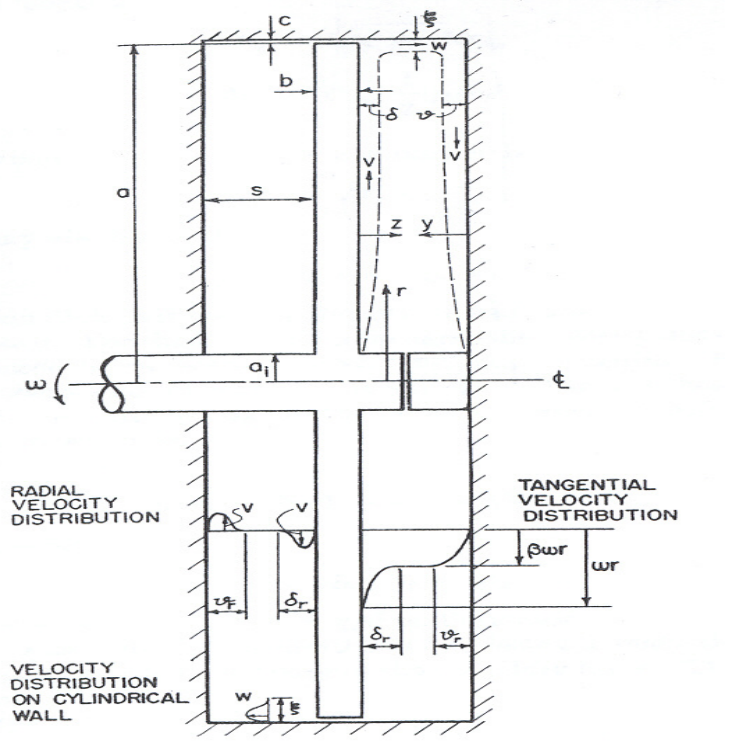

Figure 4.1: Experimental Set-Up as used by Daily and Nece (1960).

This case has previously been analysed numerically by Chew and Vaughan (1988) using finite difference computer codes (3 codes were used for comparison) and a mixing length turbulence model. An earlier paper, Chew (1985), highlighted the difficulties of predicting rotor-stator flow using the $k-\epsilon$ turbulence model. The results from Chew and Vaughan (1988) will be included as appropriate. For this study FLUENT using the $k-\epsilon$ turbulence model was used throughout. Several levels of grid refinements were used for each case analysed thus checking for grid independent solutions. The cases that have been replicated have been highlighted in table (4.1). The radius ratio refers to the radial location of the velocity traverse as a fraction of the total radius, and the aspect ratio refers to the cavity width as a fraction of the radius.

For both test situations (A and B from table (4.1)) radial and transverse

	Radius Ratio	Aspect Ratio	Re_{ROT}
A	0.765	0.0637	4.4 x 10^6
B	0.765	0.0255	4.4 x 10^6

Table 4.1: Test Data Replicated Using CFD

velocity profiles can be seen in figs. (4.2) and (4.3) for an aspect ratio of 0.0637. The rotating surface is on the right hand side of these figures.

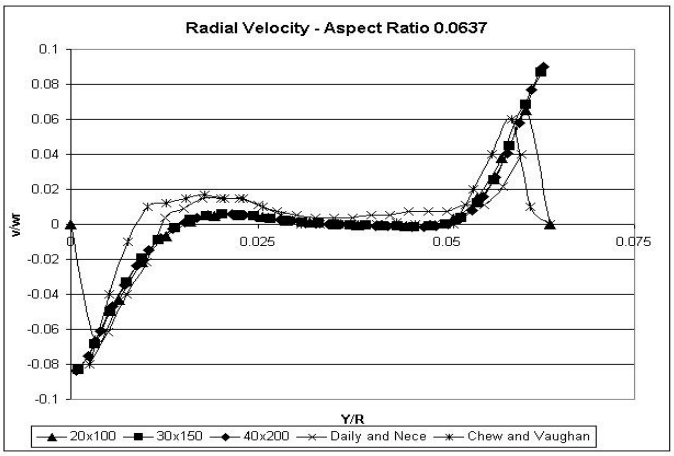

Figure 4.2: Radial velocity profile taken corresponding to test point A in table (4.1) .

For an aspect ratio of 0.0637 the results from CFD have compared well to the experimental results of Daily and Nece (1960). An improvement has been made when compared to Chew and Vaughan (1988), particularly in the tangential direction (fig. (4.3)). A high level of grid independence can be seen with very little deviation seen between solutions of 20x100, 30x150 or 40x100 nodes. The main difficulty arose in predicting the radial velocity accurately, although errors in these viscosity dominated areas should be expected due to the limitations of the wall functions. Radial and transverse velocity profiles for an aspect ratio of 0.0255 can be seen in figs. (E.1) and (E.2). Again, a high level of grid independence can be seen for both profiles which would be expected for the narrower profile but the same problems highlighted for an aspect ratio of 0.0637 prevail. The improvements made over Chew and Vaughan (1988) are more obvious for an aspect ratio of 0.0255 although again resolution of the flow in high velocity gradient regions using wall functions has proved problematic.

Daily and Nece (1960) measured the rotor moment for different Re_{ROT} using

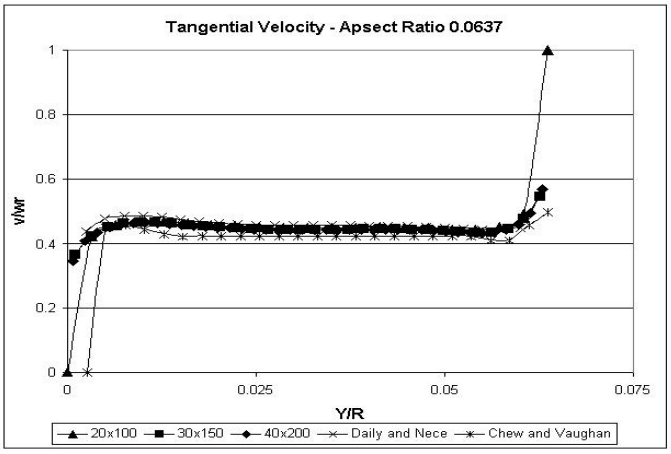

Figure 4.3: Transverse velocity profile taken corresponding to test point A in table (4.1) .

the larger aspect ratio of 0.0637. The results for several levels of grid refinement can be seen in tables (4.2) and (4.3) for Re_{ROT} of 2×10^6 and 5×10^6 respectively.

Author	Grid Size	C_m	Deviation (%)
Daily and Nece	N/A	0.0022	N/A
Chew and Vaughan	65x65	0.002276	3.45
FLUENT	20x100	0.002036	7.46
FLUENT	30x150	0.002105	4.30
FLUENT	40x200	0.002071	5.86

Table 4.2: Rotor Moment Coefficient Data Replicated Using CFD - $Re_{ROT} = 2 \times 10^6$

Author	Grid Size	C_m	Deviation (%)
Daily and Nece	N/A	0.00175	N/A
FLUENT	60x200	0.001718	1.85
FLUENT	70x200	0.001711	2.24
FLUENT	80x200	0.001711	2.22

Table 4.3: Rotor Moment Coefficient Data Replicated Using CFD - $Re_{ROT} = 5 \times 10^6$

As can be seen predictions of rotor moment coefficient agree well with the experimental data of Daily and Nece (1960) and the grid independence has highlighted optimum grid densities. This is due to using wall functions on a structured grid, as

the boundary layer thickness will change along the rotating surface. Therefore using a structured grid limits the acceptability of the wall function along the whole radius of the rotating component. However, using the wall function approach still achieves answers within 5% for the slower case (and therefore thicker boundary layer).

A further numerical study of rotor-stator cavity flow, this time involving through flow and air, was taken from Zimmermann and Wolff (1987). This paper involved looking at the rotor moment coefficients from several set-ups. These included rotating bolts, rotating covers, rotating grooves and a plain disc with the latter being the case for numerical analysis. Their experimental set-up can be viewed in fig. (4.4). Some of the geometry and conditions required for the analysis needed to be estimated as insufficient detail was available in the paper. Throughout their study the through-flow Reynolds number (as defined in eqn. (4.11)) was held constant at 2.6x10^4.

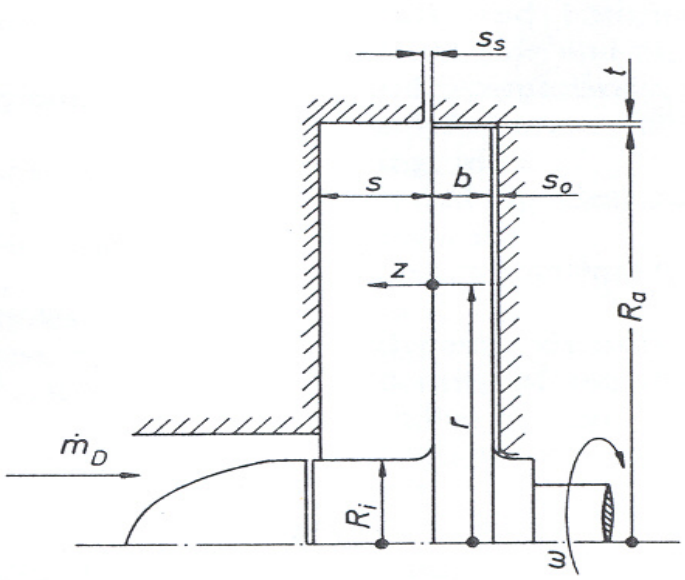

Figure 4.4: Experimental set-up as used by Zimmermann and Wolff (1987).

$$Re_{T-F} = \frac{\dot{m}}{r\mu} \tag{4.11}$$

This led to a mass flow ($\dot{m}$) of 0.1861 $\left(\frac{kg}{sec}\right)$ and a velocity at inlet of 10.5 $\left(\frac{m}{sec}\right)$ assuming ISA SLS (International Standard Atmosphere Sea Level Static) conditions prevail. In the paper the authors have also presented a derivation to calculate the

rotor moment coefficient based upon the theory of Von Karman. The results from their experiments, their derivation and the numerical simulations undertaken can be seen in fig. (4.5). Numerical simulations were undertaken at Re_{ROT} of $2\times10^6, 3\times10^6$ and 6×10^6 corresponding to $1743rpm$, $2615rpm$ and $5230rpm$ respectively.

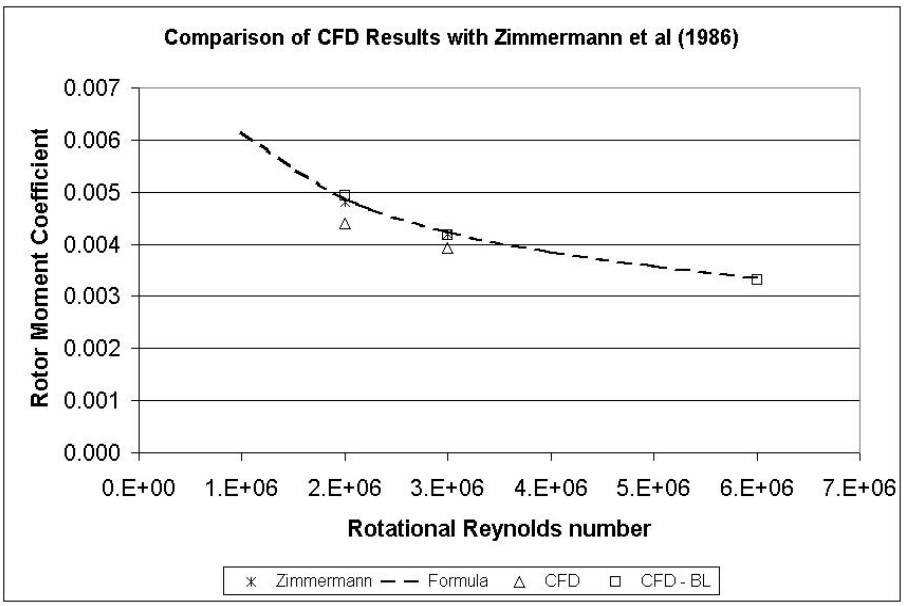

Figure 4.5: Experimental and theoretical results of Zimmermann and Wolff (1987) with their numerical simulation equivalents.

As can be seen from fig. (4.5) using CFD with wall functions to repeat the experiments revealed errors of approximately 6% or more. In order to investigate this deviation further simulations were undertaken using the near wall modelling method (described in section 4.4). This technique greatly reduced these errors to $\leq 3\%$. The benefits gained from this modelling technique can clearly be seen. As the geometry was approximately 8 times larger than that of Daily and Nece (1960) the speeds encountered are greater at the larger radii. Therefore the boundary layers are much thinner containing much steeper gradients. The wall function approach had difficulties in modelling these steep gradients accurately.

4.5.2 Orifice Plate Simulations

A second type of case to verify whether FLUENT is capable of solving labyrinth seal flow fields involved modelling the well known orifice plate. Background information

Diameter Ratio	P_t Inlet (Bar)	P_s Outlet (Bar)	C_d: ESDU	C_d: CFD
0.025	3.00	2.34	0.630	0.641
0.05	3.00	2.26	0.637	0.634
0.10	3.00	2.28	0.638	0.641
0.15	3.00	2.10	0.659	0.656
0.20	3.00	1.82	0.696	0.703

Table 4.4: Orifice Plate C_d from Theory and CFD

relating to the orifice plate and details of the orifice plates used for the experiment can be found in Appendix (D). The aim of the orifice plate is to cause an obstruction to the flow that produces a flow rate dependent upon the pressure change across the device (Davis and Mattingly (1977)). Several authors have analysed the same problem numerically. These include Davis and Mattingly (1977), Reader-Harris and Keegans (1986) and Reader-Harris (1986), all of whom used the $k - \epsilon$ turbulence model. Davis and Mattingly (1977) examined a diameter ratio range of 0.40 - 0.70 finding agreement on C_d within 4%. Since 1977, work was undertaken to re-derive the equation for C_d, the conclusion of which can be seen in eqn. (D.2). Some of this development work was reported by Reader-Harris and Keegans (1986) and Reader-Harris (1986), who achieved remarkable agreements of 1% typically on C_d. However, the diameter ratios studied were typically larger than that of the labyrinth seal. Therefore comparisons between theoretical and simulated C_d using diameter ratios more typical of the labyrinth seal would clarify the capability of FLUENT to simulate the labyrinth seal performance accurately. The theoretical results were taken from BS (1042.1) and ESDU (82009). Five diameter ratios of orifice plate were analysed, each in an $80.85mm$ pipe. (This is the same size of pipe as that used in the experiment for measuring the mass flow.) The range of diameter ratios used covered the clearance to labyrinth tooth height ratios typically found in labyrinth seals (see Prasad et al. (1997)). All of the CFD cases analysed were 2-D. Pressure inlet and outlet boundary conditions provided the pressure gradient required for the mass flow. Symmetry boundary conditions were used along the centreline to reduce computational time. The walls were modelled as non-slip walls. All of the boundary condition information and the C_d comparison can be seen in table (4.4). As can be seen this equates to range of percentage errors from -0.39% to $+1.79\%$ as predicted by CFD. This proves that FLUENT is capable of predicting C_d for the range of geometries of interest.

4.6 Two Dimensional Simplification Technique

To model an abradable honeycomb labyrinth seal computationally using CFD in 3-D is expensive in both time and computational resources. Previous authors have tried to create 3-D CFD models with varying degrees of success as highlighted in section (2.8). Further, Paolillo et al. (2006) highlighted a desire to develop a method of modelling 3-D abradable honeycomb labyrinth seals. In order to model many different seal design situations using 3-D CFD would therefore be a lengthy and time consuming process. Therefore a 2-D technique that was capable of replicating the 3-D performance of the abradable honeycomb labyrinth seal was developed. This enabled many cases to be computed economically whilst still having confidence in the results. This section of work has been presented by Collins et al. (2006). A summary of the CFD simulations used to develop the routine can be seen in table (A.2).

4.6.1 Seal Geometry

The geometry of the labyrinth seal model for the current simplification study was held constant throughout with a tooth width and running gap of $1.00mm$. The honeycomb cells modelled were $5.00mm$ deep with a wall thickness of $0.125mm$. The seal pitch was set at $10.00mm$ and the cavity had an aspect ratio of 1. The upstream and downstream faces of the teeth were inclined at 5.71° to the vertical. In 3-D at least five complete honeycomb cells were modelled in the transverse-direction. The 3-D models ignored the annular design of actual labyrinth seals. Full details can be seen in fig. (4.6).

To reduce computational demands only two cavities and one full tooth were modelled. The inlet and outlet to the domain was located in the running gap above the start of the first and end of the last tooth respectively. The honeycomb surface was aligned in two directions with respect to the labyrinth teeth. For the purpose of this document these will be called the design-orientation and the alternative-orientation. Both orientations were aligned centrally to the middle of the central tooth. Figure (4.7) shows a detailed view of both honeycomb orientations with respect to the middle of the central labyrinth tooth. The honeycomb extended from above the start of the first tooth to above the end of the last tooth totalling $21.00mm$ in length.

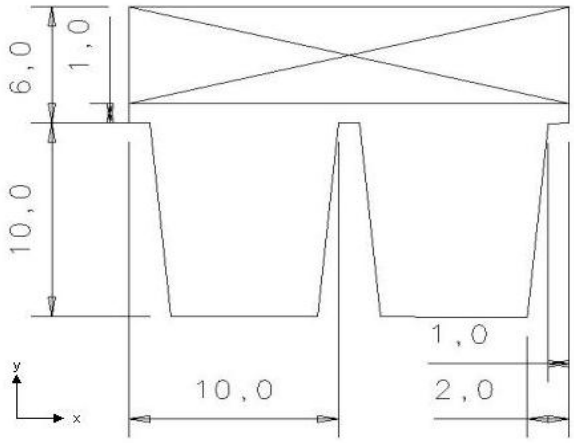

Figure 4.6: Dimensions of the Labyrinth Seal (mm). Honeycomb Positioned in Crossed Section.

4.6.2 Effective Area

Using a honeycomb lining in conjunction with a labyrinth seal can change the area available to the flow. This is because the actual gap, Cl_{eff}, can be different from the nominal gap, Cl. From Cl and Cl_{eff} the nominal and effective area can be calculated. Schramm et al. (2002) presented a thorough analysis on the principle of effective area using the ratios $(\frac{Tp}{Hs})$ and $(\frac{Cl}{Hs})$ with eqns. (4.12) and (4.13).

$$Cl_{eff} = \sqrt{\left(\frac{Hs - Tp}{2}\right)^2 + Cl^2} \tag{4.12}$$

$$\xi = \frac{Cl_{mean}}{Cl} = \frac{\frac{1}{2}Cl_{eff} + \frac{1}{2}Cl}{Cl} \tag{4.13}$$

The calculated parameter, ξ, gives an estimate for the overall increase in the flow field area whilst using honeycomb.

> *The parameter ξ describes the average change in cross-sectional area available for the through flow and gives an estimate for the increase of leakage.* Schramm et al. (2002)

For this study at design orientation the procedure gives ξ equal to 1.022 and 1.24 for $1.60mm$ and $3.20mm$ honeycomb sizes respectively. This analysis is only

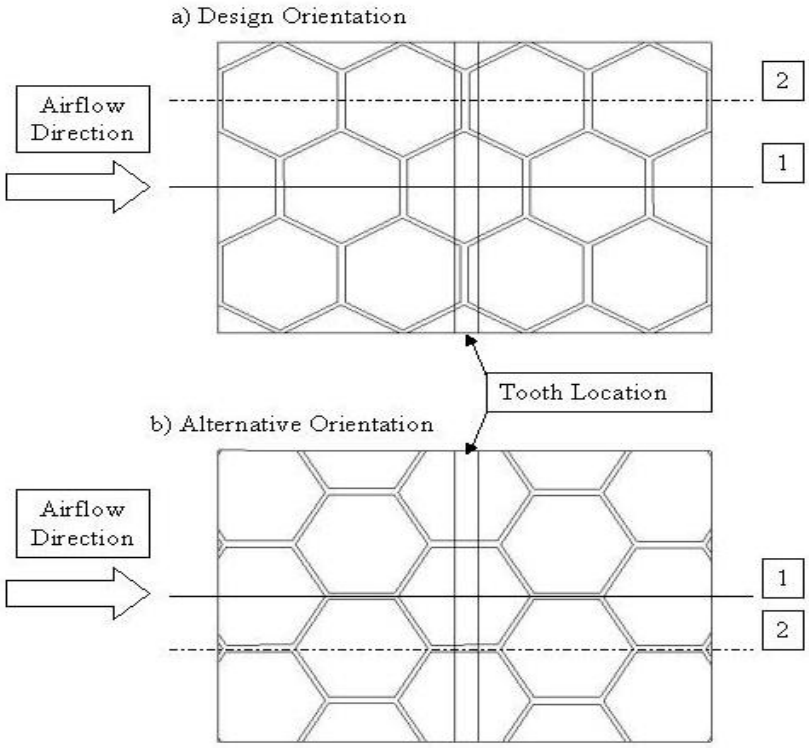

Figure 4.7: Honeycomb Position with respect to the Middle of the Central Tooth. Design Orientation is the top figure, alternative orientation is the bottom figure.

based upon seal geometry in the design-orientation case and does not consider the alternative-orientation case. An analysis carried out by Collins et al. revealed values of ξ for the alternative-orientation case equal to 1.014 and 1.467 for HC sizes of $1.60mm$ and $3.20mm$ respectively.

4.6.3 Two-Dimensional Seal Geometry

In 2-D the geometry used represents a slice of the 3-D domain. There are two planes that could be taken from the 3-D models which represent extreme conditions for the 2-D models. These have been highlighted on fig. (4.7) as positions (1) and (2). For the purposes of the current discussion these will be called the mid-position and offset-position respectively. As can be seen the actual 2-D shape that will be used to represent the 3-D case will vary from the design-orientation case to the alternative-orientation case. In order to represent the 3-D case accurately the 2-D plane has to represent an average plane of these possibilities. For the design-orientation case

the plane that best represents the 3-D case is found mid-way between these two extreme positions. For the alternative-orientation case the plane that best represents the 3-D case is found by considering the effect the geometry has on the flow. Further information on the alternative-orientation case can be found in Collins et al. (2006).

An example of the 2-D geometry can be seen in fig. (4.8) which shows the $3.20mm$ honeycomb cell size aligned in the design-orientation case. Also highlighted are the two extreme positions that the tooth could take with respect to the honeycomb surface in 2-D. These are positions $(A1)$ and $(A2)$ which represent the tooth aligning to the middle of a honeycomb cell pocket or to the middle of a honeycomb cell wall respectively.

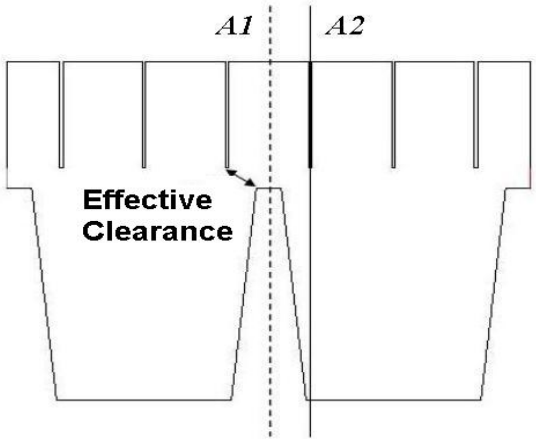

Figure 4.8: Example of Two Dimensional Geometry. HC = $3.20mm$, aligned in the Design Orientation.

In this study all of the 3-D cases have their teeth aligned so that the centre of the middle labyrinth tooth runs against a honeycomb cell pocket, as shown in fig. (4.7). Figure (4.8) graphically highlights the dimensions Cl_{eff} from eqn. (4.12), which represents the effective area available to the flow. In 3-D this dimension will vary with the honeycomb and labyrinth tooth position whilst in 2-D it is a constant dimension. Additionally, in 2-D if the honeycomb and labyrinth tooth are aligned in position $(A2)$ from fig. (4.8) then the dimensions Cl_{eff} and Cl will be the same due to the presence of the wall.

4.6.4 Three-Dimensional Modelling Technique

In order to get the 3-D computations to converge use was made of incompressible and frictionless boxes on the inlet and outlet of the flow domain. These acted to move the boundary conditions to regions of stability and aided convergence. Dong-Chung and Rhode (2003) experienced convergence problems on similar 3-D simulations. However, in their study the running gap being modelled was significantly smaller than in the current study, at $0.38mm$ maximum. In the current study, 3-D simulations at $0.50mm$ running gap and 3-D simulations using a honeycomb cell size of $0.80mm$ were tried but these did experience convergence problems. Each of these incompressible and frictionless boxes was $50.00mm$ long and used an increasing cell aspect ratio away from the seal domain. This enabled the complicated flow features to be kept within the seal domain of interest. An example of the 3-D computational domain can be seen in fig. (4.9).

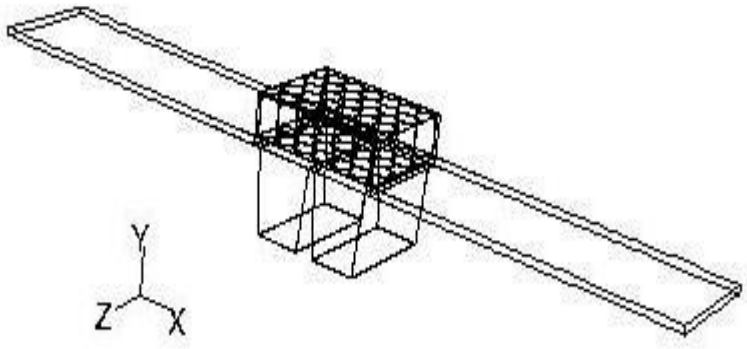

Figure 4.9: Three Dimensional Computational Grid showing Incompressible and Frictionless Boxes at Inlet and Outlet.

However, using the incompressible and frictionless boxes also meant that the total pressure at the start of the compressible domain varied by an average of 0.25% from the ideal planned conditions. An example of this variation in total pressure caused by this modelling technique can be seen in fig. (4.10).

This shows the total pressure profile through the running gap at the start of the upstream tooth where the air begins to be modelled as an ideal gas. The figure highlights the total pressure variation seen, particularly at y equal to $10.00mm$ and

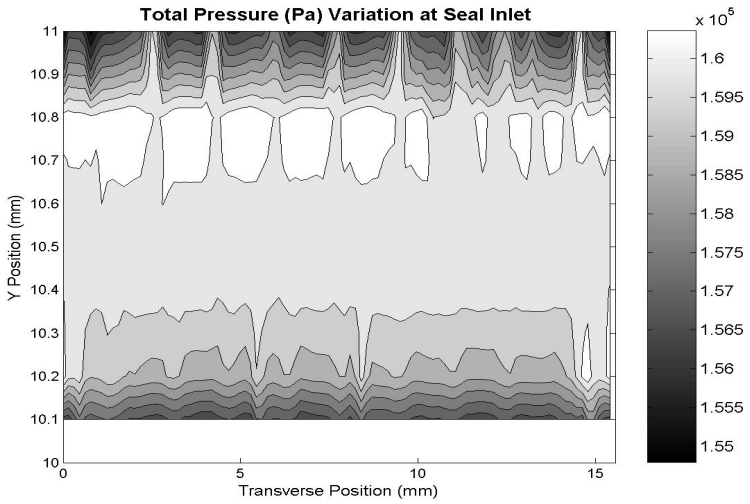

Figure 4.10: Total Pressure Profile at Entrance to the Seal Domain. HC 1.60mm at PR = 1.60, Alternative Orientation.

11.00mm, which is caused by the change in the boundary condition from a frictionless wall upstream of the inlet seal tooth tip to the non-slip wall boundary condition of the seal tooth tip or honeycomb land. This change from free-sip walls to non-slip walls starts the development of boundary layers. These incompressible boxes were not repeated in the 2-D simulations as this variation was viewed as within acceptable limits.

4.6.5 Numerical Approach

FLUENT using the $k-\epsilon$ turbulence model with standard wall functions was used for the majority of this study. (This turbulence model and wall function combination has been verified as adequate for labyrinth seal flow fields by Schramm et al. (2002), Rhode and Adams (2001a) and Wittig et al. (1987) amongst others). Additionally, in 2-D, some cases have also resolved the near wall viscous sub-layer to build confidence in the approach. Second order discretisation was achieved in all cases.

For all cases steady state solutions were sought. However, some 3-D cases at higher pressure ratios displayed convergence problems. This was particularly noticeable for the 3.20mm honeycomb cell size above pressure ratios of 1.40. When steady state solutions displayed convergence problems unsteady simulations were computed. This approach used a small time step of $10^{-6}sec$ with 20 iterations per

time step. The convergence criteria used were mass flow through the domain and average velocity seen at exit from the compressible domain.

The compressible air was modelled using the ideal gas setting and isentropic boundary conditions. For the incompressible air (used in the 3-D simulations) constant density conditions were maintained in respect of the pressure boundary conditions. Standard wall functions were used for all cases except when the boundary layer was resolved. When used the wall functions were kept within appropriate limits unless well inside the honeycomb cells. This was achieved by using a series of grids that increased in node density, with higher node densities required when simulating higher pressure ratios. The first node was placed to achieve a $Y+$ of approximately 30, with 5 further nodes placed in the viscous region. For the 2-D models that resolved the near wall viscous sub-layer a structured boundary layer mesh was used. For these models the first node was placed to achieve a typical $Y+$ of less than 1, with at least 10 nodes inside the turbulent boundary layer ($Re_y < 200$).

The initial starting point for grid construction came from Allcock et al. (2002b). In 2-D when using the wall function approach this meant that the grid consisted of up to 20,000 nodes with 10,000 iterations required for convergence. These solutions took less than four hours to converge on a PC with $1.70GHz$ processor using $256Mb$ RAM. To resolve the near wall viscous sub-layer effectively in 2-D meant using up to 80,000 nodes. These solutions took up to 20,000 interations for convergence, taking typically 12 hours for convergence on the same PC. In 3-D the mesh size varied from 440,000 to over 800,000 nodes. Steady state solutions typically took 70 hours using 4x $900MHz$ processors running in parallel with a shared memory of $8Gb$. When running unsteady simulations using the same grids the computational time more than doubled. Therefore, the efficiencies in being able to use 2-D simulations (with or without boundary layer resolution) purely in terms of computational cost and time, are significant.

Convergence of the governing equations for steady state cases was attained to leave flat residual errors of (10^{-3}) minimum, although typically (10^{-4}) or better was achieved. The under-relaxation factors for pressure and momentum were reduced by ($\frac{2}{3}$) to aid convergence. Unsteady simulations were converged until the convergence criteria deviated by less than 1% and showed a repetitive pattern. Structured grids were created in the labyrinth cavity and in the honeycomb cell domain. These were joined by an unstructured mesh created in the running gap of the seal. The 3-D models ignored the annular shape of an actual labyrinth seal. It is noted by Childs et al. (1989) that honeycomb acts to kill swirl velocities. At least 5 complete honeycomb cells were modelled in the transverse direction, dependent upon honeycomb cell size. Periodic boundary conditions were used to keep the domain a realistic size.

4.6.6 Results

Global parameters and inter-cavity pressure profiles were compared between the 3-D and 2-D CFD cases. In 3-D the generation of transverse-velocity components has also been analysed to verify the assumption of the 2-D model.

Global Comparison of Results

The global comparisons came from comparing the C_d calculated for non-critical pressure ratios using eqns. (4.14) and (4.15), (Willenborg et al. (2001)). The results for HC 3.20mm in the design orientation can viewed in fig. (4.11) with further results in figs. (E.3) through (E.5).

$$C_d = \frac{\dot{m}_{ACT}}{\dot{m}_{ID}} \tag{4.14}$$

$$\dot{m}_{ID} = \frac{AP_{t(0)}}{\sqrt{T_{t(0)}}} \sqrt{\frac{2\gamma}{R(\gamma-1)} \left[\left(\frac{P_{s(n)}}{P_{t(0)}} \right)^{\left(\frac{2}{\gamma}\right)} - \left(\frac{P_{s(n)}}{P_{t(0)}} \right)^{\left(\frac{\gamma+1}{\gamma}\right)} \right]} \tag{4.15}$$

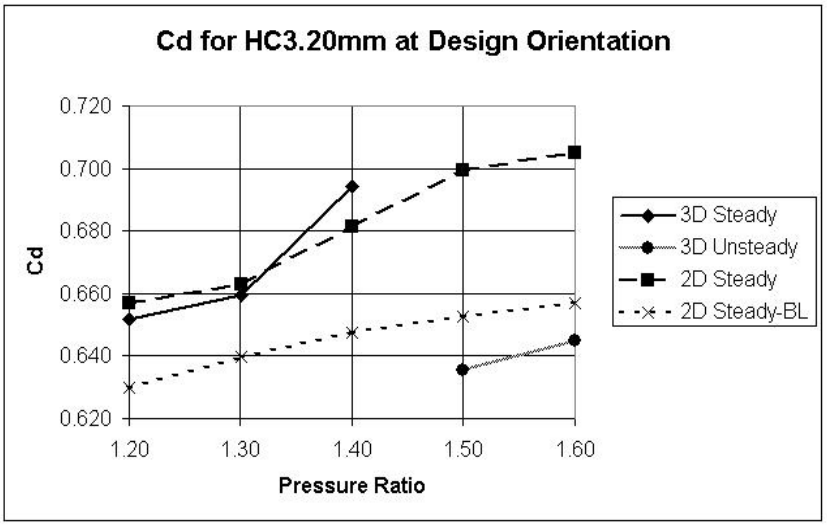

Figure 4.11: C_d for HC = 3.20mm, Design-Orientation Condition.

As can be seen for a honeycomb cell size of $3.20mm$ (figs. (4.11) and (E.3)) the 2-D simulation using the wall function approach (2D Steady) repeats the answers of the 3-D steady (3D Steady) simulation within 2%. However, for cases and conditions where the 3-D models had to be solved as time-dependent problems (3D Unsteady) the comparison with the 2-D simulations using the wall function approach is not as accurate. In these cases variations of up to 6% are seen. This shows the different levels of blockage, or effective area, when using a time-dependent approach versus a steady state wall function approach. To investigate this variation, 2-D steady state simulations that resolved the near wall viscous sub-layer (2D Steady BL) were calculated. This approach gave consistent variations of 5 - 6% less C_d when compared with 3-D steady state simulations. However, when comparing the 2-D cases that resolved the near wall viscous sub-layer with their equivalent time-dependent 3-D simulations differences of 2.5% or lower have been recorded.

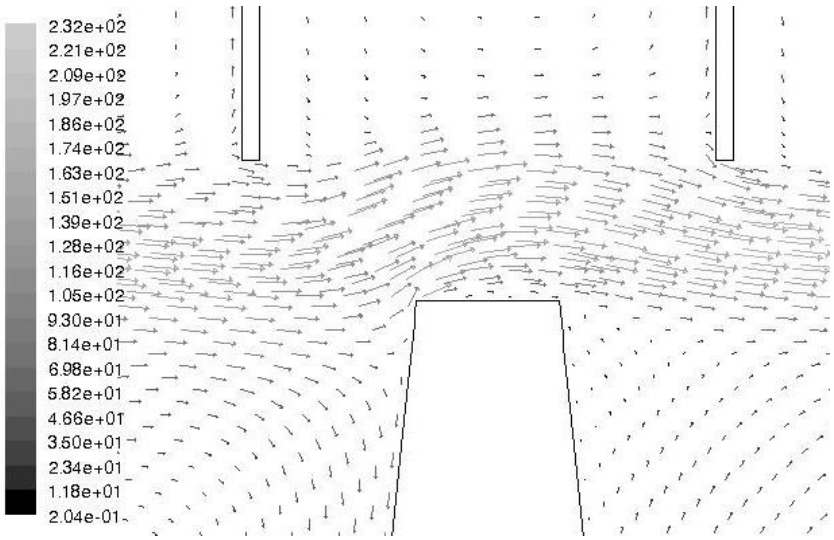

Figure 4.12: Vectors of Velocity Magnitude at the Middle Tooth Tip Using Wall Function Approach. 2-D Simulation, HC $3.20mm$, design orientation, PR = 1.60.

For a honeycomb cell size of $1.60mm$ (figs. (E.4) and (E.5)) the 3-D steady-state solutions converged better, particularly for the alternative-orientation case with no unsteady simulations required. Again the 2-D steady state answers predicted the 3-D steady state answers within 2%. For the 3-D unsteady simulations, using the design-orientation case at pressure ratios of 1.50 and 1.60, the variations with the 2-D wall function simulations are within 0.6%. This reduced level of variation is thought to be because as the honeycomb cell size reduces the honeycomb surface will act more like a flat plate (Allcock et al. (2002a)) and a reduced small

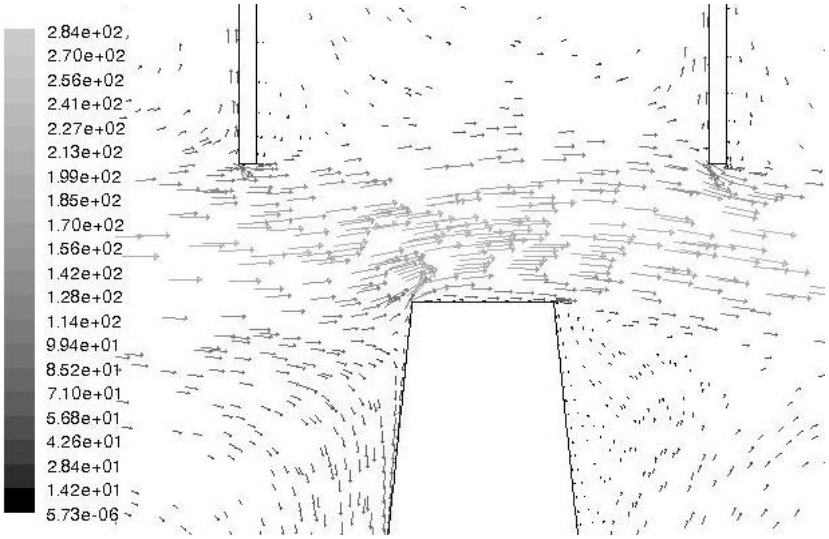

Figure 4.13: Vectors of Velocity Magnitude at the Middle Tooth Tip Resolving Boundary Layer. HC 3.20mm, design orientation, PR = 1.60.

clearance effect will be registered. The effects found when the boundary layer was resolved for the 3.20mm honeycomb cell size are not as dominant for this cell size and geometry. Therefore it is envisaged that the boundary layer is more likely to require resolution if the ratio ($\frac{Tp}{Hs}$) or running clearance is reduced, both of which would add importance to the viscous boundary layer effects.

To highlight the variation between the two 2-D approaches two figures, (4.12) and (4.13), are presented. This shows the velocity vectors seen at the middle tooth tip region using the wall function approach and resolving the near wall viscous sub-layer respectively. As can be seen the level of separation and stagnation is much greater when resolving the near wall viscous sub-layer, as is the degree of contraction over the tooth. This can be easily verified by looking at the maximum velocities seen in both figures, whilst noting that the wall function approach actually passes more mass flow having a higher C_d.

As the C_d is driven by the effect of contraction at the teeth tips this means that the 2-D planes taken offer a similar constriction. The advantage of using the design-orientation compared to the alternative-orientation can clearly be seen with C_d, and therefore actual mass flow (see eqn. (4.14)), reduced throughout, particularly when using the 3.20mm cell size. This confirms the Cl_{eff} reasoning for the 3.20mm honeycomb cell size but contradicts the same reasoning for the 1.60mm honeycomb cell size. However, the difference in Cl_{eff} for this cell size is very small,

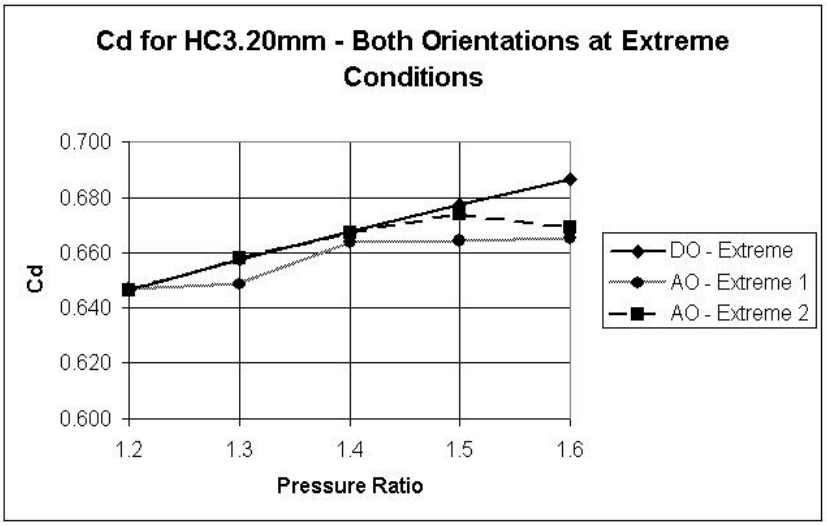

Figure 4.14: C_d for HC $3.20mm$. 2-D simulations Using the Wall Function Approach. Extreme Alignment Condition.

$< 1\%$, as are the differences registered in C_d between the 2-D cases. The differences seen between the 3-D cases whilst larger are still within acceptable limits.

To check the variation due to the honeycomb surface position both $3.20mm$ orientations were also solved with the labyrinth tooth aligning to the honeycomb wall (refer to fig. (4.8), posn. *A2*). These 2-D solutions used the wall function approach. The calculated C_d is shown in fig. (4.14). For the alternative-orientation case there are two offset positions due to the fraction used to offset. However, both conditions return equivalent answers. These offset conditions for both orientations return lower values of C_d, and therefore pass less mass flow than their mid-position counterparts that also used the wall function approach. Typically reductions of 2% in C_d are seen between 2-D simulations aligned centrally and aligned in extreme conditions. However, these simulations have not resolved the near wall viscous sub-layer. It would be expected from the previous near wall viscous sub-layer simulations that increased levels of blockage and the associated reductions in mass flow would be calculated if the viscous boundary layer was resolved.

Inter-Seal Cavity Comparison

To further compare the 3-D simulations with their respective 2-D counterparts, total pressure profiles along 10 x-y planes were taken in the z-direction (refer to fig. (4.9)

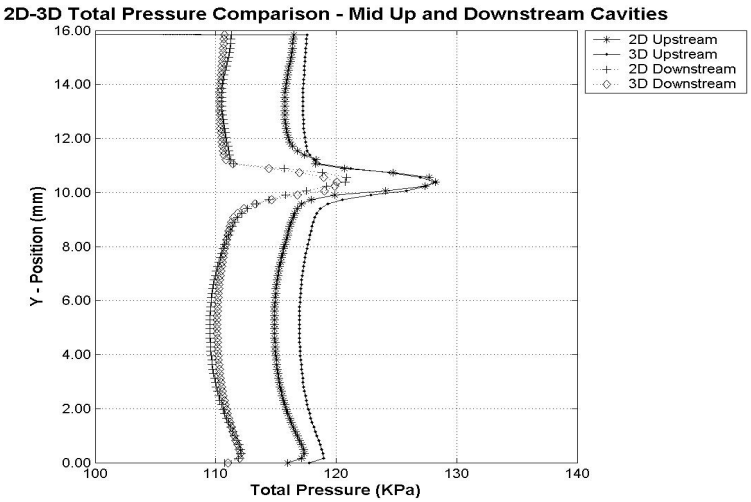

Figure 4.15: Comparison of Total Pressure Profile Between 2-D and 3-D Simulations. $3.20mm$ Honeycomb, PR = 1.30 Design Orientation.

for co-ordinate directions) across two full honeycomb cells and averaged. This averaged 3-D plane and the 2-D plane were then both interpolated onto a neutral grid prior to comparing against each other. The points taken for comparison between the 2-D and 3-D simulations lie along the middle of the upstream (Up) and downstream (Dn) cavity. Simulations in 2-D that use the wall function approach (2D) and that resolved the near wall viscous sub-layer (2DBL) are compared to their 3-D (3D) equivalent. Figures (E.6) and (E.7) display these calculated average variations for a honeycomb cell size of $3.20mm$ at design-orientation and alternative-orientation respectively. Figure (E.8) displays the same average variation for a honeycomb cell size of $1.60mm$ at both the design-orientation (DO) and alternative-orientation (AO). Simulations that resolved the near wall viscous sub-layer are not available for this cell size. All of the 3-D simulations above a pressure ratio of 1.40 are unsteady except for a honeycomb cell size of $1.60mm$ aligned in the alternative-orientation. The RMS variation has been used throughout to account for positive and negative variations.

For all cases analysed the variations between 2-D and 3-D simulations generally increase with pressure ratio. From fig. (E.7) variations of 5.35% (the largest of all variations) have been recorded when comparing 3-D unsteady simulations with 2-D simulations using the wall function approach. However, when comparing the same 3-D cases with 2-D simulations that resolve the near wall viscous sub-layer, these variations have reduced to less than 2.00%. Overall the variations recorded

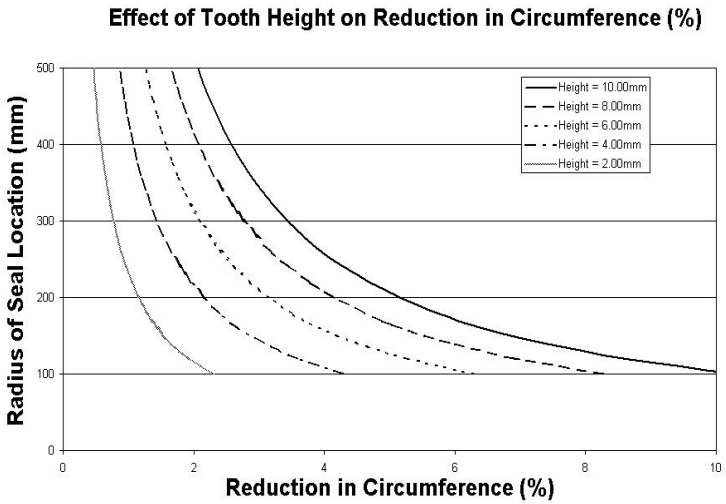

Figure 4.16: Reduction in Circumference Between Stationary Land and Rotor as a Percentage of the Original Circumference. Nominal Running gap taken as $1.00mm$.

between 2-D and 3-D simulations are within 3.00%. An example of the graphical total pressure comparison can be seen in fig. (4.15). From the analysis of these variations confidence is gained in the numerical modelling approach used.

Applicability of 2-D Assumption

The assumption of 2-D flow has been checked by looking at the generation of transverse-velocity component due to the honeycomb surface. Figures (E.9) and (E.10) show the effect typically seen throughout all cases analysed. (In these figures the middle tooth tip is located between the axial position of $9.00mm$ and $10.00mm$.) Even at a Y-position of $7.00mm$ (fig. (E.9)), $4.00mm$ away from the honeycomb surface and $3.00mm$ away from the teeth tips into the seal cavities, an effect due to the honeycomb surface can be seen on the teeth faces. However, the effect is counter-balanced with equally large positive and negative velocities. For example, the average of the transverse-velocity components shown in fig. (E.9) and fig. (E.10) are $0.024\left(\frac{m}{sec}\right)$ and $0.032\left(\frac{m}{sec}\right)$ respectively. When compared with overall average velocity magnitudes of $19\left(\frac{m}{sec}\right)$ and $141\left(\frac{m}{sec}\right)$ for the same figures this shows the small effect that transverse-velocity has on the overall velocity magnitude.

As these 3-D simulations ignore the annular shape of the labyrinth seal it would be reasonable to assume that the size of these variations would diminish faster than

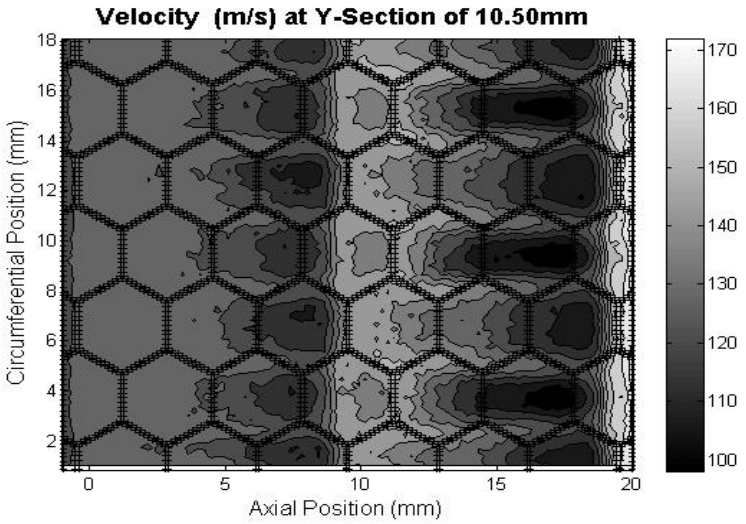

Figure 4.17: Velocity Magnitude at Y=10.50mm. HC 3.20mm, PR 1.40, Design-Orientation.

shown. This is because as the flow moves into the seal cavity the area available for the flow will diminish due to the tighter circumference thus encouraging more mixing. However, if the abradable honeycomb labyrinth seal operates at a large radius the effect of the diminishing area will be small. This effect can be seen graphically in fig. (4.16) which highlights the percentage reduction in circumference achieved by various tooth heights plotted against the outer radius of the seal. For this figure the running gap was held constant at 1.00mm.

Variations Between Design- and Alternative-Orientations

The variations in velocity magnitude between the design- and alternative-orientations are presented in figs. (4.17) and (4.18). These figures show the velocity magnitude at a position of $Y = 10.50mm$, half-way between the teeth tips and honeycomb land, at a pressure ratio of 1.40. The middle tooth-tip is located between an axial position of 9.00mm and 10.00mm, with the entrance and exit tooth located between $-1.00mm$ and 0.00mm, and 19.00mm and 20.00mm respectively. The lower velocities over the middle tooth-tip in the design-orientation case (fig. (4.17)) indicate the increased level of blockage and associated reduction in mass flow achieved when compared to the alternative orientation. Equally, the regions of slow velocity before the exit tooth are significantly larger in the design-orientation case indicating that this orientation has an increased overall energy loss when compared to the alternative-orientation.

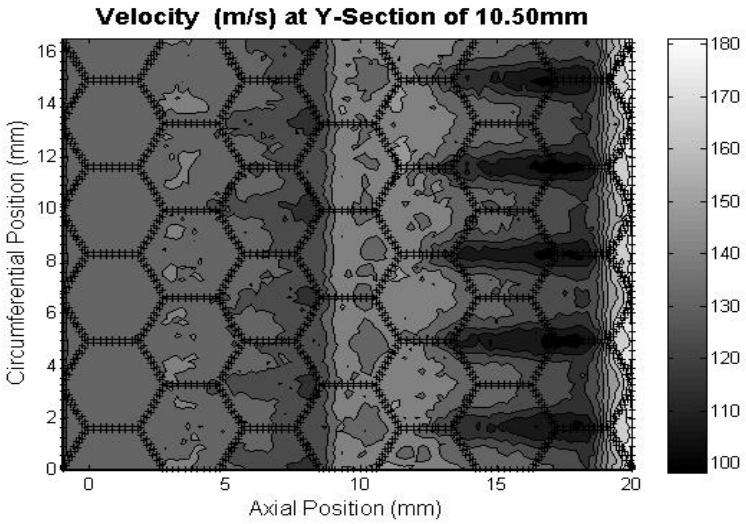

Figure 4.18: Velocity Magnitude at Y=10.50mm. HC 3.20mm, PR 1.40, Alternative-Orientation.

4.7 Conclusion

An investigation to verify wether FLUENT is capable of modelling labyrinth seal flow fields was undertaken. This was carried out by modelling two rotor-stator cases from the literature and by simulating several orifice plate flow fields. Through the process it was found that FLUENT was capable of predicting the C_{mr}, velocity profiles and effects due to contraction with reasonable accuracy. Further, the importance of modelling the near wall viscous sub-layer correctly was highlighted with increasing errors in velocity profile with very thin boundary layers. However, the overall accuracy of the simulations is good and confidence can be taken that FLUENT is capable of predicting labyrinth seal flow fields accurately.

Through replication of well known flow situations it was found that FLUENT is capable of replicating the flow field accurately. The primary weakness experienced was in simulating boundary layer flow accurately using wall functions. This is particularly true when the boundary layer is very thin and therefore the large changes in fluid properties associated with boundary layer flow occur across very small distances. Therefore when simulating experimental labyrinth seal conditions both wall function and boundary layer resolution approaches shall be tested.

In order to simulate the experimental rig using 3-D CFD significant time and computational resources would be required to create the computational mesh, iter-

ate to a solution and to post process the results. Therefore an investigative study was undertaken to find a simpler method of CFD investigation that predicted the flow field accurately. Results comparing 2-D and 3-D CFD simulations of abradable honeycomb labyrinth seals have been presented. The analysis has focused on two honeycomb cell sizes, $1.60mm$ and $3.20mm$, aligned in two orientations with respect to the labyrinth teeth. One seal geometry with a tooth width of $1.00mm$ was studied throughout with the pressure ratio varying from 1.20 up to 1.60.

The comparisons have shown that the 2-D technique developed has proved capable of offering a representative description of the 3-D flow field. Comparison of the global parameter C_d have been repeated within 2.65% and 4.00% for the design-orientation and alternative-orientation respectively when using the large honeycomb cell size. For the small honeycomb cell size these variations reduce to less than 2.00% and 1.00% respectively. Reductions in mass flow are achieved by using the design-orientation over the alternative-orientation. Further mass flow reductions in 2-D simulations are achieved by aligning the labyrinth tooth to the honeycomb cell wall. This effect requires further investigation. It is noted however that the alternative-orientation case may offer benefits for high performing seals in a contact situation. This is because less honeycomb wall is aligned with the labyrinth teeth and therefore the stator will easily deform. Additionally there is likely to be less temperature rise.

The flow field variations between the 2-D simplification technique and their 3-D equivalent have been compared using inter-cavity pressure profiles. The maximum average RMS variation recorded of 3.00% was found at a pressure ratio of 1.60 whilst using the $1.60mm$ honeycomb aligned in the alternative-orientation.

The 2-D assumption has been checked by looking at the generation of the transverse-velocity component in the 3-D simulations. This has shown that the honeycomb has an effect on the transverse-velocity component that is transmitted into the labyrinth seal cavity and is particularly noticeable at regions of high velocity, like that found on teeth faces. However, as the study has not analysed the effect of rotation the transverse-velocity components act to cancel each other out.

Chapter 5

Numerical Simulation of the Experiment

Through successful repetition of the experimental results numerically, confidence can be gained in numerical techniques that can be used to compute labyrinth seal flow fields. To undertake this comparison three numerical methods have been investigated: CFD, theoretical derivations and special purpose computer codes. Use was made of the easiest experimental set-up to replicate, namely the test using the blank stator. Each numerical method was applied in turn in a search for the most suitable method. Further, any shortcomings of the different techniques have been highlighted with explanations of them. A summary of the CFD simulations undertaken can be found in tables (A.3) through (A.5). Further, all of the CFD simulations in this chapter are 2-D and therefore when replicating the honeycomb experimental data use was made of the simplification technique reported by Collins et al. (2006).

There are many publications that have used CFD for labyrinth seal analysis. However, no definitive approach has been found. Of those detailed in section (2.3) the $k-\epsilon$ turbulence model is the most popular having been used by Rhode and Adams (2004a), Paolillo et al. (2006) and Vakili et al. (2005) amongst others. The $k-\epsilon$ realsiable and $k-\epsilon$ RNG turbulence models have each been used by one author respectively: Denecke et al. (2005b) and Wang et al. (2004). Regarding modelling the near wall viscous region most authors have used standard wall functions. Wang et al. (2004) used standard wall functions and non-equilibrium wall functions finding no overall gain in accuracy. Therefore several turbulence models and methods of resolving the near wall region were investigated with successful strategies carried forward. Comparisons between the CFD simulations and experimental data involved comparing both overall flow data and inter-seal static pressure distribution. To compare the experimental inter-seal static pressure tappings with CFD, short lines were created in the numerical models near the position of the static tappings and parallel

to the wall with the average value calculated. The length of these lines matched the diameter of the static tapping for that location. Further lines that reached across the seal domain and coincided with the centreline of each static tapping were created thus enabling a line average to also be computed. These average values were used to compare with the experimental data.

Further comparisons were undertaken using theoretical derivations as highlighted through the literature and two pre-existing computer codes, THESEUS and KTK, as designed by Allcock (1999) and Shapiro and Chupp (2004) respectively. These techniques used different methods to predict seal performance, primarily based upon loss coefficients. This section discusses the differences in their design and compares the results obtained with the current study.

5.1 Simulation of Experimental Results: Blank Metal

Initially CFD simulations were unsuccessful at replicating the experimental data, typically underpredicting mass flow. However, it was found that this variation was due to deviations between the tooth corner radii on both the experimental equipment and the computational grids created for CFD simulations. The experimental labyrinth teeth tips had a manufacturing tolerance of $0.10mm$ radius applied and it was checked that this tolerance was not exceeded. Therefore further CFD simulations including this radius were also calculated. At a clearance of $0.50mm$ it was found that simulations using no corner radii typically under-predicted the experimental mass flow by 15-20% approximately, primarily due to the increased level of separation caused by having sharp corners. Inclusion of tooth corner radii significantly reduced this variation, as highlighted in fig. (5.1). This figure highlights results calculated by the $k-\epsilon$, $k-\epsilon$ RNG and $k-\epsilon$ realisable turbulence models, all of which resolved the near wall viscous sub-layer (BL). This varying level of separation on the labyrinth teeth tips due to corner radii was previously found by Paolillo et al. (2006) and Rhode and Guidry (1993a) who predicted up to 30% improvement in seal performance from perfectly sharp corners. However, Zimmermann et al. (1994) showed that straight seals are the least sensitive to tooth corner rounding.

As can be seen the modelling errors have been significantly reduced with clear variations between different turbulent models. The standard $k-\epsilon$ turbulence model shows variations of up to 15%, with the $k-\epsilon$ realisable and $k-\epsilon$ RNG models exhibiting similar variations of $\leq 5\%$ approximately. In a further step to reduce modelling complexity, simulations using the simpler wall function (WF) approach

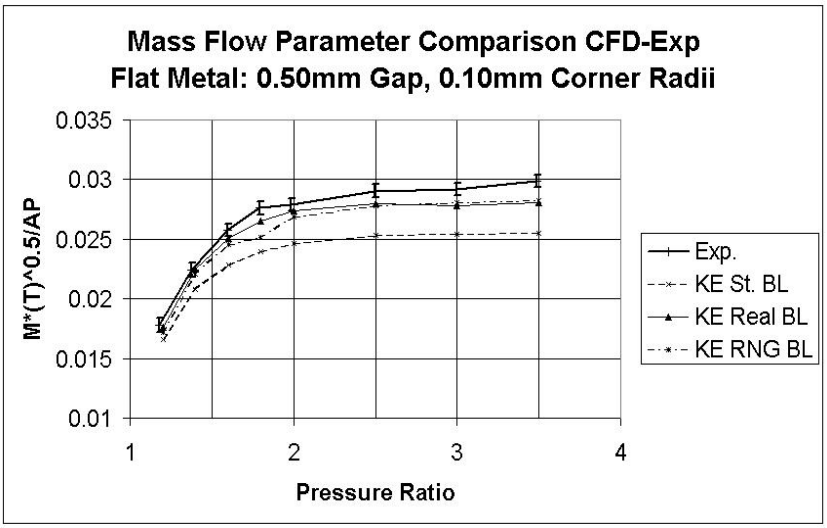

Figure 5.1: $\frac{\dot{m}\sqrt{T_{t(0)}}}{AP_{t(0)}}$ comparison between the experimental data and CFD simulations.

to describe the viscous region were calculated. The results of these simulations can be seen in fig. (5.2). From this figure it is clear that when using the wall function approach the $k-\epsilon$ RNG turbulence model has clear advantages and the modelling complexity introduced by resolving the near wall viscous sub-layer is not required for details on overall seal performance.

To further investigate the suitability of the $k-\epsilon$ RNG turbulence model a comparison of the inter-seal pressure measurements was undertaken. This can be seen in fig. (5.3) for a clearance of $0.50mm$ at a pressure ratio of 3.50. Firstly, CFD has proved capable of predicting the general experimental trends. Further, the CFD data highlights the basic operation of the seal. As the flow accelerates over the teeth the dynamic head of the flow is increased reducing the plane static pressure compared to the wall static pressure. Then, as the flow decelerates into the cavity, the plane static pressure and wall static pressure converge. This also shows that the first and last teeth generate the largest decreases in static pressure. The results for other flat metal cases at $0.50mm$ clearance and other pressure ratios are presented in figs. (F.1) and (F.2).

The agreement between the experimental and CFD data for non-choked cases (pressure ratio ≤ 2.50) is good with typical variations of $\leq 5\%$. The largest variations between the experimental and CFD data are found on the final tooth. Simulations that resolved the near wall viscous sub-layer typically achieve better levels

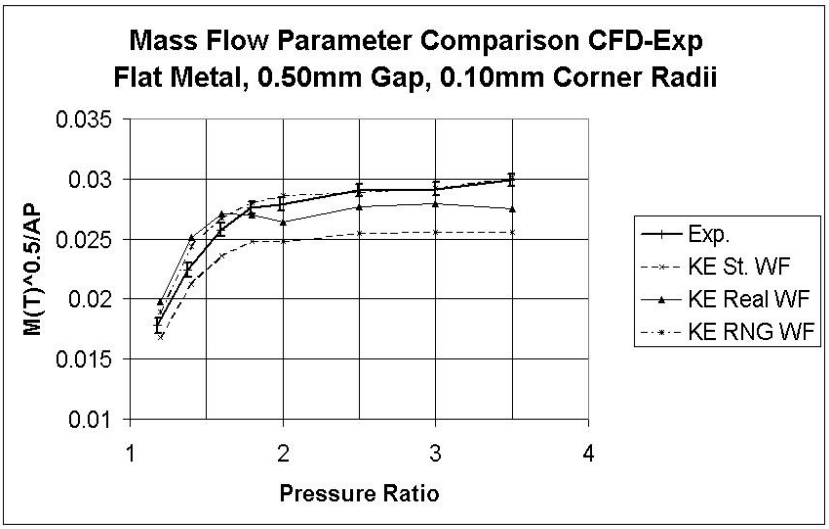

Figure 5.2: $\frac{\dot{m}\sqrt{T_{t(0)}}}{AP_{t(0)}}$ comparison between the experimental data and CFD simulations. Blank metal, $0.50mm$ gap.

of agreement but the improvements are small considering the increased computational cost. As the pressure ratio increases beyond choking the variations between the experimental and CFD data increase, again most noticeably for the final tooth. However, larger variations for the final tooth are expected, particularly at or near choking conditions, due to the formation of shocks. Shock waves cause rapid variations in flow conditions over extremely small distances, the details of which are difficult to accurately replicate using CFD. Therefore, excluding the final tooth, CFD has proved capable of predicting the seal pressure distribution. Further, these simulations have proved capable of predicting overall labyrinth seal performance.

Due to the confidence gained using the $k-\epsilon$ RNG turbulence model further experimental predictions were undertaken for different geometries. At $1.00mm$ clearance the simulated $\left(\frac{\dot{m}\sqrt{T_{t(0)}}}{AP_{t(0)}}\right)$ (fig. (5.4)) using the $k-\epsilon$ RNG turbulence model again had enhanced accuracy when compared to the standard $k-\epsilon$ turbulence model. Typically these variations on overall flow data between CFD and experimental data were $\leq 5\%$ with no significant gains in accuracy by resolving the near wall viscous sub-layer. Further, static pressure variations comparing the experimental and CFD data for the 3.50 pressure ratio case can be seen in fig. (5.5) with further pressure ratios shown in figs. (F.3) and (F.4). For this geometry the simulations that resolved the near wall viscous sub-layer have typically proved more accurate at repeating the experimental inter-seal pressure measurements. Again accurate repetition of exper-

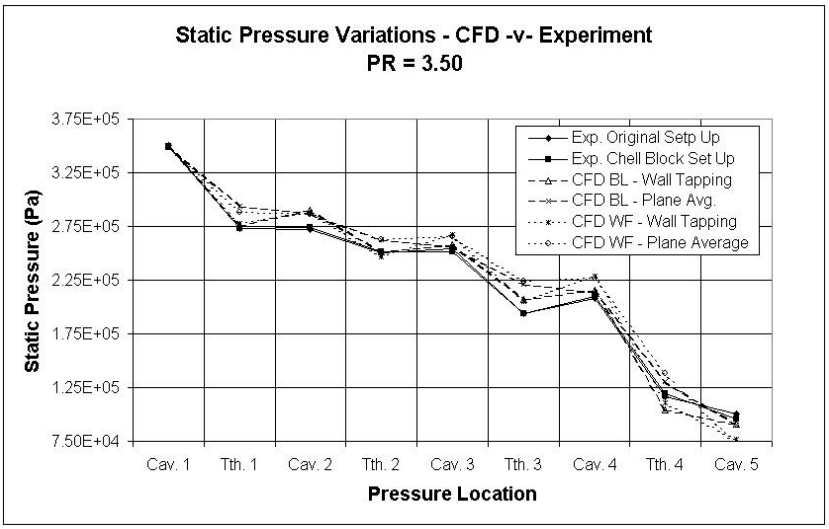

Figure 5.3: Static pressures recorded by both experimental techniques and CFD. Blank metal, 0.50mm gap.

imental data for the final tooth proved troublesome.

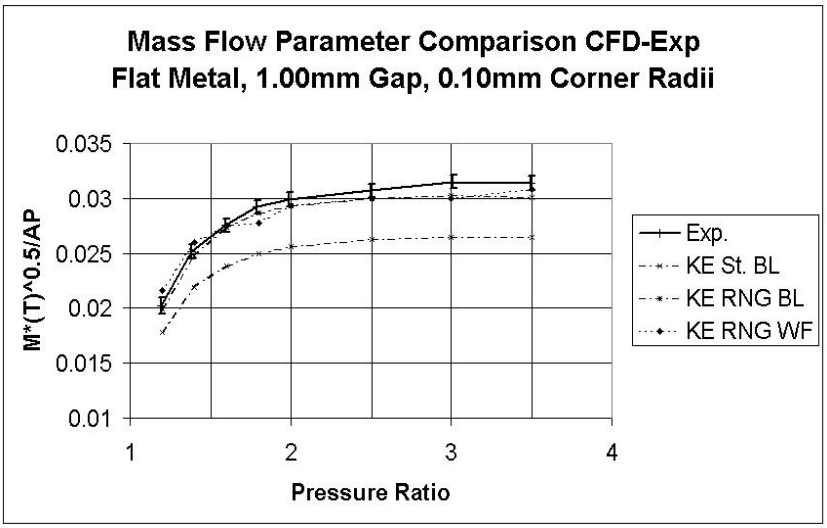

Figure 5.4: $\frac{\dot{m}\sqrt{T_{t(0)}}}{AP_{t(0)}}$ comparison between the experimental data and CFD simulations. Blank Metal, 1.00mm Gap.

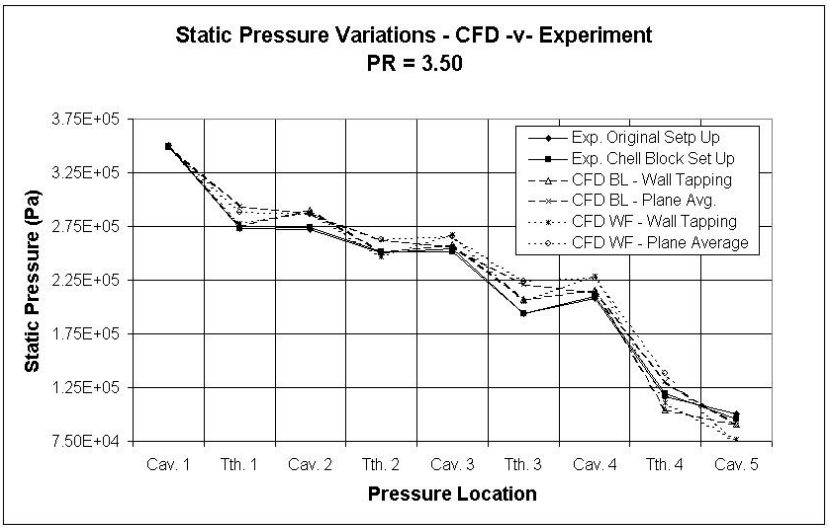

Figure 5.5: Static pressures recorded by both experimental techniques and CFD. Blank metal, $1.00mm$ gap.

Comparisons of $\left(\frac{\dot{m}\sqrt{T_{t(0)}}}{AP_{t(0)}}\right)$ for the $2.00mm$ clearance can be seen in fig. (5.6). When comparing the overall flow characteristics yet again typical variations of $\leq 5\%$ have been obtained with boundary layer resolution making no real impact on the the overall accuracy. However, the accuracy of the calculated static pressure has been enhanced through resolution of the near wall viscous sub-layer. This can clearly be seen for the 3.50 pressure ratio case in fig. (5.7) with further pressure ratios shown figs. (F.5) and (F.6).

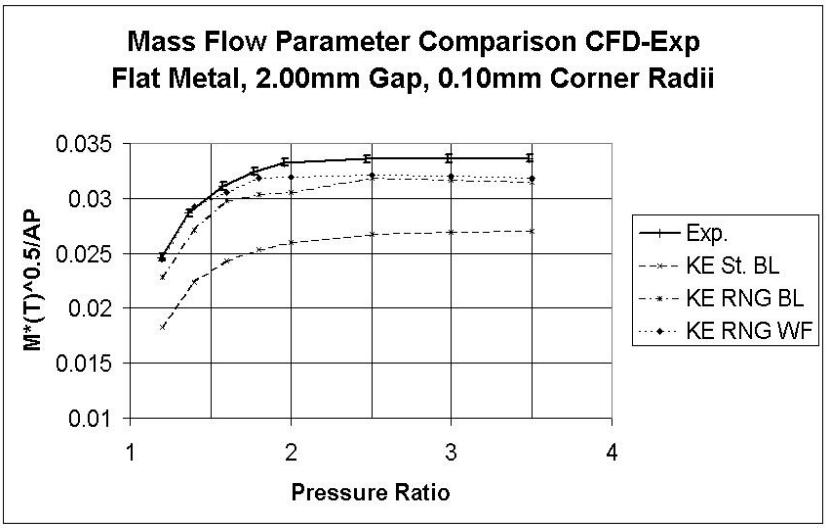

Figure 5.6: $\frac{\dot{m}\sqrt{T_{t(0)}}}{AP_{t(0)}}$ comparison between the experimental data and CFD simulations. Blank metal, 2.00mm gap.

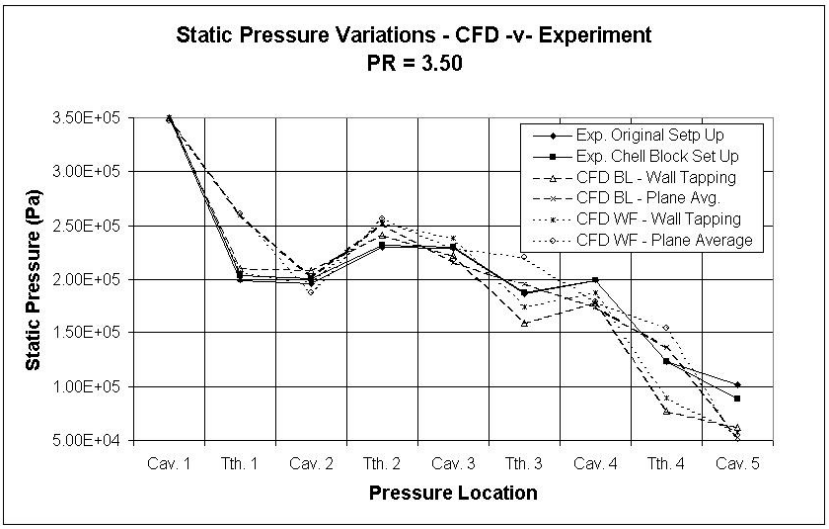

Figure 5.7: Static pressures recorded by both experimental techniques and CFD. Blank metal, 2.00mm gap.

Further insight into the labyrinth seal flow field can be gained by studying contours of Mach number as highlighted for a pressure ratio of 1.80 in fig. (5.8) for all clearances. In each case there is a large acceleration and change of flow direction upstream of the first tooth. For the 0.50mm and 1.00mm case the flow then forms a jet which only partially expands until the final tooth when a full expansion is achieved. For the 2.00mm case the flow separates from the upstream tooth causing further contraction of the jet prior to the next tooth. Therefore the largest accelerations that the flow experiences are upstream of the first tooth and downstream of the last tooth. These accelerations cause larger pressure losses at the first and final teeth. The increased work of the first tooth has been highlighted by Morrison et al. (1988), Zimmermann and Wolff (1987) and Benvenuti et al. (1980). The work undertaken by the final tooth has been highlighted by many authors, including Martin (1908).

More understanding of the labyrinth seal flow field can be gained through fig. (5.9) which shows detailed Mach number contours for each tooth at 0.50mm clearance and a pressure ratio of 2.50. The differences experienced by the first and final teeth can be seen clearly, as can the similarity of the intervening second and third teeth. Further, the downstream side of the first tooth and upstream side of the final tooth share similar flow patterns to the intervening teeth. These Mach number distributions were typical of those found throughout.

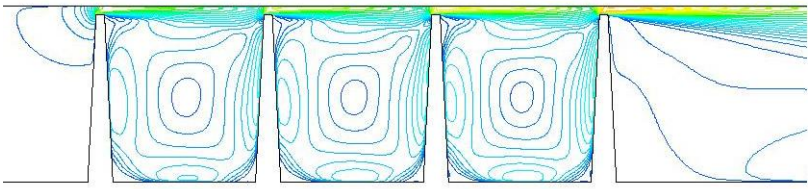

(a) 0.50mm Clearance

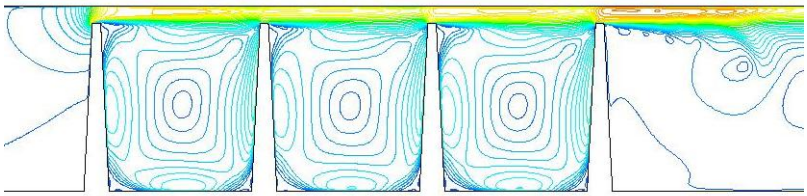

(b) 1.00mm Clearance

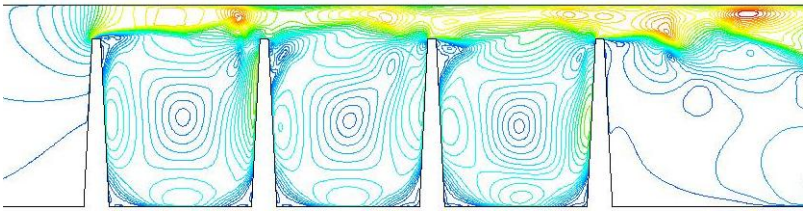

(c) 2.00mm Clearance

Figure 5.8: Mach Number Contours. 1.80 Pressure Ratio. All Clearances. Flow from left to right.

To further analyse labyrinth seal performance velocity profiles were extracted from the CFD simulations. These profiles were aligned with the centreline of each cavity floor static pressure tapping giving 5 velocity profiles for each case. An example of velocity profiles for the 0.50mm clearance at a pressure ratio of 3.50 can be seen in fig. (5.10). The labyrinth teeth are located between y co-ordinates of 0.00m

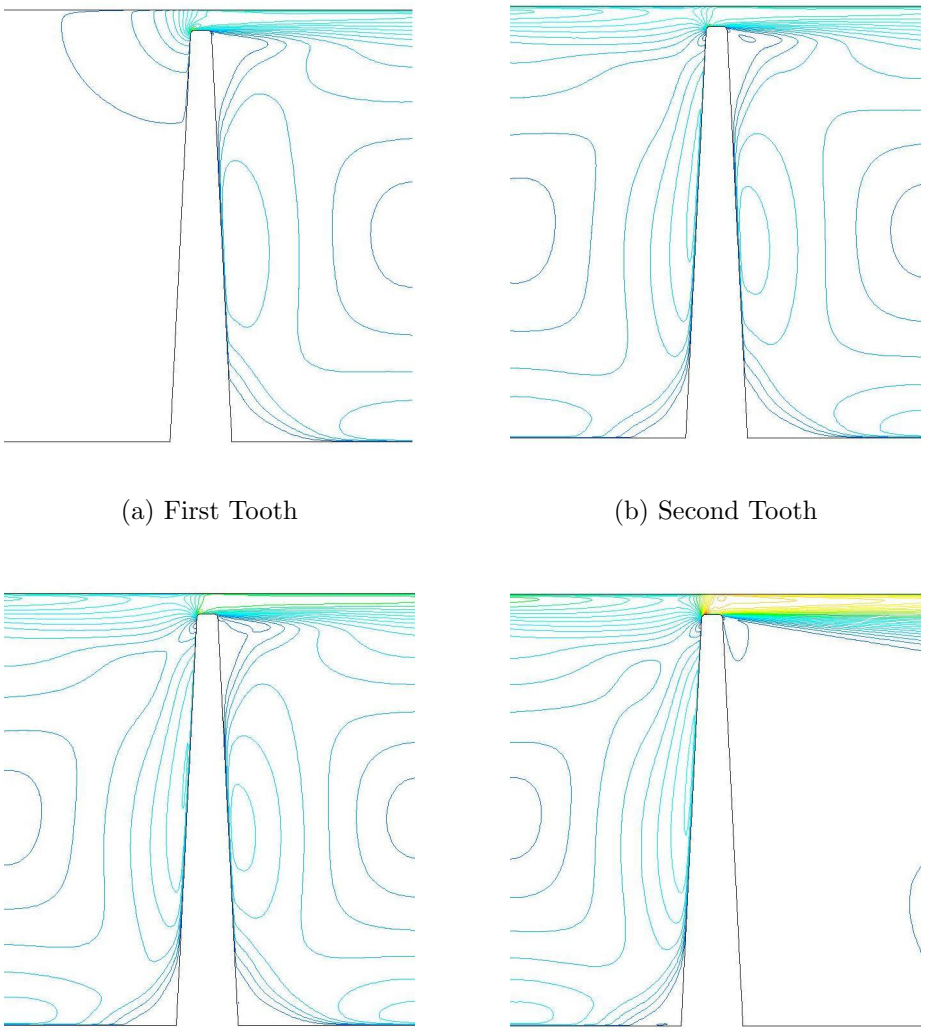

(a) First Tooth

(b) Second Tooth

(c) Third Tooth

(d) Fourth Tooth

Figure 5.9: Mach Number Contours by Tooth at a Pressure Ratio of 2.50. Blank metal, $0.50mm$ gap. Flow from left to right.

to $0.01m$ with the gap located at a y co-ordinate of $0.01m$ upwards.

The entrance profile has a velocity profile that has a uniform gradient across the section with a significantly lower magnitude than the other profiles, even for this high pressure ratio case. The first, second and third cavity profiles clearly show the

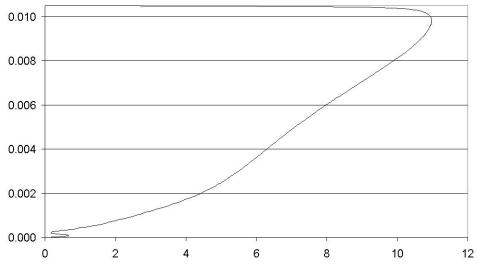

(a) 5.00mm Upstream of First Tooth

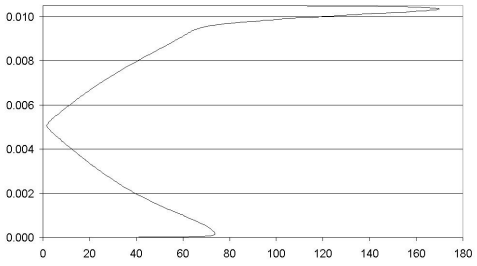

(b) Middle of First Cavity

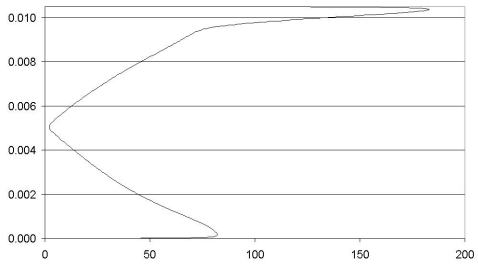

(c) Middle of Second Cavity

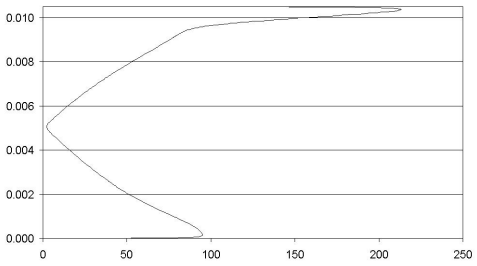

(d) Middle of Third Cavity

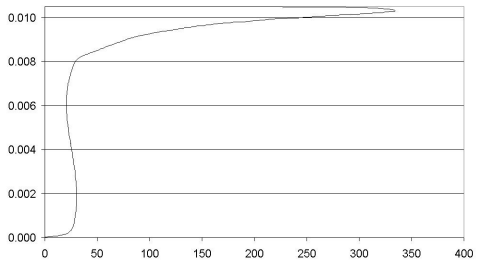

(e) 5.00mm Downstream of Final Tooth

Figure 5.10: Velocity Profiles by Cavity Location. Blank metal, 0.50mm gap PR = 3.50. $X - Axis$: Velocity $\left(\frac{m}{sec}\right)$, $Y - Axis$: Y Position (m)

effect of the jet, which is primarily carried over, and the recirculating cavity flow, which stagnates at the centre of the cavity. After the final tooth a full expansion and rapid equalisation is achieved. Further, the velocity in the jet can be seen to increase as the flow passes though the seal with the exit velocity profile showing the highest velocity. This is then dissipated downstream of the seal. These large accelerations and changes of flow direction upstream and downstream of the seal correspond to the largest pressure drops at the first and last teeth. With confidence gained in being able to predict labyrinth seal flow fields with reasonable accuracy further analysis on the primary loss coefficients for the blank metal case was undertaken.

5.2 Loss Coefficients

The primary method of describing labyrinth seal performance is to use the loss coefficients of C_d and COF. Various definitions exist for COF as highlighted in chapter (2) although generally there is only one accepted formulation of C_d as shown in eqn. (3.1). The primary difficulty in using these loss coefficients is the level of inaccuracy that they introduce due to the underlying assumptions used in their derivation. This is particularly true because effects due to the two loss coefficients are very difficult to separate. Therefore, using the current experimental and numerical data, this section will compare different approaches to calculating these loss coefficients.

5.2.1 Carry Over Formulation

The first author to highlight the effect of COF was Egli (1935). The COF was treated in a manner that effectively reduced the number of knives in the seal. The COF was found to increase with clearance to pitch ratio and number of teeth, having a minimum value of unity by definition. Hodkinson (1939) was the first author to treat the flow downstream of a restriction as an expanding jet in which he assumed a constant angle of expansion of 1°. Vermes (1961) further developed the labyrinth seal understanding including that of COF. The mass flow equation derived can be seen in eqn. (B.4) with the COF, which is purely based on geometry, defined as shown in eqn. (B.5). For the current geometry this formulation of COF gives 0.325, 0.509 and 0.711 respectively for the three clearances of $0.50mm$, $1.00mm$ and $2.00mm$. Whilst the COF as defined produces values less than one for the majority of geometrical situations the actual effect that COF has on the overall mass flow is to increase the actual mass flow as can be seen in eqn. (5.1). The COF, as defined by Vermes, had no influence on the calculation of $\dot{m}_{ID}$ (see eqn. B.4).

$$\dot{m}_{ACT} \propto \frac{1}{\sqrt{1 - COF^2}} \tag{5.1}$$

Komotori and Miyake (1977) analysed the kinetic energy carry over by highlighting the differences found between ideal and actual mass flows. Further, a method to calculate seal performance on a tooth by tooth basis was presented by assuming a value for C_d equal to 0.85 for each tooth. Theoretical values of COF based purely upon geometry and operating conditions can be seen in table (5.1) both for non-choked and choked cases.

This approach was further developed by Benvenuti et al. (1980). They derived seal performance dependent upon flow velocity, geometry and pressure ratio. The

C(mm)	$\frac{Cl*C_d}{Ph}$	COF	COF_{Crit}
0.50	0.043	1.2	1.1
1.00	0.086	1.4	1.125
2.00	0.172	1.6	1.3

Table 5.1: Graphically derived COF from Komotori and Miyake (1977)

starting point for the analysis of COF came from Vermes (1961) with modifications included using the Komotori and Miyake (1977) method.

McGreehan and Ko (1988) numerically modelled COF using a different approach as defined in eqn. (2.8). Shapiro and Chupp (2004) did not try to model the carry over directly preferring model the flow as a jet with an expansion angle. The geometric expansion area ratio was used as the foundation of an equivalent total pressure loss coefficient. This can be seen in eqn. (5.2) where (δ_e) represents the geometric expansion of the jet.

$$\Delta\left(P_t\right) = \left(1 - \frac{Cl}{Cl + \delta_e}\right)^2 \left(P_{t(n-1)} - P_{s(n-1)}\right) \tag{5.2}$$

Allcock (1999) used the same approach as that of McGreehan and Ko (1988) to calculate COF using CFD. These were latterly included in a 1-D computer code, THESEUS.

Of these techniques there are two distinct approaches to calculating COF. Firstly the technique developed by McGreehan and Ko (1988) and latterly used by Allcock (1999) shares similarities with that used by Shapiro and Chupp (2004) and Vermes (1961). These methods do not compute the effect of COF using mass flow directly preferring instead to model the effects of COF on pressure loss through the seal. Further, the first two approaches base COF on pressure distribution within the seal whilst the last two approaches base COF on geometry. Results using these approaches are compared in fig. (5.11). As can be seen the approaches of Allcock et al. (THESEUS) and Shapiro and Chupp (KTK) agree very well, with the results of Vermes being quite different. However, this difference is primarily due to the fact that Vermes derived the COF for the whole seal, analysing all of the cavities at once. The two other methods employed COF on a tooth by tooth basis with each tooth contributing an effect. If the Vermes approach is analysed on a tooth by tooth basis, by splitting the loss into 3 equal portions, equivalent COF of 0.69, 0.79 and 0.89 are found for the three clearances of $0.50mm$, $1.00mm$ and $2.00mm$. This step makes the three methods very similar. Interestingly, the only method of these three that include pressure ratio effects is Allcock et al. and these effects can be seen to

be marginal.

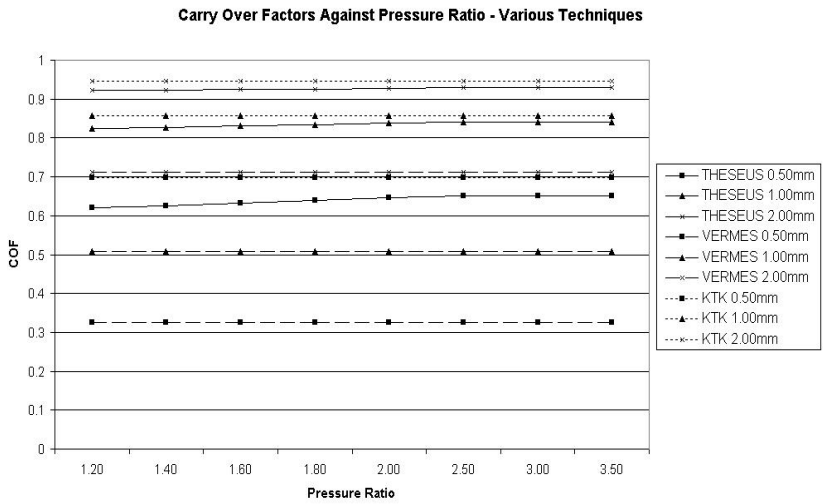

Figure 5.11: Calculated COF using various techniques.

The second technique, based on mass flow differences, was primarily developed by Komotori and Miyake (1977) with further work undertaken by Benvenuti et al. (1980). Komotori and Miyake (1977) assumed a C_d value for each tooth of 0.85 and treated the flow in the expansion phase as a jet that expanded along a 6° line. Benvenuti et al. (1980) relaxed the assumption of a constant C_d by combining the work of Vermes (1961) with effects due to an approaching flow velocity thus enabling simultaneous calculation of C_d and COF.

In order to further compare COF these different techniques were applied to the current study. The approach of McGreehan and Ko (1988) was applied first. The results for the $0.50mm$ case are shown in fig. (5.12). As can be seen the calculated values of COF exceed unity which is unexpected (see fig. (5.11)). Further, there is an unexpected and noticeable difference due to cavity number, with the final cavity (cavity 3) returning significantly larger values. Additionally, a pressure ratio effect is noticeable until choking occurs. Whilst unexpected, root causes of these effects have been highlighted previously (see fig. (5.10)) with the increase of jet velocity through the seal. This is in contrast to the theoretical performance of McGreehan and Ko (1988) which states that the dynamic head and pressure decrease through the seal. For the current experiment the dynamic head actually increases whilst the pressure decreases. Results very similar to these were repeated at $1.00mm$ clearance.

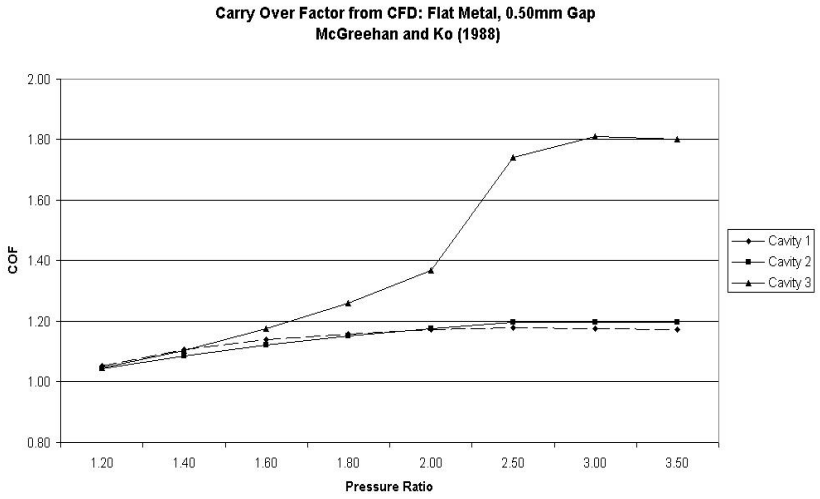

Figure 5.12: COF from CFD simulations using the technique of McGreehan and Ko (1988). Blank Metal, $0.50mm$.

The COF calculated using the approach of Komotori and Miyake (1977) can be seen in fig. (5.13). Again the results calculated using this approach are very different from the theoretical values highlighted in table (5.1). There are marked effects due to cavity location and due to pressure ratio that theoretically have not been accounted for. This implies that the modelling assumptions used to develop this technique are not entirely applicable in this case. Primarily this is due to assuming a constant C_d irrespective of tooth location. This fails to take into account velocity and pressure loss effects that have been highlighted previously. Further, for similar reasons, the assumption of a constant expansion angle is also questionable.

The method of Benvenuti et al. (1980) corrects the calculated mass flow to account for the upstream velocity thus enabling independent calculation of C_d and COF on a tooth by tooth basis. Firstly, the ideal mass flow, the mass flow that exists in the absence of C_d and COF, is calculated. This is then adjusted to account for the non-ideal nature of the flow and the velocity approaching the teeth. Using this approach for the current data at $0.50mm$ clearance returns similar values for C_d and COF of approximately unity. However, this is the only publication that uses inter-seal pressure measurements in a similar manner to that used in the present study. Therefore in the publication C_d has been reported on a tooth-by-tooth basis and has been shown to exceed unity dependent upon tooth location and tooth pressure ratio. However, C_d by definition cannot exceed unity as the ideal flow does not encounter any losses. This is a prime example of the difficulty in separating the

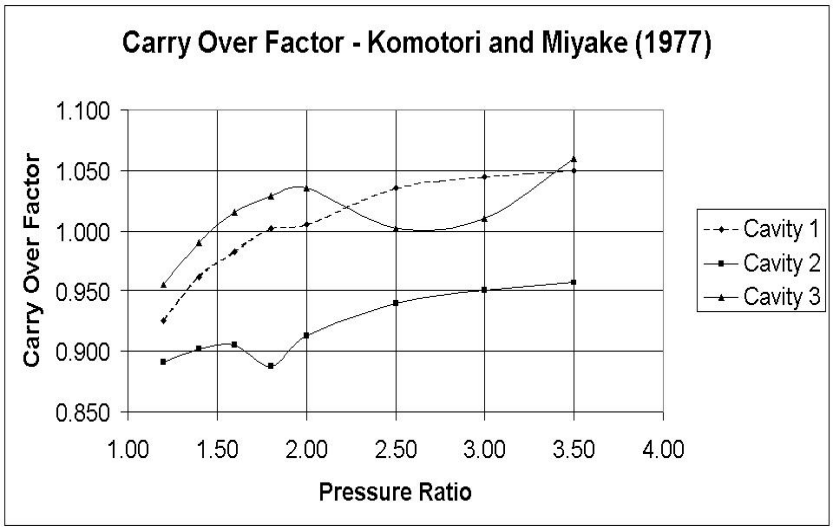

Figure 5.13: Calculated COF using technique of Komotori and Miyake (1977). Blank Metal, 0.50mm Gap.

combined effects of C_d and COF and therefore using this approach in the reported format is not valid.

Whilst both of these approaches have their limitations these do not become fully apparent until trying to analyse other clearances. Both methods calculate seal performance using overall pressure ratio and tooth pressure ratio. Additionally, both methods assume a pressure reduction after each tooth. However, as already highlighted the first and last tooth recorded larger pressure losses than the intervening teeth. This can be seen clearly through the seal pressure distributions as highlighted in fig. (3.8) for example. As can be seen with increasing clearance the pressure reduction due to the first and final teeth grows with the intervening teeth experiencing less pressure drop across them. Both methods fail to account for this variation in pressure drop due to tooth location. Therefore, it can only be concluded that available techniques to calculate the seal loss coefficients are inadequate to describe the current study. Further, the importance of COF has been highlighted previously by Rhode and Guidry (1993a), who found that by enhancing through flow deflection benefits of up to 20% can be found, Vakili et al. (2005) who recorded benefits using a flow deflection block located on the stator and Denekce et al. (2002), who highlighted that at positive clearances COF is the dominating factor.

5.3 Simulation of Experimental Results: Existing Labyrinth Computer Codes

Direct comparison between experimental data and theoretical seal calculation routines have proved inconclusive. However, several complete labyrinth seal calculation packages based on some of the highlighted theories are also available. The author has used two of these packages, KTK and THESEUS, developed by Shapiro and Chupp (2004) and Allcock (1999) respectively. Further comparisons of the current data against these pre-existing codes was undertaken. Primarily the codes have been designed around inputs of geometric data and pressure boundary conditions, calculating the actual mass flow. For this study the KTK code has been modified to enable a direct calculation of seal performance using a specified mass flow and an iterative calculation for seal performance using pressure boundary conditions. Further, due to the level of experimental-numerical agreement achieved the code was modified to accept either CFD derived expansion angles or expansion angles as calculated in the code. Both codes were verified against known datasets prior to any comparisons with the current data. Results comparing $\left(\frac{\dot{m}\sqrt{T_{t(0)}}}{AP_{t(0)}}\right)$ between the experimental data, THESEUS and KTK at $0.50mm$ clearance can be seen in fig. (5.14) with results for clearances of $1.00mm$ and $2.00mm$ available in figs. (F.7) and (F.8) respectively. The KTK code for this figure has been run iteratively using pressure boundary conditions with internally calculated flow expansion angles (KTK Iterative Ang. 1) as well as expansion angles that have been derived from CFD (KTK Iterative Ang. 2).

As can be seen across the three clearances THESEUS predicts the experimental data best. However, even this code only achieves agreement of 10-20%. Further, at $0.50mm$ clearance THESEUS under-predicts mass flow compared to the experimental measurements but at $1.00mm$ and $2.00mm$ over-predicts. KTK, whilst inaccurate in this iterative mode of operation, is capable of using mass flow as an input. Comparison of the pressure distribution as highlighted by all of these techniques can be seen in fig. (5.15) for a clearance of $0.50mm$ and pressure ratio of 3.50. This is typical of the seal static pressure variations (variations between the experimental data and investigated techniques) recorded using these techniques at other pressure ratios and clearances.

Firstly, this figure shows that the computer codes predict inlet static pressure losses that were not recorded experimentally. Secondly, the computed seal static pressure distributions do not follow the trend of the experimentally measured values. Further, when using the KTK code with a mass flow inlet (KTK Ang. 1 and KTK Ang. 2) larger pressure losses are predicted than recorded experimentally.

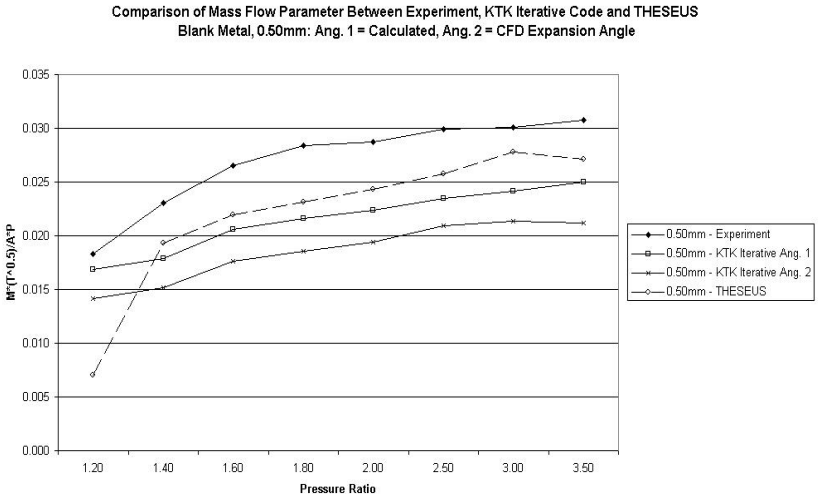

Figure 5.14: Comparison of $\left(\frac{\dot{m}\sqrt{T_{t(0)}}}{AP_{t(0)}}\right)$ between Experiment, THESEUS and KTK at $0.50mm$ clearance. KTK in iterative mode with two angles: Ang. 1 as per internal code calculation, Ang. 2 derived from CFD.

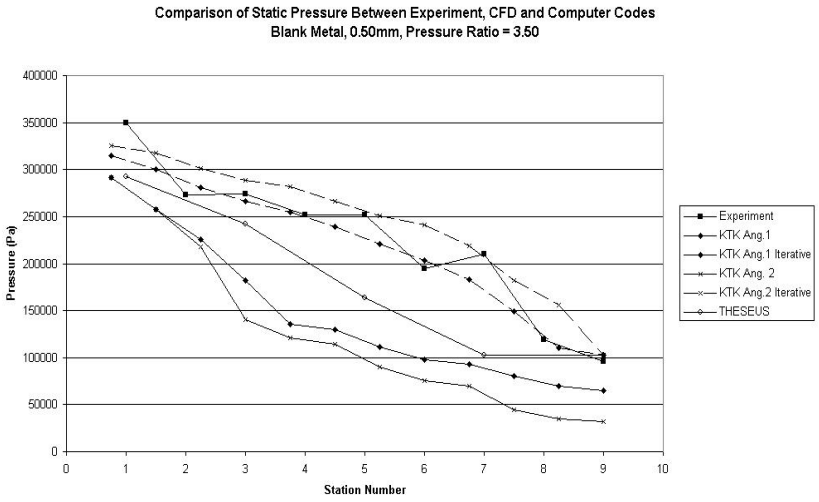

Figure 5.15: Comparison of Static Pressure Distribution between Experiment, THESEUS and KTK at a Pressure Ratio of 3.50 and $0.50mm$ Clearance. KTK in iterative and non-iterative mode with two angles: Ang. 1 as per internal code calculation, Ang. 2 derived from CFD.

However, when using pressure boundary conditions (KTK Iterative Ang. 1 and KTK Iterative Ang. 2) a better seal pressure distribution was achieved although at the expense of poor mass flow predictions (for example see fig. (5.14)). This shows that the KTK code over-predicted the experimentally recorded losses. The pressure distribution recorded by THESEUS also fails to predict the larger pressure drops recorded over the first and final teeth experimentally. This comparison has shown that existing computer codes are unable to predict the experimentally recorded performance of the labyrinth seal. Therefore further analysis of the experimental data shall only be undertaken using CFD.

5.4 Simulation of Experimental Results: Unworn Honeycomb

To ease the computational requirements the 2-D simplification technique developed in section (4.6) was used to analyse honeycomb surfaces using CFD. A similar process to that used for the blank metal cases was undertaken. This involved analysing the flat honeycomb surfaces prior to undertaking inter-seal static pressure comparisons. The results of $\left(\frac{\dot{m}\sqrt{T_{t(0)}}}{AP_{t(0)}}\right)$ and static pressure distribution for the $0.50mm$ clearance can be seen in figs. (5.16) and (5.17) respectively. Further static pressure comparisons at different pressure ratios can be viewed in figs. (F.9) and (F.10).

As can be seen at $0.50mm$ clearance the level of overall agreement (fig. (5.16)) attained when using the $k-\epsilon$ RNG turbulence model is very good, with near wall viscous sub-layer resolution making no real impact on the overall accuracy. Comparing the inter-seal static pressure distribution good agreement has been attained across all examined pressure ratios. Again, simulation of the final tooth static pressure at choking conditions proved the most difficult. Equivalent figures for $1.00mm$ clearance can be seen in figs. (F.11) through (F.13). As can be seen the number of modelling approaches used had been simplified due to the confidence gained at $0.50mm$ clearance. The level of overall agreement is still very good, typically within 5%. However, differences in the inter-seal static pressure measurements are becoming apparent. This is particularly true at the locations of the labyrinth teeth. However, compared to predictive methods previously examined the form of the pressure distribution calculated is accurate in comparison. Simulations at $2.00mm$ were tried using various different techniques (coupled and segregated solver, $k-\epsilon$ and $k-\omega$ turbulence model) but often displayed convergence difficulties. Solutions within 20% of experimental data across a range of pressure ratios proved unattainable. This was due to the turbulence caused by the honeycomb surface, the effect

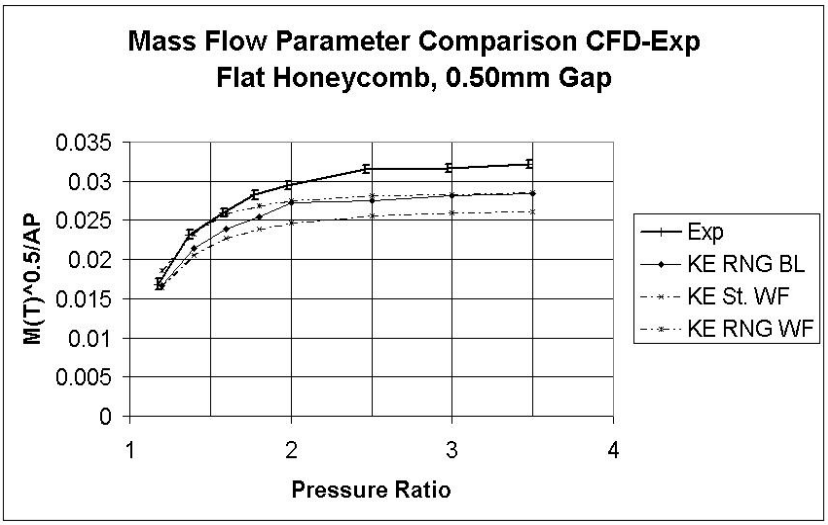

Figure 5.16: $\left(\frac{\dot{m}\sqrt{T_{t(0)}}}{AP_{t(0)}}\right)$ comparison between the experimental data and CFD simulations.

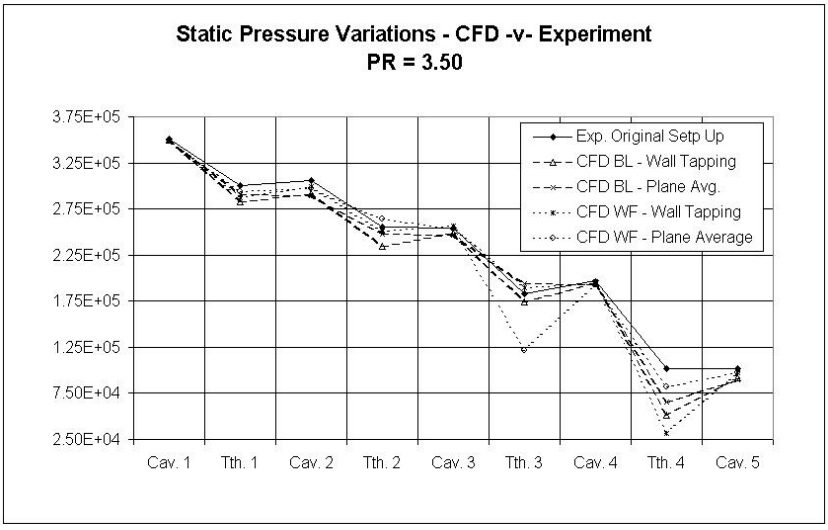

Figure 5.17: Static pressures recorded by both experimental techniques and CFD. Flat Honeycomb, 0.50mm gap.

of which grew with clearance. This effect can be seen in fig. (5.18) which highlights Mach number contours with worn honeycomb lands at a range of clearances. It can be seen that at 2.00mm clearance large flow disturbances can be seen, particularly

in comparison to the smaller clearances. Further, this increased flow disturbance at $2.00mm$ clearance has been highlighted previously in fig. (5.8) when using flat metal. Therefore simulations at $2.00mm$ using honeycomb were discontinued.

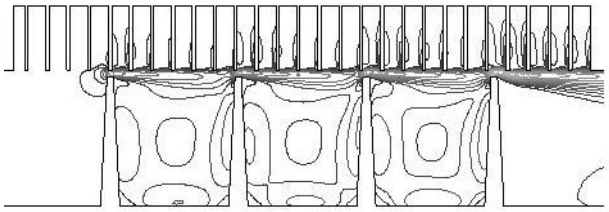

(a) 0.50mm Clearance

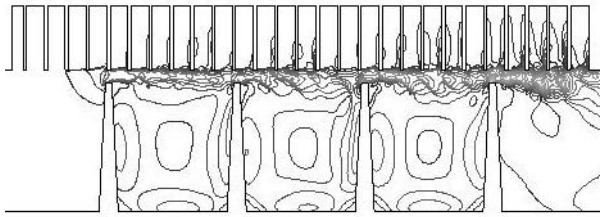

(b) 1.00mm Clearance

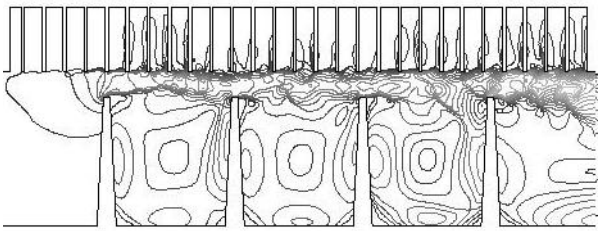

(c) 2.00mm Clearance

Figure 5.18: Mach Number Contours when using Flat Honeycomb. 2.50 Pressure Ratio. All Clearances. Flow from left to right.

5.5 Simulation of Experimental Results: Worn Honeycomb

Comparisons between worn honeycomb experimental results and their equivalent numerical simulations were undertaken at clearances of $0.50mm$ and $1.00mm$. The overall results of these simulations can be viewed in figs. (5.19) and (F.15) for clearances of $0.50mm$ and $1.00mm$ respectively. Flat honeycomb experimental results have been included throughout to aid comparison. Simulations were only undertaken with the teeth in the central position with respect to the groove.

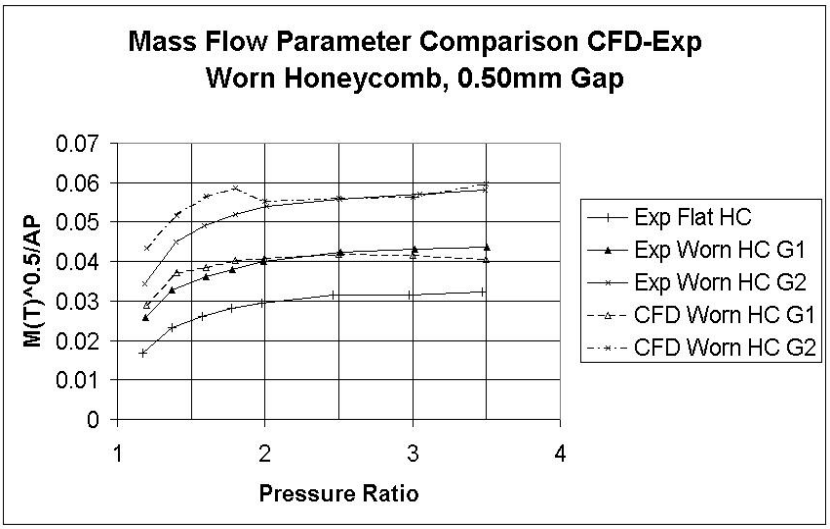

Figure 5.19: Worn Honeycomb Comparison of $\left(\frac{\dot{m}\sqrt{T_{t(0)}}}{AP_{t(0)}}\right)$ at $0.50mm$ Clearance.

As can be seen at $0.50mm$ clearance the level of agreement is very good but at $1.00mm$ the variation increases. Throughout, the worn honeycomb lining, compared to the unworn honeycomb, has had a significantly detrimental effect on the overall seal performance. At $0.50mm$ clearance the overall effect is much more marked, with the $\left(\frac{\dot{m}\sqrt{T_{t(0)}}}{AP_{t(0)}}\right)$ increasing by nearly 50% and 100% compared to the experimental unworn honeycomb values for the G1 and G2 conditions respectively. The overall effect on the Mach number distribution for both clearances and both sizes of groove can be seen in fig. (5.21). Comparing the G1 and G2 wear profiles clearly shows that for the G1 condition the jet created by the labyrinth teeth is smaller and forced significantly closer to the honeycomb surface causing more flow-honeycomb interaction. With the larger wear profile, G2, the flow can clearly be seen to snake

through the labyrinth seal with much less honeycomb surface interaction.

Further comparison of the recorded inter-seal pressure measurements can be seen in figs. (5.20) and (F.17) for the G1 worn honeycomb at clearances of $0.50mm$ and $1.00mm$ respectively, with comparisons of the G2 worn condition available in figs. (F.16) and (F.18). These figures show a good level of agreement between the experimental and numerical data, with the largest variations again found at the highest pressure ratios. Interestingly, the largest variation overall has been found when predicting the $1.00mm$ clearance using the G1 honeycomb. However, this can be explained by referring to fig. (5.21). This highlights the increased level of flow disturbance found in comparison to the G2 condition at $1.00mm$ making this simulations computationally more demanding. However, overall the level of agreement achieved is good, particularly when considering the simplification technique used.

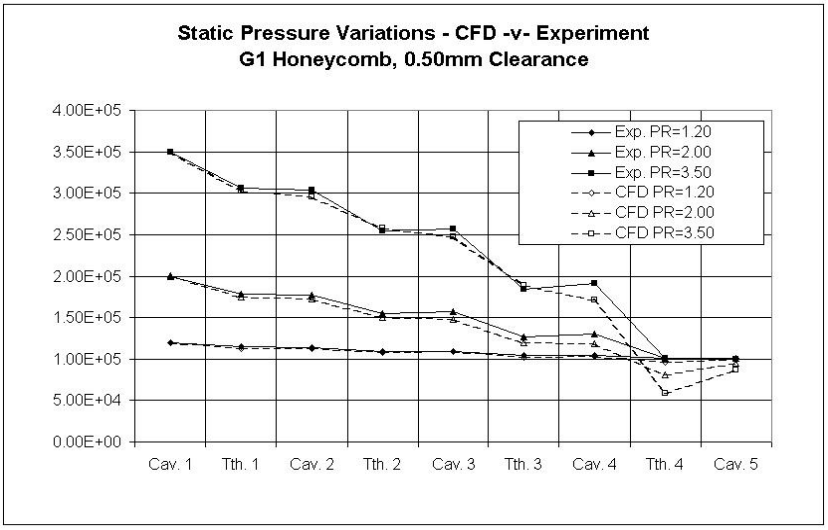

Figure 5.20: Static Pressure Comparison Between Experimental Data and CFD with G1 worn Honeycomb at $0.50mm$. Various Pressure Ratios.

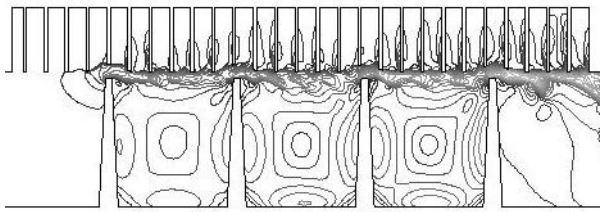

(a) 0.50mm Clearance. G1 Honeycomb

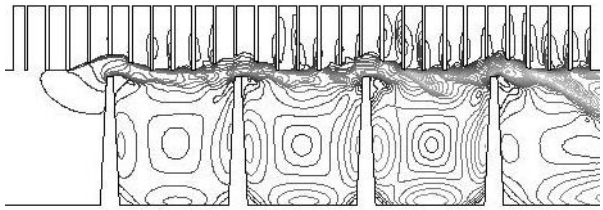

(b) 0.50mm Clearance. G2 Honeycomb

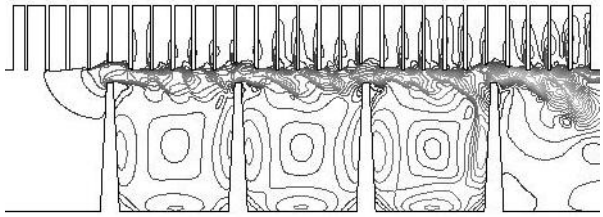

(c) 1.00mm Clearance. G1 Honeycomb

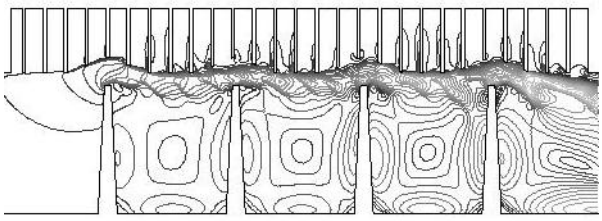

(d) 1.00mm Clearance. G2 Honeycomb

Figure 5.21: Mach Number Contours when using worn Honeycomb. 2.50 Pressure Ratio. Flow from left to right.

5.6 Simulation of Rotational Effects

As the experiment did not include rotational effects 2-D CFD was used to examine the impact of rotational effects. Two rotational velocities, 400 $\left(\frac{rad}{sec}\right)$ and 800 $\left(\frac{rad}{sec}\right)$, at a radius of $300mm$, were appropriately applied to the blank metal CFD simulation with clearances of $0.50mm$ and $1.00mm$. This gave ratios of bulk fluid velocity (1-D calculation only which assumed the geometric and effective area are equal) to surface speed of 0.65 - 1.1 and 0.3 - 0.55 for the 400 $\left(\frac{rad}{sec}\right)$ and 800 $\left(\frac{rad}{sec}\right)$ cases respectively. No rotational CFD simulations using honeycomb were undertaken because it is impossible to use the developed 2-D simplification technique realistically as each honeycomb cell would form an annular cavity. However, it is noted that honeycomb significantly reduces the development of swirl velocity so less rotational effects would be found near to the stationary surface with a honeycomb surface. For the analysed cases rotational effects were found to marginally improve the overall labyrinth seal performance compared to the stationary cases which agrees well with work highlighted in chapter (2). These recorded improvements in overall seal performance deteriorated with increased rotational velocity. At 400 $\left(\frac{rad}{sec}\right)$ reductions in $\left(\frac{\dot{m}\sqrt{T_{t(0)}}}{AP_{t(0)}}\right)$ of up to 10% and 15% were recorded for the $0.50mm$ and $1.00mm$ clearance respectively. At 800 $\left(\frac{rad}{sec}\right)$ reductions of up to 5% were recorded for both clearances, and only then at the higher pressure ratios studied. An explanation for this effect can be seen by looking at the velocity vectors recorded by the rotational simulations as shown for both clearances in fig. (5.22). The pumping action of the rotating downstream face of each tooth is seen to create further contraction downstream of the labyrinth teeth decreasing the expansion into the labyrinth cavity and increasing the COF. The mass that circulates around the labyrinth seal cavities is also reduced. The combination of these effects is more pronounced at $0.50mm$.

However, when studying rotating labyrinth seals further interesting inter-seal pressure effects were recorded, particularly at $0.50mm$ clearance where a more gradual pressure drop was found through the seal. At $1.00mm$ this gradual pressure reduction disappeared. This can be seen in figs. (5.23) and (5.24) for the $0.50mm$ and $1.00mm$ clearance respectively.

A detailed analysis of these rotational effects was not undertaken in the current study but would prove a fruitful area of future research. This work should include studying the effects of the pumping action due to the downstream face of the labyrinth tooth on the labyrinth seal flow and also study the possibility of an optimum labyrinth cavity size.

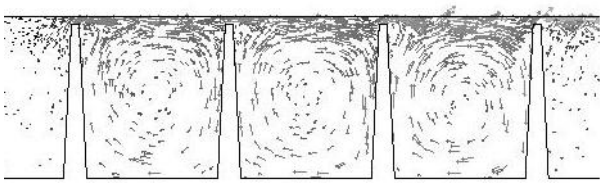

(a) 0.50mm Clearance.

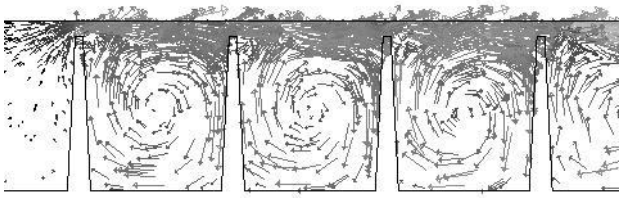

(b) 1.00mm Clearance.

Figure 5.22: Velocity Vectors at Pressure Ratio of 2.00 with a Rotational Velocity of 400 $\left(\frac{rad}{sec}\right)$.

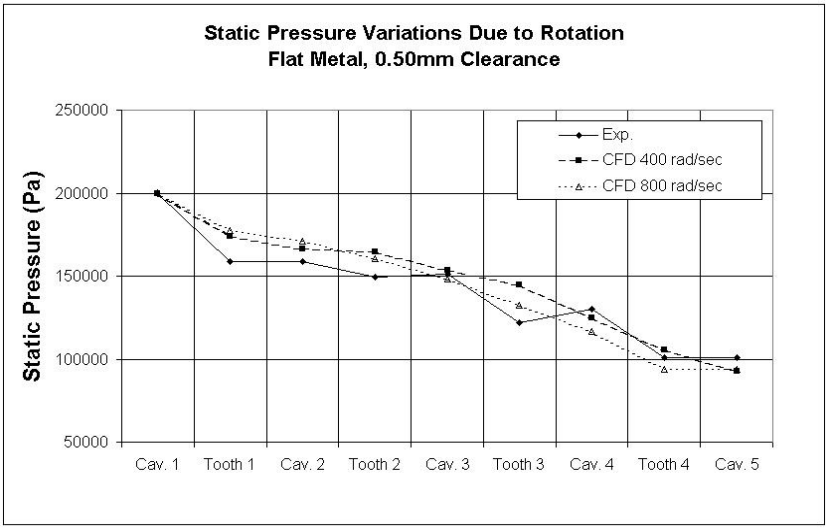

Figure 5.23: Static Pressure Comparison Between Experimental Data and CFD with rotation. $0.50mm$ Clearance, PR = 2.00.

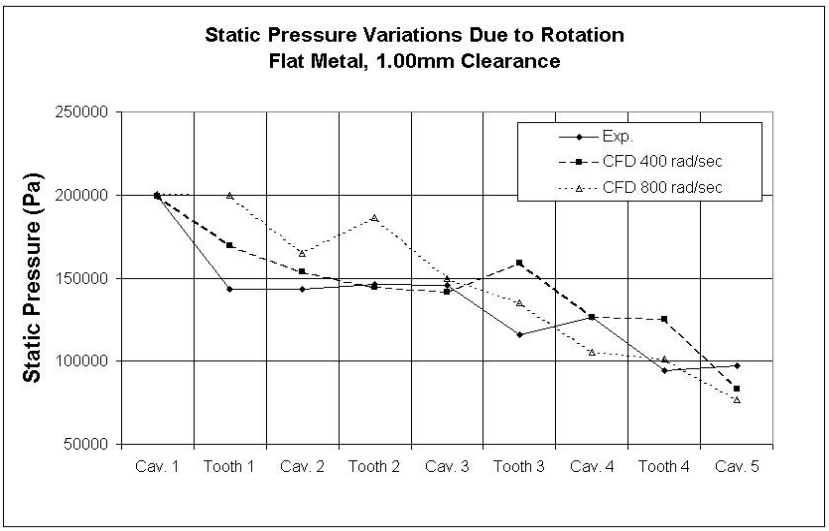

Figure 5.24: Static Pressure Comparison Between Experimental Data and CFD with rotation. $1.00mm$ Clearance, PR = 2.00.

5.7 Conclusions

Numerical analysis of the experiment using theoretical derivations has highlighted several key areas where assumptions previously used to develop labyrinth seals have proved insufficient at including a complete representation of labyrinth seal flow physics. Firstly, the inter-seal pressure distribution was calculated numerically, but only with sufficient accuracy when using CFD. The other techniques used to predict the inter-seal pressure measurements assumed a gradual reduction of pressure through the seal, which was not found experimentally or numerically using CFD. Only when rotational effects were modelled using CFD did the pressure reduction through the seal reduce gradually but only at one clearance, $0.50mm$. This is therefore an area were further work needs to be undertaken.

Additionally, the current understanding and use of loss coefficients, including computer codes based upon them, has proved incapable of calculating labyrinth seal performance accurately, including seal pressure distribution. The most accurate of the investigated methods was that of Allcock (1999) who created THESEUS. The recorded deviations are because the examined techniques have not adequately separated the effects of C_d and COF. This can be easily found by examining the literature. Komotori and Miyake (1977) assumed a constant C_d and Benvenuti et al. (1980), with this assumption relaxed, experimentally recorded C_d that exceeded unity. Further, Allcock (1999) calculated single tooth loss coefficients based upon analysis of the whole seal as one unit. Equally, of the techniques investigated, none has found effects due to tooth location and pressure ratio as highlighted in the current study.

Furthermore, the 2-D simplification technique used in CFD to model the honeycomb has proved accurate, both for unworn and worn honeycomb. This greatly enhances the computational ability of future investigations into honeycomb labyrinth seal flow fields.

Finally, rotation was seen to have a marginally beneficial effect independent of rotational velocity on the overall seal performance compared to the stationary cases. This is what has been recorded previously by Komotori and Miyake (1977), Miyake and Duh (1990) and He et al. (2001) amongst others. However, Waschka et al. (1990) did record performance improvements under laminar conditions that deteriorated under turbulent conditions and McGreehan and Ko (1989) only recorded increases in windage heating. Further, different seal pressure distributions were also recorded. However, this section of the current study has proved inconclusive due to lack of depth. Therefore this an area for future work to be undertaken.

Numerical modelling of the labyrinth seal flow field has highlighted that CFD, using the highlighted modelling techniques, is the most accurate numerical method available. CFD has proved capable of predicting overall performance and inter-seal pressure distributions, both for the flat metal, flat honeycomb and worn honeycomb conditions. The areas of greatest uncertainty in the CFD simulations are when choking occurs, which is to be expected. The other techniques investigated, using loss coefficients and using computer codes, both were incapable of accurately predicting the current study. However, both of these techniques aid the designer's understanding of labyrinth seal flow fields with significantly reduced costs and time (Hirano et al. (2003)). Therefore use of these techniques is still valid as long as the designer is aware of the assumptions, and therefore limitations, that they have.

Chapter 6

Research Impact

6.1 Introduction

The technical demands that have been placed on the performance of the internal sealing components of a gas turbine have come from the desire to operate gas and steam turbines more efficiently. Primarily these demands have been market driven by companies facing increased fuel bills, higher operating costs and therefore lower profits. Increasingly these demands are politically driven as shown by the development of the Kyoto Protocol governing CO_2 emissions. For example, the UK government has committed to a 60% reduction in CO_2 emissions by 2050 (DTI (2003)) whilst the US federal government, a non-signatory, has a goal of reducing greenhouse gas intensity $\left(\frac{Emissions}{GDP}\right)$. Whilst these demands do not directly impact the internal system of a turbine engine, the desire to operate equipment at higher efficiencies does. This leads to a requirement for cycles operating at higher pressures, temperatures and sliding speeds, all with improved reliability. For these advancements in turbine design to be maintained the internal sealing system needs to be able to keep pace with these developments without becoming a drain on efficiency or reliability. Equally, it is possible to achieve high performance gains in the internal air system at a reduced cost in comparison to other areas of the engine as highlighted by Stocker (1977) and Steinetz and Hendricks (1998) for example. However, in the majority of cases the fluid sealing component goes unnoticed by the final consumer, having been been designed, supplied and fitted at an earlier stage of the process (Sutherland (2003)).

Currently in industry an advanced gas turbine design would be expected to take 5-6 years with the design process split into several phases. The early phase includes mapping out the seals that are to be used, with the detailed design of an advanced labyrinth occurring in the later phases of the design cycle. Detailed design typically requires 2-man years. A modern high-bypass engine including seals is expected to last 35 years or 30,000 cycles (1 cycle equals 7 hours or 3,500nm). How-

ever, seals are generally replaced at suitable overhaul periods ($\approx$ 4,000 cycles). This is because the primary cost, the seal access cost (Smith (1978)), is already minimised during overhaul procedures and the seal capital cost versus engine improvement is small. Companies justify seal research either by looking at development cost against percentage improvement or by looking at fines imposed by customers if the machine is off specification ($\approx$ \$10,000 fine per 0.1% deficit in efficiency per engine). Effectively these are equivalent to each other. Therefore it is in the interests of both the power plant manufacturer and the seal supplier to achieve specified performance or better.

Cross Manufacturing Ltd. (*Cross*) work with gas and steam turbine manufacturers providing sealing solutions that are often bespoke to their customers requirements. *Cross* also have a high specification test cell that customers can use to aid their design and development process. The gas and steam turbine sealing sector of *Cross* accounts for approximately 50% of their total business.

To conduct an analysis of the research impact impact for *Cross* one needs to be able to understand their current position in the marketplace. To get a clear idea of the business drivers facing *Cross* use will be made of Porter's Five Forces as shown in fig. (6.1) (Porter (1979)).

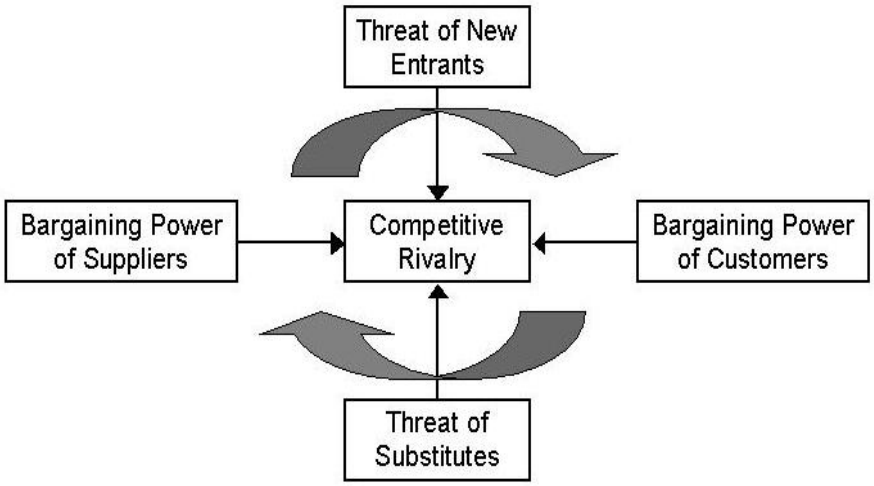

Figure 6.1: Diagrammatic Representation of Porter (1979) Five Forces.

Porter's model allows a structured, in-depth analysis of a company in a macro

sense based upon the industry's underlying economics. By understanding the size and influence of the forces in the model the profitability in an industry can be deduced. A company can also use the model to highlight critical strengths and weaknesses relevant to their position within the market. The model will enable *Cross* to analyse these competing forces whilst enabling the development of strategies that allow for their exploitation. Each of the five forces from Porter's model will be dealt with in turn in section (6.2).

6.2 Porter's Five Forces

6.2.1 Threat of New Entrants

Current players in the market already have very significant learning and experience curve gains with economies of scale that a new entrant would find difficult to replicate. However, the companies are generally medium sized enterprises reliant upon sound engineering and therefore these factors alone would not be enough to stop a knowledgeable and committed entrant.

A recent development within the aerospace industry is that of preferred supplier agreements which would make it much more difficult for a new entrant to gain an aerospace customer base. In the industrial sealing sector the development of these agreements has started, with *John Crane* (Web Reference (2006)) signing a mechanical seal installation and maintenance contract with a major UK oil refinery and *James Walker* offering a total care package called the Joint Integrity Programme (Web Reference (2006)).

Another barrier to entry, especially for the aerospace sector, is the high level of quality checks required. (For industrial turbine manufacturers quality approval checks are not required unless self imposed by the customer.) These quality controls (e.g. ISO9000, NADCAP) cost money to initiate and operate and are likely to form a bigger burden proportionately for smaller organisations. Further, quality controls have to be maintained by suppliers to *Cross* thus offering full traceability of components to the eventual customer.

Recently it has also become increasingly difficult for non-US companies to undertake work with US companies due to export controls. Whilst this is not the only country with export controls it does operates the most advanced system, especially on military projects that are often government funded. If this continues it could lead to a gap in the market for further US based companies or divisions that are not subject to these controls. However, recently *Pratt and Whitney* have invested heavily in two locations: Puerto Rico and The Netherlands. Puerto Rico affords

flexibility on export controls whilst at the same time reducing labour and operating costs. The Netherlands invstment with *NLR* and *Sulzer Metco* to develop a seal testing facility, as described by Kool et al. (2006) and Paolillo et al. (2006), shows that the export controls can be overcome under the right circumstances.

The easiest business aspect of *Cross* to replicate would be the testing and development business as this is much more independent of scale. However, *Cross* have their facility based at their manufacturing site. This has inherent advantages including exploitation of a wide range of knowledge and experience and quick turnaround of machined parts at a reduced cost. To set up a rival private testing facility would prove expensive both in the design and operation. Whilst no figures are available for the facility developed at *NLR* (Kool et al. (2006)) it has taken longer than anticipated to operate under maximum conditions.

Cross cannot afford to become complacent about the likelihood of more competition entering the market. Whilst they have considerable learning and experience curve gains the size of their operation alone is not enough to deter a committed new entrant. However, *Cross* could use several factors from the wider industry to their advantage by increasing the industry's barriers to entry. Within the aerospace industry the recent developments of preferred supplier arrangements could help *Cross* cement their position in the marketplace. Further, total care packages (e.g. Web Reference (2006) and Web Reference (2006)) could be used to develop tighter customer relations. However, the increasing difficulties of conducting business with US aerospace companies whilst being based outside the US may cause problems for *Cross*. This is especially true when considering 51% of the global aerospace market in 1997 was US based (NSF (2000)). The only way to counteract this is for *Cross* develop a US operation, possibly as part of a partnership. When considering the testing and development business, the easiest part of *Cross* to replicate, the likelihood of an entrant gaining enough work to justify developing a quality test facility is limited. Continual enhancements of the existing facility whilst at the same time developing a marketing strategy, should suffice to ensure that the test facility is heavily used into the future. Overall therefore the threat of new entrants to the gas turbine sealing market is not considered high.

6.2.2 Threat of Substitutes

For almost every product there is the threat of substitution. However, due to the demands placed upon the components of the internal air system many other types of seal would be unsuitable. As shown in table (6.1) contact seals (lip seal, mechanical gland, packed gland) do not offer the combination of pressure, velocity, temperature

and reliability that the clearance seal does. However, from a leakage viewpoint the clearance seal is at least 10 times worse and significantly more expensive.

	Lip Seal	Mechanical Seal	Packed Gland	Clearance Seal
Relative Cost	0.5-2	10-100	1-5	10-1000
Max. P_t (MPa)	0.1-1	10	3	*Leakage Dependent*
Max. V $(\frac{m}{sec})$	20	40	20	*No Specific Problems*
Max. T_t $(°C)$	150	500	500	*No Problems*
Min. T_t $(°C)$	-70	-200	*Material Considerations*	*No Problems*
Leakage Rating	≤ 1	≤ 1	≤ 100	$\leq 1,000$
Power Loss Rating	1-2	2-4	8	≈ 0
Life (hours)	5,000	15,000	5,000	$\geq 10,000$
Reliability	*Good*	*Good*	*Moderate-Good*	*Very Good*
Maintenance	*None*	*None*	*Periodic Adjustment*	*None*

Table 6.1: Typical Operating Ranges of Seal: ESDU (80012)

Therefore the main competitors to the abradable honeycomb labyrinth seal are those offered by other abradable surfaces, notably feltmetal, and more recent sealing developments including the brush seal (Ferguson (1988)) and the finger seal (Proctor and Delgado (2004)). Feltmetal is capable of sustaining similar conditions to abradable honeycomb surfaces with the primary difference being a temperature limitation of typically $925°C$. The brush seal consists of a tightly packed array of wire bristles, typically $0.07 - 0.10mm$ diameter densely packed at 100-300 $\left(\frac{bristles}{mm}\right)$. The brush seal, whilst offering performance benefits, does suffer from pressure stiffening effects that can lead to increased levels of wear. Equally hysterisis can occur in a brush seal. This is when the rotor moves out of the centreline deflecting the bristles with the bristles not returning to their original position. Both of these effects act to increase the clearance and therefore leakage of the seal. The finger seal is a variation on the brush seal consisting of larger shaped metal components primarily offering cost benefits in the assembly process.

The primary product *Cross* manufacture, the brush seal, has to compete with these other sealing solutions. Whilst the brush seal has benefits when compared to the typical labyrinth seal it is usually more expensive and therefore the cost-benefit analysis is not always clear. This is particularly true for industrial situations were the sealing conditions, including service intervals, are very different. One of the main benefits of the brush seal is the compliance of the bristles through transient situations. However, the importance of this benefit is reduced in industrial situations were less transient conditions are experienced. Equally modern design techniques can predict transient behaviour including material expansion rates better, meaning that smaller clearances can be maintained. Therefore retrofitting old engines is a significant business to *Cross* with much clearer economics. The seals in these engines, primarily labyrinth seals, have larger design tolerances and therefore the potential gains of using a modern sealing solution are much more apparent.

6.2.3 Bargaining Power of Suppliers

Whilst *Cross* carry out a large part of their final assembly in house they are reliant upon having enough stock of the right quality to meet their orders. Each brush seal uses a bought-in forged ring and a lot of specialised wire alloy to form the final product. The forged rings can be bought from a variety of manufacturers but generally only 3 suppliers are used. The lead time on forged rings can be 12 to 16 weeks. However, customers of *Cross* require lead times of 8 weeks. This leads to stocks of forged components being held. Due to the number of forged component suppliers available they do not therefore have bargaining power with *Cross* except when considering lead times. This is particularly noticeable on new products of a different size were the new forged component lead time needs to be considered in addition to the other factors. Regarding the specialised wire there are only 3 companies worldwide capable of supplying it. Further, due to quality concerns, *Cross* only use two of these companies, *Kentron* and *Fort Wayne Metals*, both US based. Again, there are problems regarding new sizes of wire that may be used in new designs. Equally, the wire, a *Haynes* alloy, has a high demand. Whilst *Cross* place orders which in terms of the scale of their business are large, the orders may not be significant in terms of their suppliers business. Therefore the suppliers of wire have a large influence on the business of *Cross*. This could put *Cross* in difficult positions in the future. Over time as the cost of raw materials increase and the supply potentially decreases *Cross* will increasingly become a price taker unable to dictate terms to either of their wire suppliers. Therefore a worthwhile exercise for *Cross* would be to develop substitute suppliers and/or materials.

A further factor that adds to the bargaining power of their suppliers is the need for quality certification throughout the supply chain. This factor has already been highlighted under another context (see section (6.2.1)). Certification increases switching costs throughout the supply chain leaving *Cross* vulnerable to supply problems in particular key areas as highlighted. Therefore it is imperative that strategies are developed to limit the impact of problems that could be encountered in the future.

6.2.4 Bargaining Power of Customers

The customers that *Cross* supply with turbine sealing solutions are not that numerous. They are also of a different scale to that of *Cross* generally being larger listed companies (e.g. *General Electric, Siemens, Rolls Royce, Alstom*). These customers have been forced to focus on costs with the general trends in aerospace and power generation being cost driven. However, with end customer trends shifting from asset ownership to asset utilisation (e.g. power by the hour) the customer focus will have shifted from purchase price towards total cost of ownership. This has both benefits and drawbacks for *Cross*. This is due to the internal air system and seals having a high cost benefit ratio (Stocker (1977)) and thus an associated increase in demand for quality products would be expected. However, the focus on cost potentially erodes any premiums that *Cross* could charge. The main advantages that *Cross* have are the approval process that many customers require and the importance of well designed sealing solutions in the eventual product. Due to these quality processes switching costs for a customer increase with time once an order is won.

The customers of *Cross* can be broken down into two main groups: aerospace and power generation or industrial. The basic model of Porter (1979) can therefore be developed to reflect the importance of these two groups of customers as shown in fig. (6.2).

To analyse the demands placed upon the customers of *Cross* further an analysis of the markets that they primarily operate in was undertaken.

Aviation Customers

Ever since the inception of affordable commercial air travel in the 1970s its environmental impact, primarily regarding noise and emissions, has been debated. More recently this debate has intensified with the case for climate change moving from a scientific theory to a certainty. Over the same period the demand for air travel has grown significantly with passenger growth predicted to continue into the future. As of 1998 1.6 billion passenger trips were recorded worldwide (GBD (2002a)) with

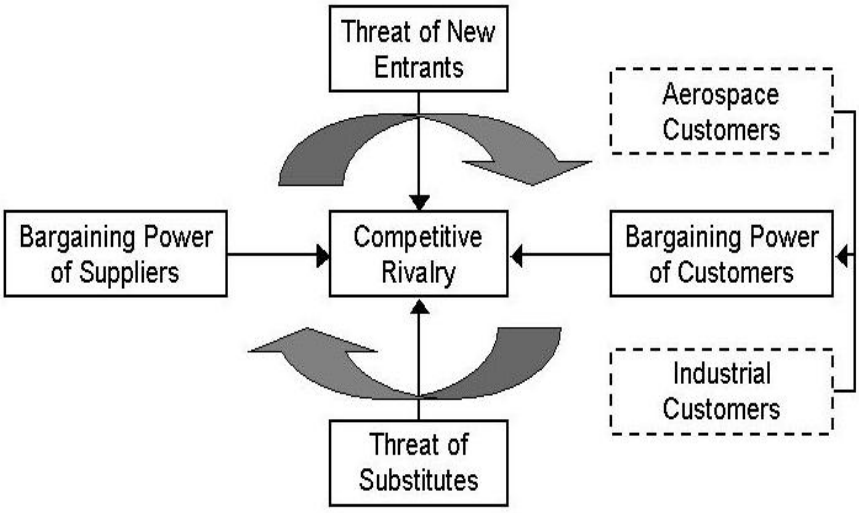

Figure 6.2: Diagrammatic Representation of Porter (1979) Five Forces Altered to Account for Customer Markets.

Boeing (Boeing (2005)) and *Airbus* (Airbus (2004)) predicting an annual growth in revenue passenger kilometres over a twenty year period of 4.8% and 5.3% respectively. This growth is being driven by both real time cost reductions achieved by airlines, particularly low cost carriers, and by the growth in global disposable incomes, most noticeable in Asia (Airbus (2004) and Boeing (2005)).

Over the same period aircraft manufacturers have made significant advancements in reducing emissions and noise in their quest for market advantage. They have typically reduced fuel consumption per passenger mile by 70% due to a combination of technological advancements and increased load factors whilst at the same time reducing the noise annoyance of their aircraft by 75% (GBD (2002a)). However, as aviation capacity has not expanded to keep up with the growth in aviation it has been suggested that an increase in aviation demand of 1% could generate a 6% increase in delays (GBD (2002a)). For example, in the UK the number of passengers per year at various airports has remained relatively static with the only major growth approved recently at Stanstead airport (POST (2003)). Equally, the UK night flight ban, estimated to cost £2.4 Billion annually (POST (2003)), means that flights are having to take place throughout an ever increasingly congested day. Combined with global time differences the night flight ban can cause late departures elsewhere, notably Asia (IATA (2004)). One of the benefits of not expanding

aviation capacity has been increasing load factors with typically 65-70% achieved, double that of road or rail (IATA (2004)). However, airlines highlight airport capacity and land use planning near airports as issues that they have no control over, paying just to use facilities that are provided. Therefore in today's modern climate with expensive oil prices and major airports near to built up areas noise and emissions are still primary drivers for airline operations. *Cross* currently make no impact on aviation noise but they can, through use of efficient sealing technology, enable emissions to be reduced. This is one method as to how *Cross* can position themselves in the marketplace. By gaining an understanding of aviation emissions and combining with the effect of efficient sealing technology potential strategies for *Cross* with respect to aviation business will emerge.

Aviation Emissions

Greenhouse gases within the atmosphere are an area of great interest to the global community. They are responsible for trapping heat which warms the earth through global warming and for reflecting heat from the sun back into space through global dimming (Stanhill and Cohen (2001) and Roderick and Farquhar (2002)). Emissions of greenhouse gases have upset the natural balance of this system, with the earth getting warmer and darker at the same time. However, governments (including the *IPCC*) are primarily interested in global warming and therefore are focussed on reducing the emissions of greenhouse gases. Aviation is one of the fastest growing emitters of greenhouse gases and therefore significant efforts have and are being made to reduce aviation emissions. With the study of global dimming still in its infancy the effects of aviation on global dimming are somewhat uncertain. Therefore this section primarily focuses on global warming.

From any combustion process several primary byproducts are produced: CO_2 (3.15 units per unit of fuel) H_2O, and NO_x. Currently aviation accounts for approximately $2-3\%$ of global CO_2 emissions from burning fossil fuels and contributes approximately 3.5% to radiative forcing, the global warming effect as defined by the *IPCC* (IATA (2004)). By 2050 these could be expected to grow to 3% and 6% respectively with total CO_2 emissions from aircraft growing from 514 million tonnes in 1992 to 1500 million tonnes in 2050 (ATAG (2000)). To fuel this aviation currently uses 12% of global oil supplies used for transport, with transport accounting for 25% of the total oil produced (GBD (2002a)). Emissions of CO_2 from various forms of transport can be seen in fig. (6.3) which highlights that road vehicles are the primary polluters. Typical CO_2 emissions due to aviation are within the range of $30-110\left(\frac{g}{ppkm}\right)$, equivalent to cars or small trucks. Emissions from coach travel are noticeably lower at $<20\left(\frac{g}{ppkm}\right)$ with rail travel between $5-50\left(\frac{g}{ppkm}\right)$ dependent

upon load factors, type of locomotive etc. (ATAG (2000)).

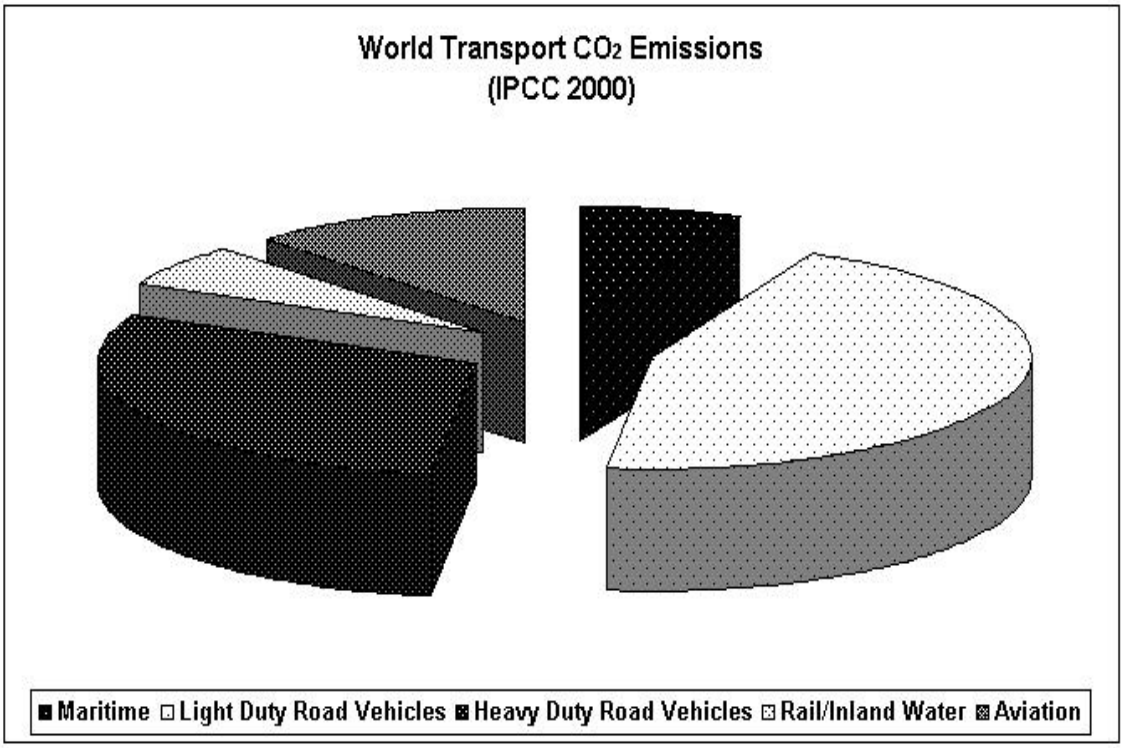

Figure 6.3: CO_2 Emissions from Transport Sources: IPCC 2000.

Water (H_2O) is a natural byproduct of combustion which in aviation creates condensation trails and cirrus clouds. This is thought to add to global warming and has an atmospheric presence of several days (ATAG (2000)). The overall effect due to this increase in water vapour is unknown.

The amount of NO_x produced is known to increase with engine pressure ratio and combustion temperature and therefore thermally efficient engines typically emit higher levels of NO_x (GBD (2002a))). Like H_2O the exact nature of NO_x emission is unknown. The *ICAO* govern emissions of NO_x but these limits are based upon landing and take off cycles only. These limits also vary with pressure ratio thus allowing a high pressure engine to emit more NO_x. However, *Zurich Airport* does imposes a levy based upon NO_x emissions irrespective of pressure ratio. Local arrangements like this are likely to grow in the future, particularly in the developed world were airports are often close to built up areas and unlikely to move to greenfield sites.

The interaction of emissions with altitude is also an area of uncertainty. The indicated greenhouse gas effect of a medium range plane at 32,000ft is 40% that of a long range plane at 40,000ft with 15% less fuel burn (GBD (2002a))). The effects of contrails, geography and seasons may all contribute but require further investigation. Equally, the effect of altitude on global dimming is also unknown.

At the same time aero-engine exhaust systems have improved significantly with massively reduced emissions of CO and emissions of unburned hydrocarbons virtually eliminated. Technology has achieved lower emissions (especially long haul) and lower noise with advanced turbo props having efficiency gains over turbofans on short haul routes. However, whilst aviation traffic is set to grow at approximately 5% per annum aviation fuel use is expected to grow at approximately 3% over the same period highlighting fuel efficiency gains over time (GBD (2002a)). Currently inefficiencies within aviation are also detrimental to its environmental performance costing 8-18% of fuel burn globally (GBD (2002a)).

Aviation Noise

Globally the IATA (2004) claims that in the developed world (USA, Australasia, Japan and Europe) only 7% of transport noise problems relate to air travel with road and rail accounting for 80% and 13% respectively. Higher bypass engines help to reduce noise (up from 5:1 to 10:1 in modern turbofans) but also require higher pressure ratios and temperatures. Overall this causes added weight, drag, fuel burn and higher levels of NO_x emission due to the increase in pressure ratio and temperature. This causes local-global conflicts, where the local population would like quieter aircraft which in a global sense are more damaging. It is expected that current noise reducing technology could bottom out by 2015. However, targets are in place to further halve noise annoyance (GBD (2002a)).

Aviation Market

Approximately 70% of ownership cost of a plane consists of plane and fuel costs. Therefore airlines are keen to buy/lease and operate new planes due to efficiency savings that are made. Efficient planes also retain their residual value better (GBD (2002a)). Currently the optimum design range $\left(\frac{payload^* range}{fuel\, weight}\right)$ is approximately $4,000km$ maximum. Regarding current jet fuel usage 66% is used on missions under $5,000km$ and 50% on missions under $2,800km$. However, the two major civil aircraft development programmes underway both plan to use ranges of approximately

$15,000km$. Table (6.2) highlights the variations between planes designed at $5,000km$ and $15,000km$ over a $15,000km$ mission using a set payload.

Range (km)	Payload ($tonne$)	Fuel ($tonne$)	Max TOW ($tonne$)	Empty Weight ($tonne$)	Fuel for 15,000km ($tonne$)
15,000	44.8	120.4	300	134.8	120.4
5,000	44.8	28.6	169	95.6	85.8

Table 6.2: Weights to Carry set Payload over $15,000km$ in one Stage or Three: GBD (2002a)

As can be seen the $5,000km$ plane should achieve a lower seat cost *per km* but will incur more landing and airport charges which have been excluded from the analysis.

The aviation market is keen to find and use new technology that has environmental or operational gains. The laminar flying wing for example has been found to reduce fuel burn by 20% with hydrogen fuel exhibiting reductions in greenhouse effects of 80% (GBD (2002a) and GBD (2002b)). The potential move towards distributed propulsion however would possibly affect *Cross* business the most. This involves replacing large engines with many smaller engines which significantly affects the sealing technology required.

Aerospace Climate

Currently in civil aerospace two major and quite different development programmes have been followed by the two largest manufacturers, *Airbus* and *Boeing*. *Airbus* has developed the *A380* aircraft, which compared to the *Boeing 747-400* carries 35% more passengers with 49% more floor space using 12% less fuel burn per seat. *Airbus* claim to have reduced direct operating costs by 15-20% and achieved efficiencies comparable to a small family car (Web Reference (2005)). All airports that are expected to receive this plane need to be modified due to the size of the aeroplane. *Boeing* have developed a smaller point to point plane, the *787*, which is planned to enable airlines to break away from the hub and spoke network of the past. *Boeing* also aim for big developments with this plane, claiming 20% lower fuel consumption than a comparable plane (The Standard (2005)). Both planes have a maximum range of approximately $15,000km$. Further design facts for both planes can be seen in table (6.3).

Product	Pass-engers	Fuel-Max ($tonne$)	Max TOW ($tonne$)	Empty Weight ($tonne$)	Cruise Speed ($MachNo.$)
A380	550-840	232.5	560	275	0.89
787	≤ 300	≈ 70	≤ 205	≈ 70	0.85

Table 6.3: Comprison Between *Airbus A380* and *Boeing 787*

Figure (6.4) shows the current and predicted aircraft fleet over a 20 year period, as predicted by *Airbus*, *Boeing* and *Rolls Royce*. It is interesting to note that while the dominant incumbents, *Airbus* and *Boeing*, are focusing on specific market segments there is large growth predicted in the single aisle/small freight market too.

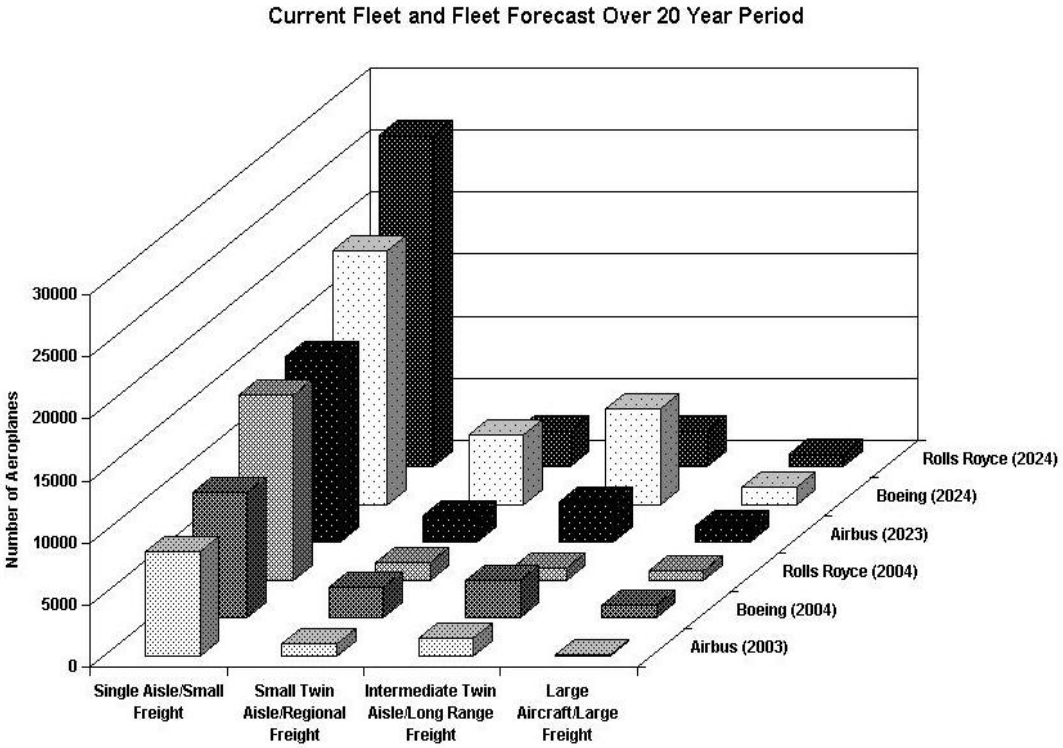

Figure 6.4: Current and Predicted Fleet Over a Twenty Year Period.

When it comes to predicting value both *Airbus* and *Boeing* are generally in agreement in terms of total value predicting \$1.9 and \$2.1 trillion dollars over a twenty year period respectively. However, from fig. (6.5) large differences are predicted in how this value will be split. This is most apparent for the intermediate twin aisle and large aircraft, which obviously contain the *787* and *A380* respectively.

Therefore the delivery numbers expected by *Rolls Royce* have also been included to help act as a balance between the two sets of figures. *Rolls Royce* predict the delivery value of new engines by thrust class and this can be seen in fig. (6.6).

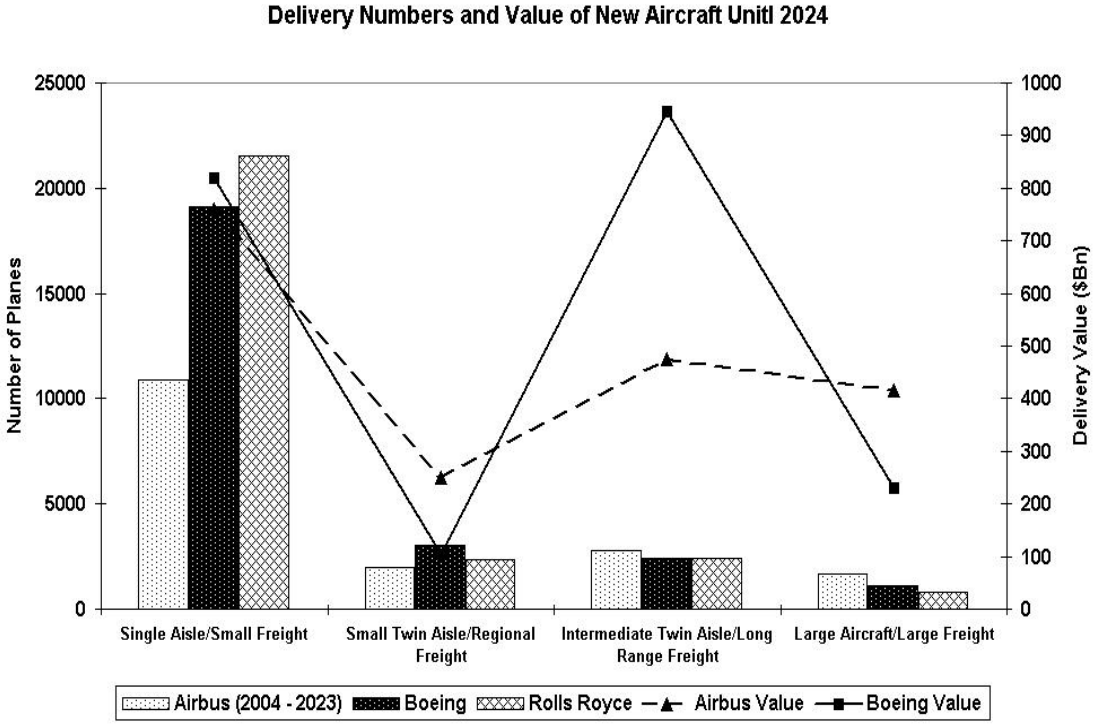

Figure 6.5: Delivery Numbers and Value of Planes Over 20 Year Period.

The *787* is offered with two engine choices, the *General Electric GENx* or *Rolls Royce Trent 1000*, both 10:1 bypass ratio engines producing $55 - 70,000lb$ thrust and costing approximately $13 million each. These engines have eliminated engine bleeds in favour of electrical systems with the only bleed function remaining being the de-icing of the engine inlet. On the *A380* the *Rolls Royce Trent 900* or *GP (General Electric/Pratt and Whitney) 7000* are offered, requiring four to power the plane as opposed to two for the *787*. The *A380* configuration offers significant noise savings of 50% whilst the *787* plane is planning similar benefits.

The eventual operators of these new planes, the airlines, purchase aeroplanes based upon differing requirements. Long haul operators primarily focus on fuel burn whilst short haul operators primarily focus on cyclical cost. However, the move towards power by the hour and total care packages changes the focus of how engine

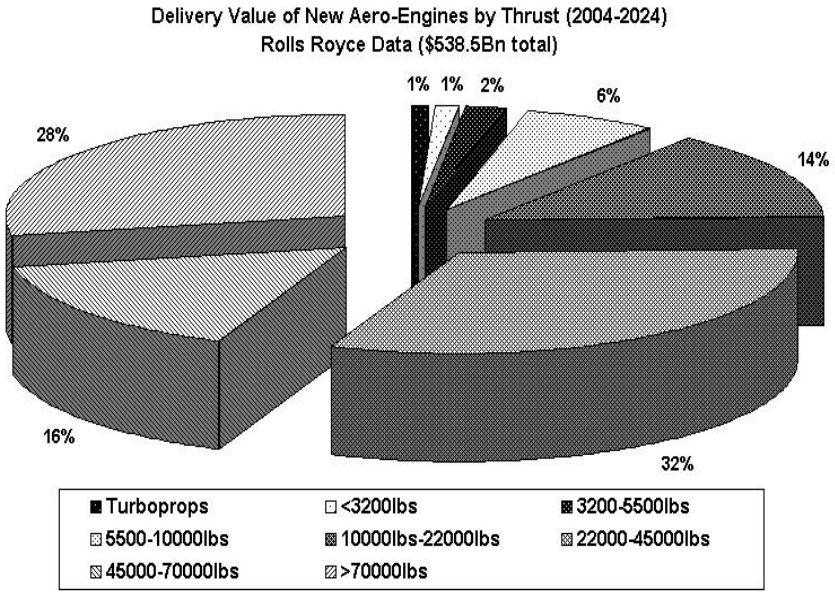

Figure 6.6: Delivery Value of Engine by Thrust Class Over 20 Year Period.

manufacturers choose to manage their business (Read (2005)). This forces engine manufacturers into risk sharing partnerships through lifetime asset ownership. *Cross* could aid engine manufacturers manage their risk by taking responsibility of their products in a similar manner. This is likely to appeal to engine manufacturers who are typically risk adverse. Additionally, by assisting proactively in the development of these contracts *Cross* has the opportunity to mould the contracts to best suit their requirements.

Industrial Customers

Other than aerospace, turbines have many uses in various industries. They can be used for oil applications, gas applications and power generation with expected growths of 57%, 71% and 74% respectively over a 25 year period to 2025 (Curley (2005)). The *International Energy Agency* expect that under current political conditions energy demand and CO_2 emissions will both be 60% higher by 2030, with the demand for electricity doubling. Overall this requires installment of $4,800GW$

in new and replacement capacity, or an investment of $568 Billion/year until 2030 (IEA (2004)). However, if governments adopt an environmentally friendly approach to energy the growths in energy demand and CO_2 emissions could be cut to 50% and 46% respectively over the same period (IEA (2004)). For example it is predicted that across the *EU* 20% of energy consumption is wasted which equates to an annual cost of £40 Billion (EC (2005)). Of this growth in emissions $\left(\frac{2}{3}\right)$ are attributable to developing economies with the majority coming from power stations and transport. At the same time the industry has steadily achieved reductions in energy intensity (energy used per unit of GDP), which is projected to continue.

This is all against a backdrop of increasing concerns about fuel supply and energy diversity. By 2030 to meet their energy requirements the *EU* will be importing 90% of their oil and 80% their gas (EC (2005)). Therefore a major concern for the power industry is balancing secure fuel supplies with emissions targets (Isles (2006) and Green (2006)).

Primarily *Cross* are able to offer efficiency gains to industrial turbine users. This helps their customers reduce their fuel use and production of emissions. However, the environment that industrial seals are required to operate in requires a different design approach. Wolfe et al. (1997) highlights the primary demands required for industrial seal locations including increased operating times, ellipticity and the increased rub potential. Therefore proving the cost benefit of a brush seal, particularly in steam turbine applications, is more difficult than in an aerospace context.

6.2.5 Competitive Rivalry

From section (6.2.2) the most likely form of substitution that *Cross* could experience is that of using a rivals products. However, when considering the design parameters of high speed, high temperature and high pressure there are only a few potential substitute companies to *Cross*. The primary competitors for this market sector can be taken as:

- *Cross Manufacturing Ltd.*
- *MTU Aeroengine*
- *Turbocare*
- *Sulzer Metco*
- *Perkin Elmer*

Company	Temperature (°C)	Sliding Speed ($\frac{m}{sec}$)	Stage Pressure $\Delta P_t(Bar)$	Diameter (mm)
Cross Manufacturing	≤ 600	384	20	20-1200
MTU Aeroengines	≤ 700	400	20	50-650
Perkin Elmer	≤ 650	365	20	150-3000

Table 6.4: Comparison Between Competing Company Brush Seals.

Company	Temperature (°C)	Sliding Speed ($\frac{m}{sec}$)	Pressure $\Delta P_t(Bar)$	Diameter (mm)
Cross Manufacturing	≤ 650	≤ 384	18	≤ 190
MTU Aeroengines	≤ 600	400	20	≤ 350
NLR/Pratt and Whitney	≤ 815	365	24	253.5
NASA	≤ 650	365	5.17 *known*	216

Table 6.5: Comparison Between Available Company Test Facilities.

- *Technetics*

Technetics primarily make a feltmetal abradable lining which can operate at temperatures up to $925°C$. For interstage seals *Technetics* recommends an abradable thickness of 3 times the expected groove depth due to the high compressive forces experienced. At blade tips this depth reduces to 2 times. For blade tip seals the labyrinth knives are designed stronger to withstand the intermittent rubbing, higher velocities and larger ΔP experienced. Therefore the ultimate tensile strength of the feltmetal used is also higher for this application. A comparison of available brush seal information can be seen in table (6.4). Cross Manufacturing do offer larger diameter brush seals in two or more segments on request with *MTU* planning to make seals up to $1000mm$ diameter. Of these companies there are only a few that offer extensive test facilities. These facilities can be seen in table (6.5). The *NASA* facility has been included for comparison using known capabilities only.

As can be seen in tables (6.4) and (6.5) these are tightly contested markets. This means that it would be difficult for any player to arbitrarily inflate their price, effectively imposing a ceiling on the amount that can be charged for goods and services. Therefore it is in the interests of *Cross* to try and differentiate their products by other means. Often this can be undertaken through branding but in this technical market the branding opportunities would prove limited. Therefore product or service enhancements are the obvious places that *Cross* could achieve differentiation. For example *Turbocare* (Sulda (1999)) have designed a retractable brush seal that engages after start-up thus avoiding when the seal is most vulnerable to wear. This

new product claimed improvements of 2-3% in kW output. Equally *John Crane* provides a range of mechanical sealing solutions covering all aspects of mechanical seal maintenance and management at one UK refinery (Web Reference (2006)). These strategies of original product design and service enhancement could be pursued by *Cross* as they are by engine manufacturers through power by the hour and total care contracts. However, for successful service enhancement the link to the eventual customer needs to be developed, possibly by *Cross* becoming a preferred supplier. This may prove detrimental to securing new business with other manufacturers.

Competitive Rivalry: Time

Another area of competition that *Cross* need to consider is time (Stalk (1988)). Time affects the whole marketplace but not necessarily equally. In a traditional factory environment products are only receiving value less than 3% of the time that they are in the factory. By decreasing this amount of wasted time relative to the competition a competitor can become flexible and responsive to market demands. Under a traditional manufacturing approach costs inherent in production grow with product variety. Therefore a traditional factory that reduces product variety can reduce their relative cost and break even points whilst enhancing economies of scale and barriers to entry. However, significant cost savings can also be made by applying the principles of flexible manufacture to an organisation. The goal of flexible manufacture is essentially to make a wide variety of goods in small quantities using the same manufacturing processes. It involves reducing the time taken to manufacture goods by focusing on reducing the production runs and lot sizes, enhancing process organisation with regard to time and enabling local scheduling of work. Even innovation time can be reduced through making smaller and more regular incremental changes, using multi-functional teams and enabling local control over product development schedules for example. A flexible organisation applies these principles throughout all of their functional departments so that gains made in one area are realised throughout.

A more flexible competitor can compete indirectly with organisations of superior resources by being more responsive to changes in the underlying market fundamentals. When a flexible competitor enters the market incumbents often choose to retreat to higher margin products. However, this approach enables the flexible competitor to enhance market share on the lower margin products. However, they still make larger profits than the retreating competition did. This profit enables expansion into higher margin products were the flexible manufacturer will also have advantages regarding cost and responsiveness. This retreating strategy is therefore unsustainable. Equally if the competition compete by reducing cost and adding ca-

pacity a flexible competitor can still maintain market share by adapting its products thus avoiding head-on competition. Therefore *Cross* need to consider how flexibility can be added to their operations whilst at the same time developing strategies that enable identification and courses of action for more flexible competitors.

As has already been highlighted in section (6.2.3) suppliers of certain components to *Cross* have longer lead times than that imposed by their customers (e.g. forged rings). This is a significant barrier to flexibility, particularly in innovation, when the lead time for the forged component needs to be taken into account. Larger organisations, notably in automotive manufacture, often work together to reduce lead times. *Cross* could adopt flexible practices in their factory whilst using similar strategies that cover key components thus enabling more flexible and profitable responses to customer and market demand.

6.3 The Customer Matrix

Through an analysis using Porter's model (see section (6.2)) an understanding of the macro business forces that *Cross* operate within has been developed. However, what does it all mean and more importantly how can *Cross* position themselves for a profitable future? As already seen this market is tightly contested with limited branding opportunities. Therefore the primary method by which *Cross* can aim to position their business is by looking at their customer matrix through perceived user value, or *PUV* (Bowman and Faulkner (1994)). The advantage of this approach as opposed to that of the Boston matrix, Directional Policy matrix or the Product Life Cycle matrix is that the Customer matrix places the emphasis on how potential customers view the marketplace, not how the product relates to the market attractiveness (Bowman and Faulkner (1994)). The Customer matrix can be seen in fig. (6.7). The two axis, perceived use value and perceived price, represent what the customer and company respectively receive from a transaction with both being components of value for money (*VFM*), highlighted through curves *VFM1* and *VFM2*. Each *VFM* curve represent equivalent combinations of quality and price. The price constraint represents the maximum an individual is prepared to pay with the acceptability constraint highlighting their minimum acceptable level of use value.

In order to represent customers on the matrix a *VFM* curve for each market segment or customer needs to be created. The price sensitivity of each customer can be easily included through an increasing or decreasing gradient for more or less price sensitive customers respectively with the goal of the customer being to swap curves by moving north west from their current position. This enables the customer

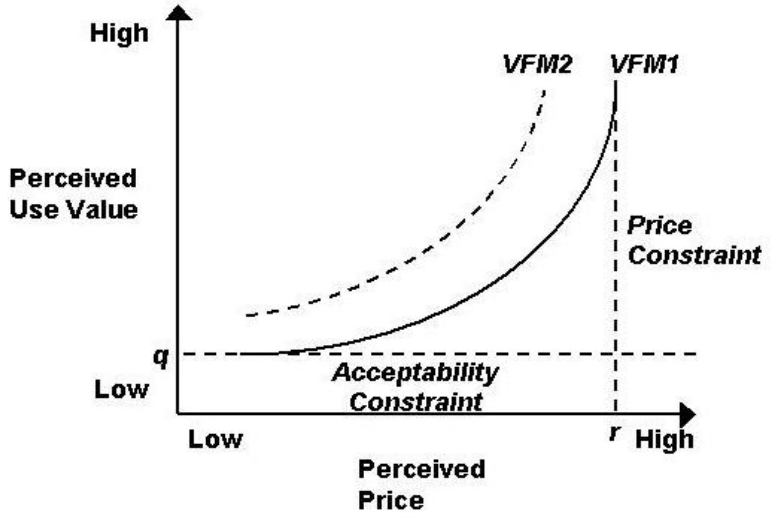

Figure 6.7: The Customer Matrix.

to achieve a higher perceived use value at a lower perceived cost. Moves to the east represent less value for money for the customer, whilst moves up or down the same curve do not change customer satisfaction levels and, by implication, market demand. Therefore the goal of the company is to change their *VFM* curves thus fulfilling their customers desires without negatively affecting their market share. In order to do this differences between their customers *PUV* need to be understood. The *PUV* for each customer can be unique due to different weightings, perceptions and/or components. Regarding the company strategy there are several options to changing the underlying *VFM* curve as shown in fig. (6.8). For an average customer differences between competing products may not be large and therefore competing products may be tightly placed on the customer matrix as shown by letters A - G. in a tightly contested market like turbine sealing this could be assumed to reflect the reality of the industry.

There are several strategies available to the company to change their underlying customers perceptions as shown in fig. (6.8):

Northerly Move:

Cross can look to move north on fig. (6.8) by adding perceived use value. However, in order to make a planned northerly move the customers needs and requirements

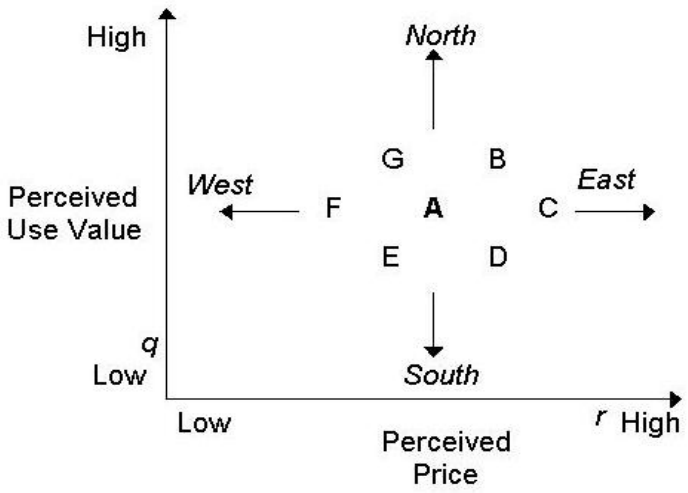

Figure 6.8: The Customer Matrix.

need to be understood. Therefore dimensions of PUV that relate to each customer need to be created, which in gas turbine sealing could include performance, quality, technical support, build and delivery time etc. Through ongoing customer contact over time these dimensions can be developed and thus the most effective way to orchestrate a northerly move becomes apparent.

Easterly Move:

This move is reliant upon finding less price sensitive customers which in turbine sealing is unlikely. However, this move can be sustainable if the underlying VFM curve is above that of their competitors or if price increases across the market.

Southerly Move:

This would involve *Cross* reducing PUV and represents what most companies strive to avoid. A planned move in this direction is dependent upon finding more price sensitive customers and needs to be highly cost focussed to ensure profitability (e.g. discount supermarkets and budget airlines). In gas turbine sealing this move is unlikely to secure new business and may loose customers if price is used as a proxy for quality. For *Cross* this move is more likely to take place in a relative sense,

dependent upon competitor strategies, than because of planned company actions.

Westerly Move:

This would require *Cross* to reduce their price and should equate to a gain in market share. However, this move is likely to be followed by competitors reducing cost and therefore the gained market share is likely to be quickly eroded. In order for this strategy to be successful *Cross* needs to be confident that either they are the lowest cost producer or that they are able to sustain losses for the longest period of time otherwise they can still be undercut. Equally, if price is being used as an indirect proxy for PUV this move can have a limited impact. This is often the case were customers feel under-informed about their purchasing decision which is unlikely to be the case in the turbine sealing market. This strategy is reliant upon knowledge of their competitors costs and may create an inwardly focussed management that misses other opportunities.

Therefore the only really sustainable strategy is through adding PUV, which is the natural process of innovation over time. However, these moves will be imitated and perhaps at times led by their competitors so therefore the goal for *Cross* is to create sustained competitive advantage. This, assuming similar technology, can only be achieved by combinations of northerly and northwesterly moves that add to their customers perceptions of perceived use value. Obviously if *Cross* developed new products or new lines of business then a significant competitive advantage can accrue which can enable an eastwardly move of the underlying VFM curves, possibly opening avenues for greater revenues. Other strategies that can also change a VFM curve include total care packages (see section (6.2)), the potential development of risk sharing partnerships or developing a US operation, possibly as part of a risk sharing partnership. For these strategies to be successful *Cross* need to get close to their customers. Regarding the first two strategies significant switching costs would be imposed onto their customers thus further cementing relationships to the benefit of *Cross*. The third strategy, developing a US based operation, would enable much easier relationships with their US based customers.

6.4 Conclusion

The goal for *Cross* has to be successful and sustainable business into the future. In order to succeed business strategies need to be developed that enable *Cross* to exploit their current strengths, reduce the potential impact of their weaknesses whilst

highlighting attractive areas for business development.

For the turbine sealing market the two primary drivers that affect *Cross* are efficient plants and cost. Generally turbine manufacturers are required to sell equipment on the understanding that they assume some risk of the total cost of ownership. Eventually turbine manufacturers will look to share this risk with their suppliers, as has already happened in the automotive sector. This can already be seen with fines for inefficient engines being introduced as a penalty for not achieving design specifications. Therefore *Cross* should analyse the possibility of entering into risk sharing partnerships with their customers. This will act as an expression of confidence in their ability whilst also providing the likelihood of securing more business from typically risk adverse customers. However, the difficulty will be in defining the contract. In the event of a problem *Cross* need to be able to prove that they met the design specification and that therefore the problem lies elsewhere. However, with the amount of factors affecting sealing this may be an unattractive option. Entering into preferred supplier agreements could give *Cross* the same benefits whilst reducing the risk to their own business. However, whilst this has benefits regarding ongoing business with preferred customers this may become a barrier to business from other manufacturers. The key to either of these options is for *Cross* to reduce business risks to the lowest possible level prior to entering into any agreements.

Another key factor that *Cross* need to address is the dominance of the US based market including the tighter export controls that this entails. These export controls will create difficulties for *Cross* to conduct business with US based customers. To overcome these barriers *Cross* could either start a US based operation or partner with a US based company.

Further, the manufacturing operation should also be analysed to look for potential savings in cost and time. With customers of *Cross* being price-sensitive, and with supply-delivery lead times out of balance, *Cross* are exposing themselves to risks that are largely out of their control. Work should be undertaken to reduce these risks, either through working with key suppliers to reduce lead times or searching for more flexible manufacturers of key components: metal forgings and specialist wire alloy. This would significantly reduce their risk exposure whilst also enabling significant time savings throughout the manufacturing process. Equally, by looking at flexible manufacture, *Cross* can find further time and cost savings whilst also enhancing their agility with respect to their competition.

All of the above points must not be undertaken if quality levels achieved are likely to be negatively affected. For aerospace customers quality levels are a legal requirement. However, for industrial customers quality levels are determined by the

customers own requirements. For *Cross* this entails a cost in meeting these differing quality goals and therefore the possibility of using one quality system should be examined. This would enable compliance of all products to aerospace standards, essentially meeting the aerospace legal requirements whilst over-assuring the industrial components. Whilst this may sound expensive and complicated, it may prove to be an order winner for the industrial based customers. Equally, the simplicity of operating one quality system should offer cost savings. This move would also increase switching costs on all of their customers.

Therefore the key for *Cross* to be successful in the future is to understand and exploit perceived user value and to use the components of it to drive north and northwesterly moves relative to their competition. This means that *Cross* needs to fully understand their customers needs and use scenario planning to help predict customer requirements in the future.

Chapter 7

Discussion

The work undertaken has experimentally and computationally analysed stationary labyrinth seal flow field behaviour with flat metal, flat honeycomb and worn honeycomb stators. The primary objective of the study, to investigate the effects of wear on the performance of an abradable honeycomb labyrinth seal, has been aided through the use of a simpler flat metal stator model. This enabled a benchmark experimental test for the whole study giving confidence in experimental repeatability and simpler geometries to investigate numerically. Additionally, the use of two experimental data recording techniques that recorded repeatable data, increases the confidence of the experimental work undertaken.

Experimentally use was made of two data collection systems due to some uncertain readings that were received. However, both data collection systems recorded results that were similar to each other thus adding confidence to the experimental work undertaken and the data collected. Deviation of the experimental equipment over time was checked for through use of a known baseline test using a flat metal stator. The data recorded using a flat honeycomb stator showed small clearance effects at both $0.00mm$ and $0.50mm$. At $0.50mm$ using a flat honeycomb stator mass flow was up to 10% higher than that recorded when using a flat metal stator, whilst at $0.00mm$ using a honeycomb stator mass flows were recorded that were $\approx 60\%$ of that found at $0.50mm$. At larger clearances the beneficial effect of the turbulence created by the honeycomb surface can clearly be seen to reduce mass flow. Whilst this small clearance effect can be significantly reduced, if not eliminated, through use of a smaller $\left(\frac{Hs}{Tp}\right)$, the $3.20mm$ size of honeycomb was chosen to match other geometric sizes found experimentally. The importance of choosing the right honeycomb for each labyrinth seal is highlighted by Stocker (1977). Further experimental work using a flat honeycomb stator investigated the effect of labyrinth tooth to honeycomb cell wall location recording no effect on overall performance. However, very local effects on the inter-seal pressure distribution were found at very

small clearances. This is because the effects were not strong enough to project through the jet to the labyrinth teeth tips unless the jet, and therefore clearance, is very small. Analysing worn honeycomb surfaces experimentally revealed interesting tooth to groove location effects. There are clear benefits to running with the labyrinth tooth in an upstream position with regards to the groove which was found for all clearances. With the groove in an upstream position with respect to the tooth, the groove actually acts like a funnel, deteriorating seal performance. Therefore if the seal movements throughout the operating range of the engine were known accurately, it may be possible to design the seal so that the position with the highest likelihood of contact and wear occurs in a downstream position with respect to the position of normal seal operation. This controlled movement, as highlighted experimentally, only needs to be small and related to the location and size of the groove and labyrinth pitch. A large movement may be detrimental to labyrinth seal performance by effectively running in a downstream position with respect to an upstream groove, leaving only the first tooth operating at design conditions. However, being able to passively control axial location of a labyrinth seal accurately using knowledge of pressure and temperature throughout the operating range of an engine would prove a difficult task. Whilst with active control the axial location of the seal would be known accurately, actively controlling a rotating shaft of substantial mass would prove very challenging and if proved possible would incur substantial costs. Regarding inter-seal pressure distributions, only the smallest clearance of $0.00mm$ recorded differences caused by the worn honeycomb surfaces. At larger clearances the effect of the groove did not significantly affect the pressure distribution within the flow at the locations of measurement. The reduced mass flow found with the tooth located in an upstream position can be explained through the v-shaped groove anaylsed. Essentially with the tooth located in a downstream position the tooth behaves like a venturi meter due to the flow re-direction caused by the v-shaped groove as opposed to the orifice meter normally associated with labyrinth seal flow.

The inter-seal pressure measurements recorded experimentally highlighted interesting effects that have not been reported in detail before. The only previous publication to record inter-seal pressure measurements, Benvenuti et al. (1980), reported tooth C_d values in excess of 1 which is non-physical. However, this paper does confirm some of the labyrinth seal behaviour recorded in the current study. Primarily the pressure distribution through the seal found by both Benvenuti et al. and in the current study does not show gradual pressure reductions through the seal. Essentially this means that the pressure ratio over the second tooth equates to an $\dot{m}m_{ID}$ below that which is recorded experimentally. Further, for some test conditions, an increase in pressure was recorded over the intervening teeth, dependent upon geometry and operating conditions. This effect means that the calculated $\dot{m}_{ID}$ is smaller than expected, or in the case of a pressure rise, albeit small, nega-

tive. Further, using the analysis technique of Komotori and Miyake (1977) similar effects were found. Whilst these findings deviated from theoretical assumptions of a reducing pressure and an increasing pressure drop through the seal, they were also recorded numerically using CFD. Therefore both of these theoretically derived performance routines proved inaccurate at replicating the current study, with the inaccuracy primarily due to the under-estimation of the effect of COF. Therefore further work to understand the combined effects of C_d and COF was undertaken using other computational techniques.

Numerical work was undertaken using CFD along with KTK and THESEUS (specific labyrinth seal computer codes) to investigate the current experimental results. Confidence was gained in CFD through accurate simulation of rotor-stator flow fields and flow through orifice plates. This section of work also highlighted the importance of modelling boundary layer flow accurately for the chosen simulation, which is where large changes in fluid properties occur in small distances. This is particularly true if the simulation being undertaken is investigating phenomena that are dependent upon accurate resolution of the boundary layer (e.g. heat transfer, frictional effects). Further, another study was undertaken to enable investigation of the experimental results both quickly and accurately. This study was based upon CFD simulations of 3-D abradable honeycomb using two honeycomb sizes in two orientations from which a 2-D CFD modelling technique was developed that was capable of replicating the 3-D equivalent. This enabled efficient use of CFD with regard to both computational resource and time. To add confidence to the applicability of the 2-D assumption the transverse velocity component generated by the honeycomb surface in the 3-D seal was analysed. It was found that this velocity was highly localised and, as an average, small, with no recorded overall effect. Interestingly this velocity penetrated through the labyrinth jet into the labyrinth seal cavity, particularly at regions of high velocity like on the labyrinth teeth faces. The 2-D simplification technique developed was capable of predicting both the overall seal performance and the inter-seal pressure distribution with a high degree of accuracy. Of the two orientations studied the design-orientation of the honeycomb surface recorded lower mass flow than the alternative-orientation. However, the alternative orientation may offer benefits in high performance labyrinth applications due to an increased level of wear absorption by the honeycomb stator. This is because in a contact situation the labyrinth tooth contacts less honeycomb wall and therefore the stator will absorb more wear with a lower heat generation. When using the 2-D technique to model the 3-D seal tooth to honeycomb effects were found that affected seal performance. It was found that when the labyrinth tooth aligned to the honeycomb cell wall a reduction of 2% in mass flow was recorded. However, to realise this benefit in an actual design the labyrinth tooth pitch would need to be sized in multiples of honeycomb cell size or for the honeycomb to be

made to match the chosen labyrinth pitch, which may be restrictive or costly. Further, accurate knowledge of labyrinth tooth location and honeycomb cell location is required to enable appropriate alignment. Designing to this level of detail would show performance benefits but only if the honeycomb stator and labyrinth seal was sized correctly and the seal location could be maintained throughout a significant range of operation. Significant savings in time, and therefore cost, were found when using the 2-D simplification technique to model the 3-D honeycomb labyrinth seal. Using the wall function approach to model the near wall viscous sub-layer gave the most economical solutions, taking approximately 4 hours to converge on a desktop computer. When resolving the near wall viscous sub-layer in 2-D the computational time tripled on the same computer, whilst when modelling the 3-D abradable honeycomb labyrinth seal 3 days were typically required for a steady state solution using a multi-processor machine. These times exclude the pre- and post-processing times which are not insignificant. Therefore the 2-D technique enabled a cost effective way of investigating many different flow situations in a fixed amount of time.

To gain confidence in the best CFD simulation technique to use in analysing the experiment use was made of the flat metal stator as it was easiest geometry to study computationally. From this work it was found that the $k-\epsilon$ RNG turbulence model consistently recorded the most accurate replication of experimental data for the geometry and operating conditions considered. Only a slight improvement due to resolving the near wall viscous sub-layer was found and only when examining the inter-seal pressure distribution. From these simulations it was found that the velocity increased as one travels downstream through the seal, although the pressure drop did not. This contradicts the findings of Rhode and Hibbs (1992), who found an increasing dynamic head and pressure drop through the labyrinth seal.

In order to study the flow through the abradable labyrinth seal rig use was made of the simplification technique previously developed. This proved both accurate and computationally efficient enabling many more simulations to be undertaken in the allotted time. The largest deviations between the numerical simulations and experimental data were experienced at the higher pressure ratios. This is because when the flow is near or above choking conditions accurate replication using CFD becomes significantly more difficult due to the formation of shock waves. This adds to the computational complexity of the solution. Further difficulties were experienced at $2.00mm$ clearance due to the increased level of flow disturbance recorded. This was also found when simulating the flat metal stator. The level of agreement found between the experimental data and the CFD simulations using the 2-D simplification technique was good, typically $\leq$5%. The inter-seal pressure comparison is also accurate, particularly if care is taken to model the boundary layer flow accurately. The final tooth proved the most troublesome pressure measurement location

to replicate using CFD, particularly at or near choking conditions, when the changes in variables are at their most rapid. The same technique also proved capable of accurately simulating the worn honeycomb experiments.

Rotation, which was only investigated using CFD, was found to have a marginally beneficial effect that deteriorated with rotational velocity. A pumping action on the downstream labyrinth tooth face was highlighted which increased with rotational velocity. The effect of this was to increase COF and therefore decrease labyrinth seal efficiency. Interestingly, rotating labyrinth seals recorded gradual pressure reductions that were not found using a stationary experiment. However, this was primarily an investigative study and therefore further work needs to be undertaken to develop understanding of these effects.

Further investigative work was undertaken using computational routines KTK and THESEUS. Prior to using these computational routines to study labyrinth seal flow fields known data-sets were recreated to enable confidence in the accurate recreation of the routines. The routines, which are dependent upon the use of loss coefficients, proved insufficient at replicating both the mass flow and inter-seal pressure distribution accurately. However, THESEUS did prove the more accurate of the two at predicting mass flow. Further development work needs to be undertaken to enhance understanding of the pressure loss mechanism through labyrinth seals and therefore accurate prediction of seal pressure distribution. However, analysis of labyrinth seals using computer codes will still be a valid method of investigation. This is because the designer can gain an enhanced understanding of general effects that can be further investigated using other investigative techniques (e.g. CFD). As long as the designer is aware of the limitations of their particular design code useful conclusions from its use can be drawn.

The best available method of numerical investigation proved consistently to be CFD. This accurately predicted overall seal performance and inter-seal pressure distribution excluding the final tooth. However, the final tooth experiences a large pressure drop and, in a constant clearance seal, is also the first to choke. The high velocities experienced, particularly at choking conditions, are very demanding to solve numerically using CFD. Unsteady effects are likely to be recorded in this location and therefore would be an area of future work. Likewise, rotational effects, which were briefly analysed using CFD, showed with very little deviation from stationary conditions and agreed well with the literature.

7.1 Recommendations for Future Work

Throughout this study the effects of rotation have only been touched on briefly when CFD was used as an investigative tool. This showed no significant effect on overall seal performance but did record interesting inter-seal pressure distribution effects. This area of work needs further clarification to fully understand what is happening in the labyrinth seal. Throughout the study beneficial performance effects have also been recorded with the labyrinth tooth located in an upstream position regarding the groove. This study only analysed two groove sizes of comparable shapes finding similar benefits. However, each labyrinth seal location in an engine could have different patterns of wear and therefore a study of different wear profiles would add insight to that reported herein. Further, the possible benefits of passive or active controls on labyrinth seal teeth to stator (and therefore groove) location could be investigated. Additionally, two other larger areas of work should be undertaken. These should be aimed at understanding the effect of kinetic energy carry over and studying the implementation of a new computational routine. Further work on these two areas has been undertaken in section (7.1.1) and (7.1.2) respectively.

7.1.1 Understanding the Carry Over Factor

Through the previously highlighted importance of the labyrinth seal COF further investigative work was initiated with the goal of reducing COF and therefore $\dot{m}$. To ease comparison with the experimental and numerical work undertaken the geometry was chosen to match the experimental rig geometry. In order to reduce COF it can be seen to be beneficial to reduce the recirculating flow traveling along the downstream face of each labyrinth tooth. This flow effectively reduces the expansion angle achieved into the labyrinth chamber, and it has been highlighted that this effect increases with the pumping action caused by rotation. Therefore two labyrinth derivatives were devised to investigate reducing this recirculating cavity flow. The first design involved using a half height labyrinth tooth located in the middle of the labyrinth cavity, with the second design using a half height labyrinth tooth attached to the downstream side of the labyrinth teeth. The overall form of these new designs and their Mach number distributions at a clearance of $0.50mm$ can be viewed in fig. (7.1). This figure highlights the enlarged flow expansion angle and the reduced recirculating velocity on the downstream side of each tooth for both designs. Further, the centre of the labyrinth cavity, which previously was an area of slow and stagnated flow has increased levels of turbulence and therefore energy dissipation taking place.

Both of the these designs achieve a reduced mass flow in comparison with the

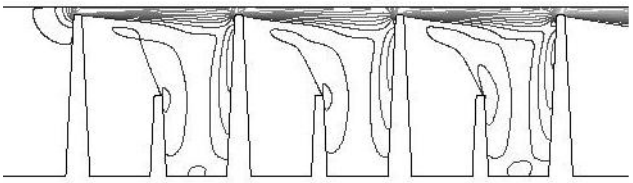

(a) 0.50mm Clearance. Design 1.

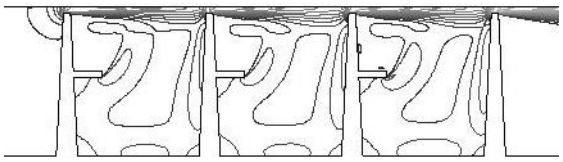

(b) 0.50mm Clearance. Design 2.

Figure 7.1: Mach Number Contours for New Designs (1) and (2) at a Clearance of $0.50mm$ and Pressure Ratio of 2.00.

flat stator experimental data at $0.50mm$ clearance. The comparison of $\left(\frac{\dot{m}\sqrt{T_{t(0)}}}{AP_{t(0)}}\right)$ can be seen in fig. (7.2) which highlights that both designs exhibit a benefit at high pressure ratios over the flat metal experimental case. Further, design (2) has an increased benefit over design (1). However, this study was simply a primary investigation and therefore whilst the recorded effects are interesting further work needs to be undertaken. This work should look at the modified physics of the flow as created by these half-height teeth including the exact size and location of these teeth for maximum benefit. Further, only one extra tooth per cavity has been modelled but is not necessarily optimum. An equally beneficial effect may be created by increasing the frictional effects created along the cavity floor, perhaps through the inclusion of further honeycomb surfaces. Again, this is further work that can be undertaken.

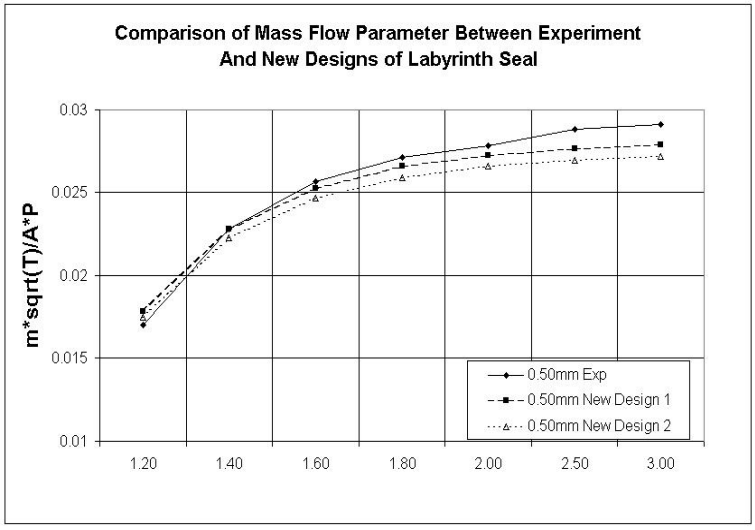

Figure 7.2: $\left(\frac{\dot{m}\sqrt{T_{t(0)}}}{AP_{t(0)}}\right)$ comparison between the experimental data and CFD simulations using New Designs 1 and 2.

7.1.2 Developing a New Computational Routine

As highlighted through the work undertaken existing methods to compute labyrinth seal performance have proved inadequate at replicating the current study. This is especially true at predicting the seal pressure distribution, and therefore by implication, the seal loss coefficients. The best of the investigated methods, THESEUS, still exhibits a variation from the current experimental and numerical data of 10-20%. Therefore this section will outline a new approach that could be further developed to compute labyrinth seal performance.

The primary difficulty encountered in trying to predict labyrinth inter-seal pressure distribution accurately is in accounting for the incomplete expansion process downstream of a labyrinth tooth. A new method, based upon jet expansion from a 2-D slit, has been developed to account for this incomplete expansion process. Several factors are widely known about the process of jet expansion. Firstly, the jet can be assumed to be turbulent within a small distance of the point of expansion. Secondly, mixing of the jet with fluid of a lower velocity reduces the velocity of the jet. However, the total jet momentum is maintained (i.e. the mass flow entrained in the jet is increased). Lastly, the jet momentum at the point of expansion is proportional to the excess jet pressure at the point of expansion (Schlichtling (1955)). It has also been found by Schlichtling (1955) amongst others that the velocity profiles in a 2-D jet are non-dimensionally similar. This can be seen in fig. (7.3) which shows how the jet velocity ratio ($y-axis$) in a 2-D jet is related to the jet width ratio ($x-axis$).

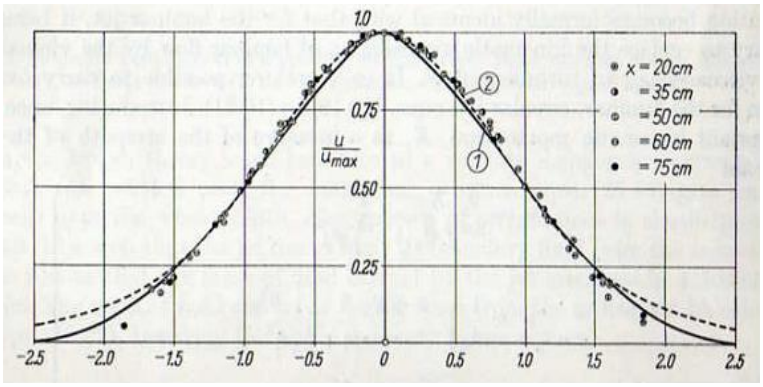

Figure 7.3: Velocity Distribution in a 2-D Turbulent Jet, taken from Schlichtling (1955).

Therefore using this knowledge of 2-D jet behaviour, similar non-dimensional velocity profiles relevant to the current experimental set-up were computed by as-

suming the velocity in the jet was the same. This enabled calculation of the velocity ratio required to conserve momentum, from which momentum and mass flow profiles away from the stationary wall were computed. The boundary of the jet expansion is found once a mass balance through the system is achieved. Further, at this location COF is given by the momentum equation. It is then possible to define COF in a slightly different manner as shown in eqn. (7.1). This effectively calculates the efficiency of the expansion process as related to the upstream dynamic head. Knowledge of the upstream velocity and therefore dynamic head can be gained from the system $\left(\frac{\dot{m}\sqrt{T_{t(0)}}}{AP_{t(0)}}\right)$ as shown in ESDU (74028).

$$COF = \frac{P_{t(2)} - P_{t(2)-MO}}{P_{t(1)} - P_{s(1)}} \tag{7.1}$$

This method of calculating COF uses two cavity pressures, the momentum mixed out pressure and the actual pressure based upon continuity. The momentum mixed out pressure (P_{t-MO}) is that which satisfies the momentum, mass and energy equations. However, if isothermal flow is assumed then the energy equation does not need to be solved. Therefore the equations of mass and momentum, eqns. (7.2) and (7.3) respectively, can be solved simultaneously to give an isothermal solution. From both of these equations the downstream static pressure ($P_{s(2)}$) can be equated enabling the calculation of the downstream Mach number ($Ma_{(2)}$) and therefore (P_{t-MO}) at that location. The actual pressure ($P_{t(2)}$), which is based upon continuity and the expansion from a 2-D slot, can therefore be calculated using the COF. As can be seen it is also possible to include the effects of friction (f_x) along the stationary wall.

$$\begin{aligned}
\dot{m} &= \int \rho A V \\
\dot{m} &= \int \left(\frac{P_{s(2)}}{RT_{t(2)}}\right)\left(\frac{T_{t(2)}}{T_{s(2)}}\right) A\sqrt{\gamma R T_{s(2)}} Ma_{(2)} \\
\frac{\dot{m}RT_{t(2)}}{A\sqrt{\gamma R T_{t(2)}}} &= P_{s(2)}\left(\frac{A_{jet}}{A_{tooth} + A_{jet}}\right) Ma_{(2)}\sqrt{1 + 0.2Ma_{(2)}^2}
\end{aligned} \tag{7.2}$$

$$
\begin{aligned}
momentum\,upstream &= momentum\,downstream \\
momentum_{(jet)} &= momentum_{(cavity)} + momentum_{(jet)} \\
\int \rho V^2 dy &= \int (P_s + \rho V^2) dy \\
\int \gamma P_{s(1)} Ma_{(1)}^2 dy &= \int (P_{s(2)} + \gamma P_{s(2)} Ma_{(2)}^2) dy \\
\left(P_{s(1)} \gamma Ma_{(1)}^2 + P_{s(1)}\right) \left(\frac{A_{jet}}{A_{tooth} + A_{jet}}\right) &= P_{s(2)} \left(\frac{A_{tooth}}{A_{tooth} + A_{jet}}\right) \\
&+ \left(P_{s(2)} \gamma Ma_{(2)}^2 + P_{s(2)}\right) \left(\frac{A_{jet}}{A_{tooth} + A_{jet}}\right) \\
&- f_x
\end{aligned}
\tag{7.3}
$$

A correlation to account for tooth location has been included based upon limited single tooth C_d data taken from Wittig et al. (1987). This enables the effects of approach velocity on tooth performance to be computed. However, this correlation is based upon limited data and needs to be extended to add confidence to the technique.

Some calculated results using this technique are compared to experimental results in fig. (7.4). As can be seen the general form of the pressure loss is in agreement with the experimental data which is encouraging. Further, the magnitudes of the calculated pressures are in reasonable agreement with the experimental data. Therefore this adds confidence to the approach. However, these calculations were undertaken using a known experimental mass flow. Errors can only be assumed to increase if a mass flow prediction method was required in addition to the routine highlighted. Therefore, with better mass flow calculation routines and better correlations for the calculation of C_d and COF, it is hoped that an improved level of agreement can be obtained. Equally, if the designer is aware of the limitations of the code useful results can still be gained in a significantly quicker time than the other techniques used for this study: experimental investigation and CFD. However, variations in seal static pressure distribution due to clearance have been recorded experimentally, as highlighted in fig. (3.8). Equally, fig. (5.8) highlighted that at $2.00mm$ further contraction occurs downstream of each labyrinth tooth. This further contraction was not recorded at $0.50mm$ or $1.00mm$. Therefore, applicability of the suggested model at larger clearances needs further investigation, particularly above a clearance of $1.00mm$. However, for these cases, if the effective area can be defined properly, then a reasonable performance could be obtained due to the use of area ratios in eqns. (7.2) and (7.3). Use of the suggested model, or another model, can change the role of CFD from a primary method of investigation to that of confirming the results of the code with time savings found, similar to that recorded by

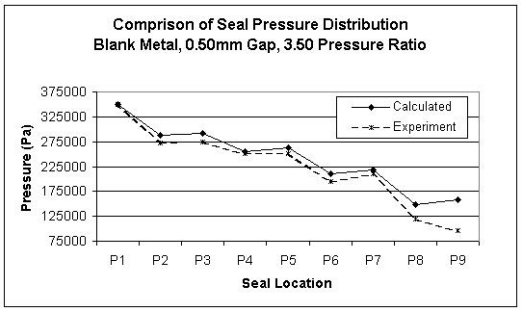

(a) 0.50mm Clearance. 3.50 Pressure Ratio.

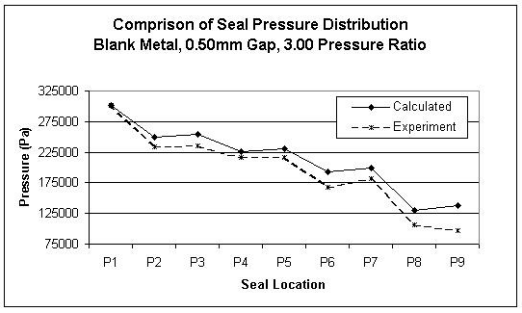

(b) 0.50mm Clearance. 3.00 Pressure Ratio.

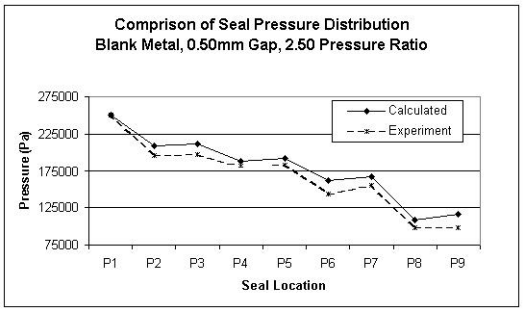

(c) 0.50mm Clearance. 2.50 Pressure Ratio.

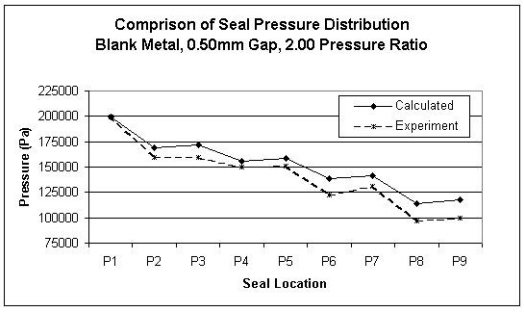

(d) 0.50mm Clearance. 2.00 Pressure Ratio.

Figure 7.4: Comparison of Pressure Distribution Between Experiment and New Computational Routine.

Hirano et al. (2003). This is an area where future research would greatly develop our understanding of labyrinth seal flow physics.

7.2 Research Impact

Labyrinth seals prove an economic area of research due to the reduced investigative costs compared to other parts of the turbine (Stocker (1977)). Further, the direct link between efficient sealing, turbine performance, fuel consumption and therefore market attractiveness has been made previously in Chapters (2) and (6). For example, Stocker (1975) highlighted for a civil aerospace engine that a 1% reduction

in seal leakage equates to an SFC improvement of 0.1%. Further, Stocker (1978) found that SFC could be improved by 2.7% by reducing seal leakages throughout by 25%. Using this figure Michaud et al. (2003) highlighted that 16 million barrels of jet fuel could be saved in the US alone. Smith (1978) found that seal deterioration accounted for 4% loss in performance and a fuel bill of $1.2 millon, based upon a 12 plane, high bypass engine fleet. Munson and Steinetz (1994) found 2.6% SFC improvements by concentrating on the most important seal locations in a regional jet. Childs et al. (2006) reported that cooling flow may equate to 6% of SFC and that a 1% SFC saving could reduce operating costs by 0.5% and save 560 $\left(\frac{tonnes}{year}\right)$ of fuel. Therefore there is a clear benefit to seal research, both for manufacturers and operators, who benefit from increased market attractiveness and reduced operational costs respectively.

The performance deteriorations that have been recorded experimentally when using worn honeycomb have significant variations dependent upon seal geometry, groove size and tooth to groove location. With the tooth located centrally in the groove the largest deteriorations of $\leq$50% are recorded when compared to the flat honeycomb stator. If this loss is applied to all seals a deterioration in SFC of 5.4% could be expected (Stocker (1978)). However, in modern turbines up to 6% SFC can be used by the cooling system (Childs et al. (2006)). This could then be expected to increase to 9% with worn labyrinth seals located centrally within the groove, equating to an increased operational cost and fuel use of 1.5% and 1680 $\left(\frac{tonnes}{year}\right)$ (Childs et al. (2006)). Therefore there is a strong incentive from an operational viewpoint to buy equipment that minimises this loss in performance and therefore profitability. However, the configurations highlighted in section (7.1.1) typically achieved leakage reductions of 10% compared to flat metal stators. Assuming that for this configuration stator wear can also deteriorate performance by $\leq$50%, a reduction in leakage of 15% over the original worn configuration is still achievable. This equates to an improvement in SFC of 1.08% (Stocker (1978)) or an operational saving of 0.54% (Childs et al. (2006)). Therefore the benefit and economic case for seal research is clear. Using these figures would help aid the development of incentives to finance future seal research. Development of the configurations highlighted in section (7.1.1) could prove particularly fruitful and eventually profitable. Further, through using these figures, *Cross* can access and offset development costs for future seal research whilst increasing and enhancing market share through clear presentation of the benefits from an operational viewpoint.

Bibliography

Abramovich, G. (1963). *The Theory of Turbulent Jets.* The M.I.T. Press.

Airbus (2004). *Global Market Forecast: 2004 - 2023.* Technical Report, Airbus.

Allcock, D. (1999). *Abradable Stator Gas Turbine Labyrinth Seals.* PhD thesis, Cranfield University.

Allcock, D., Ivey, P., and Turner, R. (2002a). *Abradable Stator Gas Turbine Labyrinth Seals Part 1: Experimental Determination and CFD Modelling of Effective Friction Factors for Honeycomb Materials.* 38th AIAA/ASME/SAE/SAEE Joint Propulsion Conference and Exhibit Indianapolis, Indiana, USA, AIAA-2002-3936.

Allcock, D., Ivey, P., and Turner, R. (2002b). *Abradable Stator Gas Turbine Labyrinth Seals Part 2: Numerical Modelling of Different Seal Geometries and the Construction of a Second Generation Desing Tool.* 38th AIAA/ASME/SAE/ASEE Joint Propulsion and Exhibit, Indianapolis, Indiana, USA, AIAA-2002-3937.

Anderson, J. (1995). *Computational Fluid Dynamics: The Basics with Applications.* McGraw Hill: ISBN 0-07-001685-2.

Arts, T., Boerrigter, H., Carbonaro, M., Charbonnier, J.-M., Degrez, G., Olivari, D., Riethmuller, M., and Van den Braembussche, R. (1994). *Meaurement Techniques in Fluid Dynamics.* ISBN:D/1994/0238/417.

ATAG (2000). *Aviation and the Environment.* Technical Report, Air Transport Action Group.

Athavale, M. and Hendricks, R. (1996). *Seal Leakages for Honeycomb or Smooth Configurations.* NASA Conference Publication, Texas A+M University, 3344, pp. 281 – 291.

Baker, R. (1988). *An Introductory Guide to Flow Measurement - 2nd Edition.* London: Mechancial Engineering, ISBN: 1-86058-348-2.

Bayley, F. and Childs, P. (1994). *Air Temperature Rises in Compressor and Turbine Stator Wells.* Proceedings of the International Gas Turbine and Aeroengine Congress and Exposition, June 13th-16th, The Hague, The Netherlands, 94-GT-185.

Benedict, R. (1959). *Temperature Measurement in Moving Fluids.* Transactions of the ASME, ASME-59A-257.

Benvenuti, E., Ruggeri, G., and Tomasini, E. (1980). *Analytical and Experimental Development of Labyrinth Seals for Process Centrifugal Pumps.* 25th ASME Gas Turbine Conference, March, New Orleans, USA.

Boeing (2005). *Current Market Outlook.* Technical Report, Boeing.

Bowman, C. and Faulkner, D. (1994). *Measuring Product Advantages using Competitive Benchmarking and Customer Perceptions.* Journal of Long Range Planning, 27 (no.1) pp. 119–132.

Brownell, J., Millward, J., and Parker, R. (1989). *Nonintrusive Investigations into Life-Size Labyrinth Seal Flow Fields.* Journal of Engineering for Gas Turbines and Power, vol. 111: pp. 335–342.

BS (1042.1). *British Standard 1042-1 and EN-ISO 5167-1 - Measurement of Mass Flow by means of Differential Pressure Devices Part 1: Orifice Plates, Nozzles and Venturi Tubes inserted in Circular Cross - Section Conduits Running Full.* (1997). Technical Report, BS1042.1.

Chan, Y., Buggeln, R., and McDonald, H. (1987). *3-D Dynamic Labyrinth Seal Analysis Aero Propulsion Laboratory.* Air Force Wright Aeronautical Laboratories, AFWAL-TR-87-2009.

Chappel, D., Howe, H., and Vo, L. (2001a). *Abradable Seal Testing: Blade Temperatures During Low Speed Rub Event.* 37th AIAA/ASME/SAE/ASEE Joint Propulsion Conference, July 8th-11th, Salt Lake City, Utah, USA, AIAA-2001-3479.

Chappel, D., Vo, L., and Howe, H. (2001b). *Gas Path Blade Tip Seals: Abradable Seal Material Testing at Utility Gas and Steam Operating Conditions.* Proceedings of the ASME Turb oExpo, June 4-7th, New Orleands, Louisiana, USA, 2001-GT-0583.

Chew, J. (1985). *Prediction of Flow in Rotating Disc Systems using the $k - \epsilon$ Turbulence Model.* International Journal of Turbo and Jet Engines, vol. 2: pp. 253–261.

Chew, J. and Vaughan, C. (1988). *Numerical Predictions for the Flow Induced by an Enclosed Rotating Disc.* ASME Gas Turbine and Aeroengine Congress and Exposition, June 6th-9th, Amsterdam, The Netherlands, 88-GT-127.

Childs, D., Elrod, D., and Hale, K. (1988). *Rotordynamic Coefficient and Leakage Test Results for Interlock and Tooth on Stator Labyrinth Seals.* Gas Turbine Aeroengine Conference and Exhibition, June 6-9th, Amsterdam, The Netherlands, 88-GT-87.

Childs, D., Elrod, D., and Hale, K. (1989). *Annular Honeycomb Seals: Test Results for Leakage and Rotordynamic Coefficients; Comparison to Labyrinth and Smooth Configurations.* Journal of Tribology, vol. 111: pp. 293–301.

Childs, P., Dullenkopf, K., and Bohn, D. (2006). *Internal Air Systems Experimental Rig Best Practice.* Proceedings of ASME Turbo Expo 2006: Power for Land, Sea and Air, May 8-11th, Barcelona, Spain, GT-2006-90215.

Chocua, G., Shyy, W., and Moore, J. (2001). *Thermophysical Modelling for Honeycomb - Stator Gas Annular Seals.* 35th AIAA Thermophysics Conference, 11th-14th June, Anaheim, California, USA, AIAA-2001-2757.

Chougule, H., Ramchandran, R., Ramerth, D., and Kandala, R. (2006). *Numerical Investigation of Worn Labyrinth Seals.* Proceedings of ASME Turbo Expo 2006: Power for Land, Sea and Air, May 8-11th, Barcelona, Spain, GT-2006-90690.

Chupp, R., Aksit, M., Ghasripor, F., Turnquist, N., and Demiroglu, M. (2001). *Advanced Seals for Industrial Turbine Applications.* 37th AIAA/ASME/SAE/ASEE Joint Propulsion Conference and Exhibit, Salt Lake City, Utah, USA, AIAA-2001-3626.

Chupp, R., Ghasripoor, F., Turnquist, A., Demiroglu, M., and Aksit, M. (2002a). *Advanced Seals for Industrial Turbine Applications: Dynamic Seal Development.* Journal of Propulsion and Power, vol. 18(no. 6): pp. 1260–1266.

Chupp, R., Ghasripor, F., Moore, G., Kalv, L., and Johnston, R. (2002b). *Applying Abradable Seals to Industrial Gas Turbines.* 38th AIAA/ASME/SAE/ASEE Joint Propulsion Conference and Exhibit Indianapolis, Indiana, USA, AIAA-2002-3795.

Collins, D., Teixeira, J., Crudgington, P., and Ivey, P. (2006). *Numerical Modelling of Three Dimensional Honeycomb Labyrinth Seals Employing a Simplified Approach.* Proceedings of ASME Turbo Expo 2006: Power for Land, Sea and Air, May 8-11th, Barcelona, Spain, GT-2006-90850.

Curley, T. (2005). *Energy 2005.* Technical Report, Rolls Royce.

Daily, J. and Nece, R. (1960). *Chamber Dimension Effects on Induced Flow and Frictional Resistance of Enclosed Rotating Disks.* Journal of Basic Engineering, pp. 217–232.

Davis, R. and Mattingly, G. (1977). *Numerical Modelling of Turbulent Flow through Thin Orifice Plates.* Proceedings of the Symposium on Flow in open Channels and Closed Conduits, February 23rd-25th, Gaithersburg, MD, USA.

Dean, R. (1974). *Reynolds Number Dependence of Skin Friction in Two Dimensional Rectangular Duct Flow and a Discussion of the Law of the Wake.* IC Areo Report No. 74-11.

Demko, J., Morrison, G., and Rhode, D. (1990). *Effect of Shaft Rotation on the Incompressible Flow in a Labyrinth Seal.* Journal of Propulsion, vol. 6 (no. 2).

Denecke, J., Dullenkopf, K., Wittig, S., and Bauer, H.-J. (2005a). *Experimental Investigation of the Total Temperature Increase and Swirl Development in Rotating Labyrinth Seals.* Proceedings of ASME Turbo Expo 2005: Power for Land, Sea and Air, June 6-9th, Reno-Tahoe, Nevada, USA, GT-2005-68677.

Denecke, J., Farber, J., Dullenkpof, K., and Bauer, H.-J. (2005b). *Dimensional Analysis and Scaling of Rotating Seals.* Proceedings of the ASME Turbo Epxo: Power for Land, Sea and Air, June 6-9th, Reno-Tahoe, Nevada, USA, GT-2005-68676.

Denecke, J., Schramm, V., Kim, S., and Wittig, S. (2003). *Influence of Rub Grooves on Labyrinth Seal Leakage.* Journal of Turbomachinery, vol. 125: pp. 387–393.

Denekce, J., Schramm, V., Kim, S., and Wittig, S. (2002). *Influence of Rub Grooves on Labyrinth Seal Leakage.* Proceedings of ASME Turbo Epxo, June 3rd-6th, Amsterdam, The Netherlands, GT-2002-30244.

Dereli, Y. and Eser, D. (2003). *Flow Calculations in Labyrinth Seals with Half Chamber Cavities.* Hardonic Journal, vol. 26: pp. 203–210.

Dereli, Y. and Eser, D. (2004a). *Flow Calcuations in Straight Through Labyrinth Seals by using Moody's Friction Factor Model.* Journal of Mathematical and Computational Applications, vol. 9(no. 3): pp. 435–442.

Dereli, Y. and Eser, D. (2004b). *Flow Calculation in Labyrinth Seals using a Two Control Volume Model.* Hadronic Journal, vol. 27: pp. 693–704.

Dinc, S., Reluzco, G., Turnquist, N., Lawen, J., Kerber, O., Brunner, F., Crum, G., Stuck, A., R., C., Marks, P., Chiu, R., Wolfe, C., and Crudgington, P.

(1998). *Brush Seals in Industrial Gas Turbines - Turbine Section Interstage Sealing.* 34th AIAA/ASME/SAE/ASEE Joint Propulsion Conference and Exhibit, July 13-15th, Cleveland, Ohio, USA, AIAA-98-3175.

Doebelin, E. (2004). *Measurement Systems - Application and Design, 5th Edition.* New York : McGrawhill - Higher Education, ISBN: 0071194657.

Dong-Chung, C. and Rhode, D. (2003). *Development of a 2-D CFD Approach for Computing 3-D Honeycomb Labyrinth Seal Leakage.* Proceedings of ASME Turbo Expo, Power for Land, Sea and Air, June 16th-19th, Atlanta, Georgia, USA, GT2003-38238.

Douglas, J., Gasiorek, J., and Swaffield, J. (1995). *Fluid Mechanics.* Harlow : Longman Scientific and Technical. ISBN: 0-582-23408-5.

DTI (2003). *Energy Review White Paper.* Technical Report, Department of Trade and Industry.

EC (2005). *2005 EU Green Paper: Doing More with Less.* Technical Report, European Comission.

Egli, A. (1935). *The Leakage of Steam through Labyrinth Seals.* Transactions of the ASME, 57: pp. 115–122.

El-Gamal, H., Awad, T., and El-Sayed, S. (1987a). *Models of Labyrinth Sealings for Turbomachinery Part 1: Formulation of the Problem and Study of Geometrical Effects.* Journal of Modelling, Simulation and Control, vol. 10 (no. 4): pp. 41–52.

El-Gamal, H., Awad, T., and El-Sayed, S. (1987b). *Models of Labyrinth Sealings for Turbomachinery Part 2: The Leakage Problem.* Journal of Modelling, Simulation and Control, vol. 10 (no. 4): pp. 53–64.

El-Gamal, H., Awad, T., and Saber, H. (1996). *Leakage from Labyrinth Seals under Stationary and Rotating Conditions.* Tribology International, vol. 29 (no. 4): pp. 291–297.

ESDU (74028). *74028 - One Dimensional Compressible Gas Flow in Ducts.* Technical Report, ESDU.

ESDU (80012). *80012 - Dynamic Sealing of Fluids. i: Guide to Selection of Rotary Seals.* Technical Report, ESDU. (1980)

ESDU (82009). *82009 - Pressure Losses Across Orifice Plates, Perforated Plates and Thick Orifice Plates in Ducts (1982).* Technical Report, ESDU. (1982)

ESDU (82035). *82035 - Temperature Measurement: Thermocouples.* Technical Report, ESDU. (1982)

Fellenstien, J., DellaCorte, C., Moore, K., and Boyes, E. (1996). *High Temperature Brush Seal Tuft Testing of Metallic Bristles versus Chrome Carbide.* 32nd AIAA/ASME/SAE/ASEE Joint Propulsion Conference, July 1-3rd, Lake Buena Vista, Florida, USA, AIAA-1996-2908.

Ferguson, J. (1988). *Brushes as High Performance Gas Turbine Seals.* ASME Gas Turbine and Aeroengine Congress, June 6th-9th, Amsterdam, The Netherlands, 88-GT-182.

Ferziger, J. and Peric, M. (2002). *Computational Methods for Fluid Dynamics.* Springer, ISBN:3-540-42074-6.

Franceshini, G., Morgan, J., Jones, T., and Gillespie, D. (2006). *A Slow Speed Rotating Test Facility for Characterising the Stiffness of Brush Seals.* Proceedings of ASME Turbo Expo 2006: Power for Land, Sea and Air, May 8-11th, Barcelona, Spain, GT-2006-91355.

Frederick, C. and Reeves, P. (1970). *Comparison of Experimental and Ideal Leakage Flows through Labyrinth Seals for Very Small Pressure Differences.* Technical Memorandum, NASA-TM X-1958.

GBD (2002a). *Air Travel - Greener by Design: Improving Operations, the Technology Challenge, Market Based Options.* Technical Report, Department of Trade and industry Foresight Programme.

GBD (2002b). *Air Travel - Greener by Design: The Challenge.* Technical Report, Department of Trade and industry Foresight Programme.

Ghasripoor, F., Turnquist, N., Kowalczyk, M., and Couture, B. (2004). *Wear Prediction of Strip Seals Through Conductance.* Proceedings of ASME Turbo Expo 2004: Power for Land, Sea and Air, June 14-17th, Vienna, Austria, GT-2004-53297.

Green, S. (2006). *Russian Roulette Sparks Cold Front.* Power Engineering International: January (2006).

Ha, T. and Childs, D. (1992). *Friction Factor Data for Flat Plate Tests of Smooth and Honeycomb Surfaces.* Journal of Tribology, vol. 114 (no. 4): pp. 722–730.

Ha, T., Morrison, G., and Childs, D. (1992). *Friction Factor Characteristics for Narrow Channels with Honeycomb Surfaces.* Journal of Tribology, vol. 114 (no. 4): pp. 714–721.

Hannis, J. and Corry, R. (1996). *Analysis and Validation of Turbine Disc Cooling.* Proceedings of the International Gas Turbine and Aeroengine Congress and Exhibition, June 10th-13th, Birmingham, UK, 96-GT-97.

He, L.-D., Yuan, X., Jin, Y., and Z.-Y., Z. (2001). *Experimental Investigation of the Sealing Performance of Honeycomb Labyrinth Seals.* Chinese Journal of Aeronautics, vol. 14 (no. 1): pp. 13–17.

Heffner, F. (1960). *A General Method for Correlating Labyrinth Seal Leak-Rate Data.* Journal of Basic Engineering (Series D), vol. 82: pp. 265–275.

Herring, S. (2006). *Exploiting the Capabilities of Experiment and Numerical Methods.* Proceedings of ASME Turbo Expo 2006: Power for Land, Sea and Air, May 8-11th, Barcelona, Spain, GT-2006-90208.

Hirano, T., Guo, Z., and Kirk, R. (2003). *Application of CFD Analysis for Rotating Machinery, Part 2: Labyrinth Seal Analysis.* Proceedings of ASME Turbo Expo 2003, Power for Land, Sea and Air, June 16-19, Atlanta, Georgia, USA GT2003-38394.

Hodkinson, B. (1939). *Estimation of Leakage through a Labyrinth Gland.* Proceedings of the Institute of Mechanical Engineers, vol. 141: pp. 283–288.

IATA (2004). *Environmental Review 2004.* Technical Report, International Air Transport Association (IATA).

IEA (2004). *2004 World Energy Outlook.* Technical Report, International Energy Agency.

Isles, J. (2006). *Inventing the Future.* Power Engineering International: June (2006).

Jerie, J. (1948). *Flow through Straight through Labyrinth Seals.* Proceedings of the 7th International Conference of Applied Mechanics, vol. 2: pp. 70–82.

Jinming, X., Ambrosia, M., and Rhode, D. (2004). *Effects of Rub Groove Shape on the Leakage of Abradable Stepped Labyrinth Seals.* 40th AIAA/ASME/SAE/ASEE Joint Propulsion Conference and Exhibit, 11-14th July, Fort Lauderdale, Florida, USA, AIAA-2004-3718.

Kearton, W. (1955). *The Flow of Air through Radial Labyrinth Glands.* Proceedings of the Insititue of Mechancial Engineers, vol. 169: pp. 539–550.

Kearton, W. and Keh, T. (1952). *Leakage of Air through Labyrinth Glands of Staggered Type.* Proceedings of the Institute of Mechanical Engineers, vol. 166: pp. 180–195.

Koening, H. and Bowley, W. (1972). *Labyrinth Seal Analysis.* Journal of Lubrcation Technology (Series F), vol. 94 (no. 1): pp. 5–11.

Komotori, K. and Miyake, K. (1977). *Leakage Characteristics of Labyrinth Seals with High Rotational Speed.* Tokyo Joint Gas Turbine Congress, May 22nd-27th, Tokyo, Japan.

Kool, G., Kloosterman, B., Rademaker, E., Soemarwoto, B., Bingen, F., Paolillo, R., and Cloud, D. (2006). *Advanced Seal Test Rig Validation and Operation.* Proceedings of ASME Turbo Expo 2006: Power for Land, Sea and Air, May 8-11th, Barcelona, Spain, GT-2006-90915.

Lewis, L. (2002). *In-Engine Measurements of Temperature Rises in Axial Compressor Shrouded Stator Cavities.* Proceedings of ASME Turbo Expo, June 3rd-6th, Amsterdam, The Netherlands, 2002-GT-30245.

Li, D. and Merkle, C. (2001). *Analysis of Leakage Characteristics of Labyrinth Seals in a Steam Turbine.* Proceedings of ASME FEDSM'01, ASME Fluids Engineering Division Summer Meeting, May 29th- June 1st, New Orleans, Louisiana, USA, FEDSM2001-18060, pp. 727–732.

Mahler, F. and Boyes, E. (1995). *The Application of Brush Seals in Large Commercial Jet Engines.* 31st AIAA/ASME/SAE/ASEE Joint Propulsion Conference and Exhibit, July 10-12th, San Diego, USA, AIAA-95-2617.

Martin, H. (1908). *Labyrinth Packings.* The Engineer, pp. 35–36.

Matthias, N., Surken, N., Sulda, E., and Walkenhorst, J. (2006). *Design Features and Performance Details of Brush Seals for Turbine Applications.* Proceedings of ASME Turbo Expo 2006: Power for Land, Sea and Air, May 8-11th, Barcelona, Spain, GT-2006-90404.

McGreehan, W., Haaser, F., and Sherwood, L. (1987). *Labyrinth Seal Flow Measurement by Tracer Gas Injection.* Gas Turbine Aeroengine Conference and Exhibition, May 31st - June 4th, Anaheim, California, USA, 87-GT-187.

McGreehan, W. and Ko, S. (1989). *Power Dissipation in Smooth and Honeycomb Labyrinth Seals.* Gas Turbine and Aeroengine Congress and Exposition, June 4th-8th, Toronto, Canada, 89-GT-220.

McGreehan, W. F. and Ko, S. (1988). *Labflo Users Manual Version 1.0 - Computer Program for Calculating Labyrinth Seal Flow and Windage.* Users Manual

Menedez, R. and Xia, J. (2000). *Recent Developments in Brush Seals for Large Industrial Gas Turbines.* 36th AIAA/ASME/SAE/ASEE Joint Propulsion Conference and Exhibit, July 16-19th, Huntsville, Alabama, USA, AIAA-00-3374.

Meyer, C. and Lowrie, J. (1975). *The Leakage through Straight and Slant Labyrinths and Honeycomb Seals.* Journal for Engineering and Power, vol. 96 (no. 4): pp. 495–502.

Michaud, M., Vakil, A., and Meganathan, A. (2003). *An Experimental Study of Labyrinth Seal Flow.* Proceedings of IJPG2003, International Joint Power Generation Conference, June 16th-19th, Atlanta, Georgia, USA, ASME-2003/40097.

Millward, J. and Edwards, M. (1996). *Windage Heating of Air Passing through Labyrinth Seals.* Journal of Turbomachinery, vol. 118(no. 2): pp. 414–419.

Miyake, K. and Duh, W.-C. (1990). *Leakage Characteristics of Labyrinth Seal.* Journal of the Chinese Society of Mechanical Engineers, vol. 11(no. 4): pp. 334–348.

Moore, J. (2001). *Three Dimensional CFD Rotordynamic Analysis of Gas Labyinth Seals.* Proceedings of DETC'01, ASME Design Engineering Technical Conferences and Computers and Information in Engineering Conference, September 9th-12th, Pittsburgh, Pennsylvania, USA, DETC2001/VIB-21394.

Morrison, G., Johnson, J., and Tatterson, G. (1988). *3-D Laser-Anemometer Measurements in a Labyrinth Seal.* Gas Turbine Aeroengine Conference and Exhibition, June 6-9th, Amsterdam, The Netherlands, 88-GT-63.

Morrsion, G., Johnson, M., and Tatterson, G. (1991). *3-D Laser Measurements in a Labyrinth Seal.* Journal of Engineering for Gas Turbines and Power, vol. 113:pp. 119–125.

Munson, J., Grant, D., and Agrawal, G. (2001). *Foil Face Seal Development.* 37th AIAA/ASME/SAE/ASEE Joint Propulsion Conference, July 8th-11th, Salt Lake City, Utah, USA, AIAA-2001-3483.

Munson, J. and Steinetz, B. (1994). *Specific Fuel Consumption and Increased Thrust Performance Benefits Possible with Advanced Seal Technology.* 30th AIAA/ASME/SAE/ASEE Joint Propulsion Conference, Indianaplois, June 27th-29th, Indiana, USA, AIAA-94-2700.

NSF (2000). *Science and Engineering Indicators 2000.* Technical report, National Science Foundation.

Paolillo, R., Cloud, D., Vashist, T., Bingen, F., and Kool, G. (2006). *Rotating Seal Rig Experiments: Test Results and Analysis Modelling.* Proceedings of ASME Turbo Expo 2006: Power for Land, Sea and Air, May 8-11th, Barcelona, Spain, GT-2006-90957.

Pastrama, R. M., Wolfe, C., Turnquist, N., and Burnett, M. E. (2001). *Improved Steam Leakage Control with a Brush Seal Design.* Proceedings of the 30th Turbomachinery Symposium, Texas A&M University, Houston, Texas, USA, pp. 33–38.

Porter, M. (1979). *How Competitive Forces Shape Strategy.* Harvard Business Review, Mar-Apr, pp. 137–145.

POST (2003). *Postnote: Aviation and the Envrionment.* Technical report, Parliamentary Office of Science and Technology. April (2003), no. 195.

Prasad, B., Sethu Manavalan, V., and Nanjunda Roa, N. (1997). *Computational and Experimental Investigations of Straight through Labyrinth Seals.* Proceedings of the 1997 International Gas Turbine and Aeroengine Congress and Exposition, Orlando, Florida, USA, 97-GT-326.

Proctor, M. and Delgado, I. (2004). *Leakage and Power Loss Test Results for Competing Turbine Engine Seals.* Proceedings of ASME Turbo Expo: Power for Land, Sea and Air, June 14-17th, Vienna, Austria.

Read, B. (2005). *A Tale of Two Engines.* Aerospace International, September (2005).

Reader-Harris, M. (1986). *Computation of Flow through Orifice Plates.* Proceedings of Flow Measurement, pp. 1907–1917.

Reader-Harris, M. and Keegans, W. (1986). *Comparison of Computation and LDV Measurement of Flow through Orifice and Perforated Plates, and Computation of the Effect of Rough Pipework on Orifice Plates.* Proceedings of the International Symposium on Fluid Flow Measurement, Washington D.C., USA, 12.1.

Rhode, D. (2002). *Measured Flow Oscillations and Instabilitities in Labyrinth Seal Cavities.* Journal of Propulsion and Power, vol. 18 (no. 6): pp. 1267–1272.

Rhode, D. and Adams, R. (2001a). *Computed Effect of Rub Groove Size on Stepped Labyrinth Seal Performance.* Tribology Transactions, vol. 44 (no. 4): pp. 523–532.

Rhode, D. and Adams, R. (2004a). *Relative Axial Dispalcement Leakage Effects on Straight through Labyrinth Seals with Rub Grooves.* 40th AIAA/ASME/SAE/ASEE Joint Propulsion Conference and Exhibit, 11-14th July, Fort Lauderdale, Florida, USA, AIAA-2004-3716.

Rhode, D. and Adams, R. (2004b). *Rub Groove Width and Depth Effects on Flow Predictions for Straight through Labyrinth Seals.* Journal of Tribology, vol. 126: pp. 781–787.

Rhode, D. and Allen, B. (1998). *Visualisation and Measurement of Rub-Groove Leakge Effects on Straight through Labyrinth Seals.* International Gas Turbine and Aero Engine Congress and Exhibition, Stockholm, Sweden, 98-GT-506.

Rhode, D. and Allen, B. (2001). *Measurement and Visualisation of Leakage Effects of Rounded Teeth Tips and Rub-Grooves on Stepped Labyrinths.* Journal of Engineering for Gas Turbines and Power, vol. 123: pp. 604–611.

Rhode, D., Broussard, D., and Veldana, S. (1993). *Labyrinth Seal Leakage Resistance and Visualisation Experiments in a Novel, Variable Configuration Geometry.* Tribology Transactions, vol. 36(no. 2): pp. 213–218.

Rhode, D. and Guidry, M. (1993a). *Importance of Labyrinth Seal Through-Flow Deflection for Enlarging Clearance without Increased Leakage.* Tribology Transactions, vol. 36 (no. 3): pp. 477–483.

Rhode, D. and Guidry, M. (1993b). *A New Approach for Stabilising Labyrinth Seal Leakage.* Tribology Transactions, vol. 36 (no. 2): pp. 219–224.

Rhode, D. and Hibbs, R. (1989). *A Comparitive Investigation of Corresponding Annular and Labyrinth Seal Flow Fields.* Gas Turbine Aeroengine Congress and Exhibition, June 4-8th, Toronto, Canada.

Rhode, D. and Hibbs, R. (1992). *Tooth Thickness Effect on the Performance of Gas Labyrinth Seals.* Journal of Tribology, vol. 114: pp. 790–795.

Rhode, D., Ko, S., and Morrison, G. (1994a). *Experimental and Numerical Assessment of an Advanced Labyrinth Seal.* Tribology Transactions, vol. 37 (no. 4): pp. 743–750.

Rhode, D., Ko, S., and Morrison, G. (1994b). *Leakage Optimisation of Labyrinth Seals using a Navier Stokes Code.* Tribology Transactions, vol. 37 (no. 1): pp. 105–110.

Rhode, D. and Nail, G. (1992). *Computation of Cavity-by-Cavity Flow Development in Generic Labyrinth Seals.* Journal of Tribology, vol. 114: pp. 47–51.

Rhode, D. and Sobolik, S. (1986). *Simulation of Subsonic Flow through a Generic Labyrinth Seal.* Journal of Engineering for Gas Turbines and Power, vol. 108 (no. 4): pp. 674–680.

Roderick, M. and Farquhar, G. (2002). *The Cause of Decreased Pan Evaporation over the Past 50 Years.* Science, vol. 298: pp. 1410–1411.

Schlichtling, H. (1955). *Boundary Layer Theory.* Pergamon Press Ltd, London.

Schramm, V., Wllenborg, K., Kim, S., and Wittig, S. (2002). *Influence of a Honeycomb Facing on the Flow through a Stepped Labyrinth Seal.* Journal of Engineering for Gas Turbines and Power, vol. 124: pp. 140–146.

Shapiro, W. and Chupp, R. (2004). *Numerical, Analytical, Experimental Study of Fluid Dynamic Forces in Seals Volume 5: Description of Sseal Dynamics Code Dyseal and Labyrinth Seals Code KTK.* NASA/CR-2004-213199/VOL5.

Smith, C. (1978). *American Airlines Operational and Maintenance Experience with Aerodynamic Seals and Oil Seals in Turbofan Engines.* AGARD (Advisory Group for Aerospace Research and Development) Conference Proceedings (vol. 273): 6-7th April, London.

Sneck, H. (1974). *Labyrinth Seal Literature Survey.* Journal of Lubrication Technology (Series F), vol. 96: pp. 579–582.

Stalk, G. (1988). *Time - the Next Source of Competitive Advantage.* Harvard Business Review; July-August (1988), pp. 41–51.

Stanhill, G. and Cohen, S. (2001). *Global Dimming: A Review of the Evidence.* Agricultural and Forest Meteorology, vol. 107: pp. 255–278.

Steinetz, B. and Hendricks, R. (1998). *Advanced Seal Technology Goals in Meeting Next Generation Turbine Engine Goals.* NASA Publication, NASA/TM 1998/206961.

Stephen, D. and Hogg, S. (2003). *Development of Brush Seal Technology for Steam Turbine Retro-Fit Applications.* Proceedings of IJPG03, International Joint Power Generation Conference, June 16-19th, 2003, Altanata, Georgia, USA, IJPG2003-40103.

Stocker, H. (1975). *Advanced Labyrinth Seal Design Performance for High Pressure Ratio Gas Turbines.* ASME Winter Annual Meeting, Nov 30th - Dec 4th, Houston, Texas, USA.

Stocker, H. (1977). *Aerodynamic Performance of Conventional and Advanced Labyrinth Seals with Solid-Smooth, Abradable and Honeycomb Lands.* NASA/CR-135307.

Stocker, H. (1978). *Determining and Improving Labyrinth Seal Performance in Current and Advanced High Performance Gas Turbines.* AGARD (Advisory Group for Aerospace Research and Development) Conference Proceedings (vol. 273): 6-7th April, London.

Stodola, A. (1927). *Steam and Gas Turbines.* New York: McGraw Hill.

Stoff, H. (1980). *Incompressible Flow in a Labyrinth Seal.* Journal of Fluid Mechanics, vol. 100(no. 4): pp. 817–829.

Sturgess, G. (1988). *Application of CFD to Gas Turbine Engine Secondary Flow Systems - the Labyrinth Seal.* AIAA/ASME/SAE/ASEE 24th Joint Propulsion Conference, July 11th-13th, Boston, Massachusetts, USA, AIAA-88-3203.

Sulda, E. (1999). *Retractable Brush Seal Optimises Efficiency and Availability for Cycling and Baseload Steam Turbines.* Power Engineering, November (1999).

Sutherland, K. (2003). *Profile of Fluid Sealing Industry: 3rd Edition.* ISBN: 1-85617-418-2.

The Standard (2005). *Focus: Japan dream rides on 787*; May 12th. Newspaper Article, The Standard - China's Business Newspaper.

Vakili, A., Meganathan, A., Michaud, M., and Radhakrishnan, S. (2005). *An Experimental and Numerical Study of Labyrinth Seal Flow.* Proceedings of ASME Turbo Expo 2005: Power for Land, Sea and Air, June 6-9th, Reno-Tahoe, Nevada, USA, GT-2005-68224.

Vakili, A., Meganathan, J., and Ayyalasomayajula, S. (2006). *Advanced Labyrinth Seals for Steam Turbine Generators.* Proceedings of ASME Turbo Expo 2006: Power for Land, Sea and Air, May 8-11th, Barcelona, Spain, GT-2006-91263.

Vermes, G. (1961). *A Fluid Mechanics Approach to Labyrinth Seal Leakage Problem.* Journal of Basic Engineering, 83(1): pp. 161 – 169.

Wang, Y., Young, C., Snowsill, G., and Scanlon, T. (2004). *Study of Airflow Features through Step Seals in the Presence of Dis-Engagement due to Axial Movement.* Proceedings of ASME Turbo Expo 2004: Power for Land, Sea and Air, June 14-17th, 2004, Vienna, Austria, GT2004-53056.

Waschka, W., Wittig, S., and Kim, S. (1990). *Influence of High Rotational Speeds on the Heat Transfer and Discharge Coefficients in Labyrinth Seals.* Gas Turbine and Aeroengine Congress and Exhibition, June 11th-14th Brussels, Belgium, pages 90–GT–330.

WEB1 (2006). *www.smiths-group.com/page.aspx?thelang=001lngdef&pointerid=c874270c2a1149* Internet Reference, John Crane, Smiths Group. (28/06/2006).

WEB2 (2006). *www.jameswalker.biz/group/pdf_downloads.html;* Joint Integrity Programme. Internet Reference, James Walker. (06/07/2006).

WEB3 (2005). *www.airbus.com/en/aircraftfamilies;* Internet Reference, Airbus. (3/11/2005).

White, F. (2003). *Fluid Mechanics: 5th Edition.* McGraw Hill, ISBN:0-07-240217-2.

Willenborg, K., Kim, S., and Wittig, S. (2001). *Effects of Reynolds Number and Rressure Ratio on Leakage Loss and Heat Transfer in a Stepped Labyrinth Seal.* Journal of Turbomachinery, vol. 123: pp. 815–822.

Willenborg, K., Schramm, V., Kim, S., and Wittig, S. (2002). *Infuence of a Honeycomb Facing on the Heat Transfer in a Stepped Labyrinth Seal.* Journal of Engineering for Gas Turbines and Power, vol. 124: pp. 133–139.

Williams, B. and Flack, R. (1992 (Revised 1993)). *The Calculation of Rotordynamic Coefficients for Labyrinth Seals: A Manual for the Computer Program Laby3.* ROMAC Report No. 344: UVA Report No. UVA/643092/MAE92/444.

Wittig, S. (1992). *Heat Transfer Analysis in Rotating Gas Turbine Components - Experimental Techniques and Non-Intrusive Diagnostics.* Proceedings of the Third International Symposium on Transport Phenomena and Dynamics of Rotating Machinery, vol. 2: pp. 3–24.

Wittig, S., Dorr, L., and Kim, S. (1982). *Scaling Effects on Leakage Losses in Labyrinth Seals.* 27th International Gas Turbine Conference and Exhibit, April 18th-22nd, London, England, 82-GT-157.

Wittig, S., Dorr, L., and Kim, S. (1983). *Scaling Effects on Leakge Losses in Labyrinth Seals.* Journal of Engineering for Power, vol. 105 (no. 2): pp. 305–309.

Wittig, S., Jacobsen, K., Schelling, U., and Kim, S. (1988). *Heat Transfer in Stepped Labyrinth Seals.* Journal of Engineering for Gas Turbines and Power, vol. 110: pp. 63–69.

Wittig, S., Schelling, U., Kim, S., and Jacobsen, K. (1987). *Numerical Predictions and Measurements of Discharge Cofficients in Labyrinth Seals.* ASME Gas Turbine Conference and Exhibition, Anaheim, California, USA, 87-GT-188.

Wolfe, C., Chiu, R. P., Cromer, R., Crum, G., Marks, P., Stuck, A.E.and Turnquist, N., Reluzco, G., and Dinc, O. (1997). *Brush Seals in Industrial Gas Turbines.* 33rd AIAA/AMSE/SAE/ASEE Joint Propulsion, Conference and Exhibit, July 6-9th, Seattle, Washington, AIAA-1997-2730.

Zabriske, W. and Sternlicht, B. (1959). *Labyrinth-Seal Leakage Analysis.* Journal of Basic Engineering (Series D), vol. 81 (no. 3): pp. 332–340.

Zhu, Y. and He, F. (1990). *Analysis of Leakage Characteristics of Labyrinth Seals.* Chinese Journal of Aeronautics, vol. 3 (no. 4): pp. 233–238.

Zimmermann, H. (1990). *Some Aerodynamic Aspects of Engine Secondary Air Systems.* Journal of Engineering for Gas Turbines and Power, vol. 112: pp. 223–228.

Zimmermann, H., Firshing, A., Dibelius, G., and Ziemann, M. (1986). *Friction Losses and Flow Distribution for Rotating Disks with Shielded and Protruding Bolts.* Journal of Engineering for Gas Turbine and Power, vol. 108 (no. 3): pp. 547–552.

Zimmermann, H., Kammerer, A., and Wolff, K. (1994). *Performance of Worn Labyrinth Seals.* Proceedings of the International Gas Turbine and Aeroengine Congress and Exposition, June 13th-16th, The Hague, The Netherlands, 94-GT-131.

Zimmermann, H. and Wolff, K. (1987). *Comparison between Empirical and Numerical Labyrinth Flow Correlations.* Gas Turbine Conference and Exhibition, May 31st - June 4th, Anaheim, California, USA, 87-GT-86.

Zimmermann, H. and Wolff, K. (1998). *Air Systems Correlations Part 1: Labyrinth Seals.* International Gas Turbine and Aeroengine Congress and Exhibition, June 2nd-5th, Stockholm, Sweden, 98-GT-206.

Appendix A

Tables Summarising Key Variables

Test Sequence	Pressure Reading System	Pressure Ratio	Stator Wall	n	Tp (mm)	Ph (mm)	Ht (mm)	Tooth Radii (mm)	Gd (mm)	Gw (mm)	Axial Position (mm)
1	Scanivalve	1.20 - 3.50	Smooth	4	0.50	10	10	≤ 0.10	N/A	N/A	0.00
2	Scanivalve	1.20 - 3.50	Flat HC	4	0.50	10	10	≤ 0.10	0.00	0.00	0.00
											+1.50
3	Scanivalve	1.20 - 3.50	Smooth	4	0.50	10	10	≤ 0.10	N/A	N/A	0.00
4	Scanivalve	1.20 - 3.50	G1 HC	4	0.50	10	10	≤ 0.10	0.60	3.00	0.00
											$\pm$1.50
											$\pm$3.00
5	Scanivalve	1.20 - 3.50	Smooth	4	0.50	10	10	≤ 0.10	N/A	N/A	0.00
6	Scanivalve	1.20 - 3.50	G2 HC	4	0.50	10	10	≤ 0.10	1.20	6.00	0.00
											$\pm$1.50
											$\pm$3.00
7	Chell	1.20 - 3.50	Smooth	4	0.50	10	10	≤ 0.10	N/A	N/A	0.00
8	Chell	1.20 - 3.50	G2 HC	4	0.50	10	10	≤ 0.10	1.20	6.00	0.00
											$\pm$1.50
											$\pm$3.00

Table A.1: Summary of key variables used in the experimental programme (see section (A.1) for further information).

CFD Sequence	2-D/ 3-D	Pressure Ratio	Stator Wall	Wall Treatment	Steady/ Unsteady	n	Tp (mm)	Ph (mm)	Ht (mm)	Tooth Radii (mm)	Orien-tation	Notes
1	3-D	1.20 - 1.40	3.20mm HC	WF	Steady	1	1.00	10	10	0.00	D	
2	3-D	1.50 - 1.60	3.20mm HC	WF	Steady	1	1.00	10	10	0.00	D	CF
2	3-D	1.50 - 1.60	3.20mm HC	WF	Unsteady	1	1.00	10	10	0.00	D	
3	3-D	1.20 - 1.40	3.20mm HC	WF	Steady	1	1.00	10	10	0.00	A	
4	3-D	1.50 - 1.60	3.20mm HC	WF	Steady	1	1.00	10	10	0.00	A	CF
4	3-D	1.50 - 1.60	3.20mm HC	WF	Unsteady	1	1.00	10	10	0.00	A	
5	3-D	1.20 - 1.40	1.60mm HC	WF	Steady	1	1.00	10	10	0.00	D	
6	3-D	1.50 - 1.60	1.60mm HC	WF	Unsteady	1	1.00	10	10	0.00	D	
6	3-D	1.50 - 1.60	1.60mm HC	WF	Steady	1	1.00	10	10	0.00	D	CF
7	3-D	1.20 - 1.60	1.60mm HC	WF	Steady	1	1.00	10	10	0.00	A	
8	2-D	1.20 - 1.60	3.20mm HC	WF	Steady	1	1.00	10	10	0.00	D	
9	2-D	1.20 - 1.60	3.20mm HC	BL	Steady	1	1.00	10	10	0.00	D	
10	2-D	1.20 - 1.60	3.20mm HC	WF	Steady	1	1.00	10	10	0.00	A	
11	2-D	1.20 - 1.60	3.20mm HC	BL	Steady	1	1.00	10	10	0.00	A	
12	2-D	1.20 - 1.60	1.60mm HC	WF	Steady	1	1.00	10	10	0.00	D	
13	2-D	1.20 - 1.60	1.60mm HC	WF	Steady	1	1.00	10	10	0.00	A	
14	2-D	1.20 - 1.60	3.20mm HC	WF	Steady	1	1.00	10	10	0.00	D	E
15	2-D	1.20 - 1.60	3.20mm HC	WF	Steady	1	1.00	10	10	0.00	A	E1
16	2-D	1.20 - 1.60	3.20mm HC	WF	Steady	1	1.00	10	10	0.00	A	E2
17	2-D	1.20 - 1.60	1.60mm HC	WF	Steady	1	1.00	10	10	0.00	D	E
18	2-D	1.20 - 1.60	1.60mm HC	WF	Steady	1	1.00	10	10	0.00	A	E1
19	2-D	1.20 - 1.60	1.60mm HC	WF	Steady	1	1.00	10	10	0.00	A	E2

Table A.2: Summary of key variables and modelling techniques used in developing the simplification routine (see section (A.1) for further information).

CFD Sequence	2-D/ 3-D	Turbu- lence Model	Pressure Ratio	Stator Wall	Wall Treatment	Steady/ Unsteady	n	Tp (mm)	Ph (mm)	Ht (mm) (mm)	Tooth Radii	Cl (mm)	Notes
1	2-D	$k-\epsilon$ Std.	1.20 - 3.50	Smooth	BL	Steady	4	0.50	10	10	0.00	0.50	PA
2	2-D	$k-\epsilon$ Std.	1.20 - 3.50	Smooth	BL	Steady	4	0.50	10	10	0.00	1.00	PA
3	2-D	$k-\epsilon$ Std.	1.20 - 3.50	Smooth	BL	Steady	4	0.50	10	10	0.10	0.50	
4	2-D	$k-\epsilon$ Std.	1.20 - 3.50	Smooth	BL	Steady	4	0.50	10	10	0.10	1.00	
5	2-D	$k-\epsilon$ Std.	1.20 - 3.50	Smooth	BL	Steady	4	0.50	10	10	0.10	2.00	
6	2-D	$k-\epsilon$ RNG	1.20 - 3.50	Smooth	BL	Steady	4	0.50	10	10	0.10	0.50	
7	2-D	$k-\epsilon$ RNG	1.20 - 3.50	Smooth	BL	Steady	4	0.50	10	10	0.10	1.00	
8	2-D	$k-\epsilon$ RNG	1.20 - 3.50	Smooth	BL	Steady	4	0.50	10	10	0.10	2.00	
9	2-D	$k-\epsilon$ Real	1.20 - 3.50	Smooth	BL	Steady	4	0.50	10	10	0.10	0.50	
10	2-D	$k-\epsilon$ Real	1.20 - 3.50	Smooth	BL	Steady	4	0.50	10	10	0.10	1.00	
11	2-D	$k-\epsilon$ Real	1.20 - 3.50	Smooth	BL	Steady	4	0.50	10	10	0.10	2.00	
12	2-D	$k-\omega$	1.20 - 3.50	Smooth	BL	Steady	4	0.50	10	10	0.10	0.50	CF
13	2-D	$k-\omega$	1.20 - 3.50	Smooth	BL	Steady	4	0.50	10	10	0.10	1.00	CF
14	2-D	$k-\omega$ SST	1.20 - 3.50	Smooth	BL	Steady	4	0.50	10	10	0.10	0.50	CF
15	2-D	$k-\omega$ SST	1.20 - 3.50	Smooth	BL	Steady	4	0.50	10	10	0.10	1.00	CF
16	2-D	$k-\epsilon$ Std.	1.20 - 3.50	Smooth	WF	Steady	4	0.50	10	10	0.10	0.50	
17	2-D	$k-\epsilon$ Std.	1.20 - 3.50	Smooth	WF	Steady	4	0.50	10	10	0.10	1.00	
18	2-D	$k-\epsilon$ Std.	1.20 - 3.50	Smooth	WF	Steady	4	0.50	10	10	0.10	2.00	
19	2-D	$k-\epsilon$ RNG	1.20 - 3.50	Smooth	WF	Steady	4	0.50	10	10	0.10	0.50	
20	2-D	$k-\epsilon$ RNG	1.20 - 3.50	Smooth	WF	Steady	4	0.50	10	10	0.10	1.00	
21	2-D	$k-\epsilon$ RNG	1.20 - 3.50	Smooth	WF	Steady	4	0.50	10	10	0.10	2.00	
22	2-D	$k-\epsilon$ Real	1.20 - 3.50	Smooth	WF	Steady	4	0.50	10	10	0.10	0.50	
23	2-D	$k-\epsilon$ Real	1.20 - 3.50	Smooth	WF	Steady	4	0.50	10	10	0.10	1.00	
24	2-D	$k-\epsilon$ Real	1.20 - 3.50	Smooth	WF	Steady	4	0.50	10	10	0.10	2.00	

Table A.3: Summary of key variables and modelling techniques used in simulating the smooth stator experimental results (see section (A.1) for further information).

CFD Sequence	2-D/ 3-D	Turbu- lence Model	Pressure Ratio	Stator Wall	Wall Treatment	Steady/ Unsteady	n	Tp (mm)	Ph (mm)	Ht (mm) (mm)	Tooth Radii	Cl (mm)	Notes
1	2-D	$k-\epsilon$ RNG	1.20 - 3.50	Flat HC	WF	Steady	4	0.50	10	10	0.10	0.50	
2	2-D	$k-\epsilon$ RNG	1.20 - 3.50	Flat HC	WF	Steady	4	0.50	10	10	0.10	1.00	
3	2-D	$k-\epsilon$ RNG	1.20 - 3.50	Flat HC	WF	Steady	4	0.50	10	10	0.10	2.00	PA
4	2-D	$k-\epsilon$ RNG	1.20 - 3.50	G1 HC	WF	Steady	4	0.50	10	10	0.10	0.50	
5	2-D	$k-\epsilon$ RNG	1.20 - 3.50	G1 HC	WF	Steady	4	0.50	10	10	0.10	1.00	
6	2-D	$k-\epsilon$ RNG	1.20 - 3.50	G1 HC	WF	Steady	4	0.50	10	10	0.10	2.00	CF
7	2-D	$k-\epsilon$ RNG	1.20 - 3.50	G2 HC	WF	Steady	4	0.50	10	10	0.10	0.50	
8	2-D	$k-\epsilon$ RNG	1.20 - 3.50	G2 HC	WF	Steady	4	0.50	10	10	0.10	1.00	
9	2-D	$k-\epsilon$ RNG	1.20 - 3.50	G2 HC	WF	Steady	4	0.50	10	10	0.10	2.00	CF

Table A.4: Summary of key variables and modelling techniques used in simulating the honeycomb stator experimental results (see section (A.1) for further information).

CFD Sequence	2-D/ 3-D	Turbu- lence Model	Pressure Ratio	Stator Wall	Wall Treatment	Steady/ Unsteady	n	Tp (mm)	Ph (mm)	Ht (mm) (mm)	Tooth Radii	Cl (mm)	Notes
1	2-D	$k-\epsilon$ RNG	1.20 - 3.50	Smooth	WF	Steady	4	0.50	10	10	0.10	0.50	400 $\left(\frac{rad}{sec}\right)$
2	2-D	$k-\epsilon$ RNG	1.20 - 3.50	Smooth	WF	Steady	4	0.50	10	10	0.10	0.50	800 $\left(\frac{rad}{sec}\right)$
1	2-D	$k-\epsilon$ RNG	1.20 - 3.50	Smooth	WF	Steady	4	0.50	10	10	0.10	1.00	400 $\left(\frac{rad}{sec}\right)$
2	2-D	$k-\epsilon$ RNG	1.20 - 3.50	Smooth	WF	Steady	4	0.50	10	10	0.10	1.00	800 $\left(\frac{rad}{sec}\right)$

Table A.5: Summary of key variables and modelling techniques used in simulating rotational effects with a smooth stator (see section (A.1) for further information).

A.1 Notes to Tables (A.1) through (A.5)

Notes to Table (A.1)

1. Gw and Gd are planned sizes. Actual sizes attained can be found in table (3.1).
2. All smooth stator experiments carried out at three clearances: $0.50mm$, $1.00mm$ and $2.00mm$.
3. All honeycomb stator experiments carried out at four clearances: $0.00mm$, $0.50mm$, $1.00mm$ and $2.00mm$.

Notes to Tables (A.2) through (A.5)

1. WF: Wall function approach used to model the boundary layer.
2. BL: Enhanced wall treatment used to model the boundary layer.
3. CF: Convergence Failure.

Notes to Table (A.2)

1. Clearance held constant throughout at $1.00mm$.
2. Standard $k - \epsilon$ turbulence model used throughout.
3. D: Design Orientation.
4. A: Alternative Orientation.
5. E: Extreme Position.
6. E1: Extreme Position 1.
7. E2: Extreme Position 2.

Notes to Tables (A.3) through (A.5)

1. PA: Poor agreement obtained with experimental data.
2. ST: Two dimensional simplification technique used.

Appendix B

Historical Formulae used for the Labyrinth Seal

In 1908 the first heavily used formula to predict labyrinth seal performance was created by Martin (1908). This equation can be seen below in equation (B.1).

$$\dot{m}_{ID} = 5.68 C_d A \frac{P_{t(0)}}{\sqrt{(RT_{t(0)})}} \left[\frac{1 - \left(\frac{P_{s(n)}}{P_{t(0)}}\right)^2}{n - ln\frac{P_{s(n)}}{P_{t(0)}}} \right]^{\frac{1}{2}} \tag{B.1}$$

It was suggested by Martin that the constant in equation (B.1) is reduced because the equation is based upon a C_d of unity. A correction is required if the last throttling reaches choking conditions. All of the analysis has been based upon the assumption that the steam behaved as a perfect gas.

Egli (1935) rationally studied the problem of labyrinth seal leakage assuming small pressure drop ratios over successive teeth (< 1.25). The equation Egli derived can be seen in eqn. (B.2) with the equation for C_d in (B.3). The C_d was found to be constant above a Reynolds number of 10,000.

$$\dot{m}_{ID} = A C_d \frac{P_{t(0)}}{\sqrt{(RT_{t(0)})}} \left[\frac{1 - \left(\frac{P_{s(n)}}{P_{t(0)}}\right)^2}{n - ln\left(\frac{P_{s(n)}}{P_{t(0)}}\right)} \right]^{\frac{1}{2}} \tag{B.2}$$

$$C_d = \frac{Reduced\,Area\,Available\,for\,Flow}{Geometric\,Area\,Available\,for\,Flow} \tag{B.3}$$

Vermes (Vermes (1961)) reworked the Martin equation including the effects of a non-isothermal process and the effects of the carry over factor (COF). The Vermes eqn. can be seen in eqn. (B.4) with a calculation for (COF) shown in eqn. (B.5). The calculation for COF is purely based on geometry and the residual energy in a flat jet.

$$\dot{m}_{ID} = 5.76 C_d A \frac{P_{t(0)}}{\sqrt{(RT_{t(0)})}} \left[\frac{1 - \left(\frac{P_{s(n)}}{P_{t(0)}}\right)^2}{n - ln\frac{P_{s(n)}}{P_{t(0)}}} \right]^{\frac{1}{2}} \tag{B.4}$$

$$COF = \frac{kinetic\,energy\,upstream\,chamber}{kinetic\,energy\,upstream\,throttling} = \frac{8.52}{\frac{Ph-Tp}{Cl} + 7.23} \tag{B.5}$$

To solve choked seal flow fields use needs to be made of the Saint Venant-Wantzel equation (eqn. (B.6)). This equation gives the mass flow function in terms

of the static pressure felt on either side of a single orifice.

$$\frac{\dot{m}\sqrt{T_{t(0)}}}{AP_{t(0)}C_d} = \sqrt{\frac{2\gamma}{R(\gamma-1)}}\left[\left(\frac{P_{s(1)}}{P_{t(0)}}\right)^{\frac{2}{\gamma}} - \left(\frac{P_{s(1)}}{P_{t(0)}}\right)^{\frac{\gamma+1}{\gamma}}\right]^{\frac{1}{2}} \tag{B.6}$$

This applies to a single constriction. If $T_{t(0)}, A, R$ are considered constants then the following pressure distribution in eqn. (B.7) is possible.

$$\frac{\dot{m}\sqrt{T_{t(0)}}}{AC_d}\sqrt{\frac{R(\gamma-1)}{2\gamma}} = P_{t(0)}\left[\left(\frac{P_{s(n)}}{P_{t(n-1)}}\right)^{\frac{2}{\gamma}} - \left(\frac{P_{s(n)}}{P_{t(n-1)}}\right)^{\frac{\gamma+1}{\gamma}}\right]^{\frac{1}{2}} \tag{B.7}$$

This can be re-written as shown in eqn. (B.8)

$$\frac{\dot{m}\sqrt{T_{t(0)}}}{AC_d}\sqrt{\frac{R(\gamma-1)}{2\gamma}} = P_{t(n-1)}\left[\left(\frac{P_{s(n+1)}}{P_{t(n)}}\right)^{\frac{2}{\gamma}} - \left(\frac{P_{s(n+1)}}{P_{t(n)}}\right)^{\frac{\gamma+1}{\gamma}}\right]^{\frac{1}{2}} \tag{B.8}$$

For a choked seal the Mach number through the last restriction is one. Therefore the following isentropic relationship can be used to find the missing unknown:

$$\frac{P_{s(n)}}{P_{t(n-1)}} = \left(\frac{2}{\gamma+1}\right)^{\frac{\gamma}{\gamma-1}} \tag{B.9}$$

The Saint Venant-Wantzel equation can be used throughout for sub and supercritical seals by using it at each restriction. in this case an iterative scheme needs to be employed.

Appendix C

Experimental Figures

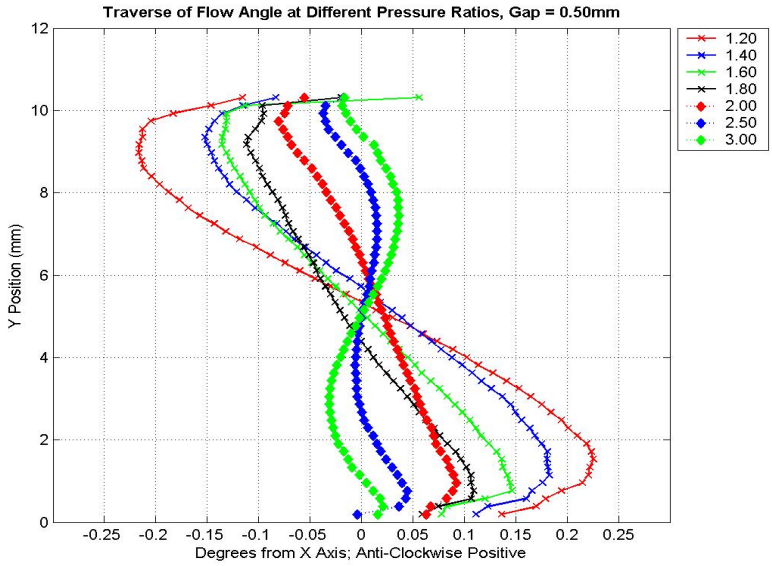

Figure C.1: Traverse of Flow Angle at Test Section Inlet versus Pressure Ratio for Running Clearance of $0.50mm$.

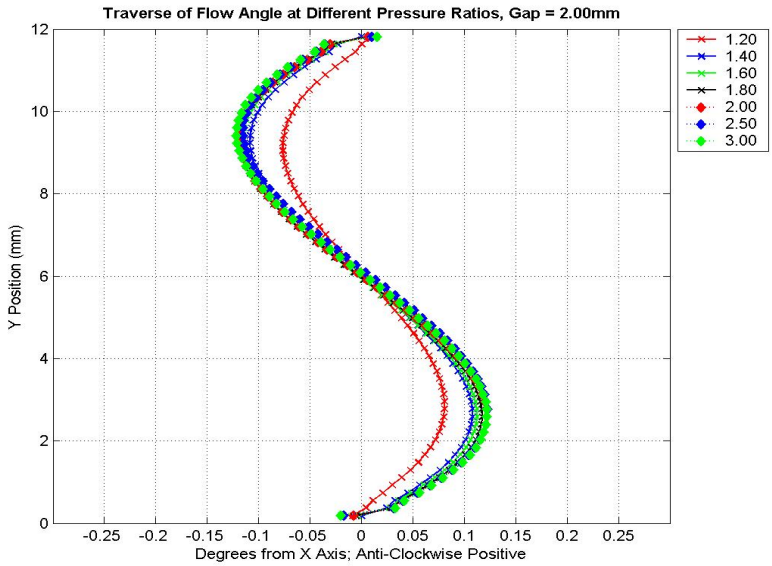

Figure C.2: Traverse of Flow Angle at Test Section Inlet versus Pressure Ratio for Running Clearance of $2.00mm$.

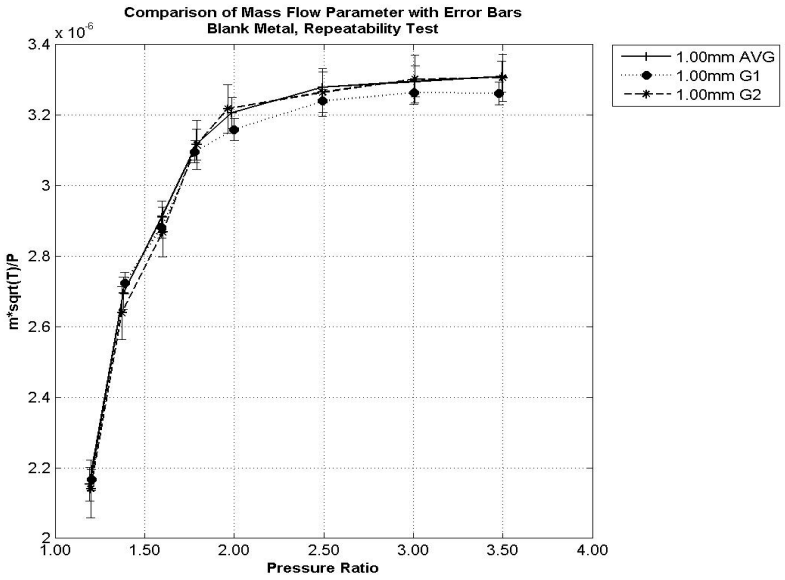

Figure C.3: $\left(\frac{\dot{m}\sqrt{T_{t(0)}}}{P_{t(0)}}\right)$ for Repeatable Tests at Gap = $1.00mm$

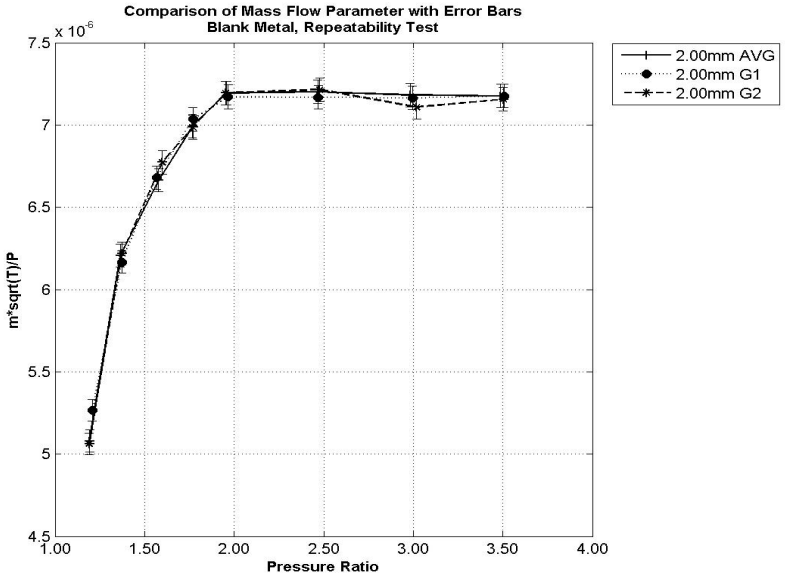

Figure C.4: $\left(\frac{\dot{m}\sqrt{T_{t(0)}}}{P_{t(0)}}\right)$ for Repeatable Tests at Gap = $2.00mm$

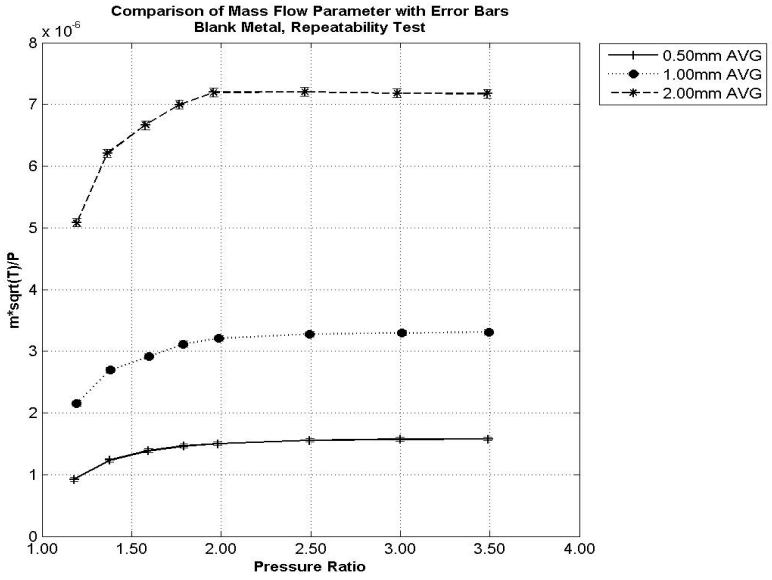

Figure C.5: $\left(\frac{\dot{m}\sqrt{T_{t(0)}}}{P_{t(0)}}\right)$: All Gaps

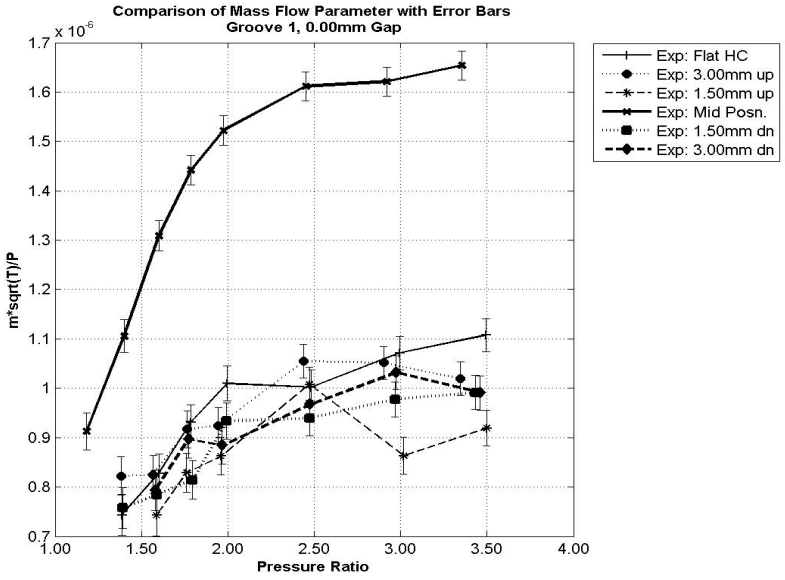

Figure C.6: $\left(\frac{\dot{m}\sqrt{T_{t(0)}}}{P_{t(0)}}\right)$ with Groove 1: Gap = $0.00mm$

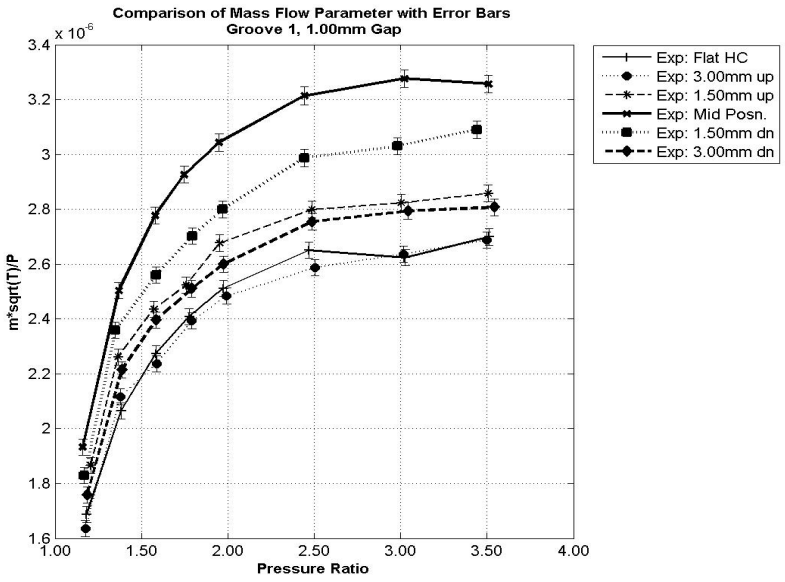

Figure C.7: $\left(\frac{\dot{m}\sqrt{T_{t(0)}}}{P_{t(0)}}\right)$ with Groove 1: Gap = $1.00mm$

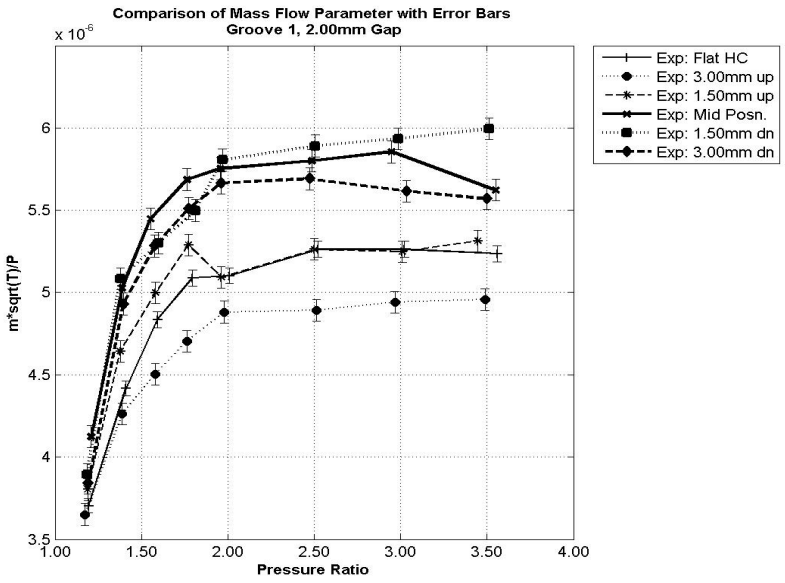

Figure C.8: $\left(\frac{\dot{m}\sqrt{T_{t(0)}}}{P_{t(0)}}\right)$ with Groove 1: Gap = $2.00mm$

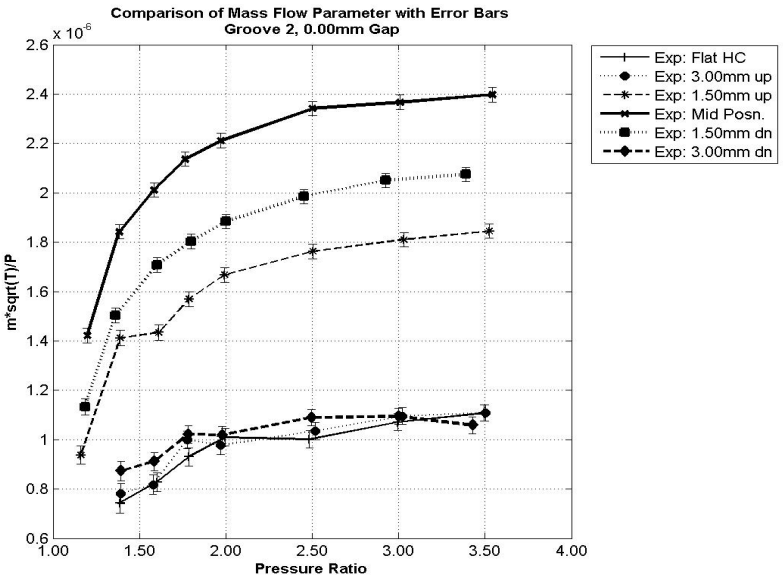

Figure C.9: $\left(\frac{\dot{m}\sqrt{T_{t(0)}}}{P_{t(0)}}\right)$ with Groove 2: Gap = $0.00mm$

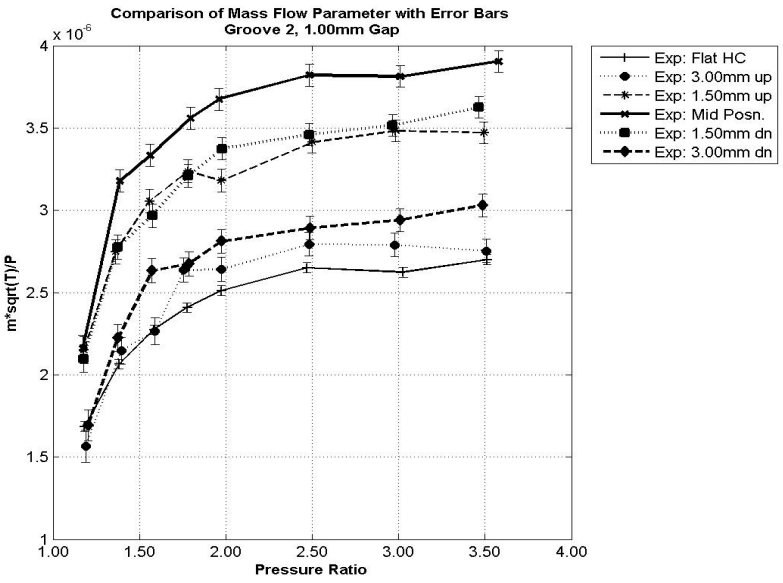

Figure C.10: $\left(\frac{\dot{m}\sqrt{T_{t(0)}}}{P_{t(0)}}\right)$ with Groove 2: Gap = $1.00mm$

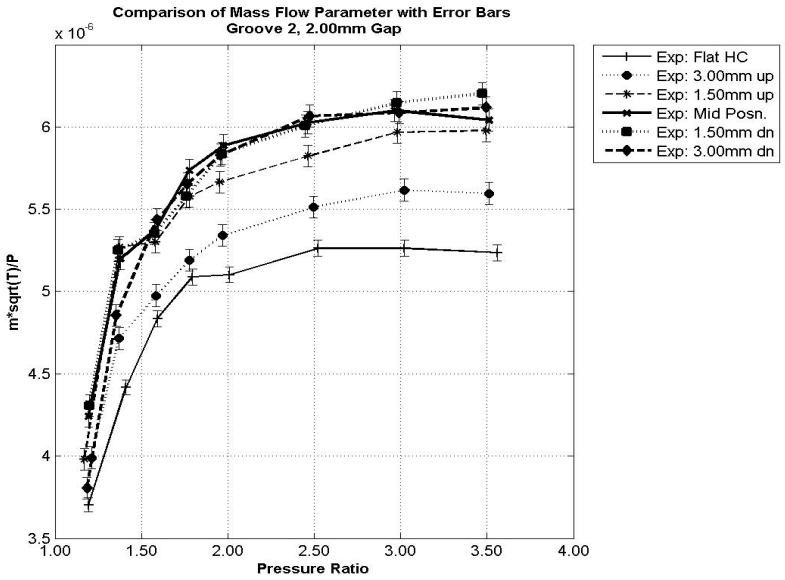

Figure C.11: $\left(\frac{\dot{m}\sqrt{T_{t(0)}}}{P_{t(0)}}\right)$ with Groove 2: Gap = 2.00mm

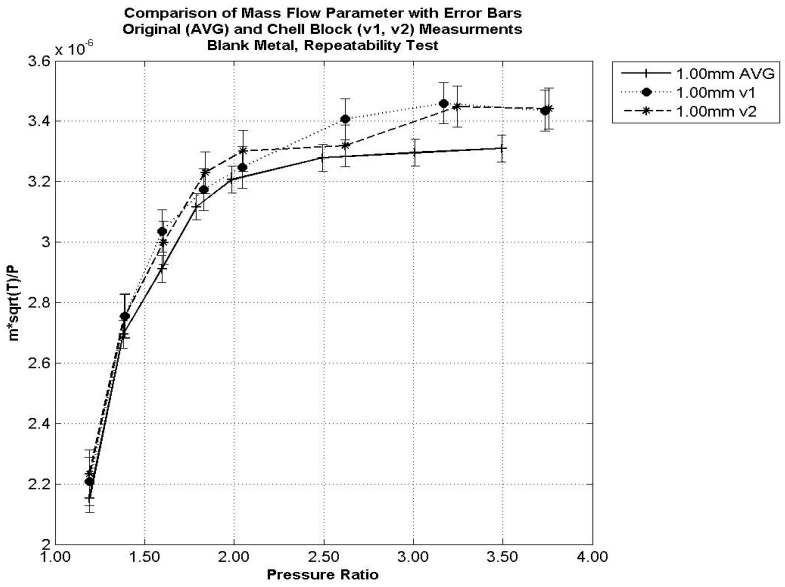

Figure C.12: $\left(\frac{\dot{m}\sqrt{T_{t(0)}}}{P_{t(0)}}\right)$ for Repeatable Tests When Using Chell Blocks (v1, v2) Compared Against Original (AVG): Gap = 1.00mm

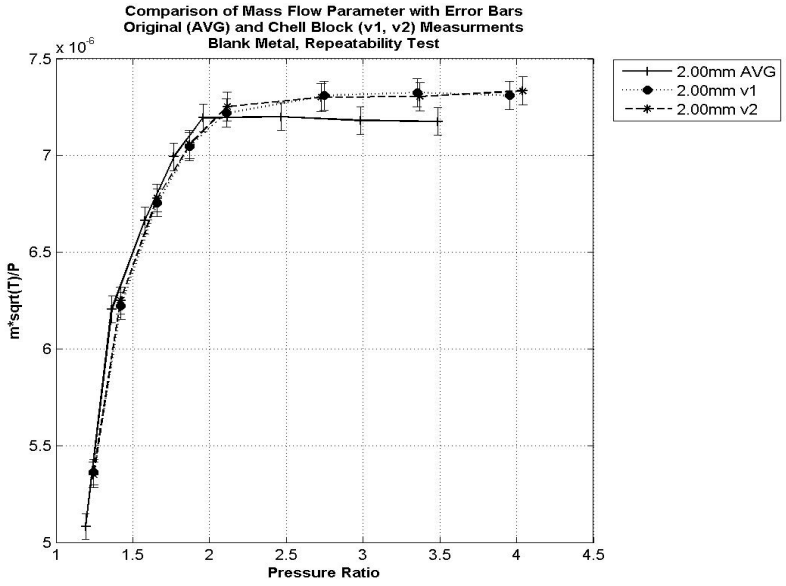

Figure C.13: $\left(\frac{\dot{m}\sqrt{T_{t(0)}}}{P_{t(0)}}\right)$ for Repeatable Tests When Using Chell Blocks (v1, v2) Compared Against Original (AVG): Gap = $2.00mm$

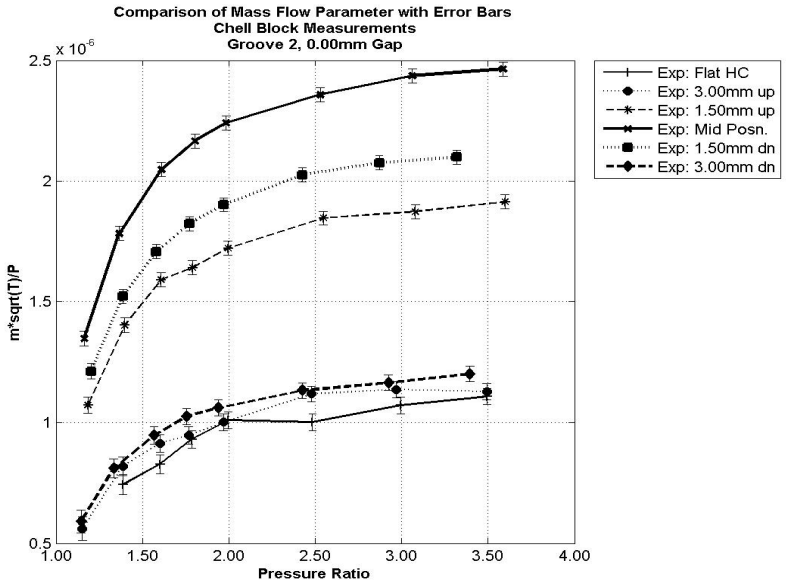

Figure C.14: $\left(\frac{\dot{m}\sqrt{T_{t(0)}}}{P_{t(0)}}\right)$ with Groove 2 Using Chell Blocks: Gap = $0.00mm$

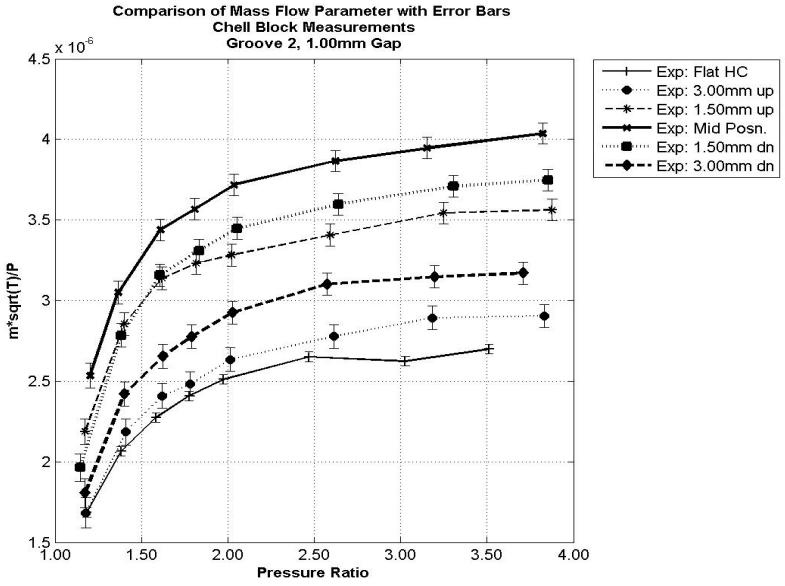

Figure C.15: $\left(\frac{\dot{m}\sqrt{T_{t(0)}}}{P_{t(0)}}\right)$ with Groove 2 Using Chell Blocks: Gap = $1.00mm$

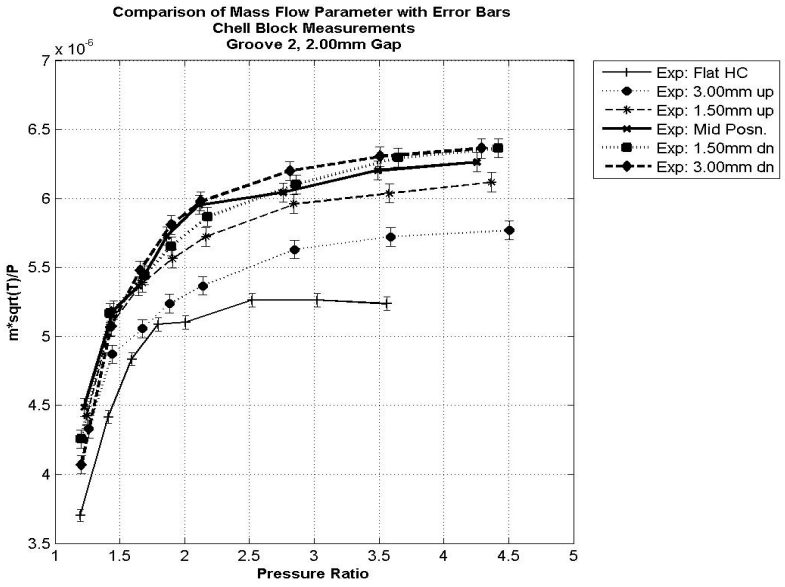

Figure C.16: $\left(\frac{\dot{m}\sqrt{T_{t(0)}}}{P_{t(0)}}\right)$ with Groove 2 Using Chell Blocks: Gap = $2.00mm$

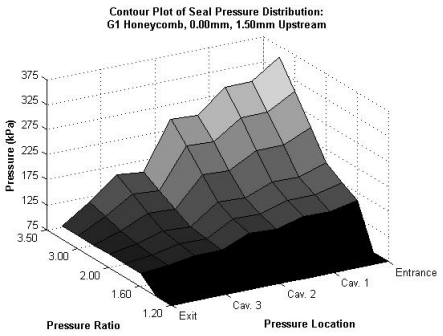

(a) 1.50mm Upstream

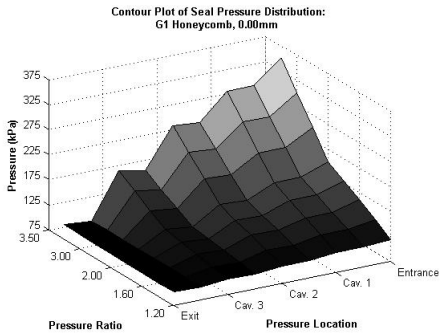

(b) Cental Position

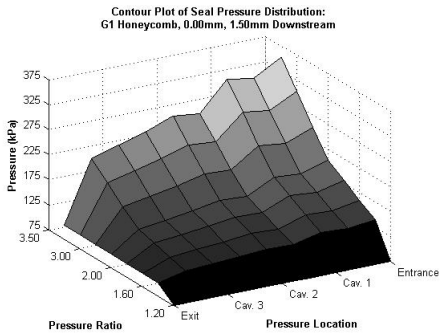

(c) 1.50mm Downstream

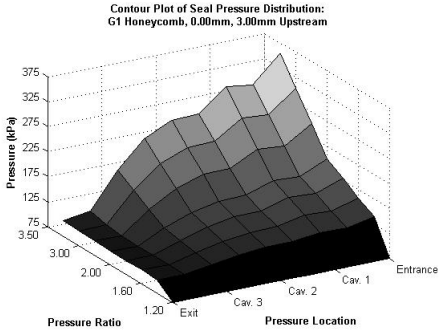

(d) 3.00mm Upstream

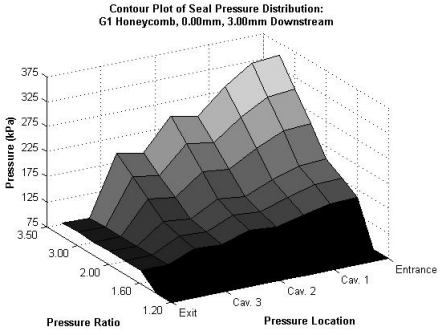

(e) 3.00mm Downstream

Figure C.17: Static Pressure Variations for G1 Honeycomb: 0.00mm Gap, All Positions
X-Axis: Pressure Location. Y-Axis: Pressure Z-Axis: Pressure Ratio.

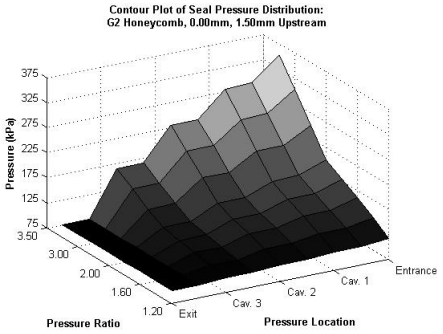

(a) 1.50mm Upstream

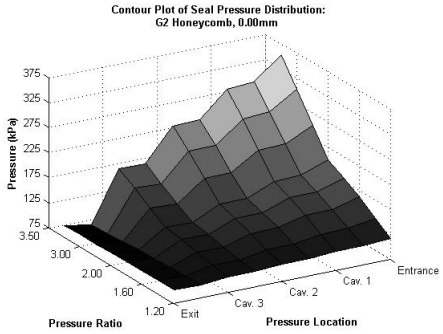

(b) Cental Position

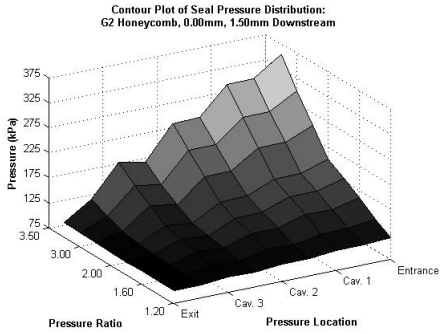

(c) 1.50mm Downstream

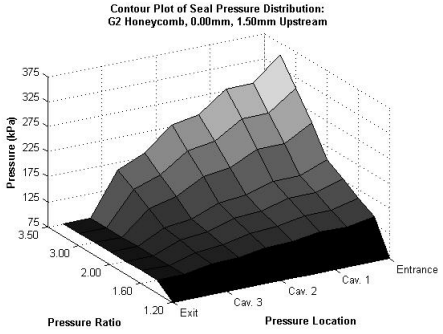

(d) 3.00mm Upstream

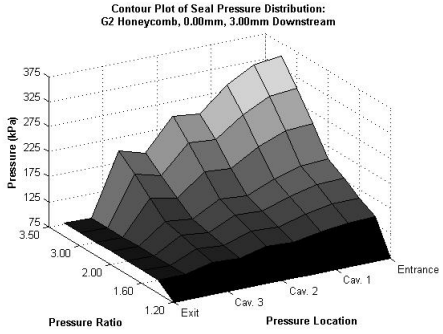

(e) 3.00mm Downstream

Figure C.18: Static Pressure Variations for G2 Honeycomb: 0.00mm Gap, All Positions
X-Axis: Pressure Location. Y-Axis: Pressure Z-Axis: Pressure Ratio.

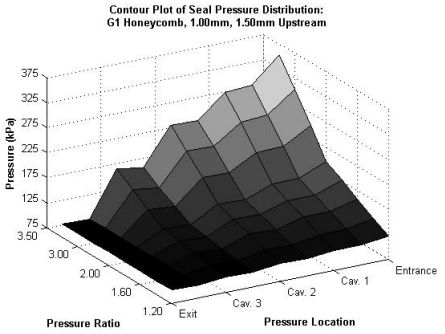

(a) 1.50mm Upstream

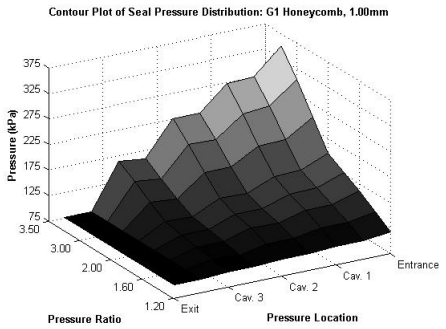

(b) Cental Position

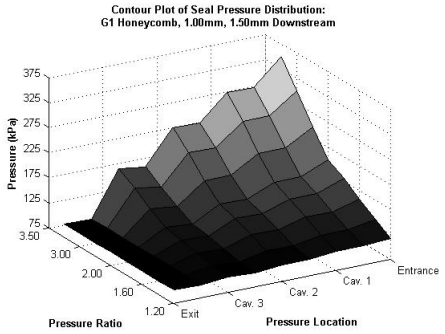

(c) 1.50mm Downstream

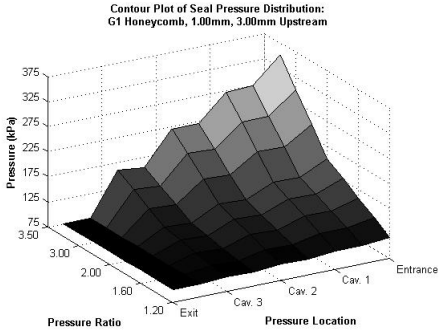

(d) 3.00mm Upstream

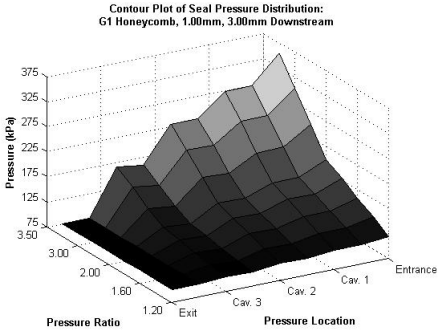

(e) 3.00mm Downstream

Figure C.19: Static Pressure Variations for G1 Honeycomb: 1.00mm Gap, All Positions
X-Axis: Pressure Location. Y-Axis: Pressure Z-Axis: Pressure Ratio.

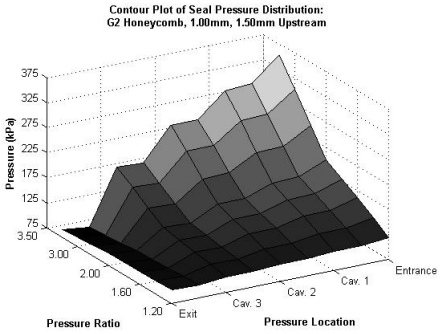

(a) 1.50mm Upstream

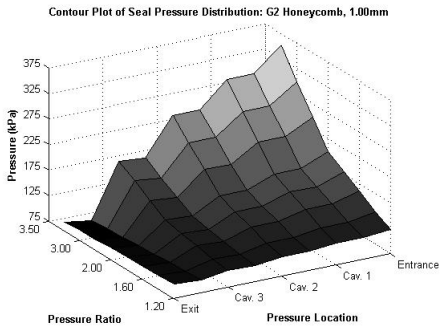

(b) Cental Position

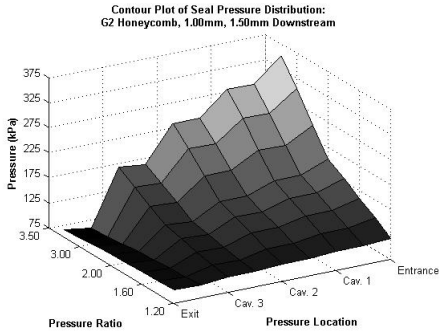

(c) 1.50mm Downstream

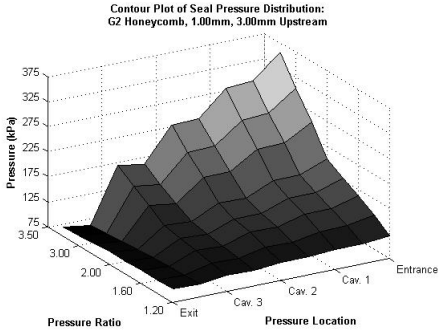

(d) 3.00mm Upstream

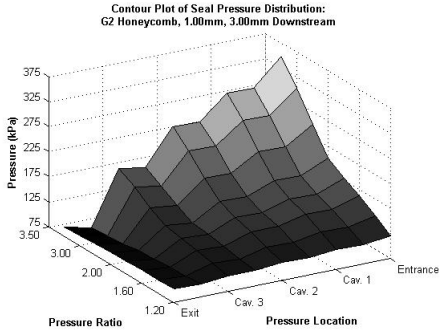

(e) 3.00mm Downstream

Figure C.20: Static Pressure Variations for G2 Honeycomb: 1.00mm Gap, All Positions
X-Axis: Pressure Location. Y-Axis: Pressure Z-Axis: Pressure Ratio.

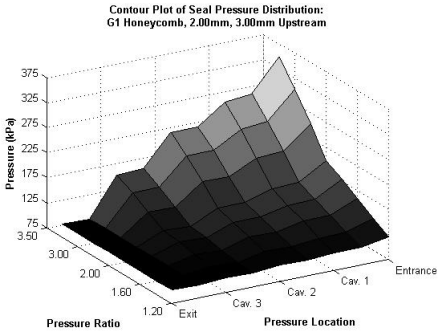

(a) 1.50mm Upstream

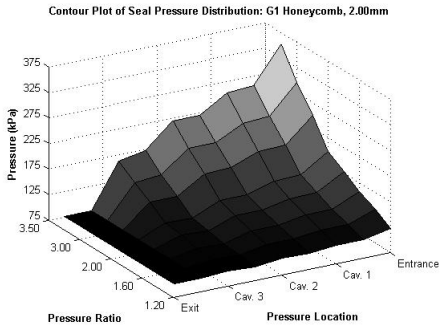

(b) Cental Position

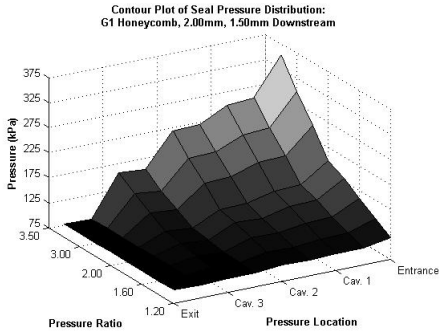

(c) 1.50mm Downstream

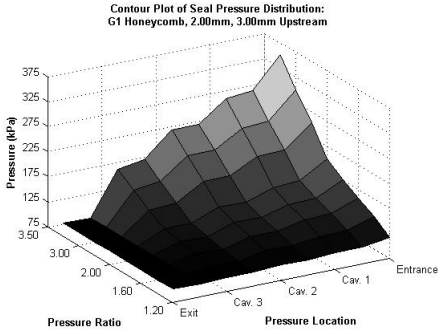

(d) 3.00mm Upstream

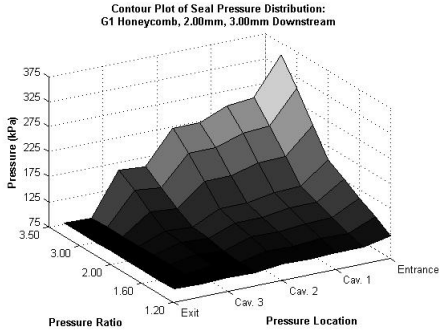

(e) 3.00mm Downstream

Figure C.21: Static Pressure Variations for G1 Honeycomb: 2.00mm Gap, All Positions
X-Axis: Pressure Location. Y-Axis: Pressure Z-Axis: Pressure Ratio.

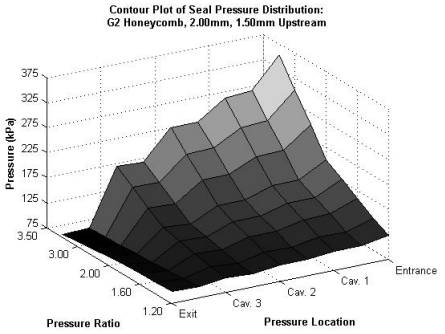

(a) 1.50mm Upstream

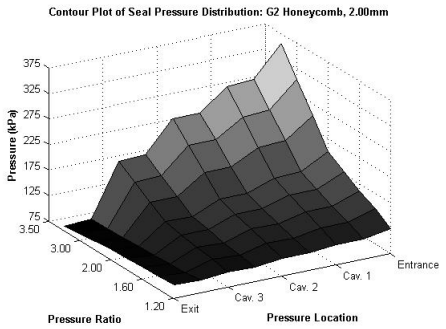

(b) Cental Position

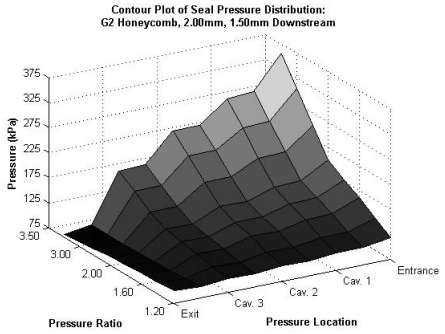

(c) 1.50mm Downstream

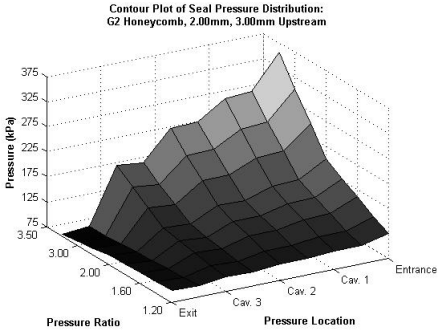

(d) 3.00mm Upstream

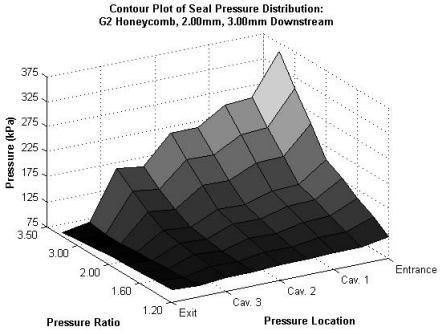

(e) 3.00mm Downstream

Figure C.22: Static Pressure Variations for G2 Honeycomb: 2.00mm Gap, All Positions
X-Axis: Pressure Location. Y-Axis: Pressure Z-Axis: Pressure Ratio.

Appendix D

Mass Flow Measurement Using Orifice Plates

A key procedure for the experiment involved determining the mass flow through the test section. The pressure ratio, and hence the mass flow, was kept constant throughout each run of the experiment. The mass flow was measured using pre-machined orifice plates, made and operated within the guidelines stated in BS (1042.1). Orifice plates are a differential pressure mass flow meter and, in line with common practice, station 1 refers to conditions upstream of the orifice and station 2 refers to conditions downstream. Limits on operation of orifice plates are given as:

- $d \geq 12.5mm$
- $50mm \leq D \leq 1000mm$
- $Re_D \geq 5000$ for $0.2 \leq \frac{d}{D} \leq 0.45$
- $\left(\frac{P_{s(1)} - \Delta P_s}{P_{s(1)}}\right) \geq 0.75$

The orifice plates used the standard (D) and $\left(\frac{D}{2}\right)$ static pressure tappings. (Other standard forms of orifice plate use corner or flange tappings). Equation (D.1) is used to calculate the mass flow.

$$\dot{m}_{ACT} = C_d E \epsilon_x \frac{\pi}{4} d^2 \sqrt{2\rho\Delta P_s} \tag{D.1}$$

Equations for C_d (based on the Reader Harris Gallagher equation: Baker (1988)), E and ϵ_x can be found in (D.2), (D.4) and (D.5) respectively. As the temperature measurement made was downstream at station 2 ϵ_x in eqn. (D.1) was replaced by ϵ_2. For an upstream temperature measurement ϵ_x in eqn. (D.1) is replaced by ϵ_1.

$$\begin{aligned}
C_d &= 0.5961 + 0.0261\left(\frac{d}{D}\right)^2 - 0.216\left(\frac{d}{D}\right)^8 + 0.000521\left(\left(\frac{10^6}{Re_D}\right)\left(\frac{d}{D}\right)\right)^{0.7} \\
&+ \left(0.0188 + 0.0063\left(19000\left(\frac{d}{DRe_D}\right)^{0.8}\right)\right)\left(\frac{d}{D}\right)^{3.5}\left(\frac{10^6}{Re_D}\right)^{0.3} \\
&+ \left(0.043 + 0.080e^{-10} - 0.123e^{-7}\right)(1 - 0.11) \\
&\times \left(19000\left(\frac{d}{DRe_D}\right)^{0.8}\right)\left(\frac{d}{D}\right)^4\left(1 - \left(\frac{d}{D}\right)^4\right)^{-1} \\
&- 0.031\left(\left(\frac{0.94}{1 - \left(\frac{d}{D}\right)^{-0.8}}\right) - 0.8\left(\frac{0.94}{1 - \left(\frac{d}{D}\right)}\right)^{1.1}\right)\left(\frac{d}{D}\right)^{13}
\end{aligned} \tag{D.2}$$

Where Re_D is based on pipe diameter, as shown in (D.3).

$$Re_D = \frac{\rho V D}{\mu} = \frac{4\dot{m}_{ACT}}{\pi D \mu} \tag{D.3}$$

E is a geometrical constant used in eqn. (D.1).

$$E = \frac{1}{\sqrt{1 - \left(\frac{d}{D}\right)^4}} \tag{D.4}$$

The expansibility factor (ϵ_x) in eqn. (D.1) can be calculated based upon upstream or downstream conditions. Formulae for these variables can be seen in eqn. (D.5).

$$\begin{aligned} \epsilon_1 &= 1 - \left(0.41 - 0.35\left(\frac{d^4}{D^4}\right)\right)\left(\frac{\Delta P_s}{\gamma P_{s(1)}}\right) \\ \epsilon_2 &= \epsilon_1 \left(\sqrt{1 + \left(\frac{\Delta P_s}{P_{s(2)}}\right)}\right) \end{aligned} \tag{D.5}$$

Uncertainties associated with the Reader Harris Gallagher equation (D.2) are given as:

- for $\left(0.10 \leq \frac{d}{D} < 0.20\right) - \left(0.7 - \left(\frac{d}{D}\right)\right)\%$
- for $\left(0.20 \leq \frac{d}{D} < 0.60\right) - 0.5\%$
- for $\left(0.60 \leq \frac{d}{D} < 0.75\right) - \left(1.667\left(\frac{d}{D}\right) - 0.5\right)\%$

Uncertainties in the expansibility factor ϵ_1 are given as:

$$\epsilon_1 = 4\left(\frac{\delta P_s}{P_{s(1)}}\right) \tag{D.6}$$

This is not to be taken as an accurate indication of the error in the mass flow measurement. For accuracy the mass flow measurement needs accurate readings of pressure and temperature. These need to be taken using an accurate method of calibration and data acquisition.
There are clear advantages when using an orifice plate to measure mass flow. These have been summarised by Baker (1988) as:

- Well defined and documented.
- Based on long experience.
- Uncertainty is calculable.
- Straightforward to install.

Orifice plate sizing needs to be an iterative process.

Appendix E

Numerical Theory Figures

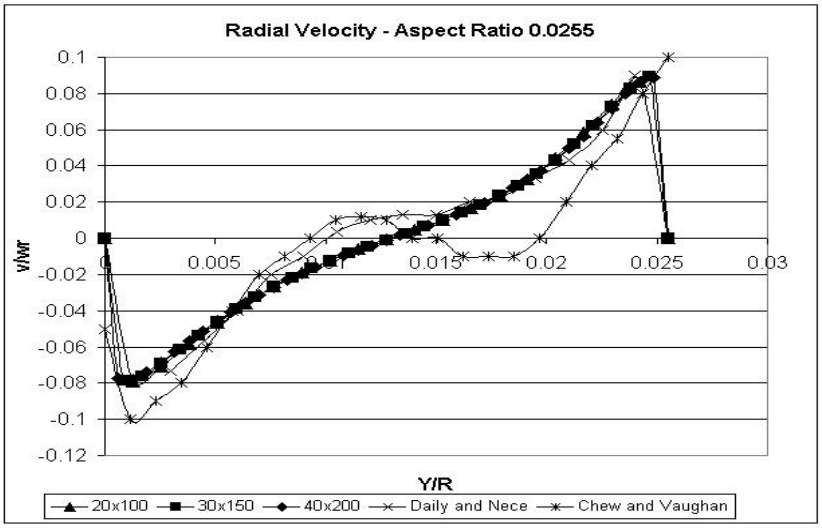

Figure E.1: Radial velocity profile taken corresponding to test point B in table (4.1).

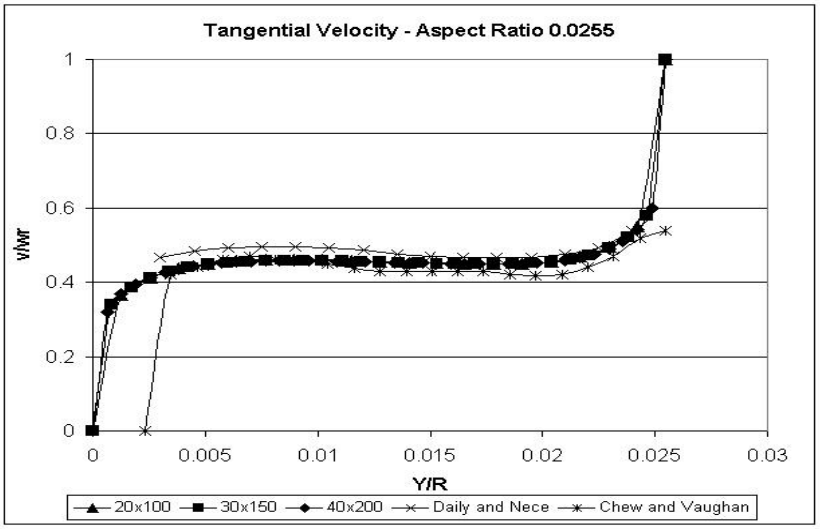

Figure E.2: Transverse velocity profile taken corresponding to test point B in table (4.1).

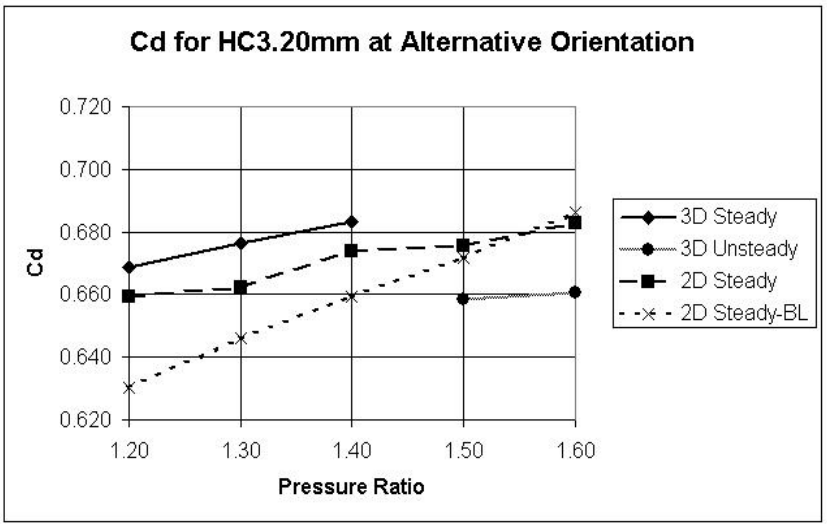

Figure E.3: C_d for HC = 3.20mm, Alternative-Orientation Condition.

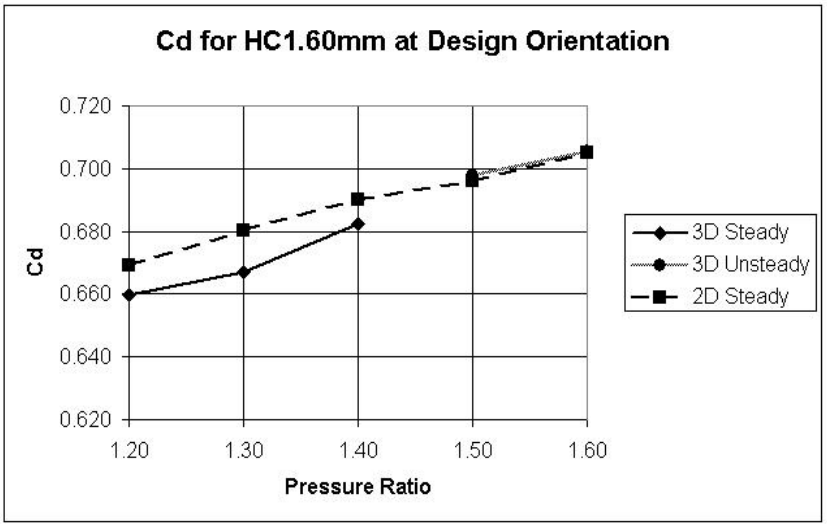

Figure E.4: C_d for HC = 1.60mm, Design-Orientation Condition.

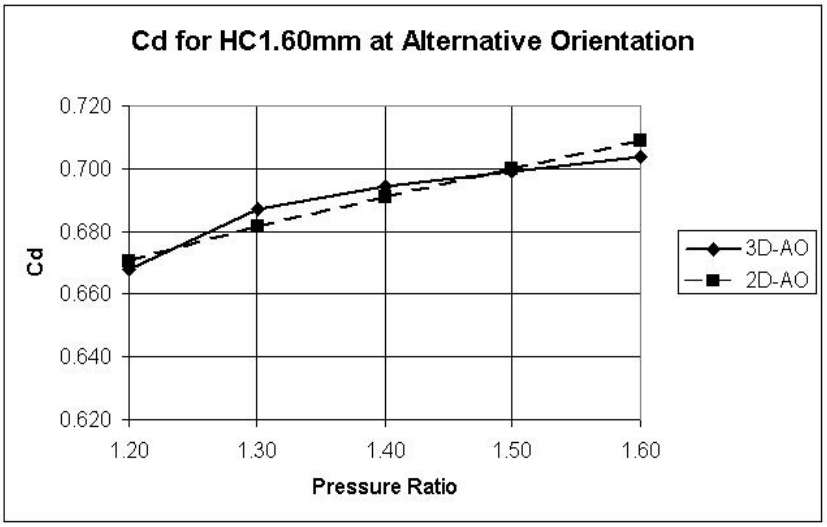

Figure E.5: C_d for HC = $1.60mm$, Alternative-Orientation Condition.

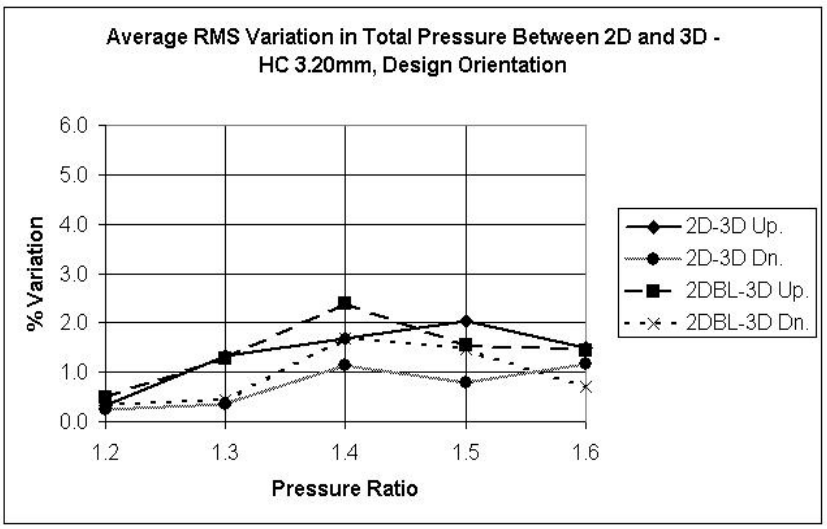

Figure E.6: RMS variation comparison at the middle of the up and downstream pockets. HC $3.20mm$, design-orientation.

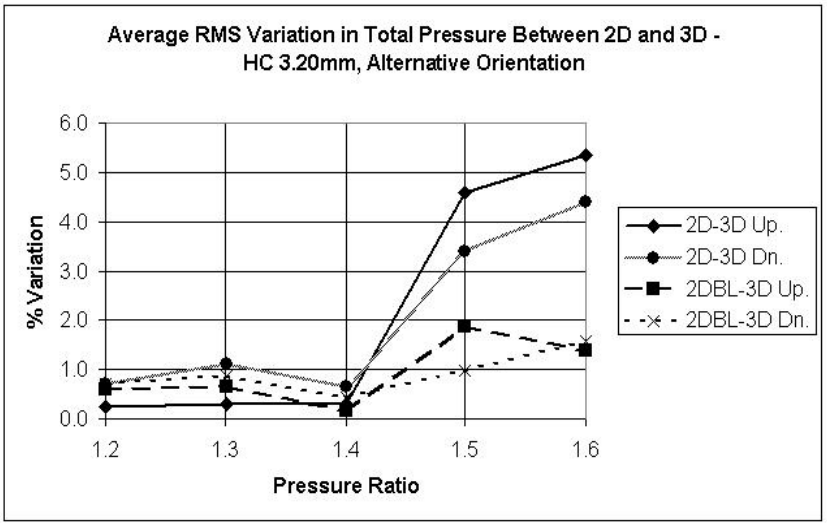

Figure E.7: RMS variation comparison at the middle of the up and downstream pockets. HC 3.20mm, alternative-orientation.

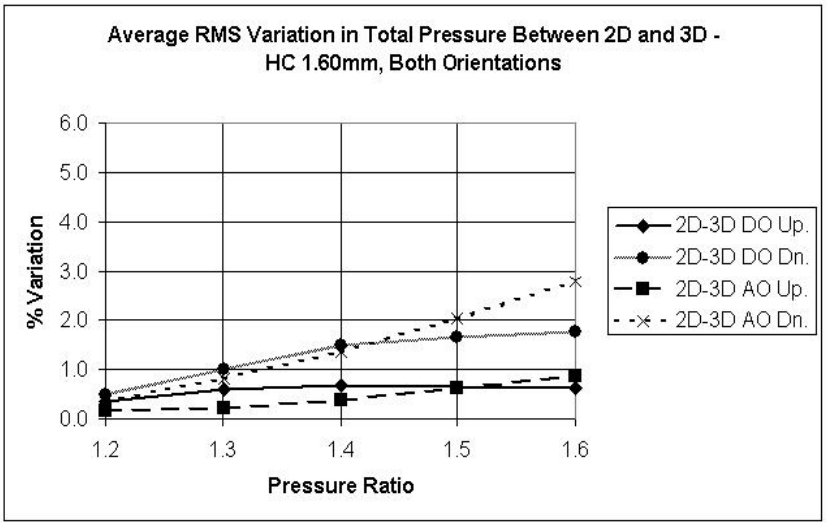

Figure E.8: RMS variation comparison at the middle of the up and downstream pockets. HC 1.60mm, both orientations.

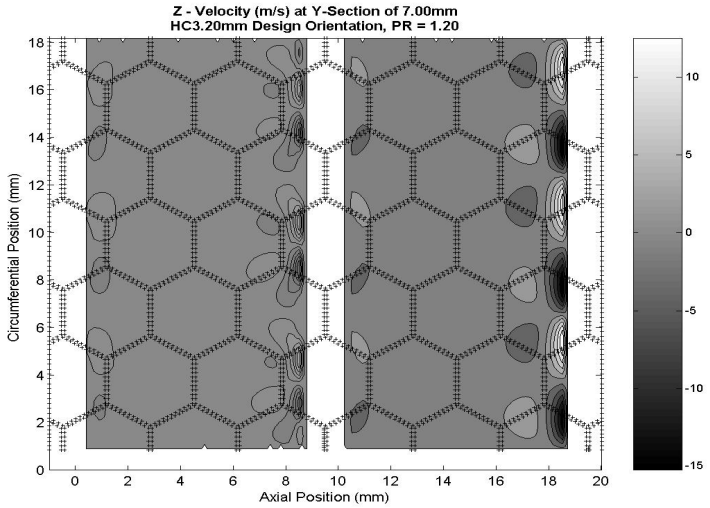

Figure E.9: Transverse-Velocity Component Generated due to honeycomb surface. Plane taken through seal at Y = 7.00mm. Honeycomb Size = 3.20mm at PR = 1.20. Design Orientation.

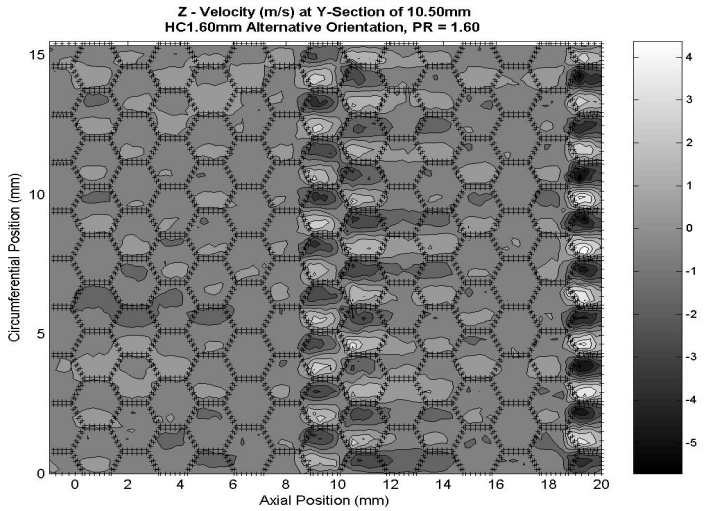

Figure E.10: Transverse-Velocity Component Generated due to honeycomb surface. Plane taken through seal at Y = 10.50mm. Honeycomb Size = 1.60mm at PR = 1.60. Alternative Orientation.

Appendix F

Numerical Simulation Figures

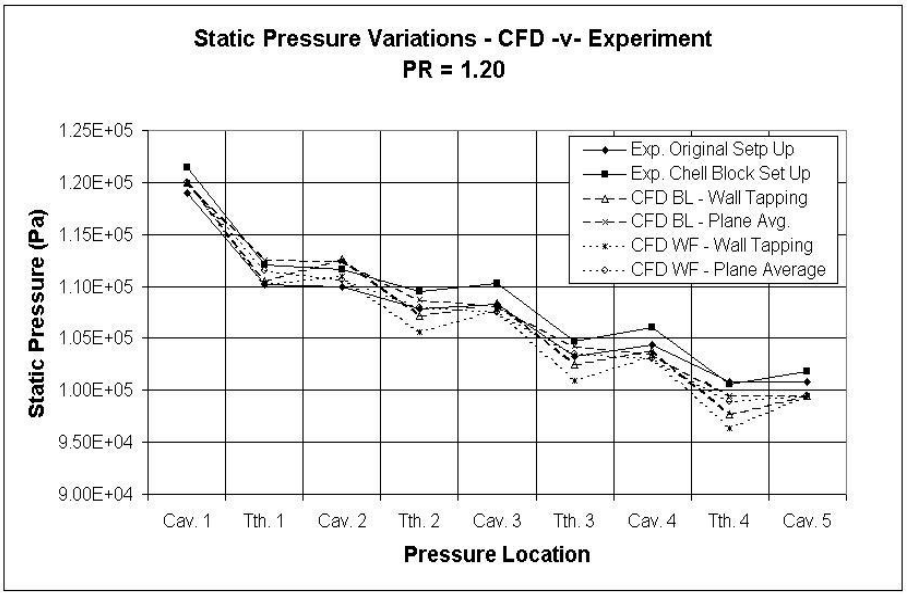

Figure F.1: Static pressures recorded by both experimental techniques and CFD. Blank metal, $0.50mm$ gap. PR = 1.20.

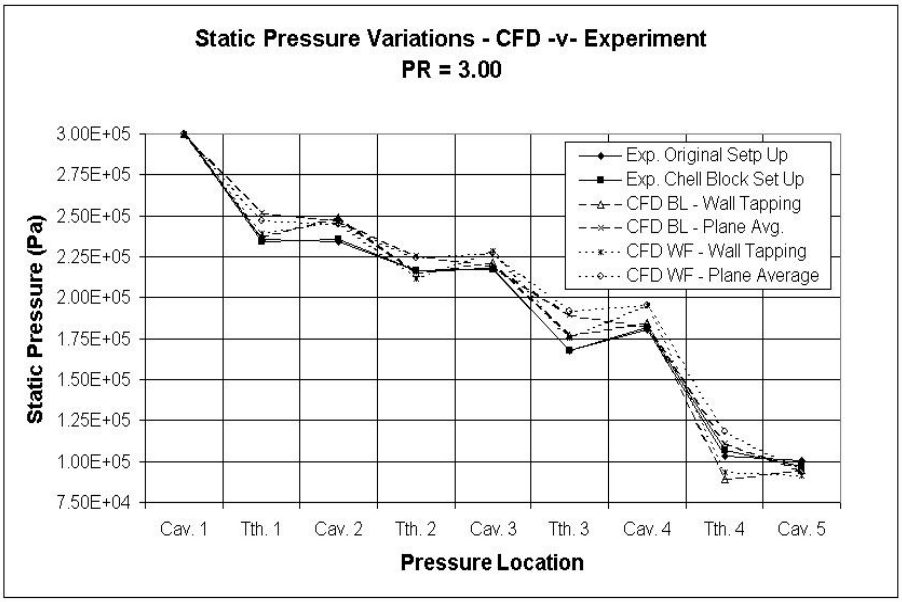

Figure F.2: Static pressures recorded by both experimental techniques and CFD. Blank metal, $0.50mm$ gap. PR = 3.00.

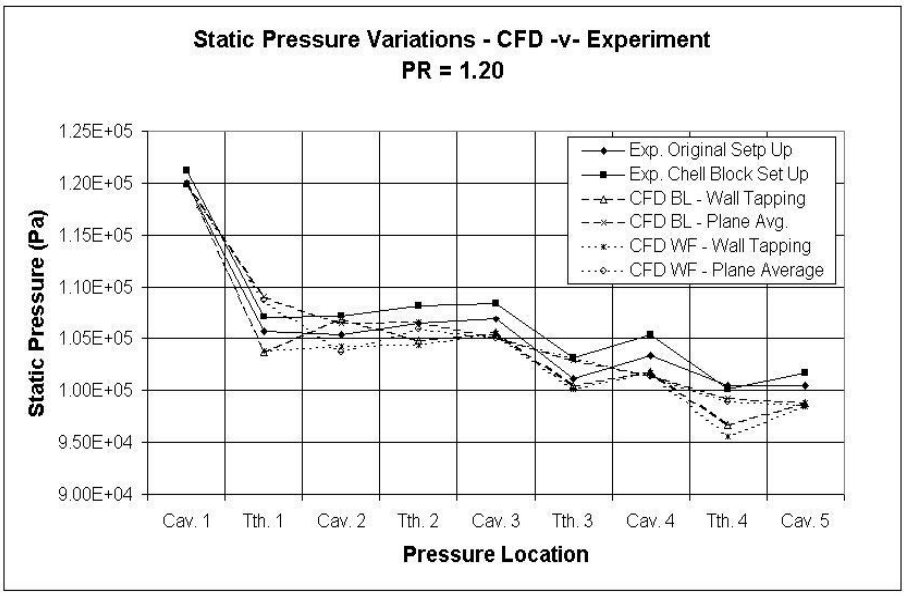

Figure F.3: Static pressures recorded by both experimental techniques and CFD. Blank metal, 1.00mm gap. PR = 1.20.

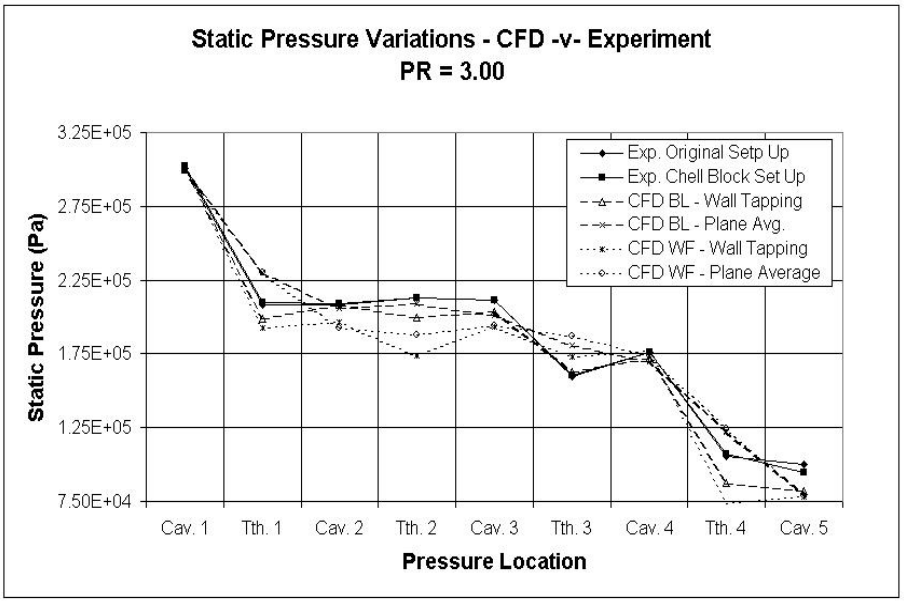

Figure F.4: Static pressures recorded by both experimental techniques and CFD. Blank metal, 1.00mm gap. PR = 3.00.

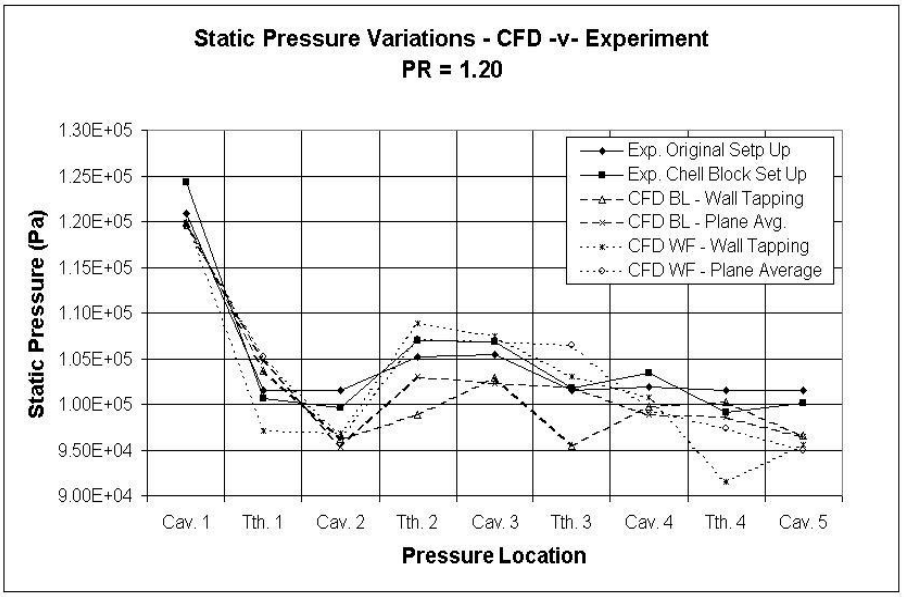

Figure F.5: Static pressures recorded by both experimental techniques and CFD. Blank metal, 2.00mm gap. PR = 1.20.

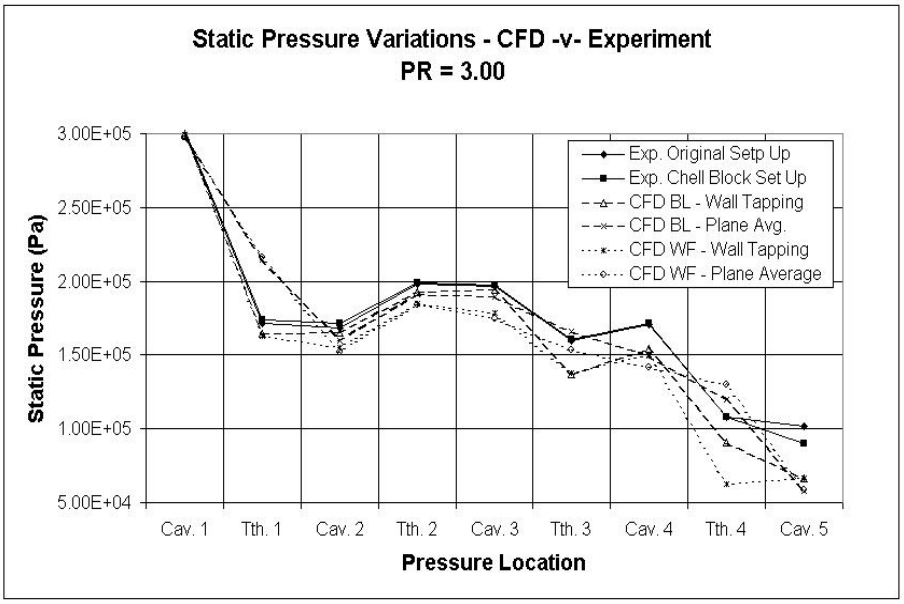

Figure F.6: Static pressures recorded by both experimental techniques and CFD. Blank metal, 2.00mm gap. PR = 3.00.

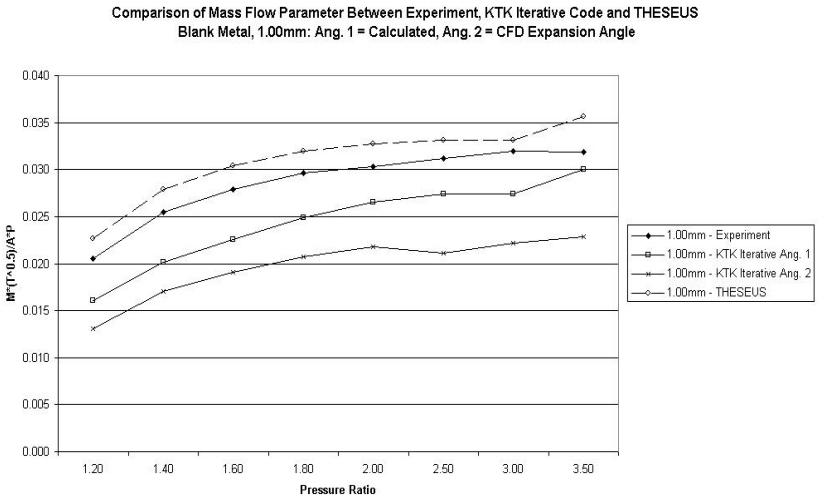

Figure F.7: Comparison of $\left(\frac{\dot{m}\sqrt{T_{t(0)}}}{AP_{t(0)}}\right)$ between Experiment, THESEUS and KTK. KTK in iterative mode with two angles: Ang. 1 as per internal code calculation, Ang. 2 derived from CFD

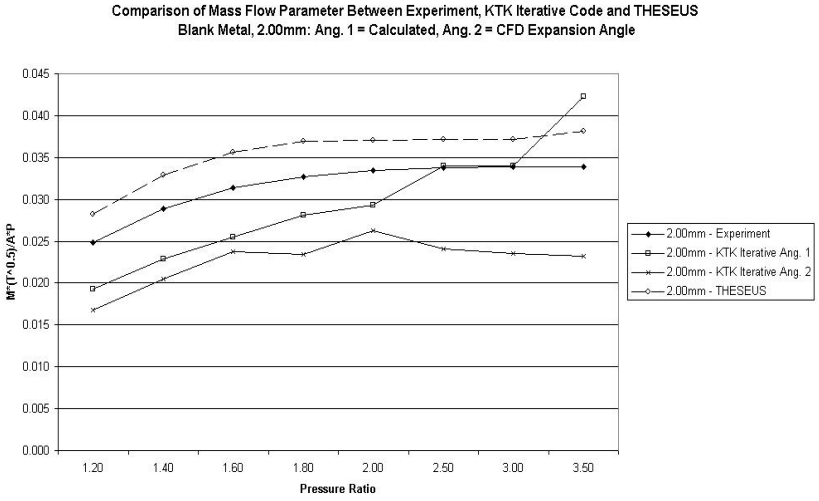

Figure F.8: Comparison of $\left(\frac{\dot{m}\sqrt{T_{t(0)}}}{AP_{t(0)}}\right)$ between Experiment, THESEUS and KTK. KTK in iterative mode with two angles: Ang. 1 as per internal code calculation, Ang. 2 derived from CFD

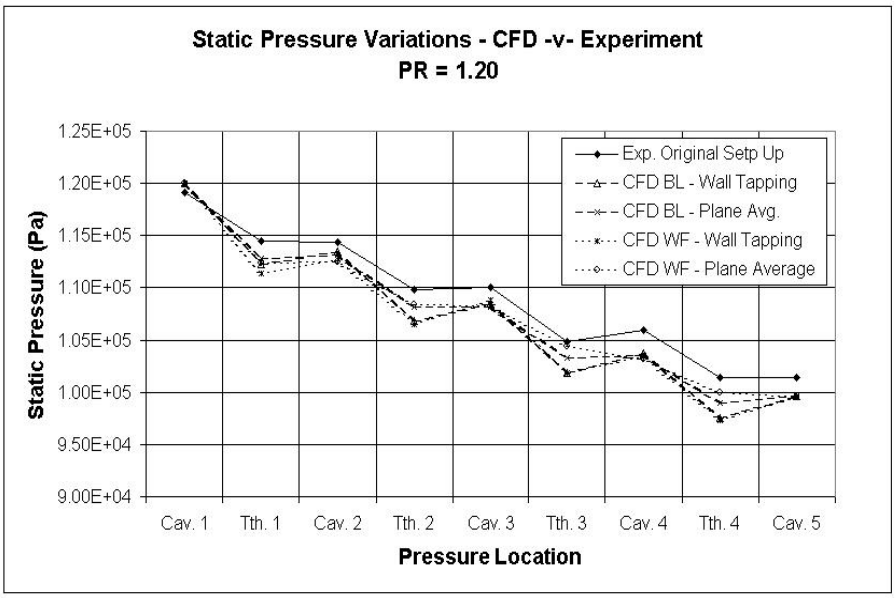

Figure F.9: Static pressures recorded by both experimental techniques and CFD. Flat Honeycomb, $0.50mm$ gap. PR = 1.20.

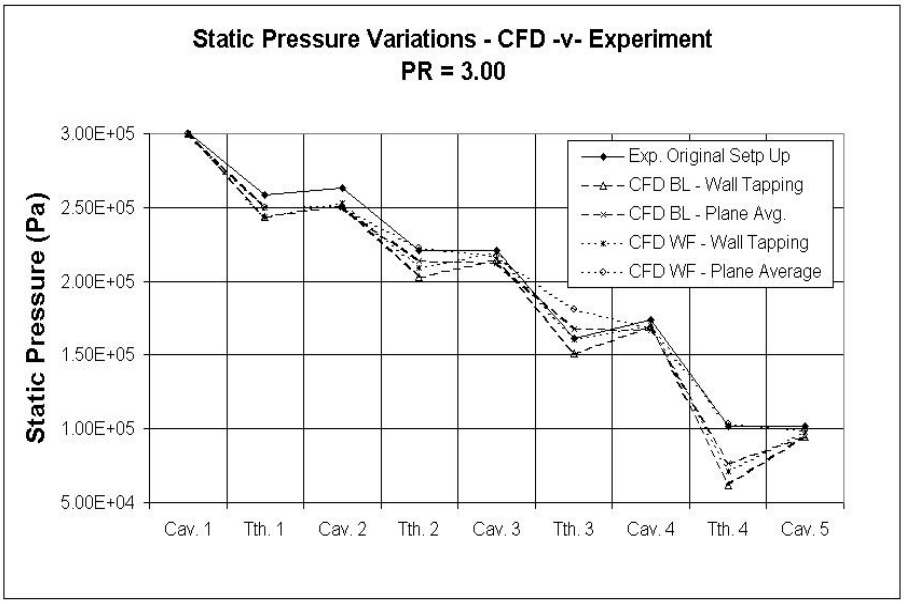

Figure F.10: Static pressures recorded by both experimental techniques and CFD. Flat Honeycomb, $0.50mm$ gap. PR = 3.00.

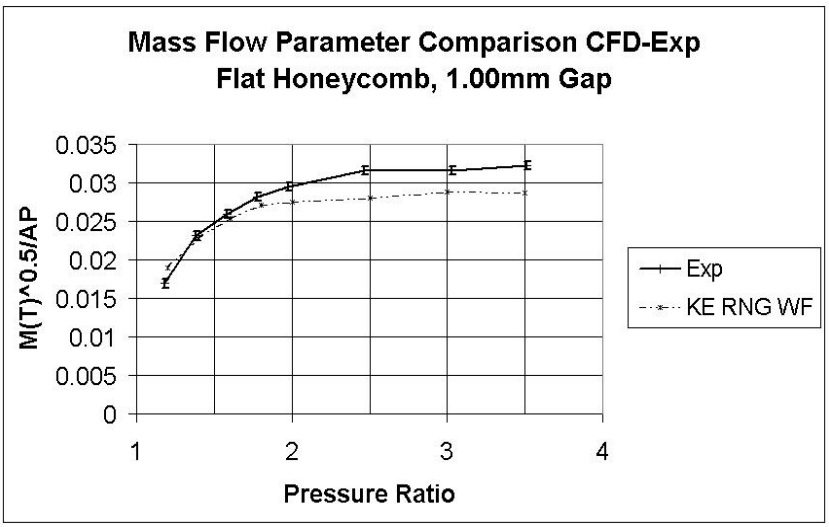

Figure F.11: $\left(\frac{\dot{m}\sqrt{T_{t(0)}}}{AP_{t(0)}}\right)$ comparison between the experimental data and CFD simulations.

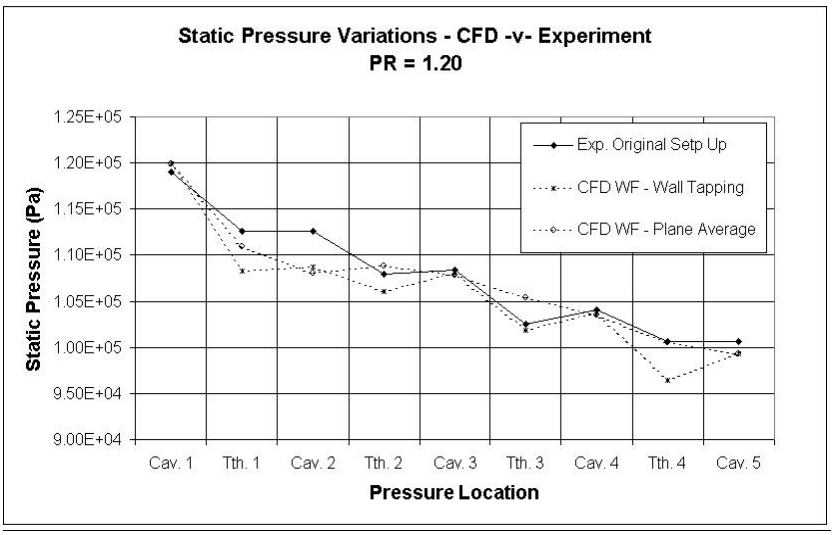

Figure F.12: Static pressures recorded by both experimental techniques and CFD. Flat Honeycomb, 1.00mm gap, Pressure Ratio = 1.20.

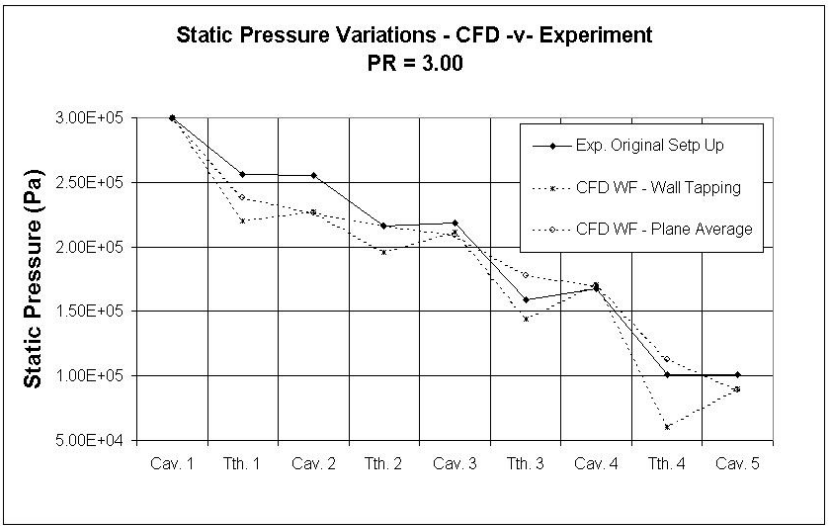

Figure F.13: Static pressures recorded by both experimental techniques and CFD. Flat Honeycomb, 1.00mm gap, Pressure Ratio = 3.00.

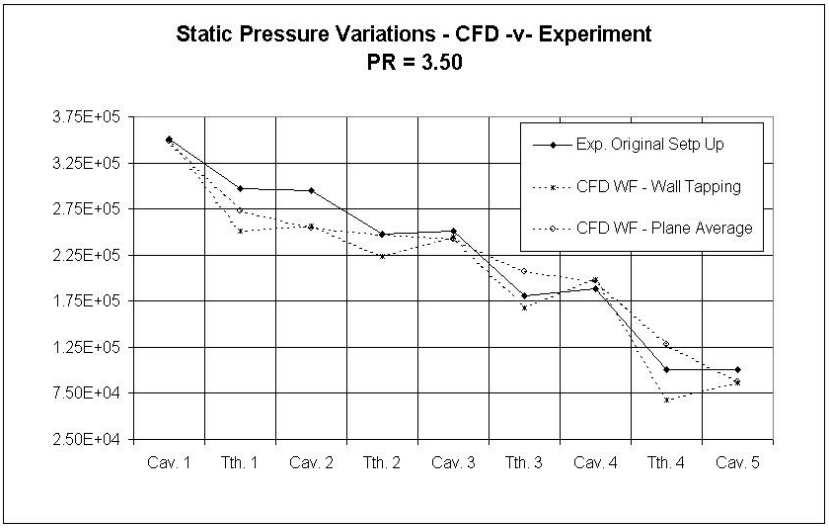

Figure F.14: Static pressures recorded by both experimental techniques and CFD. Flat Honeycomb, 1.00mm gap, Pressure Ratio = 3.50.

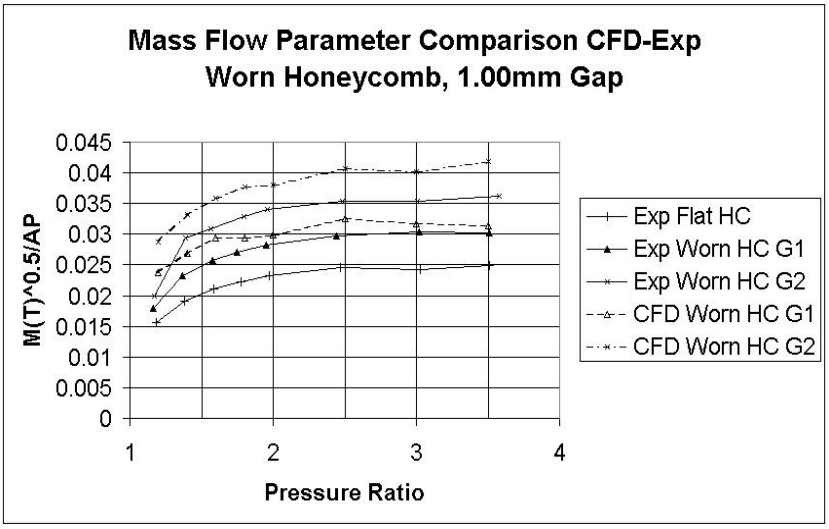

Figure F.15: Worn Honeycomb Comparison of $\left(\frac{\dot{m}\sqrt{T_{t(0)}}}{AP_{t(0)}}\right)$ at $1.00mm$ Clearance.

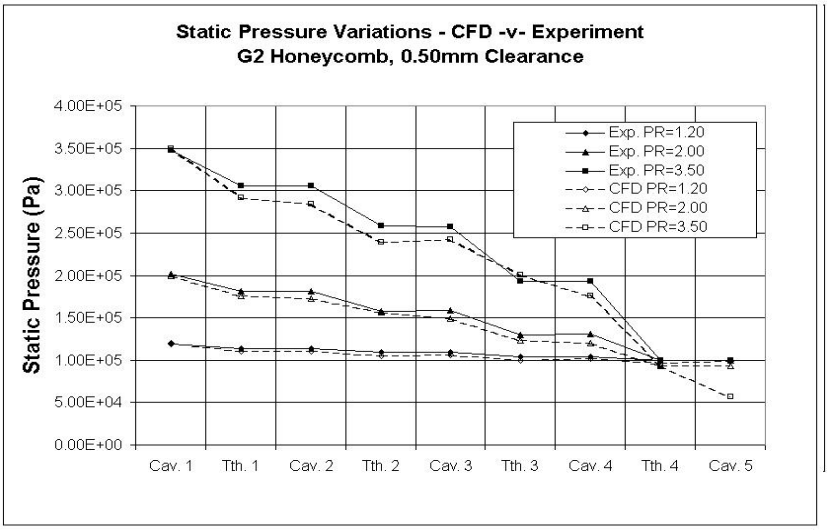

Figure F.16: Static Pressure Comparison Between Experimental Data and CFD with G2 worn Honeycomb at $0.50mm$. Various Pressure Ratios.

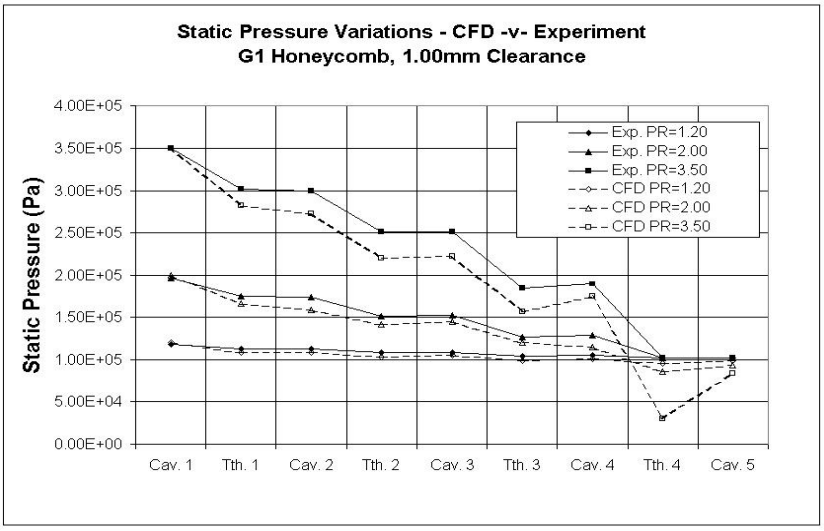

Figure F.17: Static Pressure Comparison Between Experimental Data and CFD with G1 worn Honeycomb at 1.00mm. Various Pressure Ratios.

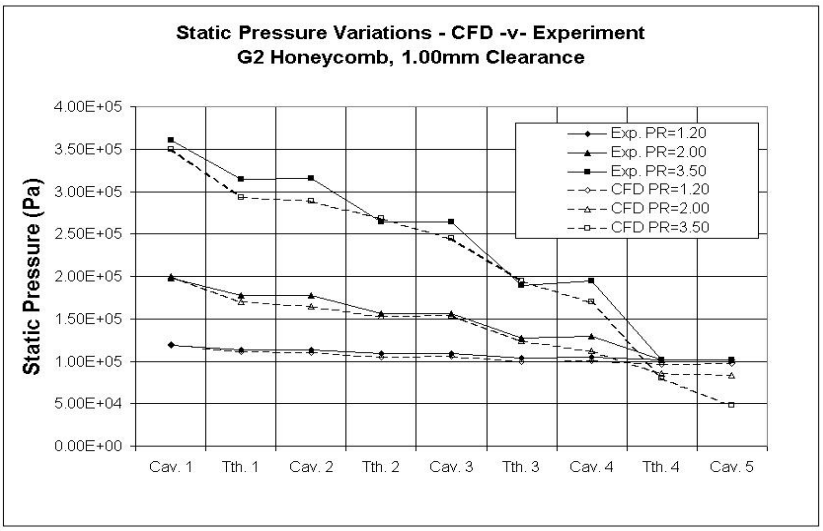

Figure F.18: Static Pressure Comparison Between Experimental Data and CFD with G2 worn Honeycomb at 1.00mm. Various Pressure Ratios.